

Analysis and visualization methods for interpretation of diffusion MRI data

Colophon:

This text was set using the freely available $\LaTeX 2_{\epsilon}$

Cover: A 5 mm thick coronal section, with fiber orientation glyphs on the left merging with fiber tracts reconstructed from them on the right.

ISBN: 978-90-393-6030-9

Cover design and layout: Sjoerd Vos

Printed by: Proefschriftmaken.nl || Uitgeverij BOXPress

Analysis and visualization methods for interpretation of diffusion MRI data

Analyse- en visualisatiemethoden voor de interpretatie van
diffusie MRI data

(met een samenvatting in het Nederlands)

Proefschrift

ter verkrijging van de graad van doctor aan de
Universiteit Utrecht

op gezag van de rector magnificus, prof. dr. G.J. van der Zwaan,
ingevolge het besluit van het college voor promoties
in het openbaar te verdedigen
op donderdag 24 oktober 2013 des middags te 2.30 uur

door

Sjoerd Bjintze Vos
geboren op 3 april 1986 te Utrecht

Promotor: prof. dr. ir. M.A. Viergever

Copromotor: dr. A.L.G. Leemans

The work described in this thesis was financially supported by the project Care4Me (Cooperative Advanced REsearch for Medical Efficiency) in the framework of the EU research program ITEA (Information Technology for European Advancement). The publication of this thesis was financially supported by Alzheimer Nederland, Biogen Idec International, Quantib, Röntgen Stichting Utrecht, and ImagO.

Contents

1	Introduction	1
2	The influence of complex white matter architecture on the mean diffusivity in diffusion tensor MRI	19
3	Partial volume effect as a hidden covariate in DTI analyses	39
4	Automated longitudinal intra-subject analysis for diffusion MRI tractography	61
5	HARDI and fiber tractography at 1 mm isotropic resolution	87
6	Multi-fiber tractography visualizations for diffusion MRI data	113
7	General discussion	139
	References	155
	Abbreviations	169
	Samenvatting	171
	Publications	177
	Prizes and awards	179
	Dankwoord	181
	About the author	187

Chapter 1

Introduction

Parts of this chapter are based on :

S.B. Vos, C.M.W. Tax, and A. Leemans, “Diffusion MRI and fiber tractography: The State-Of-The-Art and its Potential Impact on Patient Management”, PET Clinics 8:3 PET/MRI and Evolving Techniques, eds. T.C. Kwee, H. Zaidi, published by Elsevier B.V.

1.1 From diffusion to diffusion tensor magnetic resonance imaging

To introduce diffusion-weighted MRI (DWI), we must go back to the 19th century, when Robert Brown observed random motion of pollen particles suspended in water (Brown, 1828). All molecules in a fluid inherently have thermal energy that causes them to move around in a random fashion—a phenomenon now known as Brownian motion. Later, Albert Einstein described this physical process theoretically with the diffusion equation (Einstein, 1905): $\langle x^2 \rangle = 2Dt$. Here, $\langle x^2 \rangle$ denotes the mean squared displacement in one dimension, D the solution's diffusion coefficient, and t the diffusion time. So, for a certain value of D , the longer a group of molecules is allowed to move, the larger the spread of these molecules will be. In this equation, the medium in which particles diffuse is assumed to be homogeneous. In such a case, the mean squared displacement $\langle x^2 \rangle$ is independent of the direction in which particles move (hence, isotropic diffusion) as can be seen in Fig. 1.1a. If the medium is inhomogeneous, i.e., structured in some way, diffusion is not equal in all directions (hence, anisotropic diffusion), shown in Fig. 1.1b.

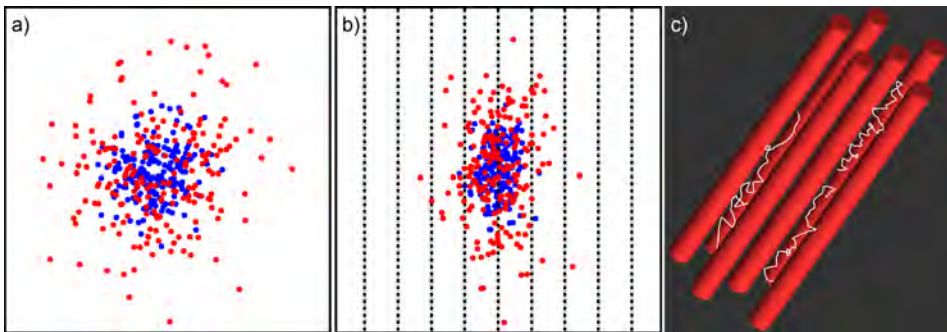


Figure 1.1: a) The dots visualize the displacement of 200 particles over a certain time t (blue dots) and $2t$ (red dots). b) Semi-permeable barriers, as indicated by the dashed lines, can hinder diffusion along one direction but not the other. This results in diffusion that is not equal in all directions, called anisotropic diffusion. c) Axons—represented as red cylinders—can be regarded as (semi-permeable) barriers, causing an anisotropic diffusion pattern (white trajectories) in the brain tissue.

Diffusion not only takes place in pure fluids, it is also present in tissue that contains fluid particles, such as the brain (over 75% of the brain consists of water molecules). The brain consists of roughly 100 billion (10^{11}) neurons (Lange, 1975), and each neuron has a complex cell structure—including cytoskeletal filaments, membranes, a myelin sheath—that hinders or restricts diffusion within and in between these neurons (Fig.

1.1c, Beaulieu, 2002). As a result, the diffusion medium in the brain is very inhomogeneous, making diffusion highly anisotropic (Moseley et al., 1990).

1.1.1 Basic concepts of MRI

Magnetic resonance imaging (MRI) is a versatile non-invasive imaging technique that can give very high contrast between different soft tissues in our body. As a result, it is an essential imaging method for diagnostic purposes, being performed roughly 815.000 times in the Netherlands in 2010¹.

The MRI signal originates from protons in the tissue, each of which can be regarded as a tiny magnet, with a north- and a south-pole. When these protons are placed in a strong magnetic field, such as an MR scanner, they will align with the field—just as the needle in a compass will align with the Earth's magnetic field. The main magnetic field in an MR scanner, called the B₀-field, causes an equilibrium magnetization along the direction of this field, conventionally called the z-direction. This magnetization is the net sum vector of protons—or spins—along this direction, and is called the longitudinal magnetization, M_Z. Even though the protons are aligned with the B₀-field, they also spin around their axis, which is called precession. This precession occurs at a single frequency, the Larmor frequency or resonance frequency, which is an essential concept in MRI. This Larmor frequency does not only describe how fast spins precess, but it is also the frequency we need to use when manipulating these spins. Energy from radio-frequency (RF) pulses at this Larmor frequency can be absorbed by the spins, and will change the orientation of the spins. We need this because we can only measure the part of the magnetization that is in the transverse plane (called M_{XY}), so perpendicular to M_Z. When spins are in their equilibrium position along the B₀-field, we can use an RF pulse to flip the spins into the transverse plane, which is called excitation.

The simplest way is to flip the magnetization by 90° degrees until M_Z is completely transformed into M_{XY} (Fig. 1.2a). Directly after excitation, all spins are aligned perfectly, called 'in-phase' (a), which means they all start their rotations around their axes at the same time. Due to the interaction of spins with surrounding spins, the magnetic properties vary slightly from spin to spin, causing their precession frequency to alter slightly as well. Consequently, spins they are no longer all 'in-phase', but have 'de-phased', due to the difference in frequency (b,c). Because at any moment in time the spins will not be perfectly aligned, this effectively decreases the net sum of all these spins, M_{XY}. This is called spin-spin relaxation, or T₂-relaxation. To generate an image, the signal (M_{XY}) can be read out directly or some time after excitation. Over time, the spins will also realign along the B₀-field depending on the structure within which the spins are located, a process called T₁-relaxation. T₁-relaxation is a slow process

1. On average 49.1 times per 1000 population, www.cbs.nl and www.oecd-ilibrary.org

compared to T2-relaxation. The timings and magnitude of the RF pulses as well as the readout timing can be changed to get a different combination of T1 and T2-relaxation, creating different image contrasts, each with specific information about the tissue.

Placing an object—such as a scan subject—in the MRI magnet causes the B0-field to be slightly altered, resulting in additional dephasing and thus signal loss. To recover this signal, a ‘spin echo’ image can be generated, where the spins are partially refocused. This is for instance used in conventional diffusion MRI methods. In a spin-echo experiment, a refocusing pulse (a 180° RF pulse) is given at a certain time after excitation. The refocusing pulse inverts the phase of the spins (d), so that each spin rephases (e) as much as it has dephased, ensuring coherence during readout which maximizes the MR signal (f).

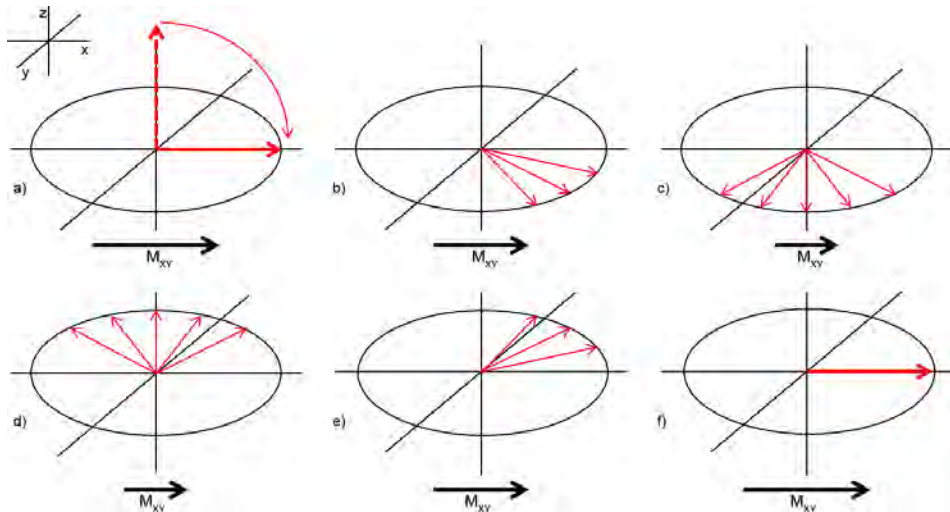


Figure 1.2: An excitation pulse flips the longitudinal magnetization to the transverse plane (a). After excitation, spins dephase due to spin-spin interaction (b,c). A refocusing pulse inverts the phase of the spins (d), and the spins will refocus (e), forming an ‘echo’ (f).

1.1.2 Diffusion weighted imaging

The ‘standard’ MR signal can be adapted to make the signal diffusion-weighted. Conventional diffusion MRI methods are based on a T2-weighted spin echo image, the sequence diagram of which is shown in Fig. 1.3. Most often, an echo-planar imaging (EPI) readout is used because this is one of the fastest methods to generate an image (Mansfield and Pykett, 1978). Acquisition of a T2-weighted spin echo image is done by excitation (90° RF pulse), followed by a refocusing pulse (180°) and readout during

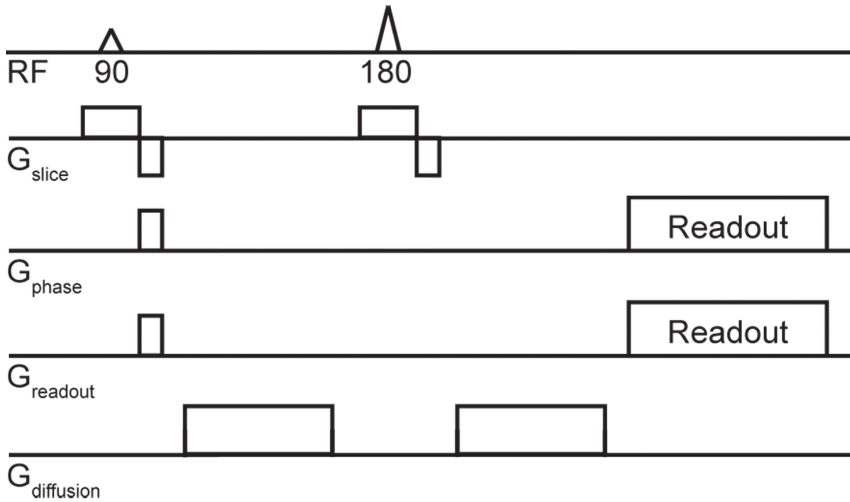


Figure 1.3: Sequence diagram of a diffusion-weighted spin echo EPI image.

the echo (a combination of G_{phase} and G_{readout}). To make a diffusion-weighted image, diffusion-weighting gradients ($G_{\text{diffusion}}$) can be applied around the refocusing pulse. The effects of these components is shown in Fig. 1.4. If a diffusion-weighting gradient is applied, spins will dephase depending on the magnitude of the magnetic field at each spin's spatial location. Static spins will experience the same gradient magnitude during the first and the second diffusion gradient, and thus refocus completely (top row). If spins diffuse, they may experience a different gradient magnitude during the first and second gradient, in which case there will be incomplete rephasing, and thus signal loss (bottom row). Only diffusion along the orientation of the diffusion gradient causes signal decay: as shown in Fig. 1.4, the spins that moved up-and-down experienced the same magnetic field during the two gradient and thus refocus completely. As a result, the direction along which the diffusion-weighted gradient is applied, denoted by \mathbf{g} is important in case of anisotropic diffusion.

With a diffusion-weighted image (DWI) being conceptually an expansion of a T2-weighted image, the diffusion-weighted (DW) signal is also an expansion of the T2-weighted signal (Stejskal and Tanner, 1965):

$$S_{\mathbf{g}} = S_0 e^{-T_2/TE} e^{-bD_{\mathbf{g}}} = S_{T_2} e^{-bD_{\mathbf{g}}} . \quad (1.1)$$

Here, $S_{\mathbf{g}}$ is the diffusion-weighted signal along gradient direction \mathbf{g} , S_0 is the signal after excitation, T_2 the tissue-specific transverse relaxation time, TE is the time at which

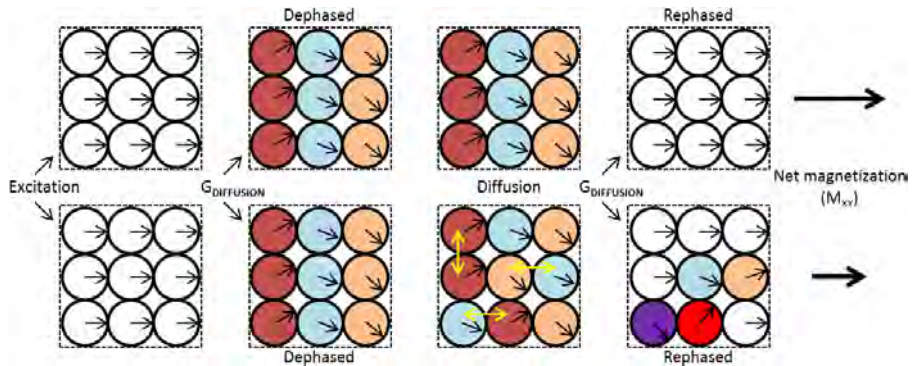


Figure 1.4: Schematic representation of diffusion-induced signal attenuation. From left to right: after excitation the spins start dephasing due to the diffusion-weighting gradients ($G_{\text{diffusion}}$). The spatially varying $G_{\text{diffusion}}$ causes spins on the left to experience a smaller gradient magnitude than spins on the right. Spins that diffuse in the orientation of $G_{\text{diffusion}}$ will experience a different gradient magnitude during the second, rephasing $G_{\text{diffusion}}$. Consequently, these spins will not be fully in-phase, resulting in signal loss due to a lower net magnetization of the spins. By contrast, stationary spins (top row) will be fully rephased after the second diffusion gradient.

the signal echo is read out, S_{T_2} is the T2-weighted or non-diffusion weighted signal (Fig. 1.5a), b is the ‘b-value’ (i.e., the magnitude of diffusion weighting) and $D_{\mathbf{g}}$ is the diffusion coefficient along \mathbf{g} . The b-value depends on the magnitude and timing of the diffusion gradients (Fig. 1.3): i) longer time between the gradients allows for more diffusion, and thus more spins that will rephase incompletely; ii) larger gradients will cause a larger phase differences between spins at different locations, so spin that diffuses will rephase less. In DWI, it is common to name the diffusion coefficient (D , or $D_{\mathbf{g}}$) the apparent diffusion coefficient (ADC), because it reflects the estimated diffusion from our MR measurements, not the “true” microstructural diffusion. From Eq. (1.1) it is clear that the ADC can be quantified using one DW and one non-DW measurement. The anisotropic diffusion in the brain can be observed when acquiring diffusion-weighted images (DWIs) with different diffusion gradient directions \mathbf{g} (Moseley et al., 1990), as shown in Fig. 1.5b,c. The decrease in signal with b-value is shown comparing Fig. 1.5c and d.

1.1.3 Diffusion tensor imaging

Diffusion is largest parallel to the orientation of brain fibers, and smallest perpendicular to the fiber orientation (Moseley et al., 1990; Cleveland et al., 1976). Moseley et al. (1990) suggested using this knowledge to determine fiber orientations from the MR measurements, but a generalized quantification was first described in 1994, when

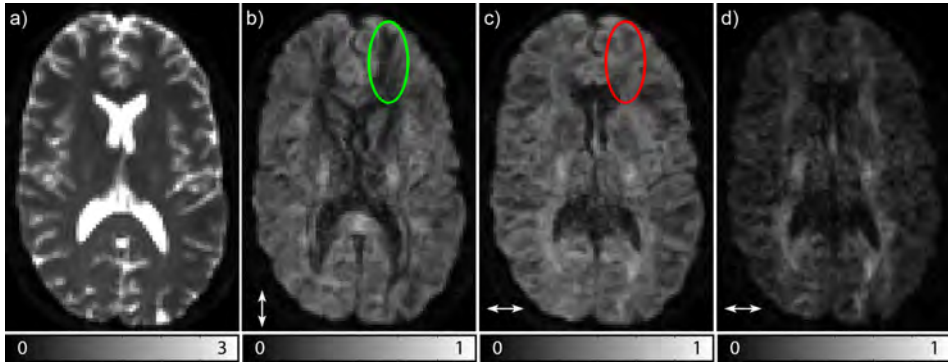


Figure 1.5: Non-diffusion weighted image (a) and diffusion-weighted images (DWIs) with different diffusion directions indicated with the arrows in b-d. Throughout the brain, differences in contrast between the different diffusion directions can be observed, caused by anisotropic diffusion. The ellipses in b and c indicate regions of highly anisotropic diffusion. Diffusion causes signal attenuation, so regions of low intensity—e.g., the ellipse in b—are caused by a high diffusivity in that direction, whereas hyperintense regions—e.g., the ellipse in c—by a low diffusivity along that direction. DWIs in b and c were acquired with $b = 1000 \text{ s/mm}^2$; d) with $b = 2500 \text{ s/mm}^2$, illustrating how signal decreases with the b-value.

(Basser et al., 1994) proposed diffusion tensor imaging (DTI). In DTI, the diffusion profile in each imaging voxel is modeled as a second-rank tensor, \mathbf{D} :

$$\mathbf{D} = \begin{pmatrix} D_{xx} & D_{xy} & D_{xz} \\ D_{yx} & D_{yy} & D_{yz} \\ D_{zx} & D_{zy} & D_{zz} \end{pmatrix}.$$

Here, the diagonal components D_{xx} , D_{yy} , and D_{zz} are the ADC values in the x-, y-, and z-direction, and the off-diagonal components denote the correlations between the diagonal values. For instance, a high D_{xy} would indicate a high correlation between diffusion in the x- and y-direction. Conceptually, \mathbf{D} can be visualized as an ellipsoid with its surface representing the probability distribution of the mean squared displacement (Fig. 1.6A). Because diffusion does not occur in a direction but along an axis (e.g., not from x to $-x$ but rather along the x-axis), it is impossible to distinguish between diffusion from $-x$ to x and diffusion from x to $-x$. This means that D_{xy} and D_{yx} are equal (similarly, $D_{xz} = D_{zx}$ and $D_{yz} = D_{zy}$), making \mathbf{D} a symmetric tensor. This symmetry means there are only six unknown components in \mathbf{D} , so we need at least six unique diffusion measurements, i.e., six DW and one non-DW image. These six DWIs must be

acquired with gradient directions that are non-collinear, i.e., orientationally independent of each other.

The tensor describes the estimated diffusion profile based on the standard global coordinate system (x, y, z), as used in the MRI. Defining a local coordinate system for each voxel separately enables us to formulate the tensor independent of the orientation of the tensor (Fig. 1.6). The diffusion tensor can be defined by three perpendicular vectors, called eigenvectors, along which diffusion can be measured independently of the other orientations. The magnitudes of diffusion along these three eigenvectors (ϵ_1, ϵ_2 , and ϵ_3) are called the eigenvalues (λ_1, λ_2 , and λ_3). The eigenvectors and -values are ordered such that the first eigenvector, ϵ_1 , corresponds to the largest eigenvalue, λ_1 . In other words, the first eigenvector is the orientation along which the diffusion is highest. Assuming that this dominant diffusion oriented is parallel to the fiber pathways, ϵ_1 reflects the main axis of these fiber trajectories.

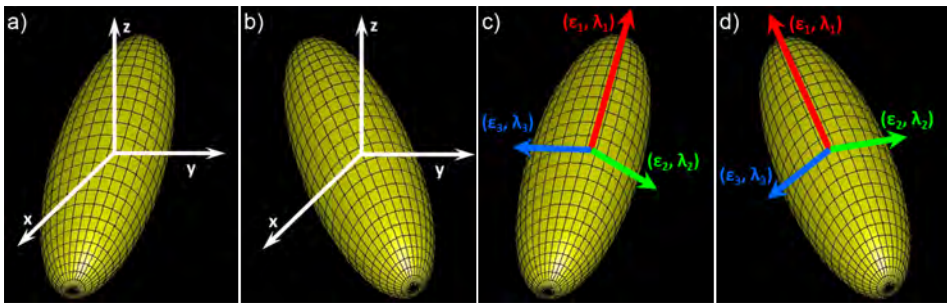


Figure 1.6: The diffusion tensor can be visualized as an ellipsoid, where the surface represents the surface of mean displacement. This means that at a given time t , there is equal probability of finding a diffused molecule anywhere on the surface. In a global coordinate system (a & b), each tensor component—e.g., D_{xx} —is dependent on the orientation of the tensor. In a local coordinate system (c & d), the eigenvectors ($\epsilon_1 - \epsilon_3$) and eigenvalues ($\lambda_1 - \lambda_3$) describe the principal diffusion directions and their magnitudes, respectively.

1.1.4 DTI and quantitative measures

There are several scalar measures that can be extracted from the diffusion tensor. The most intuitive of these is the mean diffusivity (MD)—equal to the average of the three eigenvalues—describing the overall magnitude of the diffusion. In cerebro-spinal fluid (CSF) regions, for instance, MD values are in the order of $3 \times 10^{-3} \text{ mm}^2/\text{s}$. By contrast, the MD of brain white and gray matter is roughly 0.7×10^{-3} and $0.8 \times 10^{-3} \text{ mm}^2/\text{s}$, respectively (Le Bihan et al., 2001). Another popular property of the diffusion tensor is the degree of anisotropy with which diffusion occurs. While there are several anisotropy metrics (Pierpaoli et al., 1996), the most common measure is the fractional anisotropy

(FA), which basically represents the standard deviation of the eigenvalues, scaled between 0, isotropic, and 1, totally anisotropic (Basser, 1995). Example images of these two DTI metrics are shown in Fig. 1.7a,b. The local fiber orientation can be visualized in a diffusion-encoded color (DEC) map (Fig. 1.7c), where the FA image is color-encoded based on the orientation of largest diffusion, ϵ_1 (green indicates that ϵ_1 is oriented anterior-posterior, red means left-right, blue is inferior-superior).

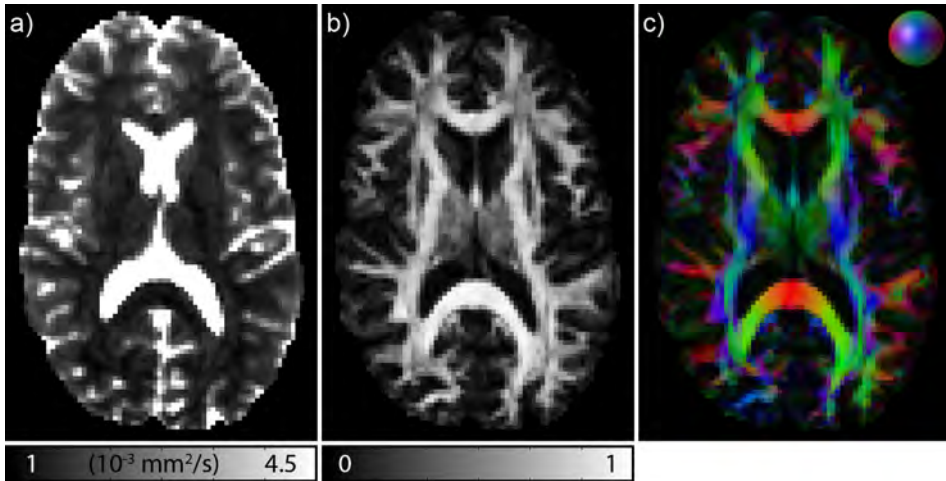


Figure 1.7: a) Mean diffusivity; b) fractional anisotropy (FA); and c) diffusion-encoded-color (DEC) map. The DEC-map in c) is color-encoded by the direction of the first eigenvector (ϵ_1), as indicated by the color index sphere in the top right corner: green indicates anterior-posterior; red means left-right; and blue is inferior-superior. The intensity in c) is scaled by the FA, so that regions of low anisotropy, where ϵ_1 is less informative, have a lower intensity.

Changes in brain microstructure modulate both the magnitude and anisotropy of diffusion. For instance, Hanyu et al. (1997) have shown that in Alzheimer disease these diffusional changes can be observed before any abnormalities could be observed in conventional MR images (later in this chapter Alzheimer disease, and other pathologies, will be discussed in more detail). Despite being sensitive, it should be clear that changes in FA are not specific. For instance, a decrease in FA could be caused by either a decrease in λ_1 , increases in λ_2 and/or λ_3 , or both of these happening simultaneously. To further understand what is driving the diffusion anisotropy, two other DTI measures are often used (Basser, 1995; Song et al., 2002): the axial diffusivity, i.e., the diffusion parallel to the fiber orientation ($\lambda_{\text{par}} = \lambda_1$); and the radial diffusivity, the average of the diffusivities perpendicular to the fiber ($\lambda_{\text{rad}} = (\lambda_2 + \lambda_3)/2$).

1.2 Fiber tractography

The principal diffusion direction of the diffusion tensor (ellipsoid) is given by ϵ_1 and can be calculated for each voxel. Plotting these first eigenvectors therefore yields a discrete representation of the main diffusion directions throughout the brain. This is shown in Fig. 1.8b, where diffusion ellipsoids (left hemisphere) and first eigenvectors (right hemisphere) are shown. From these voxel-wise ‘glyph objects’, or glyphs, one can already appreciate the voxel-by-voxel continuity in the diffusion orientations. From the first eigenvectors at each voxel, one can also create continuous representations of the principal diffusion orientations. This virtual reconstruction of fiber tract pathways is called fiber tractography (FT) or fiber tracking (Mori et al., 1999; Basser et al., 2000). Starting from a certain voxel within the brain, one can create a fiber tract pathway in a step-wise way by following ϵ_1 in each subsequent voxel. This fiber pathway (Fig. 1.8c) gives a more continuous representation than the eigenvectors, resulting in a more intuitive image of the data. Reconstruction of fiber tracts throughout the entire brain,

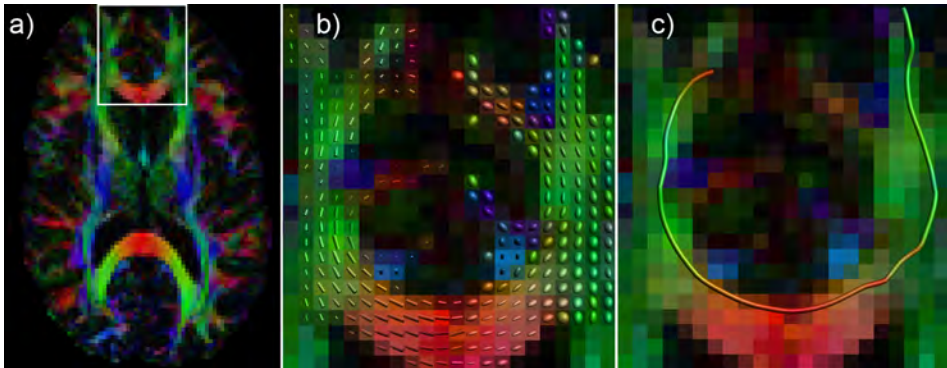


Figure 1.8: a) Axial slice of a diffusion-encoded color (DEC) map. Enlargement of the genu of the corpus callosum, indicated, is shown in b) and c). b) Diffusion tensor properties are visualized as voxel-wise glyph objects: the diffusion ellipsoid for the left hemisphere; the first eigenvectors (ϵ_1), shown as tubes, for the right hemisphere. Like the DEC map, the glyphs are colored by the orientation of ϵ_1 . From these discrete representations, fiber tractography can be used to generate a continuous fiber tract pathway, shown in c).

termed ‘whole brain’ tractography, is possible by tract propagation at each location (Fig. 1.9a-c). Although such a set of fiber tracts may seem one big tangle, it can be disentangled with a priori anatomical knowledge of the location of specific fiber bundles. For instance, post-mortem anatomical studies have shown that the arcuate fasciculus is known to connect the language areas of Broca, Wernicke, and Geschwind (Dejerine, 1895; Benson et al., 1973; Geschwind, 1965). As such, identification of these areas

can guide us to select the pathways of the arcuate fasciculus, Fig. 1.9d-f (Wakana et al., 2004; Catani et al., 2005).

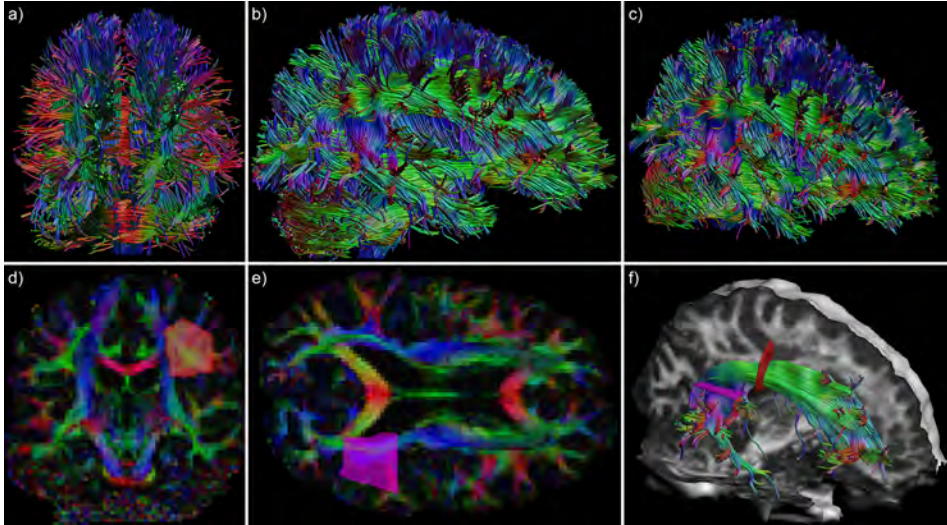


Figure 1.9: ‘Whole brain’ tractography results shown from a coronal (a), sagittal (b), and oblique (c) angle. By delineating two regions-of-interest (ROIs) around the known locations of a specific white matter fiber bundle, only those reconstructed tract pathways are selected that intersect both these regions. For the left arcuate fasciculus, a coronal (d) and axial (e) ROI are sufficient to select the whole bundle, f), shown in the same orientation as C).

Selection of fiber bundles can also be used to investigate diffusion metrics in specific brain regions. For instance, FA or MD values can be averaged over the voxels along the selected fiber tract bundle (Jones et al., 2005b; Reijmer et al., 2013b). Manual delineation of the ROIs is very reproducible with a high intra- and inter-rater agreement (Ciccarelli et al., 2003; Heiervang et al., 2006; Wakana et al., 2007; Kristo et al., 2013a), however, for large population studies this can be very time-consuming. Several methods have previously been proposed for (semi-) automated segmentation in various ways (including Lebel et al., 2008; Guevara et al., 2012; de Luis-García et al., 2013). However beneficial these methods are to decrease manual effort in analyses, the high accuracy and precision of manual segmentations for quantitative analyses have not been demonstrated for these (semi-) automated approaches. Other ways of analyzing DTI data have been used in the literature—including ROI-based, voxel-based, atlas-based, or network-based (e.g., Ashburner and Friston, 2000; Snook et al., 2005; Smith et al., 2006; Hagmann et al., 2008; Mori et al., 2008)—but are not used in this thesis. A detailed overview of these methods is given in Cercignani (2011).

1.3 Clinical and preclinical use of diffusion MRI

There are a myriad of brain pathologies, with each disease originating from different physiological changes, causing different clinical symptoms, and requiring specific treatment (if available). This variety in tissue changes means there is a huge potential for the use of diffusion MRI to investigate what happens on a microstructural level during the course of these diseases. DTI is used extensively in clinical research studies, with most studies comparing DTI parameters like FA and MD between patients and controls, trying to correlate these changes with clinical parameters. A few pathologies are described with recent studies showing important conclusions based on diffusion MRI.

1.3.1 Alzheimer disease

In Alzheimer disease, patients initially have deficits in mental functioning like emotional behavior, perception and memory. Neurons and synapses in the cerebral cortex and subcortical regions degrade, which results in atrophy of the affected structures (Fox et al., 1999). Diffusion MRI can detect these changes in WM microstructure, and can give insight in the type of microstructural damage by looking at changes in MD and FA (Bozzali et al., 2002). Mild cognitive impairment is a syndrome that often leads to Alzheimer disease, and it is important to distinguish those patients that do and those that don't progress to Alzheimer. Traditional biomarkers such as CSF levels of tau protein and amyloid β_{42} are good diagnostic predictors of conversion from mild cognitive impairment to Alzheimer. Recently, in a small patient population, FA, MD, and the radial diffusivity have been shown to be even better predictors of disease progression (Selnes et al., 2013).

1.3.2 Cancer

DTI is also sensitive to microstructural changes after cancer treatment. After chemotherapy treatment of breast cancer, patients experienced cognitive deficits that were correlated with lower FA values in the corpus callosum (Abraham et al., 2008). Changes in FA and MD were detected in patients—as compared to controls—throughout the brain, with larger changes in patients with cognitive impairment (Deprez et al., 2011; de Ruiter et al., 2012). Concomitant changes in radial diffusivity observed in these studies indicate that myelin degradation is the most likely underlying cause (Song et al., 2002; Deprez et al., 2013).

1.3.3 Traumatic Brain Injury

In traumatic brain injury, DTI has the potential to detect subtle changes throughout the WM in the sub-acute or chronic phases, showing axonal injury where conventional

MR images show no change (e.g., Arfanakis et al., 2002). This diffuse brain damage can result in long-term behavioral and cognitive changes that are associated with changes in DTI parameters (Kraus et al., 2007). As a result, DTI measures such as FA may provide an important noninvasive marker of microstructural injury to predict clinical outcome of patients (Huisman et al., 2004; Niogi and Mukherjee, 2010).

1.3.4 Neurosurgery

Already since the early development of diffusion MRI, the potential of tractography in neurosurgical planning was evident. With complete removal of the lesion being the primary goal of neurosurgery, it is important not to cause too much functional damage during surgery that can worsen the situation of the patient. The position of nearby fiber tract pathways can be visualized relative to the lesion (Clark et al., 2003), which is why the use of fiber tracking in pre-operative planning may improve post-surgical outcome (Witwer et al., 2002).

1.4 From DTI to state-of-the-art diffusion MRI

The cellular components that hinder diffusion, and thus cause the diffusion contrast, include the cell membranes and myelin sheaths around the axons, which have a size in the order of microns (Beaulieu, 2002). The standard MR imaging voxel in DTI has dimensions in the order of millimeters, a difference in length scale of 10^3 with the diffusion that we intend to estimate. The diffusion tensor framework is based on the assumption that the diffusion profile in each imaging voxel can be characterized with a Gaussian distribution (i.e., the diffusion tensor). In voxels with multiple fiber populations (e.g., fibers crossing within a voxel) or multiple fiber orientations (e.g., bending fibers), however, the diffusion signal can no longer be described accurately by the diffusion tensor (Frank, 2001), and this intravoxel heterogeneity causes two main problems. Firstly, with more than one fiber population or orientation in a voxel, the principal diffusion direction no longer corresponds to the underlying fiber orientation (e.g., Pierpaoli et al., 2001). Secondly, the quantitative metrics derived from DTI do not reflect the measured diffusion profile in an accurate way (e.g., Alexander et al., 2001), which will be discussed in more detail in Chapters 2 and 3. With high percentages of WM voxels estimated to contain two or more fiber populations (Behrens et al., 2007; Jeurissen et al., 2012), there is a need to go beyond the tensor model to characterize the diffusion profiles in a more reliable manner.

1.4.1 High angular resolution diffusion imaging

One of the first to propose alternative acquisition and signal estimation methods were Frank (2002); Tuch et al. (2003). Commonly known under the term high angular resolu-

tion diffusion imaging (HARDI), these techniques used a higher number of diffusion-weighted directions, e.g., around 40 or more, to sample the 3D diffusion profile at a higher angular resolution. From the measured diffusion signal one can describe the 3D diffusion probability, called the orientation distribution function (ODF). In recent years, a multitude of HARDI methods have been proposed to reconstruct the ODF from the diffusion signal. Most notably, the methods can be divided into two main groups: parametric and non-parametric methods. The technique initially proposed by Tuch et al., Q-ball imaging (QBI), is a non-parametric approach, where a mathematical approximation converts the diffusion signal to the diffusion ODF (dODF; Tuch et al., 2003; Tuch, 2004). The q -value is another feature to describe the diffusion weighting—closely related to the b-value—on which the name QBI is based. The parametric methods are originally based on modeling the signal attenuation profile for a single fiber population, and the assumption that the measured signal attenuation profile can then be represented as a sum of these 'single fiber profiles' (Frank, 2002). One example of this is constrained spherical deconvolution (CSD), where a single fiber response function can be used to deconvolve the diffusion signal to obtain the fiber ODF (Tournier et al., 2004, 2007) (fODF). This response function can be estimated from the diffusion signal in regions with a single fiber population. These fODFs have their maximum along the directions of the underlying fiber populations. Using the ODFs from these advanced techniques, multi-fiber tractography uses the peak orientations obtained from the ODFs, as an alternative to the first eigenvector obtained from DTI. Fillard et al. (2011); Jeurissen et al. (2011) have shown that multi-fiber tractography can be used to track through regions of multiple fiber populations, as illustrated by the simulation in Fig. 1.10.

1.4.2 Alternative diffusion MRI approaches

Several other approaches have been proposed to describe the measured diffusion signals. Diffusion spectrum imaging (DSI; Wedeen et al., 2005) uses many different q -values along a high number of directions to fill a 3D Cartesian grid in q -space. K-space—used in MR image generation—samples the spatial positions of the signal. Similar for k-space and image space, the Fourier transform is a direct mathematical relation between q -space and the probability density of diffusion. However, to fill the entire q -space, many more DWIs are required and at higher q -values, putting high demands on scan time for clinical MR systems, resulting in a low use of DSI in (pre-) clinical diffusion MR studies.

Another alternative is diffusion kurtosis imaging (DKI; Jensen et al., 2005), already extensively used in preclinical as well as clinical research studies (Fieremans et al., 2011; Van Cauter et al., 2012). The kurtosis is a measure of how non-Gaussian the diffusion is. Full quantification of the anisotropic kurtosis is done by estimating the kurtosis ten-

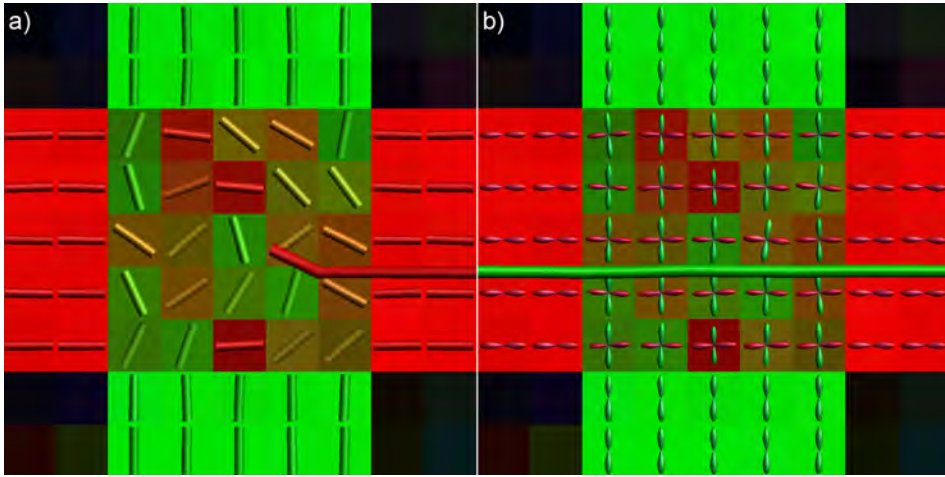


Figure 1.10: Simulation of two individual fiber populations crossing at a 90° angle. a) The first eigenvectors, ϵ_1 ; and b) the ODFs in this region. At such crossings, the ϵ_1 's do not reflect the underlying fiber architecture (a). Fiber tractography through such a region of a crossing is therefore unreliable. The tract terminates at the region of crossing fibers because the angular deviation is too large. The ODFs (b) are more accurate, and can be used more reliably to perform tractography.

sor, requiring at least 15 diffusion directions and two non-zero b-values, which can be acquired clinically in acquisition times as low as 5 minutes.

1.5 Outline of thesis

To best describe the diffusion properties in brain tissue, a complex and inter-related process of data acquisition, processing, and quantification precedes the interpretation of diffusion MRI data. In this thesis, several aspects of this process are investigated, aiming to improve the quantification and interpretation of diffusion properties in the brain.

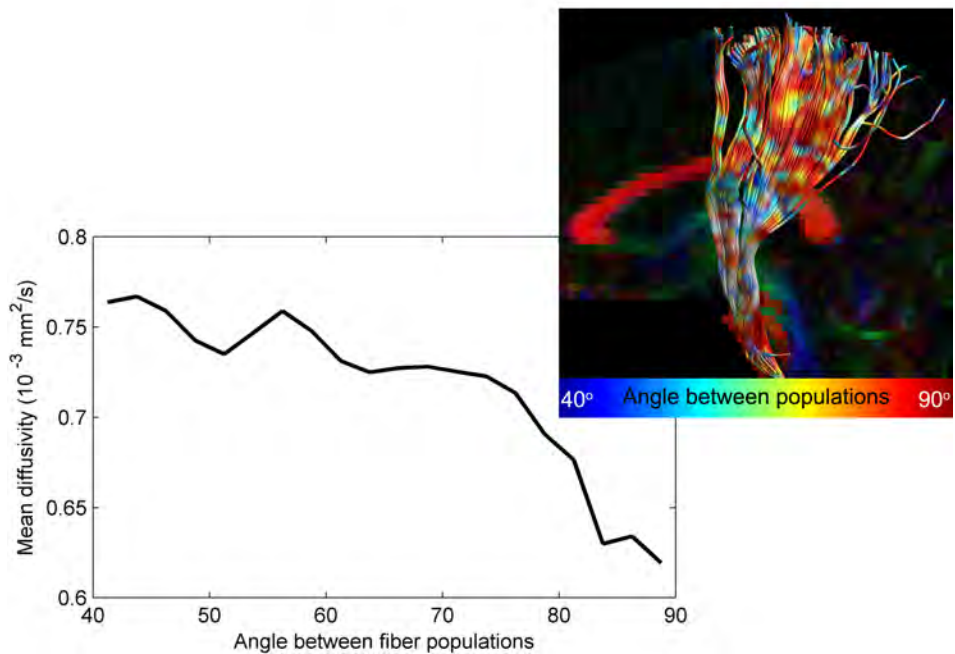
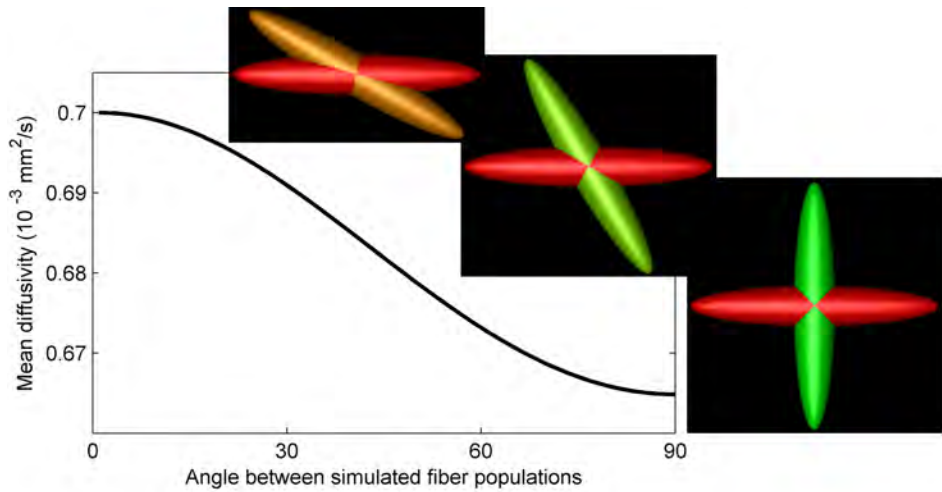
In **Chapter 2**, we look at how complex fiber architecture affects the mean diffusivity. Where directional diffusion metrics—such as the FA—are known to depend on tissue complexity, the MD is generally assumed to be independent on fiber architecture. We demonstrate that the mean diffusivity *is* dependent on the amount of fiber populations and/or orientations in a voxel, with MD values lower in voxels with “crossing fiber” populations than in “single fiber” populations. This means that the mean diffusivity in a specific voxel is not solely a reflection of the diffusivity of the underlying tissue population, but is confounded by the tissue architecture.

Chapter 3 addresses another confound on the quantification of DTI metrics. Partial volume effects (PVEs) are known to affect estimated DTI measures sampled along reconstructed tracts, but the size of these effects differs between fiber bundles and subjects. For instance, for thicker fiber bundles, the contribution of PVE-contaminated voxels to the mean value for the entire fiber bundle will be smaller, and vice-versa—which means that the extent of PVE-contamination will vary from bundle to bundle.

In longitudinal DTI studies, multiple scans of each subject are acquired at different time points to investigate the evolution of diffusion metrics within a subject. As discussed, manual tractography segmentations are highly reproducible yet time-consuming to perform, whereas automated approaches may be less accurate due to large inter-subject variation in brain morphology. In **Chapter 4**, we propose an automated longitudinal intra-subject analysis framework for tractography segmentations, termed ALISA, reducing the amount of manual input required while maintaining the high levels of accuracy and precision from manual tract segmentations.

In diffusion MRI, one would ideally want a high spatial resolution (small voxels) and a high angular resolution (many diffusion-weighted images). Given that scan times in clinical settings are generally very limited, it would be interesting to know what trade-off between spatial and angular resolution provides the best results. In **Chapter 5** we provide such a trade-off for the specific purpose of fiber tractography. A dataset with a very high spatial resolution—1 mm isotropic resolution—is acquired with a high angular resolution to determine which of these two factors, if any, provides the largest gain and when (if at all) there are diminishing returns.

A multitude of new diffusion MRI approaches have been proposed to address the conceptual limitations of DTI, with special focus on the accurate reconstruction of crossing fiber configurations. However, inconsistencies between these multi-fiber methods remain a source of debate on the accuracies and reliabilities of each method. **Chapter 6** describes a method to better visualize tractography results from multi-fiber methods, displaying the local diffusion information from the ODF along the reconstructed tracts. This new visualization techniques helps to compare different diffusion MRI methods to interpret subtle differences between these methods.



The mean diffusivity is affected by the angle between fiber populations (top: simulations; bottom: cortico-spinal tracts)

Chapter 2

The influence of complex white matter architecture on the mean diffusivity in diffusion tensor MRI

This chapter has been published as:

S.B. Vos, D.K. Jones, B. Jeurissen, M.A. Viergever, and A. Leemans, “The influence of complex white matter architecture on the mean diffusivity in diffusion tensor MRI of the human brain”. *NeuroImage*, 2012, 59 (3), pages 2208-2216.

Abstract

In diffusion tensor magnetic resonance imaging (DTI), limitations concerning complex fiber architecture (when an image voxel contains fiber populations with more than one dominant orientation) are well-known. Fractional anisotropy (FA) values are lower in such areas because of a lower directionality of diffusion on the voxel-scale, which makes the interpretation of FA less straightforward. Moreover, the interpretation of the axial and radial diffusivities is far from trivial when there is more than one dominant fiber orientation within a voxel. In this work, using (i) theoretical considerations, (ii) simulations, and (iii) experimental data, it is demonstrated that the mean diffusivity (or the trace of the diffusion tensor) is lower in complex white matter configurations, compared with tissue where there is a single dominant fiber orientation within the voxel. We show that the magnitude of this reduction depends on various factors, including configurational and microstructural properties (e.g., the relative contributions of different fiber populations) and acquisition settings (e.g., the b-value). These results increase our understanding of the quantitative metrics obtained from DTI and, in particular, the effect of the microstructural architecture on the mean diffusivity. More importantly, they reinforce the growing awareness that differences in DTI metrics need to be interpreted cautiously.

2.1 Introduction

Many diffusion tensor MRI (DTI) studies aim to determine whether differences in white matter (WM) microstructure can be observed between different groups of subjects, e.g., between healthy and diseased subjects, or to correlate some aspect of behaviour or performance with WM structural attributes. The two most frequently used metrics for characterizing tissue microstructure are the fractional anisotropy (FA) and the mean diffusivity (MD, which is defined as one third of the trace, Tr), which can be calculated from the diffusion tensor model (Basser et al., 1994; Jones, 2010; Tournier et al., 2011). Although DTI is still the most widely used approach to analyze diffusion MRI data, there are many confounding factors that may affect the analyses and interpretation (e.g., Jones and Cercignani, 2010, and Chapter 3). One of the most important confounds is the inability of the tensor model to describe the diffusion correctly in regions of complex fiber architecture (e.g., bending or interdigitating fibers) (Basser et al., 2000; Frank, 2001; Alexander et al., 2002; Jones, 2003; Tuch, 2004). The FA, in particular, is known to be strongly affected in areas of complex fiber architecture, as described in detail in previous studies (Pierpaoli et al., 1996; Alexander et al., 2001; Tuch et al., 2003).

In this work, we will use the generic phrase of “crossing fibers” (abbreviated forthwith as “CF”) for any WM configuration where there is more than one dominant fiber orientation within a voxel, including crossing, “kissing”, twisting, splaying, kinking and bending configurations. By contrast, configurations where there is only one dominant fiber orientation will be referred to as “single fiber” configurations, and abbreviated forthwith as “SF”.

Recently, the interpretation of two other DTI metrics, the axial and radial diffusivities (AD, the largest eigenvalue of the tensor; and RD, the average of the second and third eigenvalues of the tensor) was shown to be non-trivial in CF-configurations (Wheeler-Kingshott and Cercignani, 2009). Upon simulating a voxel with two crossing fiber populations and fitting a single tensor to that signal, increases in the AD of this tensor were observed when the RD of one of the underlying populations was increased. Similarly, decreases in the RD of such a CF-configuration were found when reducing the AD of one underlying population.

In this work, we expand upon previous simulations that show that the trace is influenced by the architectural configuration of the WM (Alexander et al., 2001). Many issues concerning this dependence are still unclear, such as the effect of the exact architectural configuration and whether the dependence can actually be observed in experimental data. Based on (i) a mathematical derivation of the trace of an ensemble of fiber populations, (ii) simulations, and (iii) experimental data, we demonstrate that the mean diffusivity is lower in CF-configurations compared to SF-configurations. We

also show that the magnitude of this reduction depends on several factors that include microstructural and configurational properties (e.g., the intrinsic diffusivities of the fiber populations) and acquisition parameters (such as the b-value). These findings improve our understanding of quantitative DTI indices and, in particular, show how architectural aspects and configurational properties of complex WM diffusion profiles can affect the estimation of the mean diffusivity.

2.2 Theory

In this section, a general mathematical formulation is given for the trace in a CF-configuration, in relation to the diffusion properties of the individual fiber populations. To simplify the mathematical expressions, we provide this derivation for the trace of the diffusion tensor, being equivalent to three times the MD. Using an extension of the Stejskal-Tanner equation (Stejskal and Tanner, 1965) to describe a diffusion signal originating from more than one fiber population (Alexander et al., 2001; Frank, 2001; Assaf et al., 2002), we find a lower trace in CF-configurations with respect to SF-configurations. Consider the Stejskal-Tanner equation for a diffusion-weighted signal $S_{\mathbf{g}}$ along diffusion weighting direction \mathbf{g} (Stejskal and Tanner, 1965):

$$S_{\mathbf{g}} = S_0 e^{-b \mathbf{g}^T \mathbf{D} \mathbf{g}} = S_0 e^{-b D_{\mathbf{g}}}, \quad (2.1)$$

where S_0 is the signal without diffusion weighting, b is the scalar value of diffusion weighting, \mathbf{D} is the diffusion tensor, and $D_{\mathbf{g}}$ the apparent diffusion coefficient (ADC) along orientation \mathbf{g} . Consequently, along a given gradient orientation \mathbf{g} , the estimated diffusion coefficient $D_{\mathbf{g}}$ is:

$$D_{\mathbf{g}} = -\frac{1}{b} \ln \left(\frac{S_{\mathbf{g}}}{S_0} \right). \quad (2.2)$$

When multiple populations are present in one voxel, the signal originating from that voxel may be regarded as an average of the diffusion-weighted signals of the underlying fiber populations, if we assume that the spins of the different populations are in slow exchange (Alexander et al., 2001; Frank, 2001; Assaf et al., 2002). Eq. (2.1) can then be generalized to:

$$S_{\mathbf{g}} = S_0 \sum_{\alpha} f^{\alpha} e^{-b D_{\mathbf{g}}^{\alpha}}, \text{ with } \sum_{\alpha} f^{\alpha} = 1, \quad (2.3)$$

where $D_{\mathbf{g}}^{\alpha}$ represents the ADC of population α along orientation \mathbf{g} , and f^{α} is the relative volume fraction of population α .

The influence of complex white matter architecture on the mean diffusivity

Combining Eqs. (2.2) and (2.3), one can calculate the estimated diffusivity in a CF-configuration along any direction \mathbf{g} , denoted as $D_{\mathbf{g}}^{CF}$, as follows:

$$D_{\mathbf{g}}^{CF} = \frac{1}{b} \ln \left(\frac{1}{\sum_{\alpha} f^{\alpha} e^{-bD_{\mathbf{g}}^{\alpha}}} \right). \quad (2.4)$$

The trace is mathematically derived from the sum of the diffusivities along any three orthogonal orientations. These measurements can be taken along the orientations of the three eigenvectors of a specific population A , provided the diffusion profile is Gaussian or a low b -value ensures that the Gaussian part of the displacement profile dominates the signal attenuation (Basser, 2002). By defining orientation \mathbf{e}_1 as the first eigenvector of population A , so that $D_{\mathbf{e}_1}^A = \lambda_1^A$, the diffusivity in a CF-configuration along this orientation (denoted as $D_{\mathbf{e}_1}^{CF}$) can be derived from Eq. (2.4) as:

$$\begin{aligned} D_{\mathbf{e}_1}^{CF} &= \frac{1}{b} \ln \left(\frac{1}{f^A e^{-b\lambda_1^A} + \sum_{\alpha \setminus A} f^{\alpha} e^{-bD_{\mathbf{e}_1}^{\alpha}}} \right) \\ &= \lambda_1^A - F(b, f^A, f^{\alpha}, \mathbf{e}_1, \lambda_1^A), \end{aligned} \quad (2.5)$$

where

$$F(b, f^A, f^{\alpha}, \mathbf{g}, \lambda) = \frac{1}{b} \ln \left(f^A + \sum_{\alpha \setminus A} f^{\alpha} e^{-b(D_{\mathbf{g}}^{\alpha} - \lambda)} \right) \quad (2.6)$$

and the summation over $\alpha \setminus A$ indicates that this summation is over all populations α with the exception of population A .

Equivalently, $D_{\mathbf{e}_2}^{CF}$ and $D_{\mathbf{e}_3}^{CF}$, the diffusivities along \mathbf{e}_2 and \mathbf{e}_3 (the second and third eigenvectors of population A) can also be calculated with Eq. (2.5). By definition, the trace in a ‘‘crossing fibers’’ voxel, i.e., $\text{Tr}(\mathbf{D}^{CF})$, can now be calculated as:

$$\begin{aligned} \text{Tr}(\mathbf{D}^{CF}) &= D_{\mathbf{e}_1}^{CF} + D_{\mathbf{e}_2}^{CF} + D_{\mathbf{e}_3}^{CF} \\ &= \lambda_1^A + \lambda_2^A + \lambda_3^A - \sum_{i=1}^3 F(b, f^A, f^{\alpha}, \mathbf{e}_i, \lambda_i^A) \\ &= \text{Tr}(\mathbf{D}^A) - \underbrace{\sum_{i=1}^3 F(b, f^A, f^{\alpha}, \mathbf{e}_i, \lambda_i^A)}_{\mathbf{C}}. \end{aligned} \quad (2.7)$$

Eq. (2.7) describes the trace after combining any number of fiber populations, in terms of the trace of population A and a correction factor \mathbf{C} . This equation is valid for any set

of relative volume fractions f^α and any geometric configuration of the fiber populations. From this general expression, it is trivial to derive a formulation for the trace for any specific fiber configuration. As an example, for an orthogonally oriented two-fiber population with equal volume fractions, Eq. (2.7) can be simplified to:

$$\text{Tr}(\mathbf{D}^{CF}) = \text{Tr}(\mathbf{D}^A) - \frac{1}{b} \ln \left(\frac{(2 + e^{b(\lambda_1^A - \lambda_2^A)} + e^{-b(\lambda_1^A - \lambda_2^A)})}{4} \right), \quad (2.8)$$

when assuming equal diffusivity properties for each individual fiber population (i.e., $\lambda_1^A = \lambda_1^B$, $\lambda_2^A = \lambda_2^B$, and $\lambda_3^A = \lambda_3^B$). As the anisotropy of the fiber populations decreases, i.e., as λ_1^A and λ_2^A differ less, the correction factor \mathbf{C} will be smaller.

2.3 Materials and methods

2.3.1 Simulations

The mathematical framework presented in the previous section provides theoretical evidence for a change in trace for a voxel with more than one fiber population or orientation. In these calculations, however, several factors were not included that may influence the estimate of the trace, for example the choice of tensor estimation routine or the set of diffusion gradient sampling vectors. For a detailed characterization of these effects, simulation experiments were performed (Leemans et al., 2005).

To examine the influence of the angle between fibers in a CF-configuration, two identical fiber populations were defined (with FA = 0.7 and trace = 2.1×10^{-3} mm²/s) (Le Bihan et al., 2001; Jones and Basser, 2004), in which one population (characterized by diffusion tensor \mathbf{D}^A) was then rotated over a range of 0–90° with respect to the other population (characterized by diffusion tensor \mathbf{D}^B). For each rotation, the diffusion-weighted signals along 60 gradient directions ($b = 1000$ s/mm²) were computed for the resulting CF-configuration, assuming equal volume fractions (i.e., $f^A = f^B = 0.5$), according to Eq. (2.3). From this set of signals, a single tensor, \mathbf{D}^{CF} , was estimated and the trace of that single tensor ($\text{Tr}(\mathbf{D}^{CF})$) was compared with the trace of the underlying SF-populations ($\text{Tr}(\mathbf{D}^{SF})$). This experiment was performed using three types of tensor estimation: (i) linear least squares, (ii) weighted linear least squares, and (iii) nonlinear least squares (initialized with the fitted values from a weighted linear least squares estimation) (Marquardt, 1963; Basser et al., 1994; Koay, 2011). For a more in-depth analysis, the eigenvalues of \mathbf{D}^{CF} were compared to the eigenvalues of the individual diffusion tensors, \mathbf{D}^{SF} (using only nonlinear least squares tensor estimation).

To determine the impact on the trace of changing the relative volume fractions of the individual fiber populations in an orthogonal crossing configuration, the volume frac-

tions f^A and f^B (of populations A and B, respectively) were varied from 0 to 1, with $f^A + f^B = 1$ (while $FA = 0.7$, $\text{trace} = 2.1 \times 10^{-3} \text{ mm}^2/\text{s}$, $b = 1000 \text{ s}/\text{mm}^2$, and with 60 unique diffusion encoding vectors). Again, $\text{Tr}(\mathbf{D}^{\text{CF}})$ was calculated from \mathbf{D}^{CF} estimated with the three different estimation procedures.

Furthermore, the impact of varying the relative orientations of three fiber populations on the trace was simulated, maintaining the same microstructural properties and acquisition properties as described above.

Previous work has shown that, in simulations of SF-voxels, there is variation in the estimated trace depending on the orientation of this population with respect to the diffusion encoding gradient set (Jones, 2004). This variation in trace decreased with increasing numbers of diffusion encoding directions, and the variation diminished at between 10–30 directions, depending on the FA of the simulated fiber population. Analogous to that work, we simulated two fiber populations crossing orthogonally with equal volume fractions using a range (6 to 60) of gradient directions (with b -value = $1000 \text{ s}/\text{mm}^2$ and the FA and trace values of the underlying fibers populations were 0.7 and $2.1 \times 10^{-3} \text{ mm}^2/\text{s}$, respectively). For each number of gradient directions, the whole configuration of crossing populations was rotated over the sphere in 2° steps around the azimuthal and polar axes (corresponding to over 4000 samples). After tensor estimation for each sample, the mean and standard deviation of $\text{Tr}(\mathbf{D}^{\text{CF}})$ were calculated for each of the 6 to 60 gradient directions.

From Eq. (2.7) it becomes apparent that, apart from the configurational aspects, there are other factors that affect the trace values in CF-voxels, i.e., the FA and trace values of the individual fiber populations (FA^{SF} and $\text{Tr}(\mathbf{D}^{\text{SF}})$, respectively), and the b -value. We have therefore simulated two fiber populations, crossing perpendicularly and with equal volume fractions, and varied FA^{SF} , $\text{Tr}(\mathbf{D}^{\text{SF}})$ and the b -value in a range of relevant values. Since $\text{Tr}(\mathbf{D}^{\text{SF}})$ is one of the parameters of interest in these simulations, the differences in $\text{Tr}(\mathbf{D}^{\text{CF}})$ are shown relative to the simulated $\text{Tr}(\mathbf{D}^{\text{SF}})$.

2.3.2 Data acquisition

Cardiac-gated DTI datasets were acquired from six healthy subjects (3 males and 3 females) aged 23.7 to 29.1 years (mean age 26.1 years), on a 3 T HDx MRI system (General Electric) using a single-shot spin echo EPI sequence with a b -value of $1200 \text{ s}/\text{mm}^2$, 60 gradient directions distributed uniformly over the half sphere (Jones et al., 1999a), 6 $b = 0$ images and an ASSET factor 2. The acquisition matrix of 96×96 was reconstructed to 128×128 with a field-of-view of $230 \times 230 \text{ mm}^2$, and 60 contiguous axial slices with thickness 2.4 mm were acquired, with an effective TR of 15 R–R intervals and a total acquisition time of approximately 25 min. In addition to the DTI scans, 3D T_1 -weighted FSPGR scans were obtained with 1 mm isotropic resolution, using the following acqui-

sition parameters: TR/TE/TI = 7.9/3.0/450 ms and a flip angle of 20° . All subjects gave a written informed consent to participate in this study under a protocol approved by the Cardiff University School of Psychology.

2.3.3 Pre-processing of experimental data

Prior to data analysis, each DTI dataset was corrected for eddy current induced geometric distortions and subject motion by realigning all diffusion-weighted images (DWIs) to the $b = 0$ images using *elastix* (Klein et al., 2010), with an affine coregistration technique (with 12 degrees of freedom) and mutual information as the cost function (Pluim et al., 2003). In this procedure, the diffusion gradients were appropriately reoriented to account for subject motion (Leemans and Jones, 2009). The tensor model was fitted with the Levenberg-Marquardt nonlinear regression method (Marquardt, 1963), using the fitted values from a weighted linear least squares estimation as initialization.

2.3.4 Experimental data analysis

To characterize how complex fiber architecture affects the trace in experimental diffusion MRI data, we examined two WM fiber bundles that are known to have regions of complex fiber architecture, the cortico-spinal tracts (CST) and the arcuate fasciculus (AF) (Tuch et al., 2003; Behrens et al., 2007). These bundles were reconstructed with fiber tractography based on the estimated fiber orientation distribution obtained from constrained spherical deconvolution (CSD), in which spherical harmonics were limited to maximum harmonics of order $L = 8$ (Tournier et al., 2007; Jeurissen et al., 2011). For each bundle, all voxels that were intersected by the fiber tracts were used to investigate the impact of “crossing fibers” on the trace. In addition, a WM segmentation was obtained from the T_1 -weighted MR images using the Unified Segmentation algorithm (Ashburner and Friston, 2005) to examine the effect of complex fiber architecture on the trace in the global WM.

The linear and planar diffusion tensor geometry indices (Westin et al., 2002; Ennis and Kindlmann, 2006) were used as criteria to distinguish SF-voxels from CF-voxels. More specifically, all voxels where the planar diffusion coefficient (C_p) is largest—i.e., larger than the linear, C_L , and spherical, C_S , coefficients—were classified as CF-configuration voxels; all voxels where C_L was largest were classified as SF-configuration voxels; all voxels where C_S was largest were not included in the analyses, because a high C_S may not only arise from multiple fiber populations but also from partial voluming with cerebrospinal fluid. The average trace of the CF-regions ($\text{Tr}(\mathbf{D}^{\text{CF}})$) and the SF-regions ($\text{Tr}(\mathbf{D}^{\text{SF}})$) was calculated for all subjects, and compared using the non-parametric Wilcoxon signed rank test. Image processing, tractography, and experimental analyses were performed in *ExploreDTI* (Leemans et al., 2009).

The influence of complex white matter architecture on the mean diffusivity

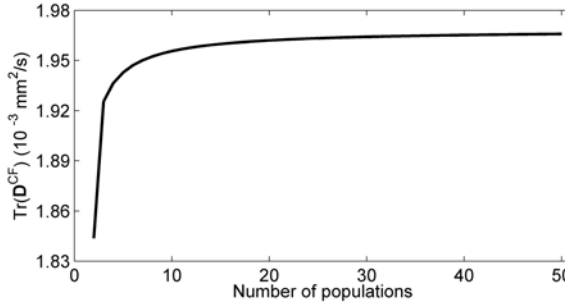


Figure 2.1: The calculated trace in a “crossing fibers” voxel, $\text{Tr}(\mathbf{D}^{\text{CF}})$, is shown for a crossing with a varying number of orientations in a plane. Such a configuration could be considered analogous to fibers fanning out in a voxel, as for instance can be found in the cortico-spinal tracts. Compared with the trace in a voxel with one fiber orientation ($\text{Tr}(\mathbf{D}^{\text{SF}}) = 2.1 \times 10^{-3} \text{ mm}^2/\text{s}$), the $\text{Tr}(\mathbf{D}^{\text{CF}})$ is strongly reduced for two orientations. With more orientations, $\text{Tr}(\mathbf{D}^{\text{CF}})$ gradually increases, stabilizing in the range of 30–50 fiber orientations.

2.4 Results

2.4.1 Mathematical derivation of $\text{Tr}(\mathbf{D}^{\text{CF}})$ values

From Eq. (2.7), the trace can be computed for a voxel with any number of fiber populations—once the FA and trace of each population has been specified, along with their volume fractions f^α , their geometric configuration and the b-value. As an example of a voxel with multiple fiber orientations, consider a voxel with one fiber bundle fanning out. To emulate such a voxel, Eq. (2.7) can be used to calculate the trace for any number of orientations. Assuming a set of in-plane orientations distributed uniformly along one quadrant of a circle (e.g., 0° , 45° and 90° for 3 populations, or 0° , 30° , 60° and 90° for 4 populations, etc.), one can observe an increase of the trace with more orientations, as shown in Fig. 2.1 (with $\text{FA}^{\text{SF}} = 0.7$, $\text{Tr}(\mathbf{D}^{\text{SF}}) = 2.1 \times 10^{-3} \text{ mm}^2/\text{s}$, b-value = $1000 \text{ s}/\text{mm}^2$).

2.4.2 Simulations

In a voxel with two fiber populations, the trace in that voxel ($\text{Tr}(\mathbf{D}^{\text{CF}})$) is not only dependent on the trace values of the underlying populations ($\text{Tr}(\mathbf{D}^{\text{SF}})$), but also depends on the angle of intersection between these two fiber populations, as shown in Fig. 2.2a. With increases in the angle between the two populations, $\text{Tr}(\mathbf{D}^{\text{CF}})$ gradually decreases with respect to $\text{Tr}(\mathbf{D}^{\text{SF}})$, reaching its minimum when the populations are orthogonal, where $\text{Tr}(\mathbf{D}^{\text{CF}})$ is 5% lower than $\text{Tr}(\mathbf{D}^{\text{SF}})$. Performing this simulation for three different types of tensor estimation (linear, weighted linear, and nonlinear least squares) shows that the choice of tensor estimation during data analysis also influences the estimate

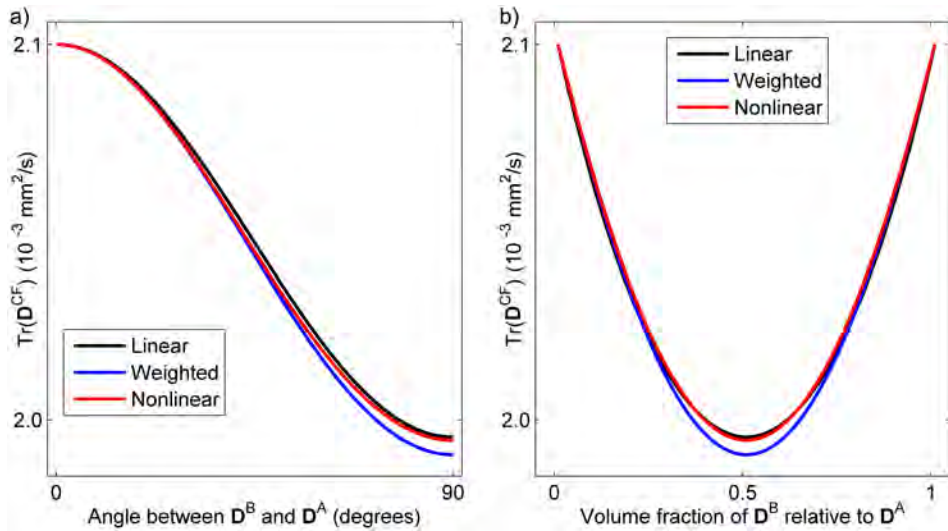


Figure 2.2: (a) Increasing the angle of intersection between two fiber populations (\mathbf{D}^{A} and \mathbf{D}^{B}) up to 90° decreases the trace in a “crossing fibers” configurations, $\text{Tr}(\mathbf{D}^{\text{CF}})$. Performing this simulation with three types of tensor estimation shows that the choice of tensor estimation also affects the trace (linear least squares estimation is illustrated in black, weighted least squares in blue, nonlinear least squares in red). (b) The volume fractions of the two populations in one voxel also modulates $\text{Tr}(\mathbf{D}^{\text{CF}})$. As in (a), the type of tensor estimation also affects the trace in (b).

of $\text{Tr}(\mathbf{D}^{\text{CF}})$. The weighted linear least squares estimator consistently yields lower values of $\text{Tr}(\mathbf{D}^{\text{CF}})$ than linear or nonlinear least squares estimation. The larger the decrease in trace, the bigger this difference between different tensor estimators becomes.

Fig. 2.2b illustrates that $\text{Tr}(\mathbf{D}^{\text{CF}})$ also depends on the volume fractions of the two populations, with a minimum when both populations contribute equally (similar to the setting in Fig. 2.2a). In addition, there is a small effect of the different tensor estimators on $\text{Tr}(\mathbf{D}^{\text{CF}})$, with the weighted linear least squares estimation giving the lowest trace values.

To examine the reduction in $\text{Tr}(\mathbf{D}^{\text{CF}})$ with larger angles between the individual populations in more detail, the eigenvalues ($\lambda_1 \geq \lambda_2 \geq \lambda_3 > 0$) of the tensor in a CF-configuration are investigated. Fig. 2.3 shows that λ_1 is lower in CF-voxels, with larger differences as the angle between the two individual populations increases. By contrast, λ_2 and λ_3 values are higher in CF-configurations than in SF-configurations.

The influence of complex white matter architecture on the mean diffusivity

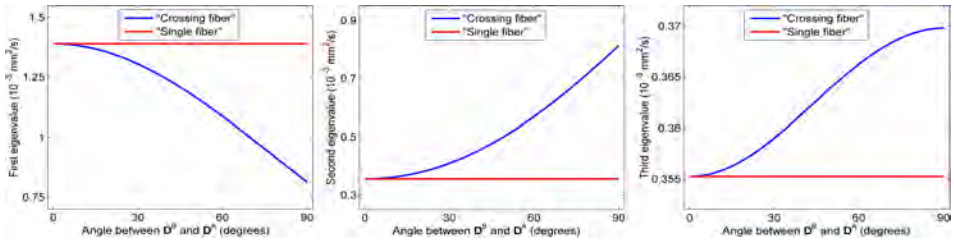


Figure 2.3: Diffusivity profiles of the first, second, and third eigenvalues depending on the angle of intersection between the two fiber populations (\mathbf{D}^A and \mathbf{D}^B). The first eigenvalue is smaller in “crossing fibers” configurations than in “single fiber” configurations, whereas the second and third eigenvalues are larger.

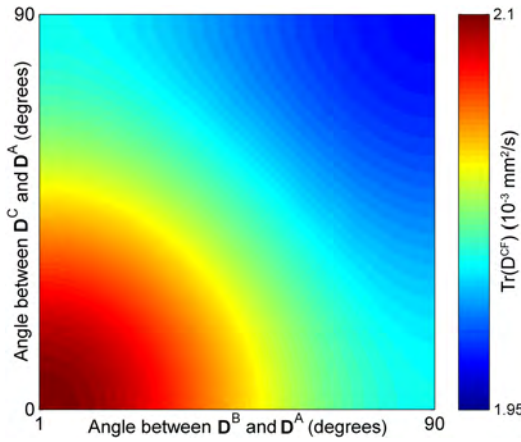


Figure 2.4: When three fiber populations intersect, the trace ($\text{Tr}(\mathbf{D}^{\text{CF}})$) is affected by the angle of both the second (\mathbf{D}^B) and third (\mathbf{D}^C) population with respect to the first population (\mathbf{D}^A).

In a CF-configuration with three fiber populations, the change in trace depends on the angles between all three populations (Fig. 2.4). Note that if the three populations are orthogonal, $\text{Tr}(\mathbf{D}^{\text{CF}})$ is 6.5% lower than $\text{Tr}(\mathbf{D}^{\text{SF}})$, lower than if there are only two orthogonal populations (Fig. 2.2).

The dependence of the mean and standard deviation of the trace values on the number of gradient directions is shown in Fig. 2.5. Independent of the number of gradient directions, $\text{Tr}(\mathbf{D}^{\text{CF}})$ was consistently lower than $\text{Tr}(\mathbf{D}^{\text{SF}})$. In the range of 10–30 gradient directions, the orientational dependence of the trace estimates is mostly reduced.

Fig. 2.6 shows that the b-value, as well as both microstructural parameters present in Eq. (2.7), FA^{SF} and $\text{Tr}(\mathbf{D}^{\text{SF}})$, all modulate $\text{Tr}(\mathbf{D}^{\text{CF}})$.

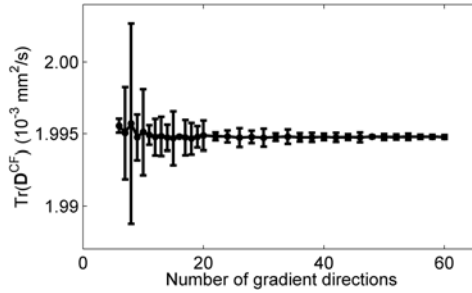


Figure 2.5: Variation in the estimated trace in a “crossing fibers” configuration, $\text{Tr}(\mathbf{D}^{\text{CF}})$, depending on the number of unique sampling directions for two populations crossing at 90° . The average $\text{Tr}(\mathbf{D}^{\text{CF}})$ and standard deviation (error bars) have been calculated from over 4000 different orientations. $\text{Tr}(\mathbf{D}^{\text{CF}})$ is lower than the trace in single fiber voxels ($\text{Tr}(\mathbf{D}^{\text{SF}}) = 2.1 \times 10^{-3} \text{ mm}^2/\text{s}$) for all number of gradient directions.

2.4.3 Experimental data

In experimental data, the trace in CF-voxels is significantly lower than in SF-voxels, confirming the results of the simulations. For all subjects, $\text{Tr}(\mathbf{D}^{\text{CF}})$ is lower than $\text{Tr}(\mathbf{D}^{\text{SF}})$ in the CST, AF, and the total WM (Table 2.1). Fig. 2.7 illustrates the regions of linear and planar diffusion along the CST and AF. In Fig. 2.8, it can be seen that this differentiation between regions of linear and planar diffusion is also consistent across subjects within the WM.

Table 2.1: Mean diffusivity values of “single fiber” and “crossing fibers” voxels (in $10^{-3} \text{ mm}^2/\text{s}$)

Subject	Cortico-spinal tracts		Arcuate fasciculus		Global white matter	
	MD^{SF}	MD^{CF}	MD^{SF}	MD^{CF}	MD^{SF}	MD^{CF}
1 (F)	0.80 ± 0.09	0.74 ± 0.05	0.81 ± 0.07	0.79 ± 0.05	0.80 ± 0.07	0.76 ± 0.06
2 (M)	0.77 ± 0.08	0.71 ± 0.06	0.78 ± 0.08	0.75 ± 0.04	0.77 ± 0.07	0.73 ± 0.06
3 (M)	0.81 ± 0.10	0.73 ± 0.07	0.79 ± 0.07	0.77 ± 0.05	0.79 ± 0.08	0.74 ± 0.06
4 (F)	0.78 ± 0.11	0.70 ± 0.05	0.78 ± 0.06	0.75 ± 0.04	0.77 ± 0.07	0.73 ± 0.05
5 (F)	0.75 ± 0.09	0.70 ± 0.05	0.74 ± 0.06	0.72 ± 0.04	0.73 ± 0.07	0.69 ± 0.06
6 (M)	0.74 ± 0.10	0.70 ± 0.06	0.76 ± 0.08	0.72 ± 0.05	0.75 ± 0.08	0.71 ± 0.06

Values shown in this table are mean diffusivity values (trace/3), for easy reference with values reported in literature; F/M indicates whether subject is female of male; $\text{MD}^{\text{SF}}/\text{MD}^{\text{CF}}$ is the mean diffusivity (trace/3) in “single fiber”/“crossing fiber” voxels. For all subjects and all white matter structures, MD^{CF} was significantly lower than MD^{SF} .

The influence of complex white matter architecture on the mean diffusivity

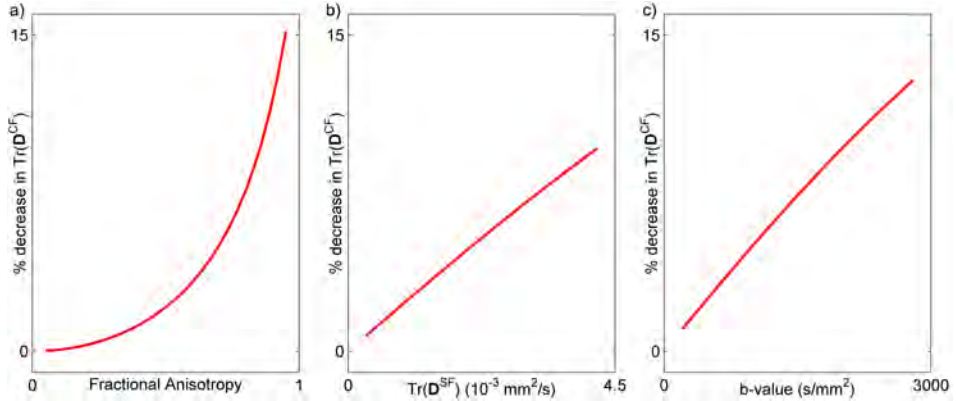


Figure 2.6: The effect of simulation parameters (a: fractional anisotropy; b: trace of a “single fiber” population, $\text{Tr}(\mathbf{D}^{\text{SF}})$; c: b-value) on the relative decrease in trace in a “crossing fibers” configuration, $\text{Tr}(\mathbf{D}^{\text{CF}})$, with two orthogonally oriented fiber populations (with equal volume fractions).

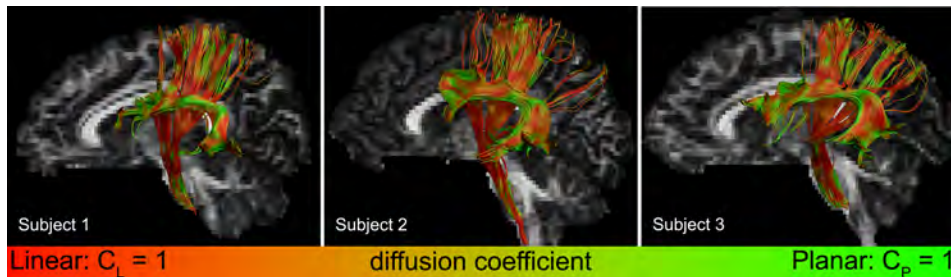


Figure 2.7: Sagittal views of a fractional anisotropy map with the cortico-spinal tracts and arcuate fasciculus for three subjects. Tracts are color-encoded by the linear and planar diffusion coefficients (C_L and C_p , respectively), where red indicates linear diffusion and green indicates planar diffusion.

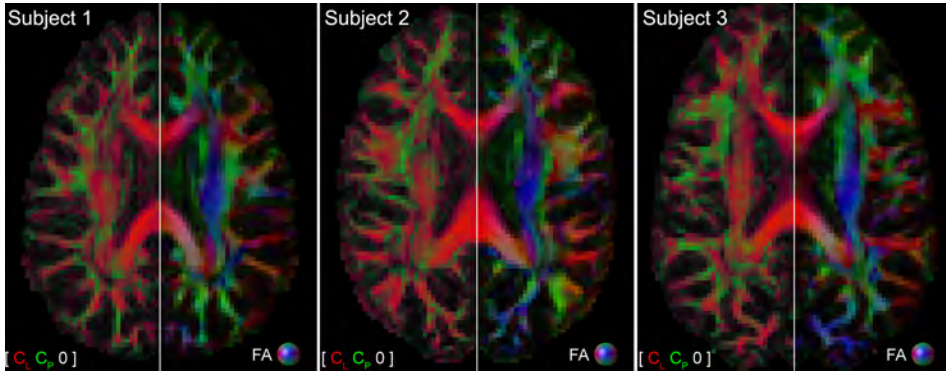


Figure 2.8: For three subjects, axial slices at the level of the corpus callosum are shown with geometric and direction-encoded color coding. In the geometric image, red and green voxels correspond with the linear (C_L) and planar (C_P) diffusion coefficients, respectively. Regions of linear and planar diffusion can clearly be differentiated throughout the white matter.

2.5 Discussion

In DTI, the issue of “crossing fibers” is well-known. Apart from a single study showing that the trace is affected in simulated fiber crossings (Alexander et al., 2001), no research has been conducted to validate this finding *in vivo*. In this work, we have studied this observation in further detail, starting from a general theoretical basis that can explain these results. In addition, simulations have been performed to highlight the effect of several aspects related to “crossing fibers”. Finally, to the best of our knowledge, we have demonstrated for the first time that the expected reduction in trace in complex WM tissue can also be shown in real diffusion MRI data.

2.5.1 Mathematical derivation of $\text{Tr}(\mathbf{D}^{\text{CF}})$ values

The mathematical correction factor derived in this work (Eqs. (2.7) and (2.8)) shows that the trace in a CF-voxel is not always equal to the trace in an SF-voxel. For two orthogonal populations, it can be deduced from Eq. (2.8) that $\text{Tr}(\mathbf{D}^{\text{CF}}) \leq \text{Tr}(\mathbf{D}^{\text{SF}})$ will always hold. The fraction in the logarithm in Eq. (2.8) will never be smaller than one, so the correction factor to the $\text{Tr}(\mathbf{D}^{\text{SF}})$, C , will always be equal to or larger than zero.

2.5.2 Simulations

Following the mathematical derivation demonstrating a decrease in trace in “crossing fibers”, results from simulation experiments support a reduction in trace in voxels with complex fiber architecture. Moreover, this decrease depends on the configuration of the crossing, i.e., the angle of intersection between the populations and the volume

fraction of each of the fiber populations in a voxel (Fig. 2.2). It is apparent from Eq. (2.7) that the number, orientation, FA, and trace of the individual populations, and the b-value affect $\text{Tr}(\mathbf{D}^{\text{CF}})$. In simulations, all these configurational (Figs. 2.2 and 2.4), microstructural (Fig. 2.6a, b) and acquisition (Fig. 2.6c) parameters are confirmed to modulate $\text{Tr}(\mathbf{D}^{\text{CF}})$. Note that the relative change in $\text{Tr}(\mathbf{D}^{\text{CF}})$ with all these parameters is nonlinear.

Variability in the estimated tensor depending on the chosen tensor estimation method has been described previously by Jones and Basser (2004) (see also Jones and Cercignani, 2010). To examine the effect of various tensor fitting procedures on the results presented in this work, the effects of changing the angle between two populations and the volume fractions of these populations have been investigated with three types of tensor estimation. From Fig. 2.2 we can see that the weighted least squares systematically yields lower trace estimates in CF-configurations than linear and nonlinear tensor estimation. These simulations were noise-free, so comparable results for the linear and nonlinear estimators were expected (Jones and Basser, 2004). The lower trace estimates from the weighted least squares algorithm can be explained by the fact that this estimator weights each diffusion measurement as a function of its signal magnitude. Given that the highest signals are obtained in directions with lowest diffusion, the estimator gives greater weights to low diffusion measurements, yielding a lower trace estimate.

Eigenvalue simulations

With lower MD values in regions of complex fiber architecture, an associated reduction in one or more of the tensor's eigenvalues ($\lambda_1 \geq \lambda_2 \geq \lambda_3 > 0$) would be expected. With two fiber populations in a voxel, the diffusivity will become more planar, which would intuitively lead to an underestimation of λ_1 and an overestimation of λ_2 . These expected changes are confirmed for λ_1 and λ_2 , as shown in Fig. 2.3. The increase in λ_3 (Fig. 2.3), on the other hand, is counter-intuitive. The third eigenvector of the CF-configuration is oriented perpendicular to the plane of the crossing. In the simulations, both individual tensors were defined to be axially symmetric, which results in equal diffusivities perpendicular to their crossing. As a result, theory dictates that λ_3 would not be affected in such a "fiber crossing". In the simulations, however, λ_3 is slightly overestimated. This overestimation of λ_3 originates from the finite number of sampling directions in data acquisition protocols: in a two-fiber crossing, λ_3 will only be the same as in a "single fiber" population when sampled precisely perpendicularly to the plane of the crossing.

Number of gradient directions

Until now, only one study has previously shown that, in simulations, the trace is underestimated in CF-configurations (Alexander et al., 2001). When simulating a crossing between two fiber populations with two different sets of six gradient directions, Alexander et al. (2001) observed trace values that were lower than the simulated trace values of the individual constituent fiber populations. However, the decrease in trace that was observed with the two sets of gradient orientations varied drastically. More recently, it was shown in simulations that in SF-voxels, variation in the estimated trace was observed depending on the orientation of this population with respect to the diffusion encoding gradient set (Jones, 2004). This variation in trace decreased as the number of gradient encoding directions was increased, with the variation diminished at between 10–30 directions, depending on the FA of the simulated fiber population. To confirm that the observed reduction in trace seen in the simulations carried out by Alexander et al. (2001) was not due to the relatively low number of gradient directions, we have investigated whether such variations in trace values are also present in CF-voxels. As shown in Fig. 2.5, $\text{Tr}(\mathbf{D}^{\text{CF}})$ was consistently lower than $\text{Tr}(\mathbf{D}^{\text{SF}})$ for all number of gradient directions. In agreement with the findings for SF-configurations (Jones, 2004), the orientational dependence of the trace estimates is largely reduced in the range of 10–30 unique gradient directions.

2.5.3 Experimental data analysis

Previous studies have shown that in experimental data, MD values can differ between fiber bundles (e.g., Eluvathingal et al., 2007; Lebel et al., 2008). Even within one bundle, however, there can already be a large heterogeneity of MD values (Jones et al., 2005b). In this work, we show such heterogeneity, and, more specifically, we demonstrate that MD values in CF-configurations are significantly lower than in SF-configurations (Table 2.1, Fig. 2.9). This difference, observed in the two bundles of interest, the CST and the AF, is also valid for the global WM (Table 2.1).

It can be observed from Table 2.1 that while $\text{Tr}(\mathbf{D}^{\text{SF}})$ values are not different for the CST and the AF, the mean $\text{Tr}(\mathbf{D}^{\text{CF}})$ values are lower in the CST than in the AF for all subjects. For the CST, $\text{Tr}(\mathbf{D}^{\text{CF}})$ is 8% lower than $\text{Tr}(\mathbf{D}^{\text{SF}})$, whereas this decrease is only 3% for the AF. This variation may be attributed to a difference in configurational properties between the two bundles. Other WM bundles crossing the CST may be more orthogonally oriented to the CST than is the case for bundles intersecting the AF, which could explain the larger decrease in $\text{Tr}(\mathbf{D}^{\text{CF}})$ in the CST than in the AF (as is illustrated in Fig. 2.2a). In addition, there could be a larger portion of equally distributed volume fractions in the CST compared to the AF, which could also contribute to lower $\text{Tr}(\mathbf{D}^{\text{CF}})$ values in the CST than in the AF (Fig. 2.2b).

The influence of complex white matter architecture on the mean diffusivity

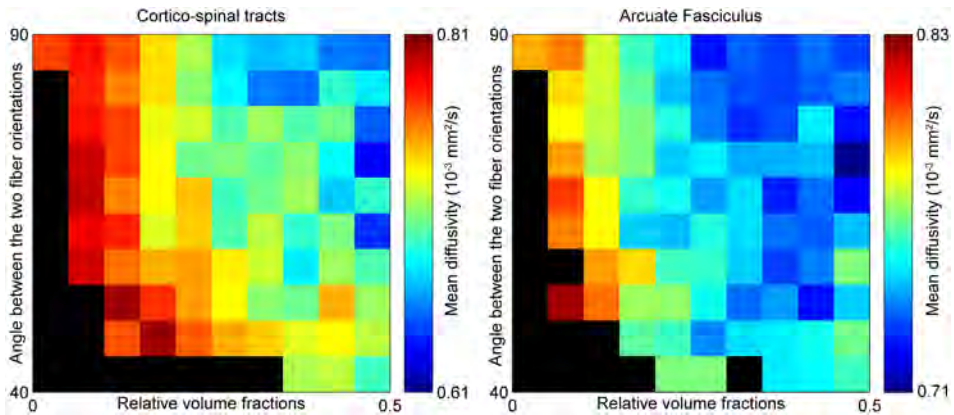


Figure 2.9: The mean diffusivity (trace/3) is affected by configurational properties of the white matter. The mean diffusivity decreases as the angle between two fiber populations increases, and the relative volume fractions become more equal. The angles between two fiber populations, as well as the relative volume fractions of these populations, have been determined from constrained spherical deconvolution. The black regions are configurations that were not present.

The dependence of the MD on the tissue geometry has implications for statistical testing. In regions that are comprised of voxels with purely SF-configurations, the MD will be relatively uniform. Likewise, for areas of tissue where there is a uniformity in the complexity of the tissue, the MD may be lower—but it will be uniformly lower. However, in regions that contain a mixture of SF- and CF-configurations, or CF-configurations that take different geometrical forms, there will be a larger variation in MD. Consequently, there will be a higher variance in such regions, and therefore less statistical power to detect differences in the MD.

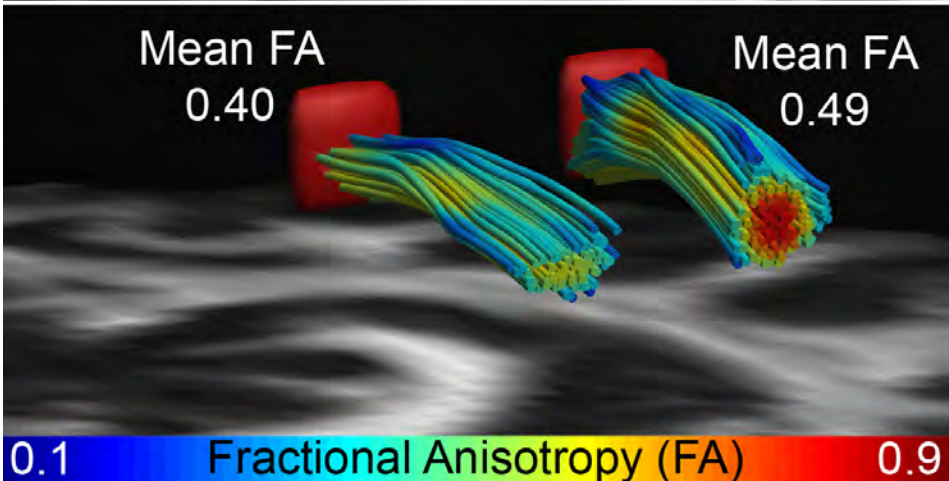
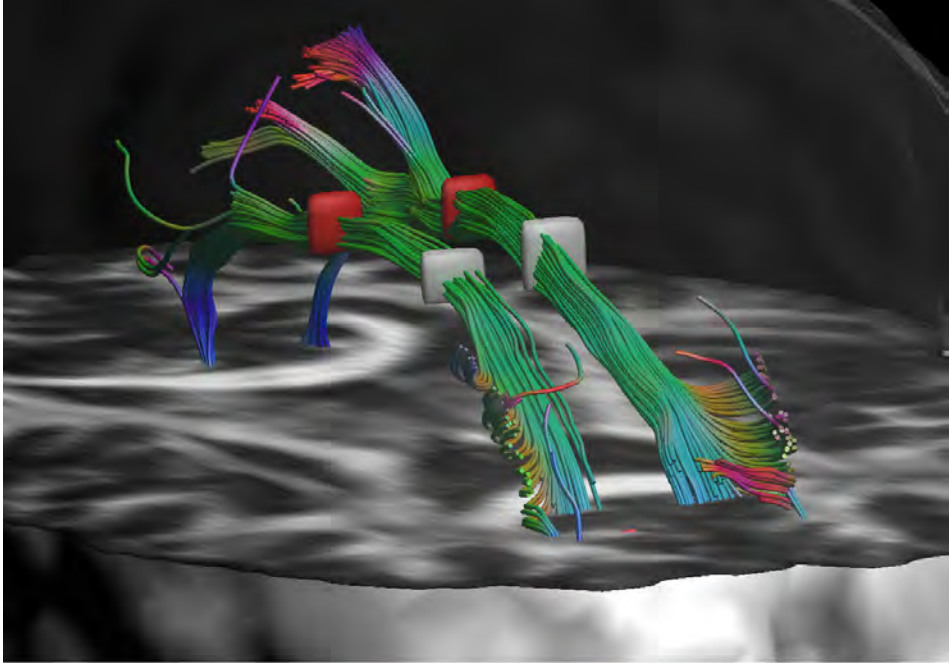
In some neuropathological studies, investigating Wallerian degeneration and mild cognitive impairment, higher FA values were observed in patients than in healthy controls (Pierpaoli et al., 2001; Douaud et al., 2011). In any CF-configuration, degeneration of one fiber bundle could cause the other fiber bundle to become more dominant, resulting in an increase in FA. Similarly, such a physiological change could cause an increase in MD, which, in the context of our findings, may not be indicative for a change in MD of one of the underlying fiber bundles.

In recent years, “crossing fibers” has been one of the foci of diffusion MRI research, resulting in alternative methods that aim to describe the estimated diffusion more accurately in regions of complex fiber architecture, such as CSD, Q-ball Imaging, diffusion spectrum imaging, the ball-and-multiple-sticks model, or multi-tensor modeling

(Tuch et al., 2002; Tuch, 2004; Behrens et al., 2007; Tournier et al., 2007; Wedeen et al., 2008). Fiber tractography based on these new techniques can resolve complex fiber architecture more accurately, even in regions with three fiber populations, e.g., the intersection of the CST, superior longitudinal fasciculus, and lateral projections of the corpus callosum (Descoteaux et al., 2009; Fillard et al., 2011; Jeurissen et al., 2011). When using such techniques to obtain fiber tract segmentations for analyses of the underlying DTI metrics (Zarei et al., 2009), the amount of CF-voxels is increased (since tracking can continue through complex fiber architecture where tensor-based tracking would terminate). As a result, the average MD for the whole bundle may be affected more than when tensor-based tractography algorithms are used for tract segmentations, an effect that may need to be considered during data analysis.

To estimate the MD of individual fiber populations in voxels with complex fiber architecture, one could opt to model the diffusion signal using multiple tensors (Tuch et al., 2002). Multi-tensor tractography aims to model two or three tensors per voxel, propagating the fiber tract by selecting the tensor with its direction most consistent with the tract (Peled et al., 2006). For each tract, the MD of the tensor chosen by the tractography algorithm could be used to calculate bundle-specific diffusion measures, dubbed “tensor selection”. Ideally, this yields more accurate estimates of the MD for that specific bundle (and, similarly, also for other DTI metrics). Current two-tensor methods estimate all three eigenvalues of both tensors (assuming prolate tensors), and can thus be used for this “tensor selection” methodology (Rathi et al., 2010). However, the most recent estimates on the amount of WM voxels with CF-configurations show that roughly 30 to 40% of all WM voxels contain three or more populations (Jeurissen et al., 2010), indicating that two-tensor models may be inadequate for modeling the underlying diffusion signals in these regions. Furthermore, multiple-tensor models may not provide unique solutions for each of the underlying fiber populations, which further complicates data interpretation.

In conclusion, we have provided a theoretical framework and concomitant simulations demonstrating a reduced MD in complex WM configurations. For the first time, this reduction is observed in experimental data (e.g., the CST and the AF). These results improve our understanding of quantitative indices derived from DTI in areas of “crossing fibers” and the impact of numerous factors, including configurational and microstructural properties (e.g., the relative contributions of different fiber populations) and acquisition settings (e.g., the b-value). Most importantly, our findings strengthen the increasing awareness that DTI metrics need to be interpreted with care, and that it is essential to characterize the effects of complex fiber architecture on the MD in order to improve the specificity of observed MD changes *in vivo*.



Bundles with different cross-sectional areas have different partial volume effect contributions, affecting the DTI metrics averaged over the bundle

Chapter 3

Partial volume effect as a hidden covariate in DTI analyses

This chapter has been published as:

S.B. Vos, D.K. Jones, M.A. Viergever, and A. Leemans, "Partial volume effect as a hidden covariate in DTI analyses". *NeuroImage*, 2011, 55 (4), pages 1566-1576.

Abstract

During the last decade, diffusion tensor imaging (DTI) has been used extensively to investigate microstructural properties of white matter fiber pathways. In many of these DTI-based studies, fiber tractography has been used to infer relationships between bundle-specific mean DTI metrics and measures-of-interest (e.g., when studying diffusion changes related to age, cognitive performance, etc.) or to assess potential differences between populations (e.g., comparing males *vs.* females, healthy *vs.* diseased subjects, etc.). As partial volume effects (PVEs) are known to affect tractography and, subsequently, the estimated DTI measures sampled along these reconstructed tracts in an adverse way, it is important to gain insight into potential confounding factors that may modulate this PVE. For instance, for thicker fiber bundles, the contribution of PVE-contaminated voxels to the mean metric for the entire fiber bundle will be smaller, and vice-versa—which means that the extent of PVE-contamination will vary from bundle to bundle. With the growing popularity of tractography-based methods in both fundamental research and clinical applications, it is of paramount importance to examine the presence of PVE-related covariates, such as thickness, orientation, curvature, and shape of a fiber bundle, and to investigate the extent to which these hidden confounds affect diffusion measures. To test the hypothesis that these PVE-related covariates modulate DTI metrics depending on the shape of a bundle, we performed simulations with synthetic diffusion phantoms and analyzed bundle-specific DTI measures of the cingulum and the corpus callosum in 55 healthy subjects. Our results indicate that the estimated bundle-specific mean values of diffusion metrics, including the frequently used fractional anisotropy and mean diffusivity, were indeed modulated by fiber bundle thickness, orientation, and curvature. Correlation analyses between gender and diffusion measures yield different results when volume is included as a covariate. This indicates that incorporating these PVE-related factors in DTI analyses is imperative to disentangle changes in “true microstructural” tissue properties from these hidden covariates.

3.1 Introduction

Diffusion tensor imaging (DTI) is a non-invasive imaging technique that can provide information about brain microstructure and the directional organization of neural fiber tissue *in vivo* by measuring the self-diffusion of water molecules (Basser et al., 1994). In brain white matter (WM), diffusion of water is less hindered along than perpendicular to axons, making the local diffusion dependent on local microstructure (Beaulieu, 2002). DTI was first used clinically in schizophrenia (Buchsbaum et al., 1998) and leuko-araiosis (Jones et al., 1999b), where regional changes in diffusion anisotropy or trace were observed in patients but not in healthy controls. These diffusion changes suggest a structural change, which could be detected more easily on DTI scans than on conventional MR images. Since then, the use of DTI in both fundamental research and clinical studies has exploded, with almost a third of all studies on DTI discussing the development of fiber tractography (FT) methods, e.g., Mori et al. (1999), or the use of FT in DTI analyses. FT was initially applied as a method to investigate “brain connectivity” (Basser et al., 2000) and is now often used to increase specificity of observed radiological findings with respect to patient disability, for instance in multiple sclerosis (Wilson et al., 2003; Ciccarelli et al., 2008).

In recent years, DTI and FT have been used extensively to study the microstructural properties of WM fiber pathways. The developing/aging brain, in particular, has been the research topic of many investigations¹, with studies including subjects ranging from neonates to aging adults. It has been shown repeatedly that the FA of several WM regions (e.g., the cingulum bundles and the uncinate fasciculi) increases during maturation and subsequently decreases with age above the age of approximately 30 years (Bastin et al., 2010; Hasan et al., 2009; Hsu et al., 2008, 2010; Jones et al., 2006; Lebel et al., 2008, 2010; Sala et al., 2010; Salat et al., 2005; Voineskos et al., 2010, 2012). Most of these studies also show an inverse relationship (decrease followed by increase) for the mean diffusivity (MD) and link these diffusion changes to differences in microstructural organization within the WM (Dubois et al., 2008; Lebel et al., 2008). More specifically, changes in radial diffusivity (RD, diffusivity perpendicular to the predominant diffusion direction) and axial diffusivity (AD, diffusivity along the predominant diffusion direction) are believed to reflect different microstructural processes in the WM (Pierpaoli et al., 2001; Song et al., 2002, 2003).

A particular aspect that is known to affect the accuracy of estimated DTI metrics—but which is not always considered a potential cause for correlations or differences in quantitative diffusion analyses—is the partial volume effect (PVE). Reflecting the intra-

1. 57 publications on “DTI brain aging” and 84 on “DTI brain development” since 2009 alone, according to Pubmed.

voxel heterogeneity of different tissue organizations (Alexander et al., 2001; Frank, 2001; Oouchi et al., 2007), Alexander et al. (2001) mentioned that *“the PVE could cause diffusion-based characterization of cerebral ischemia and white matter connectivity to be incorrect”*. Pfefferbaum and Sullivan (2003) have shown that the PVE is also present in the calculation of diffusion measures when averaging data values over regions of interest (ROIs). WM segmentation and semi-automated ROI delineation were used to outline the genu and splenium of the corpus callosum (CC), yielding increased MD values compared to the MD at the center of the WM bundles. This indicates a contamination of the outer WM voxels with its surrounding tissue, which, for the midsagittal genu and splenium of the CC, consists mostly of cerebrospinal fluid (CSF). Several options to mitigate such a CSF contamination have been proposed, such as CSF suppression using fluid-attenuated inversion recovery (FLAIR) acquisition sequences (Papadakis et al., 2002; Cheng et al., 2011), or using a two-tensor model (Pierpaoli and Jones, 2004; Pasternak et al., 2009) to remove the CSF contamination during tensor estimation. However, most DTI studies use neither of these techniques, which leave PVEs with CSF a relevant issue. As partial voluming is not only between WM bundles and CSF, but also, for instance, between different WM bundles, investigations into the effects of the PVE are important to improve quantitative diffusion analyses.

There are several confounding factors related to the PVE that may affect DTI metrics indirectly. For instance, as total WM volume changes with age, and therefore the thickness of some fiber bundles, the relative contribution of PVE-contaminated voxels will be different between bundles of different size (thicker bundles will have a lower contribution of PVE voxels to the entire bundle than thinner bundles), which may introduce a bias in the estimated measures (see Fig. 3.1 for a schematic example). Not only is bundle volume potentially a hidden covariate in the analysis of DTI metrics, but the orientation and curvature of a bundle may also alter the PVE and thus the diffusion measures.

In this work, we hypothesize that hidden covariates, such as bundle thickness (in the following also referred to as “volume”, assuming a constant bundle length and cross-sectional shape), orientation, curvature, and shape modulate the PVE intrinsically and, subsequently, affect the estimated DTI metrics. Previous studies show support for this hypothesis. For instance, investigations of brain volume changes with age show a decline in total WM volume from around the age of 30 (Courchesne et al., 2000; Liu et al., 2003; Resnick et al., 2003), matching the age-FA relation mentioned previously. Another study shows a left-sided co-lateralization of FA and concomitant bundle volume, potentially indicative of a more general agreement between morphometry and diffusion properties (Huster et al., 2009).

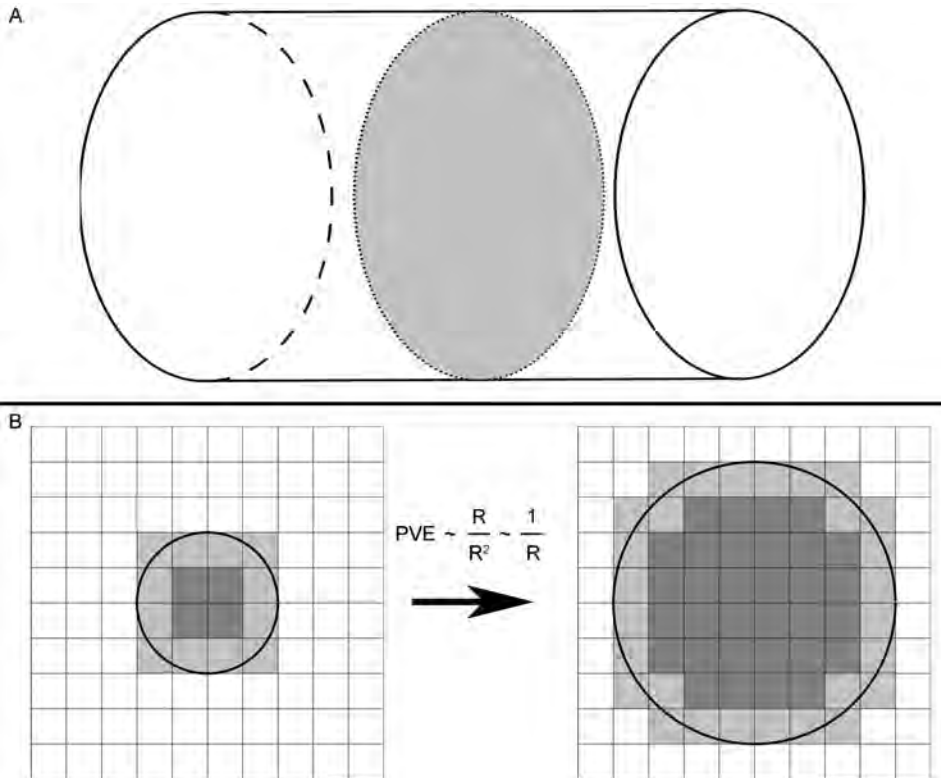


Figure 3.1: Schematic representation of the partial volume effect (PVE) in a 3D object. The PVE is defined as the volume-to-surface ratio of an object. For a cylinder, which has a circular cross-section (indicated as the shaded area in A), this can be simplified to a circle, which has a surface-to-circumference ratio. Further simplification yield that the PVE scales with $1 / R$ (with R the radius of the circle), showing that increasing volume means a reduction in PVE. This is shown in B, where a small and big circle have been plotted on a square grid. The relative number of PVE voxels (light gray) compared to voxels enclosed completely by the circle (dark gray) is larger for a small circle (left) than for a big circle (right).

Using simulations of synthetic diffusion phantoms (Leemans et al., 2005) we determine whether the PVE-related covariates (volume, orientation, and curvature) affect the estimated diffusion measures. With these simulations, it is possible to change the volume, orientation, or curvature of a bundle independently while keeping all other configurational properties fixed. This allows for investigations of only the specific covariate of interest in relation to the estimated DTI metrics. In addition, the cingulum bundles and the CC of 55 healthy subjects are reconstructed using FT to examine whether the PVE-related confounding factors are present in experimental DTI data. The interest by many researchers in these bundles has resulted in an abundance of information about diffusion changes, and thus valuable reference material for this study (Davis et al., 2009; Huster et al., 2009; Jones et al., 2006; Lebel et al., 2008; Malykhin et al., 2008; Salat et al., 2005). The cingulum does not interface with CSF-filled spaces, in contrast with the CC, which is partially adjacent to the lateral ventricles and the longitudinal fissure. In regions where there is proximity to the ventricles, for example, one observes “spikes” in the MD values (Jones et al., 2005b). The large difference in the surrounding tissues makes these bundles ideal candidates to determine the potential effect of PVE-related covariates on the different diffusion parameters. By investigating correlations between the volume of the bundles and specific diffusion properties of these bundles, the presence of such a hidden covariate may be revealed.

Our results demonstrate that DTI metrics are indeed correlated with volume, orientation, and curvature of a fiber bundle. As such, several conclusions drawn from previous analyses—aging studies in particular—should be nuanced in the light of these PVE-related covariates in order to correctly classify whether the observed changes in diffusion measures originate from either changes in macrostructural/morphological or microstructural properties, or a combination of both. Observed relations between age and diffusion properties are altered by the inclusion of volume as a covariate, which indicates that it is required to include this confound in quantitative analyses.

3.2 Materials and methods

3.2.1 Fiber bundle simulations

Simulations of neural fiber bundles were performed according to Leemans et al. (2005) to investigate the following potentially confounding factors in FT-based analyses: (i) fiber bundle thickness (predefined range: 9-13 mm); (ii) pathway orientation (in-plane rotation range: 0-15°); and (iii) bundle curvature (inverse radius range: 0.035-0.055 mm⁻¹). Keeping all other simulation parameters unchanged, only the contribution of PVE-contaminated voxels to the bundles differs between the simulations. The effect of these factors was examined using FA = 0.9 and MD = 0.7 × 10⁻³ mm²/s within the bundle, and two different bundle environments: one representing the CC segment en-

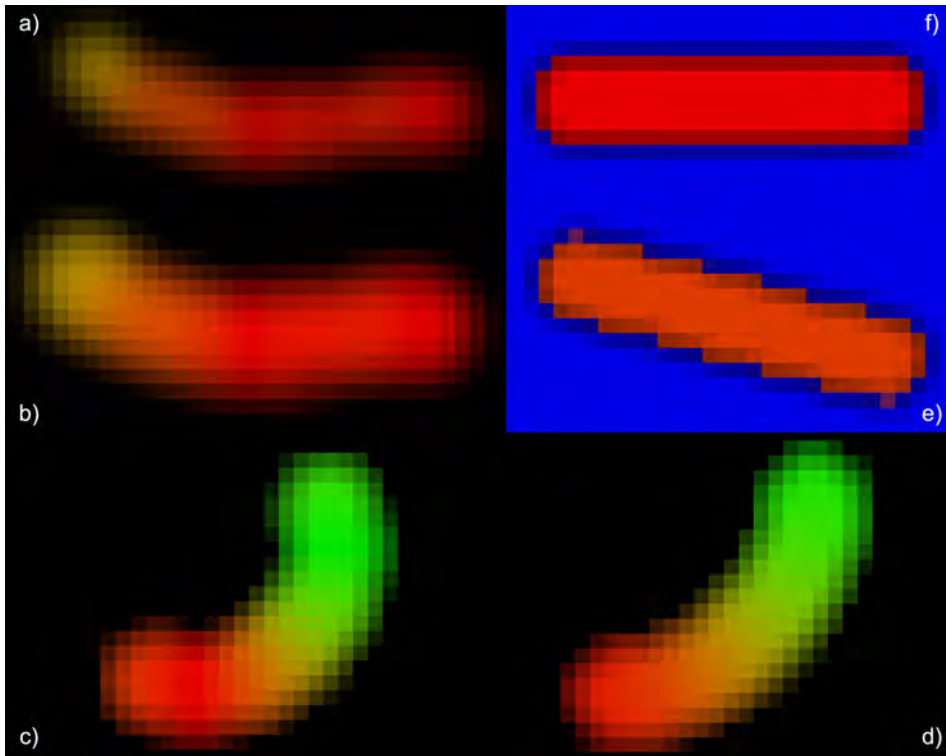


Figure 3.2: Simulated fiber bundles of varying thickness (a and b), curvature (c and d), and orientation (e and f). a-d are examples of cingulum simulations, with a fiber bundle in an isotropic surrounding with high diffusivity; whereas e-f are examples of CC simulations, with an anisotropic environment oriented perpendicularly to the simulated bundles.

environment (in the following referred to as “CC simulations”, with background FA = 0 and MD = $3.2 \times 10^{-3} \text{ mm}^2/\text{s}$); and one representing the cingulum environment (in the following referred to as “cingulum simulations”, with background FA and MD values equal to the values within the fiber bundle, albeit with a different orientation) (Le Bihan et al., 2001; Jones and Basser, 2004). In total, six sets of simulations were performed (Fig. 3.2). Fiber bundles were simulated with 2 mm isotropic voxel size and a Gaussian profile across the bundle. For more detailed information on the simulation framework, the reader is referred to Leemans et al. (2005). Deterministic FT (Basser et al., 2000) was performed in *ExploreDTI* (Leemans et al., 2009) with an FA tracking threshold of 0.2 and an angle threshold of 30° .

3.2.2 Data acquisition

Cardiac-gated DTI data were acquired from 55 healthy volunteers (37 female, 18 male), aged 18.4 to 44 years (median age 31.9 years), on a 3 T system using a single-shot spin-echo EPI sequence with a b-value of 1200 s/mm^2 along 60 directions (Jones et al., 1999a), with 6 B0-images and ASSET factor = 2. The acquisition matrix of 96×96 was reconstructed to 128×128 with a field-of-view of $230 \times 230 \text{ mm}^2$ and 60 axial slices with thickness 2.4 mm were acquired without gap. This resulted in an effective TR of 15 R-R intervals and a total acquisition time of approximately 25 min. All subjects gave written informed consent to participate in this study under a protocol approved by the Cardiff University Ethics Committee.

3.2.3 Image processing

Prior to data analysis, the acquired images were corrected for eddy current induced geometric distortions and subject motion by realigning all diffusion-weighted images (DWIs) to the B0-images (non-diffusion weighted images) with *elastix* (Klein et al., 2010) using an affine coregistration technique (12 degrees of freedom) with mutual information as the cost function (Pluim et al., 2003). In this procedure, the diffusion gradients were adjusted with the proper b-matrix-rotation as described by Leemans and Jones (2009). The diffusion tensor model was fitted using the Levenberg-Marquardt nonlinear regression method (Marquardt, 1963), initiated with the fitted values from a weighted linear least squares estimation. All DTI scans were rigidly transformed to MNI space in the motion-distortion correction procedure (Rohde et al., 2004).

3.2.4 Tractography

To determine whether PVE-related confounds affect FT-based analyses of DTI metrics in experimental data we investigated the characteristics of the cingulum and the CC. Whole brain FT parameters were identical to the ones used for the simulated diffusion data. To investigate the existence of the aforementioned covariates when analyzing diffusion measures of the cingulum bundle, a specific segment was selected in the dorsal part of the cingulum. The segments were defined by placing three “AND” ROIs at selected anatomical landmarks (Emsell et al., 2009) and placing two ROIs 10 mm anterior (S1) and posterior (S2) of the central “AND” ROI (Fig. 3.3). Only the tract segment, i.e., the part of the fiber bundle between ROIs S1 and S2, was investigated. In doing so, there were no intersubject differences in segment length, which ensures consistency in estimating the volume of the fiber bundles. Bundle characteristics were calculated by averaging diffusion measures for all voxels intersected by that bundle, with each voxel only counted once (Concha et al., 2005a,b, 2009; Eluvathingal et al., 2007; Lebel et al., 2010), and defining segment volume as the total volume of the voxels intersected by that bundle. ROIs were defined by a single blinded rater.

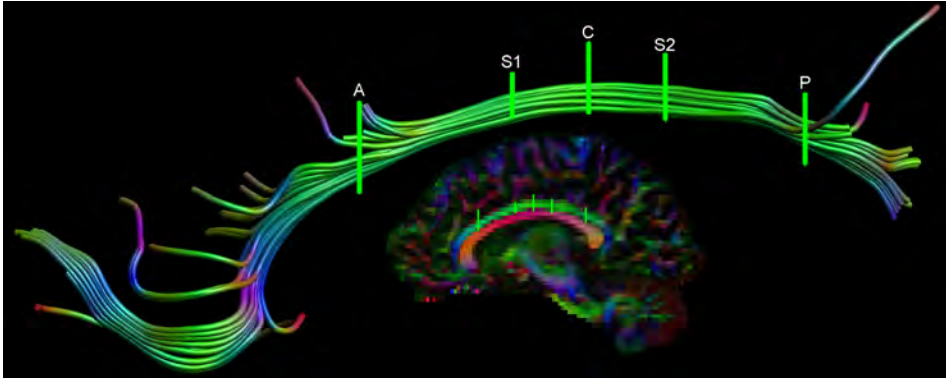


Figure 3.3: Selection of the cingulum segment. Anterior (A) and posterior (P) regions of interest (ROI) were placed at the most posterior slice showing the genu in full profile and the most anterior slice showing the splenium in full profile, respectively. Central (C) ROI was placed at midpoint between A and P, with segment-selecting ROIs placed five voxels (10 mm) anterior (S1) and posterior (S2) of C.

The second bundle that was studied was the CC. Only the medial part of the CC, which is (almost) entirely surrounded by CSF, was investigated to test whether the influence of the PVE on DTI measures may be different from bundle configurations where the fiber bundles are surrounded by other WM structures and not by CSF. Segments of 4 mm length to either side of the midsagittal slice were selected (Fig. 3.4): a length that is long enough to have a large spread in segment volumes, but short enough so that the segment is still surrounded by CSF only. As all data were analyzed in MNI space, the midsagittal slice could be determined reliably in all subjects.

3.2.5 Statistical evaluation

To test the hypothesis that bundle volume is a PVE-related covariate, Spearman's rank correlation coefficients between DTI metrics (FA, MD, AD, and RD) and segment volume were calculated. According to our hypothesis, segment volume should be added as a covariate not-of-interest in further analyses, for instance, when calculating the correlation between age and bundle-specific quantitative measures. Using multiple regression we have tested whether there was a significant linear or quadratic relation between age and diffusion measures (Hsu et al., 2010), and whether the inclusion of volume as a covariate yielded a different outcome in these analyses.

Previously, diffusion values of the cingulum were found to differ between males and females and between the left and the right bundle (Huster et al., 2009). Segment volume was incorporated into these analyses as a covariate, to examine whether any observed

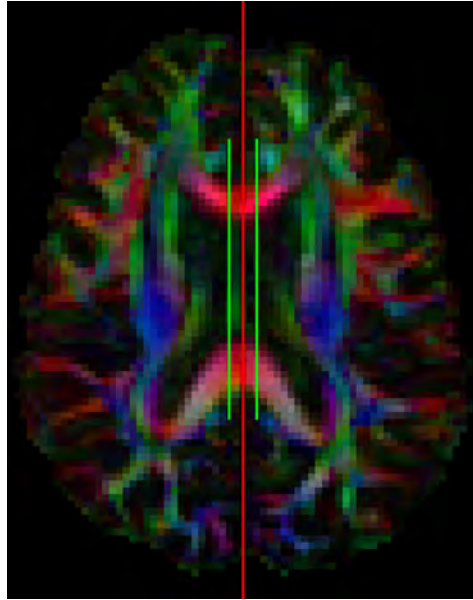


Figure 3.4: Selection of the medial segment of the corpus callosum. The red line represents the midsagittal plane in MNI space, and the two segment-selecting regions-of-interest (green) are drawn two voxels (4 mm) to either side of the midsagittal plane.

differences in diffusion measures between left and right cingulum bundles or between males and females were due to volume differences.

3.3 Results

3.3.1 PVE-related covariates in simulations

All six sets of simulations (changes in volume, orientation, and curvature, for both the cingulum and CC simulations) showed a clear effect of these PVE-related covariates on the estimated DTI metrics. Bundle volume demonstrated a monotonous relation with the diffusion measures (Fig. 3.5). By contrast, the other PVE-modulating factors generally displayed a high degree of non-monotonicity (Figs. 3.6 and 3.7).

3.3.2 Experimental data

Correlations between segment volume and DTI metrics have been visualized in Fig. 3.8 for the cingulum and in Fig. 3.9 for the CC. A positive correlation of FA with volume ($p = 0.028$) was found for the cingulum segments, and the CC segments showed a significant decrease of MD with segment volume ($p = 0.0039$). To reveal the underlying causes for these correlations, subsequent analyses were performed to determine whether AD

Partial volume effect as a hidden covariate in DTI analyses

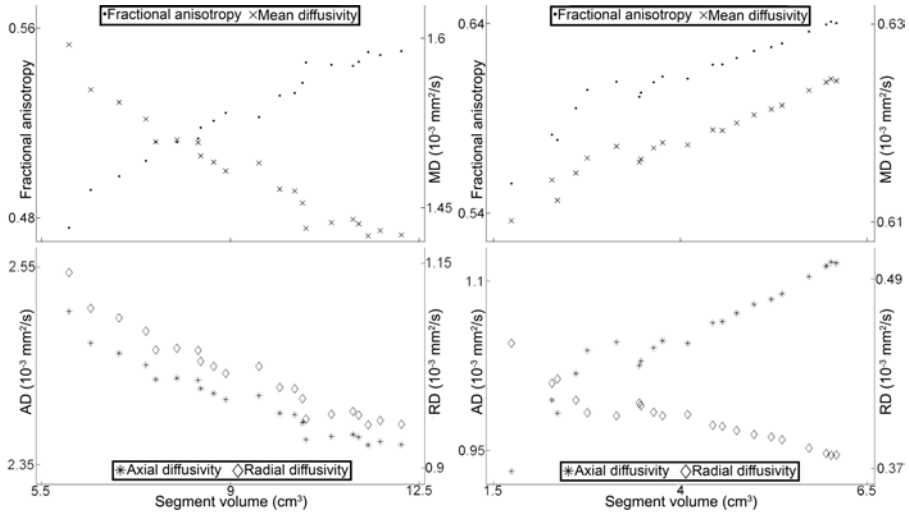


Figure 3.5: Dependence of DTI metrics on bundle volume. The plots in the left column show the results of the corpus callosum (CC) simulations; plots in the right column show the results of the cingulum simulations. These plots show that bundle volume modulates, through the PVE, all estimated diffusion parameters.

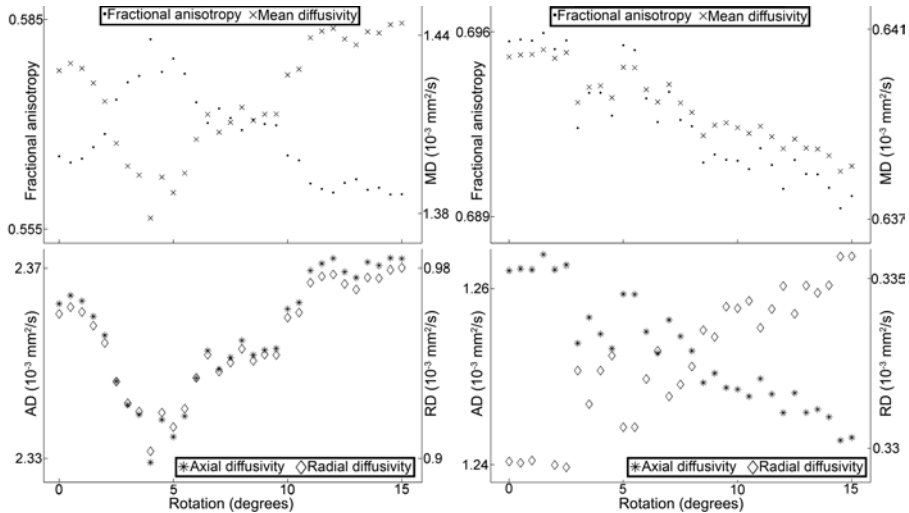


Figure 3.6: Dependence of DTI metrics on bundle orientation. The plots in the left column show the results of the corpus callosum (CC) simulations; plots in the right column show the results of the cingulum simulations. In these simulations, the simulated bundle is rotated over a range of 15° .

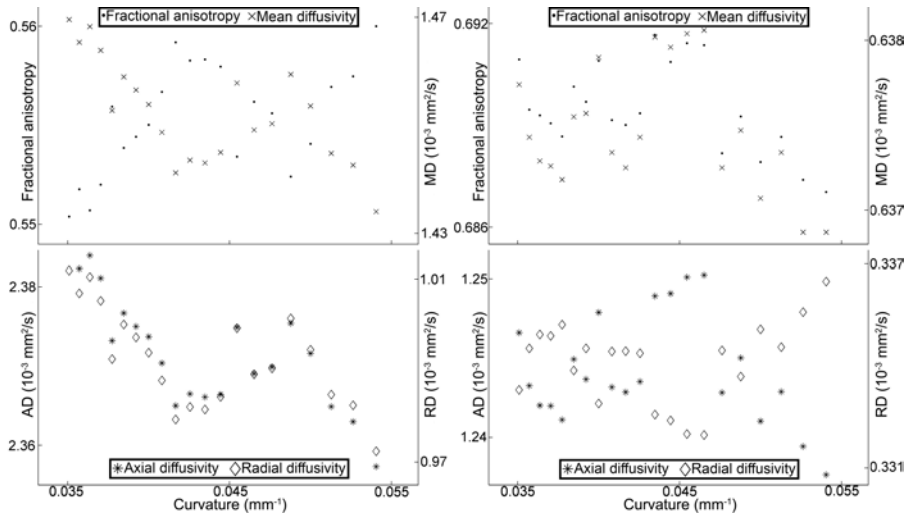


Figure 3.7: Dependence of DTI metrics on bundle curvature. The plots in the left column show the results of the corpus callosum (CC) simulations; plots in the right column show the results of the cingulum simulations. In these simulations, the curvature of the simulated bundle is increased.

and/or RD were correlated with segment volume. In the cingulum, a downward trend of RD with segment volume was observed (Fig. 3.8). In the CC, the correlation between MD and volume was due to underlying decreases of both AD and RD with segment volume ($p = 0.021$ and $p = 0.0037$, respectively) (Fig. 3.9).

Investigation of the effect of age on bundle-specific quantitative measures demonstrated that in the CC segment only the FA correlated significantly (decreasing linearly) with age ($p = 0.0056$). Inclusion of bundle volume as a covariate did not alter this relation. For the cingulum, no significant relation with age was observed, with or without including volume as a covariate.

No gender-related differences in diffusivity measures were observed for the cingulum. For the CC, including volume as a covariate yielded a significantly higher FA and lower MD, caused by a significantly lower RD, in females than in males. These effects could not be observed without segment volume as a covariate (Table 3.1).

Intrasubject analysis of left and right cingulum segments revealed a significantly higher AD left than right, with or without segment volume as a covariate. There was no significant difference in the corresponding FA, MD, or RD values between the left and the right cingulum segments (Table 3.2).

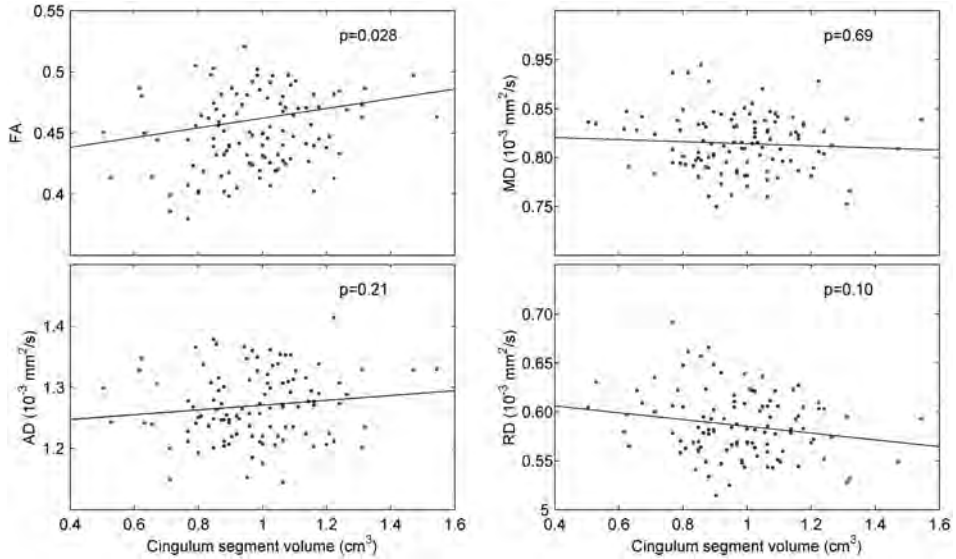


Figure 3.8: Correlation of DTI metrics and volume for the cingulum segments. A significant increase in fractional anisotropy (FA) with volume is observed, whereas no significant changes in mean, axial, or radial diffusivity are observed. The increase in FA is caused by opposite trends of axial and radial diffusivity with volume. While non-parametric tests have been used to test for correlations, parametric tests have been used for the plotted lines to show the trends in the data.

3.4 Discussion

Several factors, e.g., bundle thickness, orientation, and curvature may change the PVE and thus the analysis and estimation of bundle-averaged DTI metrics. These PVEs originate from the acquisition: signal averaging over finite-size voxels may include more than one structure. As already illustrated in Fig. 3.1, bundles can be influenced differently by the PVE depending on bundle thickness. However, a single bundle may also be affected by its position relative to the acquisition matrix. Consider the simulated fiber bundle shown in Fig. 3.10a(i), which is perfectly aligned with the voxel grid. If the bundle is not perfectly aligned with the acquisition grid (Fig. 3.10a (ii)-(iv)), the outer voxels are PVE voxels, which affect the estimated DTI metrics of the bundle, as seen in Fig. 3.10b. Such a “gridding effect” affects the reproducibility of DTI analyses negatively. Therefore, it is important to tease out possible covariates that may confound the estimation of diffusion measures in order to improve the reliability of DTI analyses.

3.4.1 Proof of principle

Previously, it has been shown that CSF contamination in PVE voxels influences voxel-wise DTI metrics (Papadakis et al., 2002; Chou et al., 2005). In this work, however, we investigated whether PVE modulating factors (i.e., bundle volume, orientation, and curvature) cause significant differences in diffusion measures of large, multi-voxel regions. To highlight this issue for experimental data, we also performed an analysis in which volume can be considered as the only PVE modulating factor. More specifically, we examined the existence of a relation between DTI parameters of the CSF and the total CSF volume. The diffusivity of CSF should be roughly the same across individuals, so no correlation with volume is expected. However, as the MD of PVE voxels is decreased compared to non-PVE voxels of the CSF (Chou et al., 2005), one can expect that for smaller CSF volumes (where the relative contribution of PVE voxels is higher than for larger CSF volumes) the estimated MD would be lower. This relation is confirmed by segmenting all CSF voxels using an automated gray-level thresholding method, performed on the MD map (Otsu, 1979), and correlating the total volume of CSF with

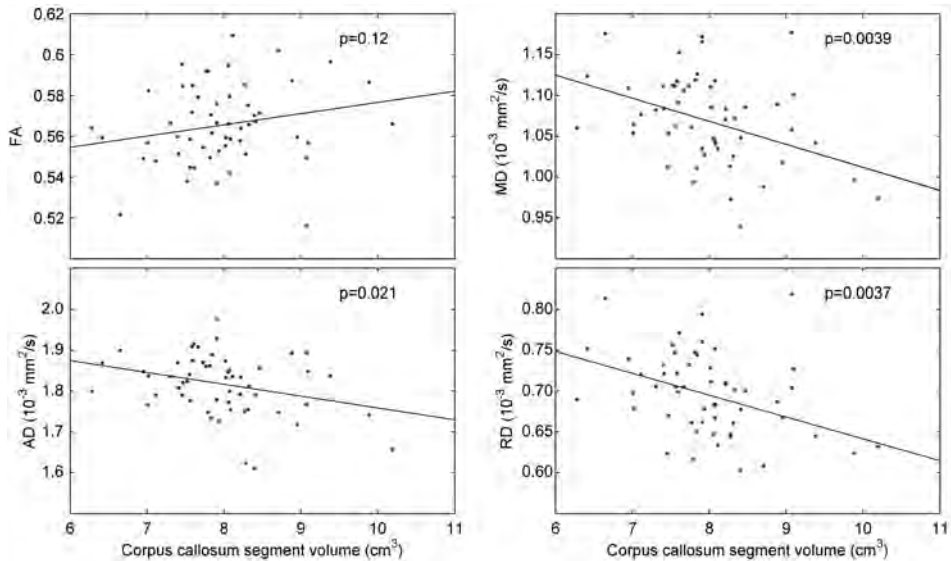


Figure 3.9: Correlation of DTI metrics and volume for the corpus callosum segments. No significant change in fractional anisotropy (FA) with volume is observed, whereas the mean diffusivity (MD) decreased significantly with volume. The decrease in MD is caused by negative correlations of axial (AD) and radial (RD) diffusivity with segment volume. While non-parametric tests have been used to test for correlations, parametric tests have been used for the plotted lines to show the trends in the data.

Table 3.1: Gender comparison of bundle segments

		Female	Male
Cingulum segment	Volume (cm ³)	0.942 ± 0.166	1.045 ± 0.195*
	Fractional anisotropy	0.448 ± 0.032	0.456 ± 0.028
	MD (10 ⁻³ mm ² /s)	0.816 ± 0.026	0.812 ± 0.036
Corpus callosum segment	Volume (cm ³)	7.857 ± 0.787	8.215 ± 0.665
	Fractional anisotropy	0.569 ± 0.019	0.559 ± 0.019 [†]
	MD (10 ⁻³ mm ² /s)	1.063 ± 0.055	1.086 ± 0.047 [†]

MD = mean diffusivity; * indicates gender difference not including volume as covariate ($p < 0.01$); [†] indicates gender difference including volume as covariate ($p < 0.05$)

Table 3.2: Intrasubject comparison of cingulum bundle segments

	Left	Right
Segment volume (cm ³)	1.031 ± 0.167	0.921 ± 0.181*
Fractional anisotropy	0.456 ± 0.031	0.445 ± 0.029
MD (10 ⁻³ mm ² /s)	0.811 ± 0.029	0.812 ± 0.029
AD (10 ⁻³ mm ² /s)	1.284 ± 0.054	1.257 ± 0.054* [†]
RD (10 ⁻³ mm ² /s)	0.584 ± 0.034	0.590 ± 0.032

MD = mean diffusivity; AD = axial diffusivity; RD = radial diffusivity; * indicates left-right difference not including volume as covariate ($p < 0.01$); [†] indicates left-right difference including volume as covariate ($p < 0.05$)

the estimated DTI metrics in that volume. The FA decreases with larger CSF volumes, whereas the MD, AD, and RD show a distinct positive correlation with CSF volume. This proof of concept clearly demonstrates the existence of a confounding factor (in this case the volume of CSF regions) that affects the PVE contribution and, in turn, the estimation of DTI measures.

3.4.2 PVE-related covariates in simulations

The effect of PVE modulation can be observed in both the cingulum and the CC simulations, where bundle volume and FA are strongly correlated ($p < 0.001$). The induced change in FA is caused by a significant reduction in RD in both sets of simulations, a decrease of AD in the CC simulations, and an increase of AD in the cingulum simulations (Fig. 3.5). In all simulations, the relative changes in RD were larger than or equal to the relative changes in AD, showing that changes in RD are the main underlying cause of the observed changes in FA. These results indicate that the contribution

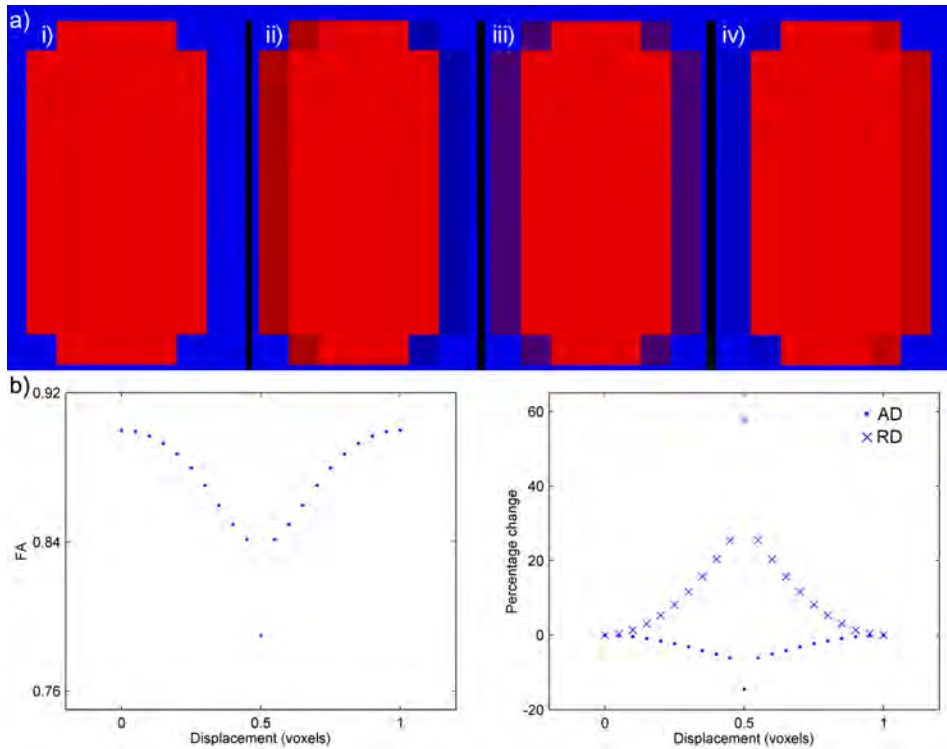


Figure 3.10: The relative position of a simulated fiber bundle on the voxel grid changes the partial volume effect (PVE). In this simulation, the background has a high fractional anisotropy (FA) and orientation perpendicular to the bundle. a) i) shows a simulated bundle aligned with the voxel grid, ii)-iv) show the bundle misaligned by 0.3, 0.5, and 0.8 voxels horizontally, respectively. b) shows the DTI metrics as a function of relative position to the voxel grid (FA; mean diffusivity, MD; axial diffusivity, AD; radial diffusivity, RD). The resulting differences in PVE of these bundles (as can be seen in A) lead to changes in the estimated DTI metrics.

of PVE-contaminated voxels reduces with increased volume and that this PVE-related covariate influences the analysis of diffusion parameters. In these simulations, a constant cross-sectional shape has been defined. It is important to note that for bundles with a more irregular shape, larger volumes do not necessarily result in a higher PVE-contamination.

A relation was also observed between DTI metrics and two other confounds, i.e., orientation and curvature, but not all simulations showed a monotonous relation (Fig. 3.6, 3.7). These changes, especially in the CC simulations, demonstrate that the effects of

orientation and curvature are non-trivial. Although the simulations showed a strong effect of PVE altering factors on diffusion measures, in particular for volume, these results can only be regarded as an approximation: in each set of simulations only one factor was varied, whereas real data will show variation in volume, orientation, and curvature between different (parts of) bundles simultaneously.

3.4.3 Experimental data

The effect of bundle volume on diffusion measures in the simulations was larger than the effects of curvature and orientation. We have therefore focussed only on bundle volume as a potential PVE-modulating covariate in the experimental DTI data.

Group analysis of the cingulum bundles showed a positive correlation between the volume of the cingulum segment and FA (Fig. 3.8). Adjacent WM-bundles have a high diffusivity perpendicular to the cingulum and low diffusivity parallel to the cingulum, and the PVE, therefore, is expected to affect both AD and RD. In the cingulum segments, however, this has not lead to significance relations with volume. Thanks to the opposite trends of AD and RD with volume, the FA increased and the MD was unchanged. These findings are in agreement with the known fact that the MD does not depend on PVE changes in the cingulum bundle, inasmuch as it is surrounded by gray matter and other WM structures, both of which have similar MD values in the Gaussian b-value regime (Pierpaoli et al., 1996; Yoshiura et al., 2001).

For the cingulum simulations (Fig. 3.5), the average MD within the bundle was affected by the hidden covariates. However, the changes were relatively small compared to the absolute values. Although these findings could not be observed in the experimental data, detecting such small changes in MD values in acquired DTI data is harder than in simulations because of noise and natural variability between subjects. Furthermore, there is more than one PVE modulating covariate affecting the diffusion metrics in experimental data, whereas only one factor was changed in the simulations. Overall, the results observed in the simulations are in very good agreement with the experimental findings of the cingulum segments.

In structures adjacent to CSF, for instance the CC, one would expect changes in PVE to affect the MD as well. CSF should exhibit unhindered diffusion and hence a high MD, so, in theory, PVE contamination with CSF will increase the estimated MD of the CC bundle (similar to the proof of concept analysis). This means that a thinner CC would have a higher MD than a thicker CC. In the group analysis of the medial part of the CC, a significant decrease of MD with increasing bundle volume was observed, showing that the MD depended on PVE-related changes due to bundle thickness (Fig. 3.9). Although the MD decreased significantly, caused by a decrease in both its axial and its radial component, only an upward trend of FA with volume was observed. Here, the inter-

Chapter 3

subject variability in terms of local curvature and orientation, or true microstructural differences (e.g., axon diameter or axon packing density) may be too large to infer a clear FA relationship.

The observed changes in MD are in accordance with previously reported measurements, showing significant increases from adolescents to older adults (mean age 18.9 years and 67.6 years, respectively) in structures adjacent to CSF (e.g., the genu of the CC and the fornix), whereas deep WM (e.g., pericallosal) areas showed no change (Bennett et al., 2010). Next to “microstructural” changes, these differences in MD between adolescents and older adults may be explained in part on the basis of WM atrophy, i.e., WM tissue loss due to aging. Shrinkage of the WM causes thinning of several fiber bundles and, as we have shown in this work for the CC, the MD depends on the thickness of this fiber bundle. Although changes in diffusion measures are observed even when correcting for volume (Bendlin et al., 2010), atrophy could still explain part of the observed variance of diffusion measures with age.

As shown in this work, bundle volume is significantly correlated with bundle-specific quantitative measures, and should therefore be included as a covariate in the analysis of age on these measures. Independent of whether segment volume has been included as a covariate, we showed a linear decrease of FA with age for the CC segment. The diffusion measures for the cingulum, and the MD, AD, and RD for the CC showed no significant age relation. This is due to the age range of the subjects, which is located at the peak of the quadratic relation between age and DTI measures (Hsu et al., 2010). In studies where an age effect has been demonstrated, such as Lebel et al. (2008) and Hsu et al. (2010), the importance of WM volume as a covariate in DTI analyses is even more essential to specify whether the cause of the observed age effects is due to changes in bundle volume, “true microstructural” change, or both.

In the investigation of differences in diffusion measures between genders, incorporating volume into the analysis yielded a significant difference in the FA, MD, and RD of the CC. A higher FA and lower MD were observed in females than in males, originating from significantly lower RD values in males. These differences were only observed when volume was incorporated in the analysis 3.1, showing that including volume as a covariate is imperative.

Besides the “gridding effect” due to discrete sampling, preprocessing of the DWIs (e.g., motion correction) introduces additional PVE. The preprocessing steps, as well as the extent of the corrected motion and distortions, are roughly equal for all subjects. This means that the intersubject variability in volume and diffusion estimates subjects may be increased, but any underlying trends will not be altered.

An FA threshold of 0.2 and an angle threshold of 30° have been used to reconstruct the fiber pathways. Although these values are often used in deterministic FT, there are also many studies using a less strict threshold, such as FA thresholds of 0.15 or 0.1. One can imagine that if such more liberal thresholds are used, FT will include more voxels on the edges of bundles, thereby increasing the PVE contribution to the bundle. A clear example of this has been shown in the work of Taoka et al. (2009), where the uncinate fasciculus (UF) has been tracked with four different FA tracking thresholds (0.1, 0.15, 0.2, and 0.25). As a result of changing this FT parameter, they found an increase in UF volume, accompanied by lower FA and higher MD values in the UF, when using lower FA thresholds. The inclusion of more PVE voxels with lower thresholds increased the bundle volume, and consequently modulated the estimated FA and MD values. We have chosen to use strict tracking parameters to show that even when using conservative parameters, the PVE-related confounds still affect the DTI metrics.

3.4.4 Implications and future work

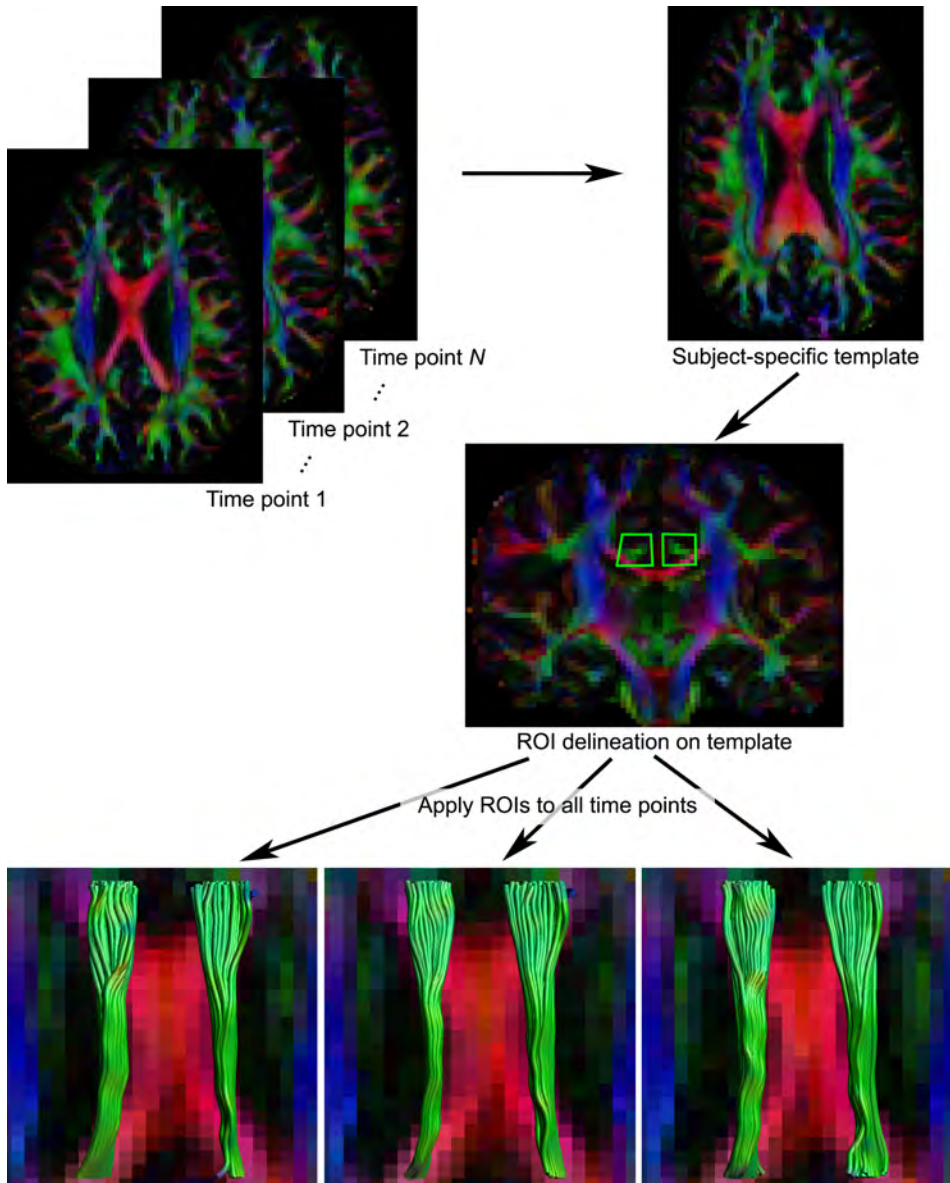
The results presented in this work are not limited to FT-based analyses. Since bundle thickness is inherently an underlying factor, ROI-based (Mukherjee et al., 2001; Bonekamp et al., 2007), voxel-based (Madden et al., 2009; Westlye et al., 2009), and atlas-based analyses (Huang et al., 2006; Fjell et al., 2008) suffer from these confounds as well. Similarly, these effects are not limited to the tensor framework, but also apply to other approaches of diffusion modeling, such as spherical deconvolution and Q-ball imaging (Tournier et al., 2004; Tuch, 2004), among others. To truly examine the extent of PVE-related confounds in diffusion analyses, future studies should aim to clarify the effect sizes of different factors influencing diffusion measures.

Being cross-sectional by design, this study cannot uncouple potentially true microstructural changes from morphological confounds, such as bundle volume, orientation, or curvature, across different subjects. Longitudinal studies could overcome this drawback by comparing bundle volume and configuration over time as well as age and DTI parameters. For instance, if in such a study covariates not-of-interest remain unchanged but diffusion measures do change, those changes truly reflect changes in microstructure. Given a sufficient total follow-up time and regular examination of bundle characteristics, such studies should be able to determine the effects of these factors on the estimated diffusion metrics, and during what stage of development and/or aging these changes occur.

In conclusion, our work shows that bundle volume, orientation, and curvature are PVE-modulating factors that, subsequently, affect the estimation of diffusion metrics when sampled along the tract. These findings further our understanding of causality when interpreting the results of DTI analyses. In other words, we have shown the

Chapter 3

existence of variables that have not been considered previously, volume in particular, contributing to the explanation of the observed differences in DTI measures between populations (e.g., males *vs.* females). To disentangle “true microstructural” from macrostructural and configurational differences/relations or, more generally, to improve the specificity of quantitative DTI analyses, we suggest to include volume as a covariate not-of-interest in future studies.



Automating intra-subject fiber bundle segmentation for analysis of longitudinal DTI data

Chapter 4

Automated longitudinal intra-subject analysis for diffusion MRI tractography

This chapter has been submitted as:

S.H. Aarnink*, S.B. Vos*, A. Leemans, T.L. Jernigan, K.S. Madsen, and W.F.C. Baaré, “Automated Longitudinal Intra-Subject Analysis (ALISA) for diffusion MRI tractography”

* these authors contributed equally

Abstract

Fiber tractography (FT), which aims to reconstruct the three-dimensional trajectories of white matter (WM) fibers non-invasively, is one of the most popular approaches for analyzing diffusion tensor imaging (DTI) data, given its high inter- and intra-rater reliability and scan-rescan reproducibility. The major disadvantage of manual FT segmentation, unfortunately, is that placing regions-of-interest for tract selection can be very labor-intensive and time-consuming. Although there are several methods that can identify specific WM fiber bundles in an automated way, manual FT segmentations across multiple subjects performed by a trained rater with neuroanatomical expertise are generally assumed to be more accurate. However, for longitudinal DTI analyses it may still be beneficial to automate the FT segmentation across multiple time points, but then for each individual subject separately. Both the inter-subject and intra-subject automation in this situation are intended for subjects without gross pathology. In this work, we propose such an automated longitudinal intra-subject analysis (dubbed ALISA) approach, and assessed whether ALISA could preserve the same level of reliability as obtained with manual FT segmentations. In addition, we compared ALISA with an automated inter-subject analysis. Based on DTI data sets from (i) ten healthy subjects that were scanned five times (six-month intervals, aged 7.6-8.6 years at the first scan) and (ii) one control subject that was scanned ten times (weekly intervals, 12.2 years at the first scan), we demonstrate that the increased efficiency provided by ALISA does not compromise the high degrees of precision and accuracy that can be achieved with manual FT segmentations. Further automation for inter-subject analyses, however, did not provide similarly accurate FT segmentations.

4.1 Introduction

To date, diffusion magnetic resonance imaging (MRI) is the only non-invasive method for probing soft tissue microstructure and its 3D architectural organization *in vivo*, offering the possibility of exploring the microstructural organization and architectural configuration of distinct anatomical fiber networks within the brain white matter (WM) (Jones, 2008b; Tournier et al., 2011). Diffusion tensor imaging (DTI; Basser et al., 1994), in particular, has been widely used to investigate e.g., WM abnormalities in pathological conditions (Concha et al., 2005a,b; Jones et al., 2006; Ciccarelli et al., 2006; Price et al., 2008; Yogarajah et al., 2008; Sage et al., 2009; Caeyenberghs et al., 2010; Van Hecke et al., 2010b; Deprez et al., 2011), WM changes in normal development (Zhang et al., 2007; Eluvathingal et al., 2007; Lebel et al., 2008, 2010; Verhoeven et al., 2010), and aging (Sullivan and Pfefferbaum, 2007; Van Hecke et al., 2008a; Hsu et al., 2008, 2010). In many of these studies, fiber tractography (FT; e.g., Mori et al., 1999; Conturo et al., 1999; Jones et al., 1999b; Basser et al., 2000) has been used to identify specific WM fiber bundles, from which diffusion characteristics, such as fractional anisotropy (FA) and mean diffusivity (MD), can be derived (Jones et al., 2005b). Other approaches for investigating DTI data include region-of-interest (ROI) (e.g., Snook et al., 2005; Madsen et al., 2011), histogram (e.g., Cercignani et al., 2001), voxel-based (e.g., Giorgio et al., 2010) including TBSS (Smith et al., 2006), network-based (e.g., Hagmann et al., 2008; Reijmer et al., 2013b), and atlas-based (e.g., Faria et al., 2011) analyses. A detailed description of these techniques is considered beyond the scope of this article—the interested reader is referred to surveys by Cercignani (2011) and Hasan et al. (2011).

With the ability to observe diffusion changes over time in the same population of subjects, longitudinally designed DTI studies can provide more specific insights into the microstructural dynamics of brain WM tissue compared to studies with a cross-sectional population setup (Beaulieu, 2002; Johansen-Berg, 2010; Lebel and Beaulieu, 2011). Boosted by the advent of more stable and high performance MR equipment, the interest to perform longitudinal DTI studies for capturing such subject-specific changes in microstructural organization is increasing rapidly (e.g., Concha et al., 2007; Gong et al., 2008; Keller and Just, 2009; Kumar et al., 2009; Schlaug et al., 2009; Scholz et al., 2009; Sullivan et al., 2010; Yogarajah et al., 2010; Ljungqvist et al., 2010; Deprez et al., 2012). Although there are several well-established methods for analyzing cross-sectional DTI data sets, they may not be ‘optimal’ for longitudinal studies. In voxel-based DTI analyses, for instance, which are notorious for their high sensitivity with respect to the amount/type of filtering (Jones et al., 2005a; Van Hecke et al., 2009, 2010a) and choice of template/atlas (Van Hecke et al., 2008b, 2011; Sage et al., 2009), subtle intra-subject changes may not be detected due to the much larger residual inter-subject misalignments. In this case, and if there is also a clear hypothesis regarding a specific WM fiber

bundle, or a segment thereof (Colby et al., 2012), FT may be preferred over the voxel-based approach.

By combining objective protocols for extracting WM fiber pathways of interest on the one hand (Wakana et al., 2004, 2007; Catani et al., 2008) and incorporating subjective prior knowledge from the neuroanatomical expert on the other hand, many studies have already demonstrated the high inter- and intra-rater reliability and scan-rescan reproducibility of manual FT segmentations (Ciccarelli et al., 2003; Pfefferbaum and Sullivan, 2003; Heiervang et al., 2006; Wakana et al., 2007; Malykhin et al., 2008; Danielian et al., 2010; Kristo et al., 2013a,b). The major drawback of manual FT segmentations, however, is that placing ROIs for tract selection can be very labor-intensive and time-consuming, which—for obvious reasons—can become problematic for large-cohort studies. Notwithstanding the existence of methods that can identify WM fiber bundles in an automated way in the absence of gross pathology (Leemans et al., 2006; Clayden et al., 2007; Lebel et al., 2008; O'Donnell et al., 2009; Hagler et al., 2009; Verhoeven et al., 2010; Zhang et al., 2010; Reich et al., 2010; Yendiki et al., 2011; Suarez et al., 2012), manual FT segmentations across multiple subjects performed by a trained rater with neuroanatomical expertise are generally more specific and, therefore, more accurate. For longitudinal DTI analyses, however, it may still be beneficial to automate the FT segmentation across multiple time points, but then for each individual subject separately. In doing so, the adverse effect of inter-subject variability on the reliability of the FT results may be circumvented, while maintaining the main advantages of the automated approach, i.e., higher efficiency and objectivity.

In this work, we developed an automated longitudinal intra-subject analysis (ALISA) for investigating FT segmentations and compared its performance in terms of precision and accuracy to the “bronze standard”, i.e. the manual FT segmentations. In addition, we compared these results to FT segmentations obtained in an automated way over all time points and all subjects (Lebel et al., 2008). Sixty DTI data sets, which are part of the HUBU cohort database (“Hjernens Udvikling hos Børn og Unge”: Brain maturation in children and adolescents; see Madsen et al., 2010, 2011, for more details), were included in this study: five acquisitions at six-month intervals for ten healthy subjects and a set of ten repeats of one control subject scanned at weekly intervals. Important to note here is that these automated methods are not intended for case-based clinical use in cases with gross pathology, but rather for the use of longitudinal group studies of healthy development and aging, and pathologies without large displacing lesions.

Without loss of generality, the analyses were evaluated with tractography results from four WM fiber bundles: (i) the superior segment of the cingulum (SSCing) bundle, part of the collection of WM fibers that interconnect limbic structures, relevant for the reg-

ulation of emotional processes (e.g., Karaus et al., 2009); (ii) the cortico-spinal tracts (CST), running from the spinal cord to the motor cortex; (iii) the uncinate fasciculus (UF), connecting the frontal and temporal lobes, which has been shown to be important in the interaction between cognition and emotion (e.g., Price et al., 2008); and (iv) the forceps major (FM), or splenium of the corpus callosum, providing interhemispheric occipital connections that are affected in, for instance, schizophrenia (Clark et al., 2011; Catani et al., 2008).

4.2 Materials and methods

4.2.1 Subjects and data acquisition

Sixty DTI data sets were acquired for this study, five acquisitions at six-month intervals for ten healthy subjects (8F/2M) aged 7.6 to 8.6 years (mean age of 8.1 ± 0.4 years) at the first acquisition date and a set of ten repeats of one control subject (female, age 12.2 years) scanned on four occasions, with respectively two, three, two, and three separate scan sessions. These four occasions were separated by two, two, and seven weeks, respectively. The data sets are part of the HUBU cohort database (see Madsen et al., 2010, 2011, for more details) and have been acquired on a 3 T Siemens Magnetom Trio MR scanner (Siemens, Erlangen, Germany) with an 8-channel head coil (Invivo, FL, USA) using a twice-refocused balanced spin echo sequence that minimized eddy current distortions (Reese et al., 2003) (TR/TE = 8200/100 ms) with a b-value of 1200 s/mm^2 along 61 directions using the electrostatic repulsion method (Jones et al., 1999a; Jansons and Alexander, 2003) available in CAMINO (Cook et al., 2006), ten $b = 0 \text{ s/mm}^2$ images, and with a GRAPPA factor of 2. The acquisition matrix of 96×96 comprised a field-of-view of $220 \times 220 \text{ mm}^2$ (2.3 mm in-plane resolution) and 61 axial slices were acquired with thickness 2.3 mm and without gap (Jones and Leemans, 2011).

4.2.2 DTI pre-processing

The diffusion-weighted (DW) images were corrected for head motion and eddy current induced geometric distortions using a global affine registration procedure, as described in Leemans and Jones (2009). In this correction procedure, the DW data were transformed directly to the ICBM-DTI-81 template ($2 \times 2 \times 2 \text{ mm}^3$) in MNI space (Rohde et al., 2004; Mori et al., 2008) by applying cubic interpolation with only a single resampling step (i.e., concatenation of transformation matrices), thereby keeping artificial data smoothing to a minimum (Klein et al., 2010). We explicitly used a 'rigid' transformation model (only 3D rotations and translations) to ensure that no additional confounds, such as partial volume effect (PVE) related modulations of the estimated DTI measures (see Ch. 3), were introduced in this processing step. Note that for the analyses applied in this study, inter-subject alignment was not required. How-

ever, by transforming all data sets to a common reference space, uniformity in terms of brain angulation was maximized across subjects, which facilitated the definition of standardized protocols for extracting the WM fiber bundles of interest (as for instance also done by Caeyenberghs et al., 2010). Finally, the diffusion tensor was estimated with the RESTORE approach (Chang et al., 2005) and the FA, MD, and radial/axial (RD/AD) diffusivities were subsequently computed (Pierpaoli et al., 1996).

4.2.3 Fiber tractography

For each DTI data set, whole-brain deterministic fiber tracking (as described by Basser et al., 2000) was performed using *ExploreDTI* (Leemans et al., 2009) with the following parameters: an isotropic 2 mm seed point resolution was applied throughout the entire brain; the FA thresholds for seed point selection and termination of tracking were 0.2; the angle threshold was 30°; and the step size was set to 1.0 mm. Tract selection ROIs ('AND' gates) were defined according to specific protocols (Conturo et al., 1999; Wakana et al., 2004, 2007; Catani et al., 2008; Hasan et al., 2009) to extract the SSCing, CST, and UF bilaterally and the FM from the whole-brain tractography results. 'NOT' ROIs, which exclude tract pathways not-of-interest, were placed only on predefined locations, identical for each data set, to minimize 'subjective tract-editing'. The FT segmentations were all performed by a trained medical physicist (S.H.A.) for the UF and SSCing, and a neurobiologist (K.S.M.) for the FM and the CST. All raters were blinded to subject identification, time of scan, and brain hemisphere. Intra- and inter-rater reliability of this approach has been demonstrated in previous studies and is therefore considered beyond the scope of this work (e.g., Ciccarelli et al., 2003; Pfefferbaum and Sullivan, 2003; Malykhin et al., 2008; Danielian et al., 2010). For each reconstructed fiber bundle, average FA, MD, AD, RD, and tract volume were computed. The following sections provide a detailed description of the protocols that were applied to extract the four fiber bundles.

Cortico-spinal tracts

To isolate the CST (see Fig. 4.1a,b), two axial 'AND' gates were placed selecting the pons and the motor cortex (M1) as described by Wakana et al. (2007). The first 'AND' gate was drawn on the slice of the pons where the decussation of the cerebellar peduncles is most visible (i.e., the "red spot", Fig. 4.1a); the latter was drawn on the most inferior axial slice where the central sulcus clearly separates S1 and M1 (Fig. 4.1b). On the midsagittal slice, a 'NOT' gate was placed to exclude false-positive pathways, such as spurious interhemispheric tracts. Another 'NOT' ROI was placed between the pons and the cerebellum to exclude the cerebellar tracts.

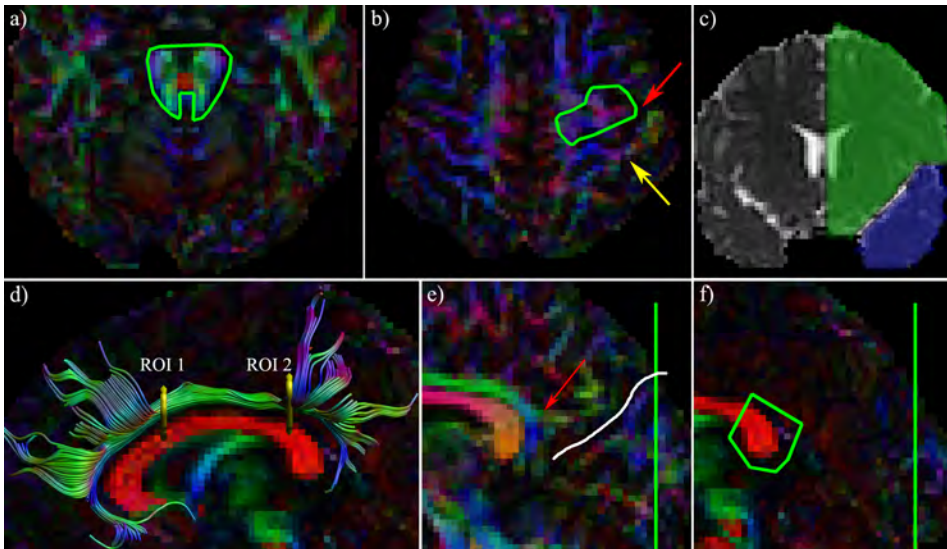


Figure 4.1: Delineation of ROIs for the segmentation of fiber tracts. For the cortico-spinal tracts, two ‘AND’ ROIs were defined: one on the axial slice showing the decussation of the superior cerebellar peduncles (the “red dot”, in A); and one on the most inferior axial slice where M1 (green ROI) and S1 (yellow arrow) are clearly separated by the central sulcus (indicated by the red arrow). ‘NOT’ gates were placed at the midsagittal slice and anterior to the cerebellum (B). For the segmentation of the uncinate fasciculus (C), two ‘AND’ ROIs were placed on the most posterior coronal slice where the Sylvian fissure (indicated in yellow in A) still clearly separates the frontal lobe (green ROI) from the temporal lobe (blue ROI). For the delineation of the superior segment of the cingulum bundle two ‘AND’ ROIs were defined (D): one on the most posterior coronal slice in which the genu of the corpus callosum could be seen in full profile; the second ‘AND’ ROI was defined by the most anterior coronal slice in which the splenium of the corpus callosum could be seen in full profile. For the forceps major, one on the sagittal slice that most clearly shows the perisplenial cingulum (red arrow in E), the parieto-occipital sulcus is detected (white line in E) and ‘AND’ ROIs are drawn on a coronal slice around the occipital lobes at the posterior edge of this sulcus (green line). On the midsagittal slice another ROI is drawn around the splenium of the corpus callosum (F).

Uncinate fasciculus

To select the UF, two ‘AND’ gates were placed on the most posterior coronal slice where the Sylvian fissure still clearly separates the frontal lobe from the temporal lobe as in Wakana et al. (2007) and Hasan et al. (2009). This slice was selected on the MD map, where the cerebrospinal fluid (CSF) provides a clear demarcation for separating these two brain regions. As shown in Fig. 4.1c, one ROI (blue) was placed around the tempo-

ral lobe, and another ROI (green) was placed around the frontal lobe. A 'NOT' ROI was placed on the midsagittal slice to exclude false-positive pathways, such as spurious interhemispheric tracts.

Superior segment of the cingulum

A consistent reconstruction of the entire cingulum bundle with DTI-based FT is known to be extremely difficult as the regions in which this tract terminates can differ substantially across multiple subjects due to error accumulation during tract propagation. To minimize the contribution of non-specific pathways only the superior segment of the cingulum (SSCing) was selected (Emsell et al., 2009). The SSCing was defined by two 'AND' gates: one on the most posterior coronal slice that would still show the genu of the corpus callosum, and one on the most anterior coronal slice in which the splenium of the corpus callosum was seen in full profile (see Fig. 4.1d).

Forceps Major

The FM was segmented by placing two 'AND' gates around the occipital lobe, i.e., one around each hemisphere to specifically capture the interhemispheric occipital connections. More specifically, for each hemisphere the sagittal slice showing the perisplenial part of the cingulum was found, and the parieto-occipital sulcus was defined on this slice (Fig. 4.1e). The 'AND' gate was then drawn on the most posterior edge of the sulcus on the corresponding coronal slice, around only the occipital lobe (Wakana et al., 2004). Additionally, one 'AND' gate around the splenium of the corpus callosum on the midsagittal slice (Fig. 4.1f).

4.2.4 Automated longitudinal intra-subject analysis (ALISA)

The ALISA approach proposed in this work computes for each subject the FT results of the data sets, acquired at multiple time points, by defining a single ROI configuration on a subject-specific DTI template. The ROI configuration is subsequently applied to each of the individual data sets to obtain the FT results for that subject at each time point. The subject-specific DTI template is created for each subject separately by averaging the multiple diffusion tensor data sets as described previously (Jones et al., 2002) using elastix (Klein et al., 2010). A flow chart illustrating the difference between the manual and ALISA approaches is shown in Fig. 4.2. In this step of the ALISA approach, the effects of brain growth (both global and/or local) and geometric variations due to acquisition imperfections are assumed to be negligible compared to the precision with which the ROI configurations for tract segmentation can be defined, which is typically in the order of magnitude of a few voxels. To verify that the assumption of spatial correspondence of the reconstructed tracts (or segments thereof) between the different time points holds, non-linear deformation fields have been computed between the

DTI data at time points one and five for each of the ten subjects (Van Hecke et al., 2007). With these deformation fields, inter-scan geometric differences and brain growth can be quantified for each voxel. The FA skeletonization procedure of TBSS (Smith et al., 2006) with an FA threshold of 0.2 is used on a representative subject's template to assess the magnitude of these deformation fields overlaid on the main WM fiber pathways.

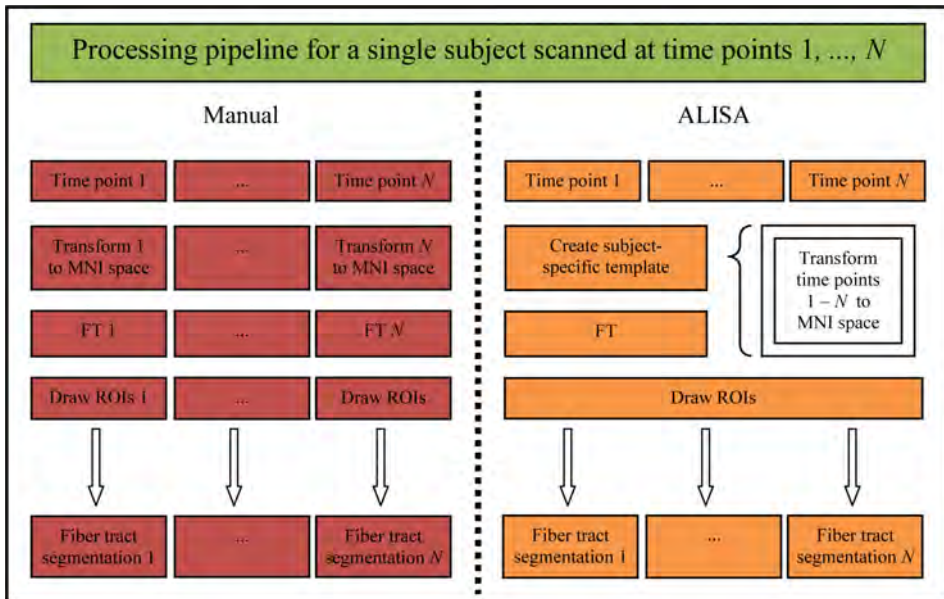


Figure 4.2: Flow chart providing a schematic overview of the automated longitudinal intra-subject analysis (ALISA) and manual fiber bundle segmentation approaches.

Performance of ALISA in terms of accuracy and precision is compared to (i) the manual FT segmentations, where ROIs were drawn manually for each bundle at every time point for all subjects; and (ii) an automated inter-subject analysis, where FT segmentations were obtained over all time points and all subjects as described by Lebel et al. (2008). For this approach—in the following referred to as “fully automated”—the DTI atlas was constructed from the ten repeats of the single subject (Jones et al., 2002) and ROI configurations were defined on this atlas for each WM fiber bundle and subsequently applied to the data of all time points of all subjects (Lebel et al., 2008). For each tractography result from ALISA, the fully automated method, and the bronze standard (i.e., the manual FT segmentations), the FA, MD, RD, AD, and volume were estimated as in Jones et al. (2005b).

4.2.5 Statistical inference

With the ten repeated DTI scans of a single subject, the precision of the aforementioned measures can be compared between the manual, ALISA, and fully automated methods. More specifically, using Levene's test (assessing equality of variances) we can determine whether ALISA or the fully automated method would introduce an additional amount of variability to the FT segmentations. In addition, the paired Kruskal-Wallis test was applied to assess any change in accuracy (a non-parametric test is preferred to avoid sensitivity to non-normal data distributions, Kitchen, 2009). In other words, this paired test will allow us to investigate the existence of any systematic deviation of the estimated measures between the three methods. For the longitudinal data sets (ten subjects scanned at five time points), a two-way repeated measures ANOVA was applied to investigate potential differences in accuracy between the manual, ALISA, and fully automated approaches if data were normally distributed (as determined with the Lilliefors test with $p = 0.05$ deemed significant) and with the nonparametric Friedman test otherwise. These are pair-wise statistical tests between different segmentation methods, providing a very high sensitivity. To assess whether both approaches have a difference in precision based on these longitudinal data sets, the estimated FA, MD, AD, RD, and tract volume values were first adjusted to account for inter-subject differences. More specifically, for each subject and for each reconstructed fiber bundle the average value across the five time points was subtracted from each of the individual time point estimates for all approaches before performing Levene's test. Differences were deemed significant at $p = 4.76e - 4$ (Bonferroni corrected for multiple hypothesis testing). Lastly, we compared the intra-subject variation in segmented tract volumes between the manual, ALISA, and fully automated methods. More specifically, for each subject and the four fiber bundles, the standard deviation of the fiber bundle volume across the five time points was computed and compared between these methods using Friedman's test.

4.3 Results

4.3.1 Subject-specific template construction

The reliability of automating fiber tractography segmentation for serial DTI data depends heavily on the coregistration quality and, consequently, the construction of the subject-specific template that was used in the ALISA approach. Indicating the quality of the applied normalization procedure (Jones et al., 2002), Fig. 4.3 shows the resulting template derived from the five serial DTI scans of a representative subject. Overlaid on the FA skeleton of this template, the dominant diffusion direction (first eigenvector) is shown for each individual DTI data set in Fig. 4.4. The tight coherence of these prin-

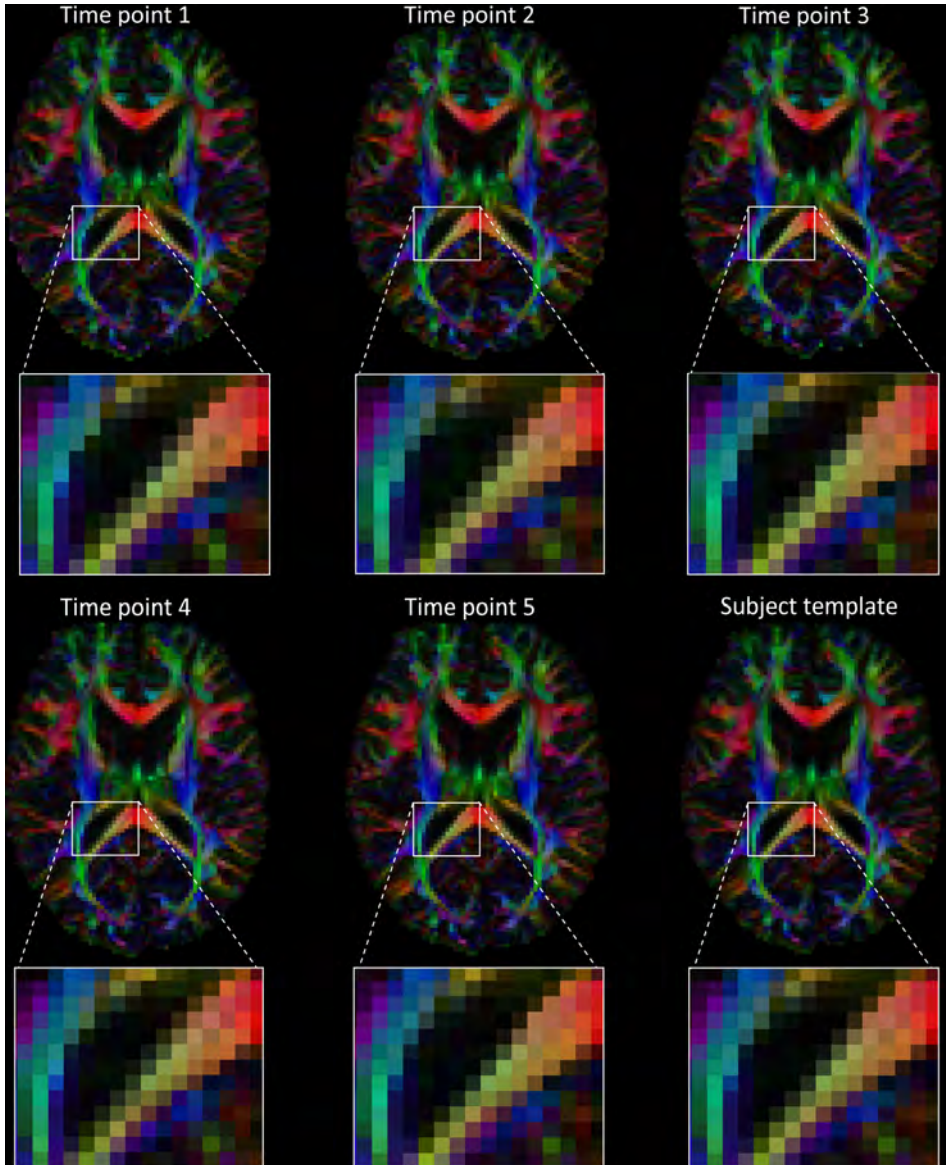


Figure 4.3: DEC maps of a representative subject: each slice represents a different time point (5 scans with 6-month year intervals); the right bottom image represents the subject-specific template (derived from the five data sets). These axial slices indicate the same location in the brain; the enlarged regions demonstrate the high level of spatial alignment across the different time points.

incipal diffusion orientations demonstrates the high level of accuracy that was obtained for our coregistration results.

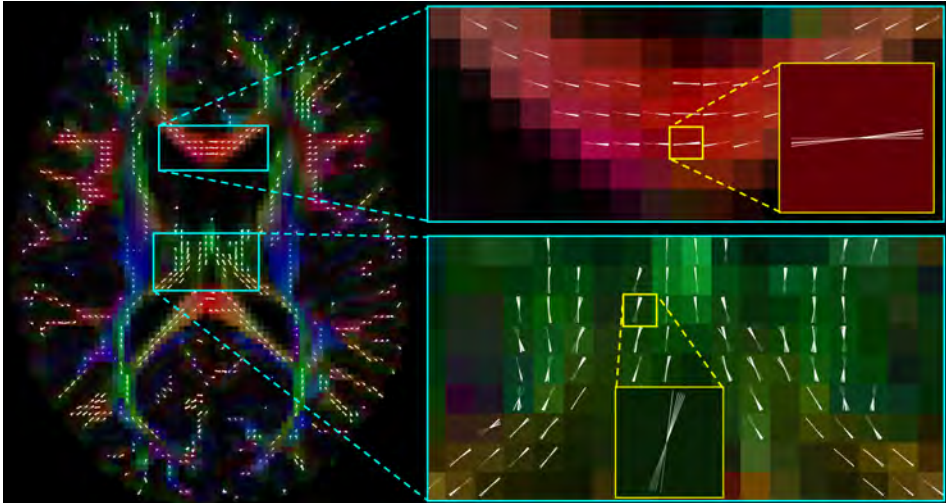


Figure 4.4: DEC map of a subject-specific template (derived from the same representative subject shown in Fig. 4.3) with the principal diffusion orientations (white lines) of each time point overlaid on the corresponding FA skeleton of this template. The enlarged regions-of-interest clearly demonstrate the tight coherence in diffusion orientation across the different time points.

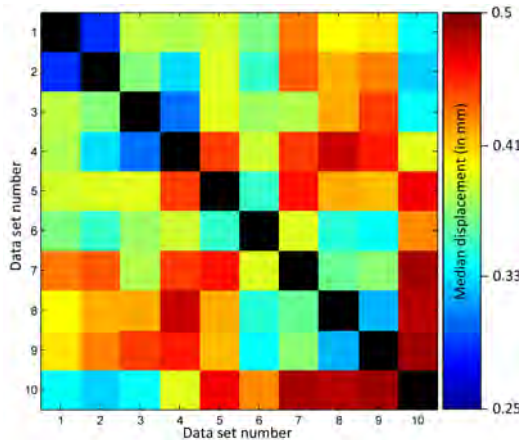


Figure 4.5: Median values of the displacement fields between each pair of the ten repeated DTI data acquisitions of the control subject. The black diagonal elements are zero by definition.

The magnitude of the non-rigid geometric deformation between time points one and five is shown in Fig. 4.6a for a representative subject (female, 7.6 year at first scan) with

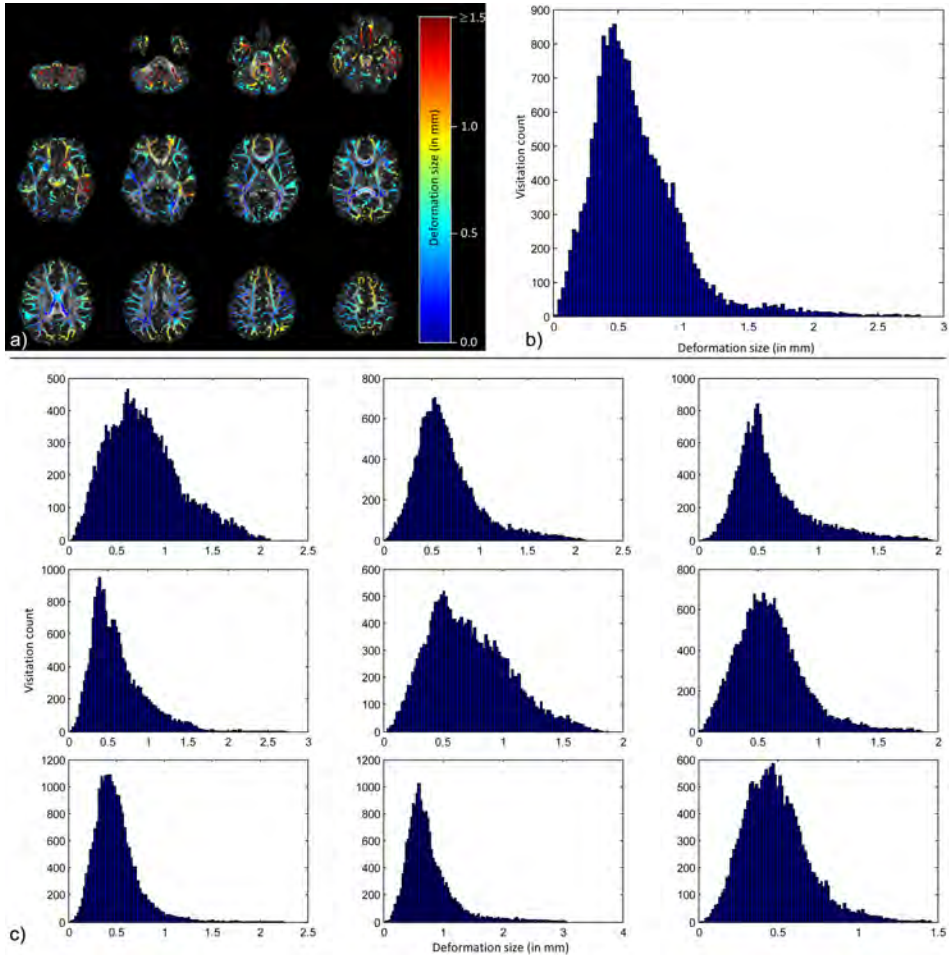


Figure 4.6: Magnitude of the voxel-wise displacement field between time points one and five for a representative subject overlaid on the FA skeleton associated with time point five (A). The corresponding distribution of the deformation values shown in (A) is displayed in (B). Histograms of the deformation fields between time points one and five for the other subjects are shown in (C). Note that y-axis scales differ to allow comparison of individual distribution.

Fig. 4.6b showing the corresponding histogram of these deformation values. Fig. 4.6c presents the same histograms of deformation values for the other nine subjects. Notice that virtually all deformations related to brain growth and/or differences in acquisition geometry are smaller than the voxel size. The same procedure was also applied to the ten repeated acquisitions of the single subject to investigate the magnitude of the deformations related to imperfections of the data acquisition in the absence of brain growth. More specifically, each of the ten repeated data sets is registered to every other data set with the corresponding warp fields summarized by their median displacement (see Fig. 4.5). The average inter-scan deformation magnitude (mean 0.40 ± 0.05 mm) is significantly smaller (independent two-sample t-test; $p < 10^{-10}$) than the deformations between time points one and five of the ten subjects (mean 0.58 ± 0.09 mm).

4.3.2 Ten repeated DTI acquisitions of one control subject

The FA, MD, RD, AD, and volume measures for each of these reconstructed fiber tracts (averaged across the ten repeated scans) are summarized in Table 4.1. Levene's test and the Kruskal-Wallis test were applied to investigate for each fiber bundle the difference in precision and accuracy of the estimated measures, respectively. As shown in Table 4.1, no significant differences were observed in either volume or diffusion measures.

4.3.3 Longitudinal data sets

Figs. 4.7-4.10 show the reconstructed pathways of the CST, UF, SSCing, and FM, respectively, of a representative subject at each of the five time points and for the three approaches. Notice that the fiber tracking results obtained with ALISA are almost identical to the manually segmented fiber bundles, but that the fully automated approach shows larger variations, mostly in the SSCing, UF, and FM. Table 4.2 summarizes the mean and standard deviation of the diffusion metrics (FA, MD, RD, AD) and volume measures of the four fiber bundles across the ten subjects that were scanned five times at roughly six-month intervals (i.e., total number of DTI data sets is 50). The only significant difference in variance was for the FM volume, which was different when segmented with the fully automated method compared to ALISA and the manual FT segmentations. In addition, significant differences across the three approaches were observed in mean values for the volume and several diffusion indices of the bilateral CST. The most striking difference is the reduced number of tracts in the left CST for the fully automated method (white arrow in Fig. 4.8). More subtle differences between the three segmentation approaches can be observed in the extent with which the tracts terminate in superior and/or inferior regions.

The intra-subject standard deviation of the fiber bundle volume across the five time points is significantly different between the three methods ($p = 2e - 6$), when all fiber bundles are pooled together. Table 4.3 shows the results of such comparisons for each

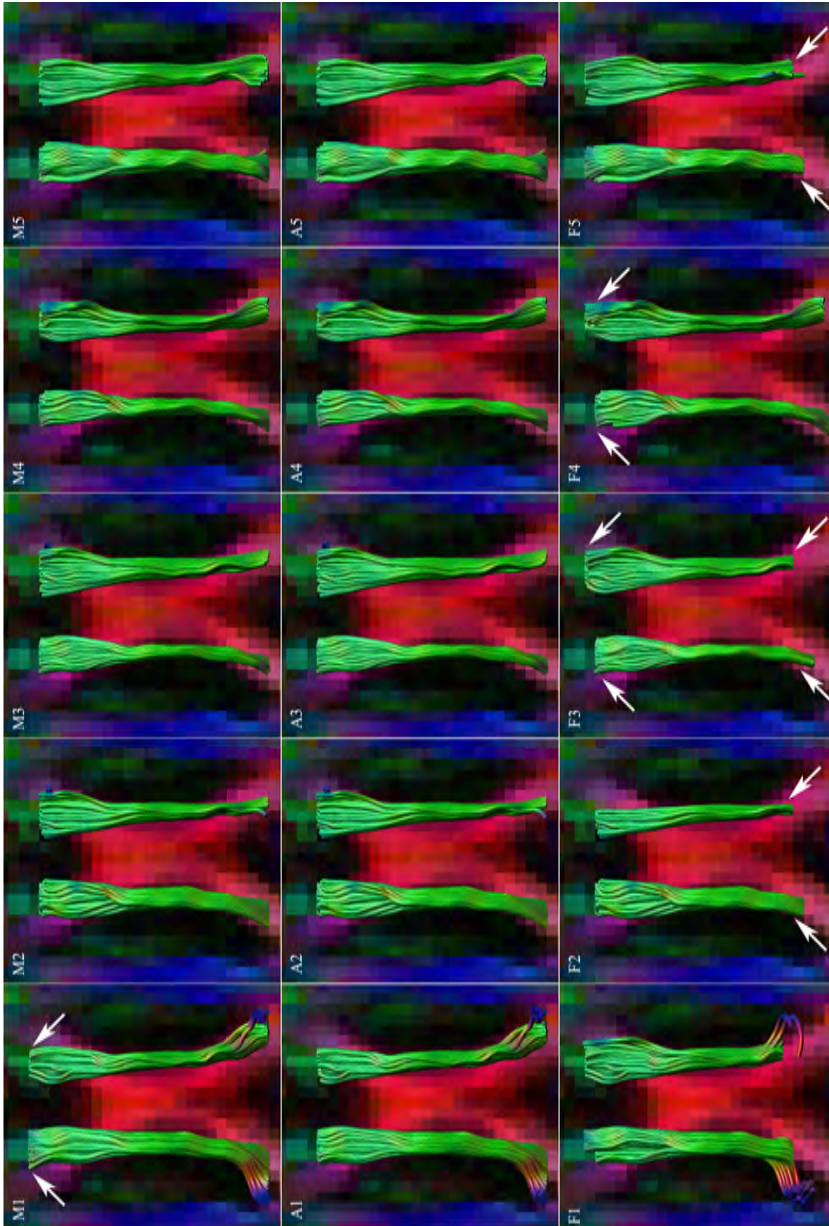


Figure 4.7: Segmentations of the cingulum segments for a representative subject (5 time points with six-month intervals), using the manual FT segmentation (M1-M5), ALISA (A1-A5), and the fully automated method (F1-F5). Notice the difference in length of the extracted cingulum segments between M1 and M2-M5, and more severely between the different fully automated segmentations (white arrows).

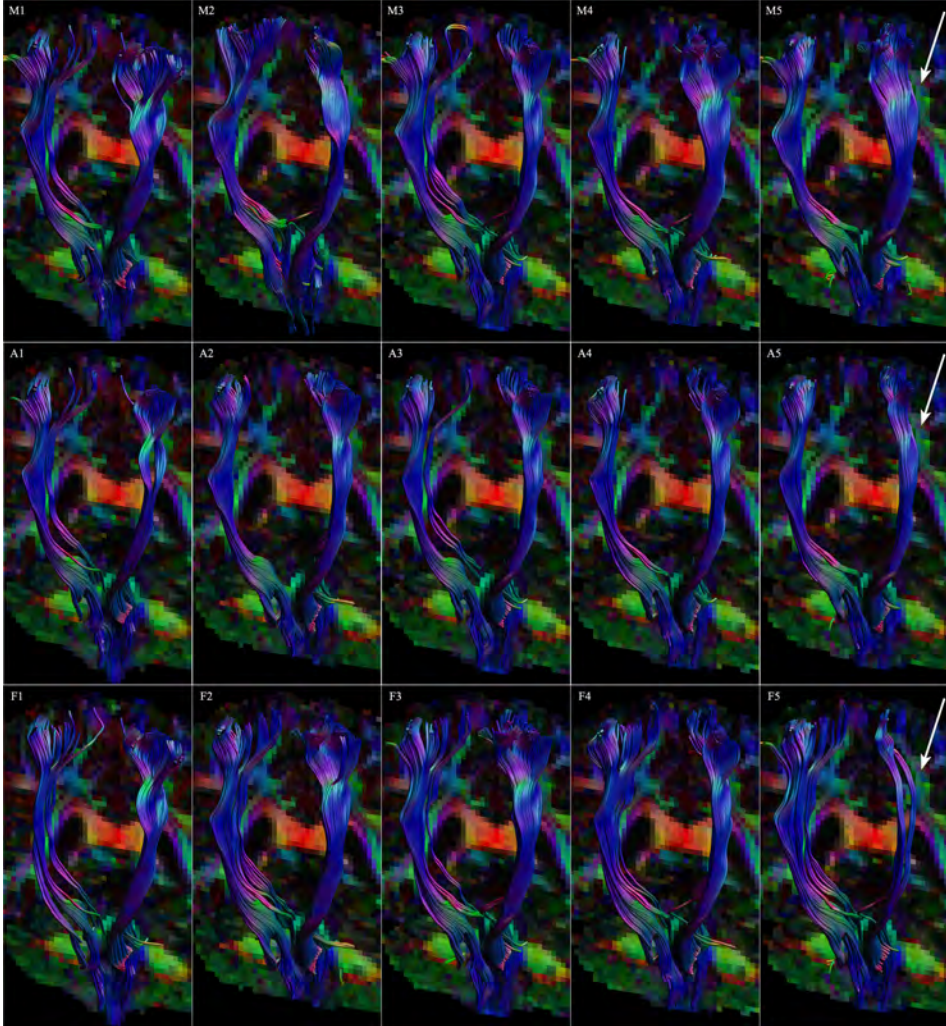


Figure 4.8: Segmentations of the bilateral cortico-spinal tracts for a representative subject (5 time points with six-month intervals), using the manual FT segmentation (M1-M5), ALISA (A1-A5), and the fully automated method (F1-F5). The white arrows indicate the reduced number of tracts in the fully automated segmentations compared to the manual and ALISA methods.

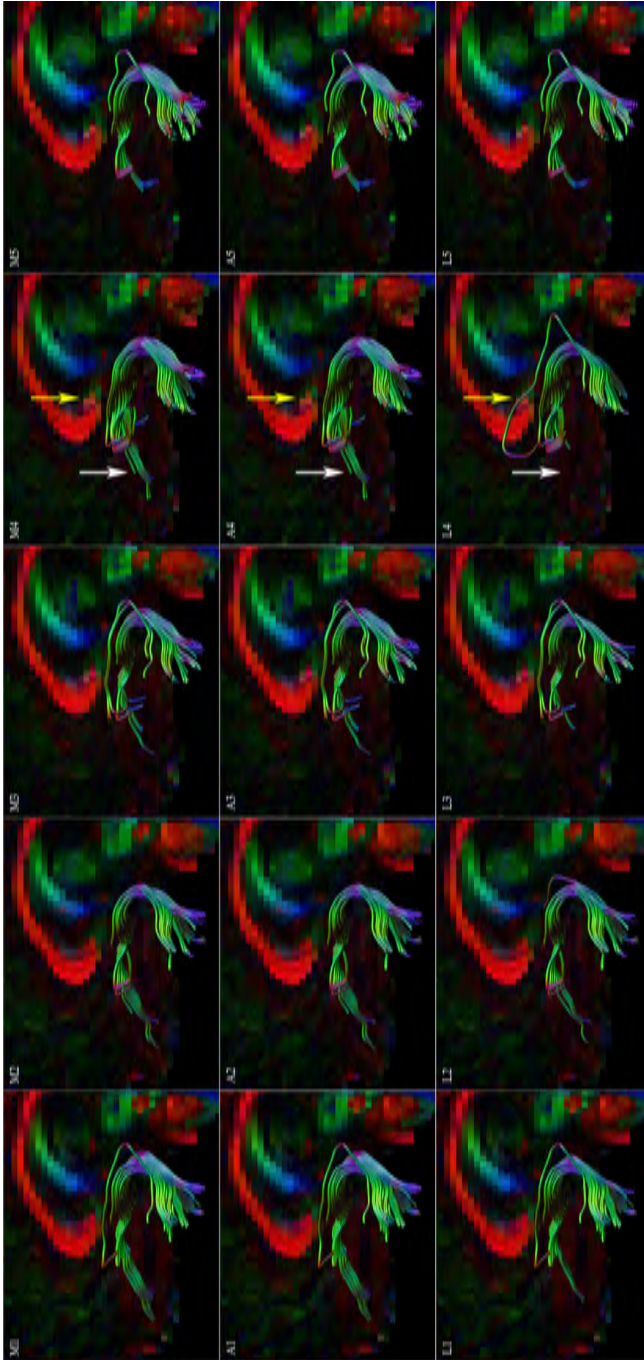


Figure 4.9: Segmentations of the uncinate fasciculus (left hemisphere) for a representative subject (5 time points with six-month intervals), using the manual FT segmentation (M1-M5), ALISA (A1-A5), and the fully automated method (F1-F5). Notice the larger variability between time points in the frontal projections in the fully automated segmentation, most notably in F4, that is not present for manual or ALISA segmentations (white arrows). The yellow arrows indicate an erroneous tract in F4 that is not present in M4 or A4.

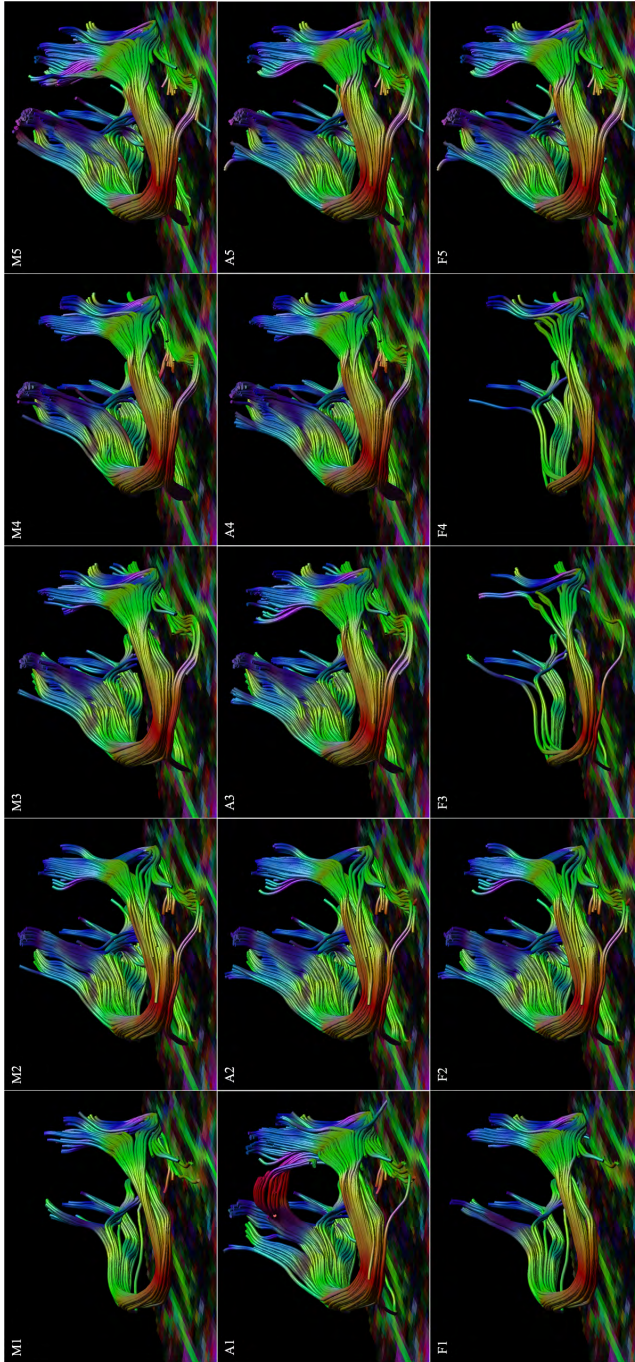


Figure 4.10: Segmentations of forceps major for a representative subject (5 time points with six-month intervals), using the manual FT segmentation (M1-M5), ALISA (A1-A5), and the fully automated method (F1-F5). For the fully automated method, there is a large variability in the segmented tracts between the different time points, most notably when comparing F2 and F5 to F3 and F4. The manual and ALISA methods show more consistent and stable tract segmentations.

Table 4.1: Comparison of DTI metrics and tract volumes of the four fiber bundles across ten repeated DTI acquisitions of a single subject between the manual FT segmentation, ALISA, and the fully automated (shortened to “full” in the table) method. Values shown are averaged over the ten repeats.

		Fractional anisotropy	Mean diffusivity (10^{-3} mm ² /s)	Axial	Radial	Volume (cm ³)
SSCing (left)	Manual	0.55	0.73	1.24	0.47	1.50
	ALISA	0.55	0.73	1.24	0.47	1.49
	Full	0.55	0.73	1.24	0.47	1.52
SSCing (right)	Manual	0.52	0.75	1.24	0.51	1.38
	ALISA	0.52	0.75	1.24	0.51	1.35
	Full	0.52	0.75	1.24	0.51	1.35
CST (left)	Manual	0.58	0.71	1.25	0.44	9.33
	ALISA	0.59	0.71	1.26	0.43	8.70
	Full	0.59	0.71	1.26	0.43	8.70
CST (right)	Manual	0.54	0.73	1.23	0.48	13.05
	ALISA	0.54	0.73	1.23	0.48	11.83
	Full	0.54	0.73	1.23	0.48	11.83
UF (left)	Manual	0.40	0.80	1.18	0.62	6.65
	ALISA	0.40	0.80	1.18	0.62	6.67
	Full	0.40	0.80	1.18	0.62	6.68
UF (right)	Manual	0.41	0.81	1.21	0.62	7.97
	ALISA	0.41	0.81	1.21	0.62	8.01
	Full	0.41	0.81	1.21	0.62	8.26
Forceps major	Manual	0.61	0.81	1.48	0.48	8.63
	ALISA	0.60	0.82	1.48	0.49	7.07
	Full	0.60	0.82	1.48	0.49	7.07

SSCing = superior segment of the cingulum; CST = cortico-spinal tracts; UF = uncinata fasciculus; FM = forceps major; ALISA = automated longitudinal intra-subject analysis. Differences in variance between the three methods were analyzed using Levene’s test; differences in mean values with the Kruskal-Wallis test; both at $p = 4.76e^{-4}$ (Bonferroni corrected). If this group comparison yielded a significant effect, post-hoc analyses were performed, and the methods that are significantly different from the other(s) in these post-hoc tests are indicated by * (Levene’s) and † (Kruskal-Wallis).

Table 4.2: Comparison of average DTI metrics and tract volumes of the four fiber bundles across ten different subjects scanned at 5 time points (half year intervals) between the manual FT segmentation, ALISA, and the fully automated (shortened to “full” in the table) method.

		Fractional anisotropy	Mean diffusivity (10^{-3} mm ² /s)	Axial	Radial	Volume (cm ³)
SSCing (left)	Manual	0.52	0.75	1.23	0.51	1.52
	ALISA	0.52	0.75	1.23	0.51	1.53
	Full	0.52	0.75	1.23	0.51	1.62
SSCing (right)	Manual	0.46	0.79	1.22	0.57	1.29
	ALISA	0.46	0.79	1.22	0.57	1.32
	Full	0.46	0.79	1.22	0.57	1.49 [†]
CST (left)	Manual	0.54	0.73	1.22	0.48	8.08 [†]
	ALISA	0.54	0.73	1.23	0.48	7.10 [†]
	Full	0.54	0.73	1.22	0.48	7.64 [†]
CST (right)	Manual	0.53 [†]	0.74	1.24	0.50 [†]	7.71 [†]
	ALISA	0.53 [†]	0.74	1.24	0.49 [†]	7.30 [†]
	Full	0.52 [†]	0.75 [†]	1.25	0.50 [†]	8.66 [†]
UF (left)	Manual	0.39	0.84	1.23	0.65	4.73 [†]
	ALISA	0.39	0.84	1.23	0.65	4.83 [†]
	Full	0.39 [†]	0.85	1.23	0.65	4.83 [†]
UF (right)	Manual	0.39	0.83	1.21	0.64	5.37
	ALISA	0.39	0.83	1.21	0.64	5.27
	Full	0.39	0.83	1.21	0.65	5.08 ^{*†}
Forceps major	Manual	0.60	0.82	1.47	0.49	9.97
	ALISA	0.60	0.81	1.47	0.48	10.33
	Full	0.59	0.83	1.48	0.51	5.61 ^{*†}

SSCing = superior segment of the cingulum; CST = cortico-spinal tracts; UF = uncinata fasciculus; FM = forceps major; ALISA = automated longitudinal intra-subject analysis. Differences in variance between the three methods were analyzed using Levene’s test; differences in mean values with repeated-measures ANOVA—or the non-parametric Friedman test (in case non-normality of the data or unequal variances were observed as determined with the Lilliefors or Levene’s test, respectively)—both at $p = 4.76e^{-4}$ (Bonferroni corrected). If this group comparison yielded a significant effect, post-hoc analyses were performed, and the methods that are significantly different from the other(s) in these post-hoc tests are indicated by * (Levene’s) and [†] (ANOVA / Friedman).

fiber bundle separately. ALISA provides the lowest standard deviations, indicating the highest intra-subject consistency in fiber bundle volumes.

Table 4.3: Comparison of the intra-subject standard deviation of the tract volume across the five time points between the manual FT segmentation, ALISA, and the fully automated (shortened to “full” in the table) method (the presented values are the average over all ten subjects, in cm^3)

	SSCing (left)	SSCing (right)	CST (left)	CST (right)	UF (left)	UF (right)	FM
Manual	0.16	0.17	1.08	1.14	0.62	0.71	2.57
ALISA	0.16	0.16	0.93	1.03	0.60	0.65	1.01
Full	0.29	0.23	1.49	1.61	1.00	1.01	1.36
Friedman's test (p)	<i>0.067</i>	<i>0.061</i>	<i>0.301</i>	<i>0.273</i>	<i>0.045</i>	0.007	<i>0.014</i>

SSCing = superior segment of the cingulum; CST = cortico-spinal tracts; UF = uncinata fasciculus; FM = forceps major; ALISA = automated longitudinal intra-subject analysis. The p -values shown in bold are significant at $p = 0.007$ (Bonferroni corrected). If Friedman's test between all methods yielded a significant result, post-hoc analyses were performed. Methods that are significantly different from the others in these post-hoc tests have the values shown in bold.

4.4 Discussion

With the advent of large-cohort DTI studies, there is an increased demand for data analyses that require minimal user input. While several methods have been developed to analyze WM fiber bundles in an automated way (Leemans et al., 2006; Clayden et al., 2007; Lebel et al., 2008; O'Donnell et al., 2009; Hagler et al., 2009; Verhoeven et al., 2010; Zhang et al., 2010; Reich et al., 2010; Yendiki et al., 2011; Suarez et al., 2012), there is typically a trade-off that needs to be made between prior knowledge incorporated by the user for the manual approach (e.g., the neuroanatomical expertise regarding the location and extent of tracts-of-interests) and the predefined parameter settings required by the automated technique. In other words, the labor-intensive and subjective—yet valuable—human input is exchanged for higher objectivity and efficiency, but potentially lower accuracy, of the automated analysis tool.

In this paper, we have proposed a new analysis pipeline, dubbed ALISA, that aims to combine the best of both worlds: increasing the efficiency by automating the subject-specific data analysis, while retaining the prior knowledge from the neuroanatomical expert on a subject-by-subject basis. In addition, we have evaluated the performance of the ALISA approach by comparing its reliability in terms of accuracy and precision with the current “bronze standard”, i.e., with the corresponding manual FT segmentations. Furthermore, we have investigated whether an existing fully-automated inter-

subject segmentation approach (Lebel et al., 2008) would give the same accuracy and precision as ALISA and/or the manual FT segmentations. To this end, FT segmentations and several diffusion measures from four different fiber bundles (SSCing, CST, UF, and FM) were compared between all three methods using (i) ten repeated data sets of a single subject, where no detectable brain changes were assumed and (ii) five serial acquisitions (half a year apart) for ten different subjects, which are all part of the HUBU cohort database (“Hjernens Udvikling hos Børn og Unge”: Brain maturation in children and adolescents; Madsen et al., 2010, 2011). ALISA will be made available via the *ExploreDTI* diffusion MRI software tool (www.exploredti.com).

The ALISA method had the smallest intra-subject variability in the organization of the fiber bundles compared to the fully automated method and the manual FT segmentation (Figs. 4.7-4.10 and Table 4.3), especially in the SSCing, UF, and FM. For the SSCing, for instance, where the aim was to extract only the segment between the ROIs, there is a strong variability in the length of this segment when extracted with the fully automated method (Fig. 4.7). This is also supported by a significant difference in variance of the segmented tract volume between the fully automated method on the one hand and the ALISA and manual segmentation on the other hand. Similarly, the tract volumes of the FM are also significantly different when segmented with the fully automated method (Table 4.2). In addition, the variability between the segmented FM tracts from the five time points of one subject is much larger for the fully automated method (Fig. 4.10). Most notably, the fully automated method was unable to segment the FM on one time point from one subject. Furthermore, the UF segmented with the fully automated method is prone to missing the frontal projections (Fig. 4.9) or the temporal projections (data not shown). Based on these results of the longitudinal datasets, one can already state that the fully automated method does not give the same high level of reliability as the manual FT segmentations. By contrast, the ALISA method shows results that are more consistent with the manual segmentations, indicating that the same regions have been investigated.

Despite the absence of any significant differences between the ALISA and manual results for the ten repeated data sets, there is a tendency towards higher variability with the manual approach, which can be appreciated from its slightly higher overall standard deviation in tract volume estimates (Table 4.1). This trend in higher variability for manual segmentations can be attributed to the different ROI positions that were used to extract the tracts-of-interest for each data set separately (data not shown), which can also be appreciated in the tract segmentations in the longitudinal dataset (Fig. 4.7). These differences in position, which by design are not present in the ALISA framework, are probably caused by the intrinsic intra-rater variability triggered by subtle differences in partial volume effects and noise distributions across the ten data sets.

Also for the five serial acquisitions from ten subjects, no significant differences in accuracy/precision of the diffusion measures between both approaches could be detected, suggesting that ALISA does not affect the precision and accuracy in an adverse way. One could argue that the higher SNR in the subject-specific templates could increase the consistency of the ROI delineations across subjects, making the ALISA approach more robust and efficient than manual delineations, especially for large-cohort studies. This consideration is supported by Table 4.3 demonstrating that ALISA has lower intra-subject variation in segmented tract volumes than the manual segmentations.

There is no significant difference in precision of the diffusivity and volume measures between manual FT segmentation and ALISA, as determined using Levene's test (Tables 4.1 and 4.2). Table 4.1 further shows minute differences in the average diffusion values between the manual and ALISA approaches. Taken together, these results indicate that the absolute values of these measures will be slightly different when using either the manual or ALISA segmentations, but the statistical power to detect any trends or changes would remain the same, or potentially higher with ALISA due to higher intra-subject consistency in tract segmentation (Table 4.3).

The ALISA approach assumes that the position of the ROI—defined on the subject-specific template—can be transformed to the same anatomical locations across different time points. This assumption holds if brain growth can be considered to be in the order of magnitude of the precision with which one can draw the ROI, so in the order of the voxel size. Although brain growth could indeed be verified by the larger median displacements of the deformation warp fields observed in the serial data sets (see Section 4.3.1), the vast majority of voxels did not exceed 2 mm (Fig. 4.6). Also qualitatively, the validity of the assumption could already be appreciated from the high spatial agreement between the five normalized DTI data sets for the representative subject shown in Figs. 4.3 and 4.4 (Jones et al., 2002). In general, brain size is relatively stable between 6-7 and 70 years of age (e.g., Dekaban, 1978; Jernigan et al., 2011). We therefore believe that the ALISA approach is suitable for a large range of ages and time spans between first and last scan point.

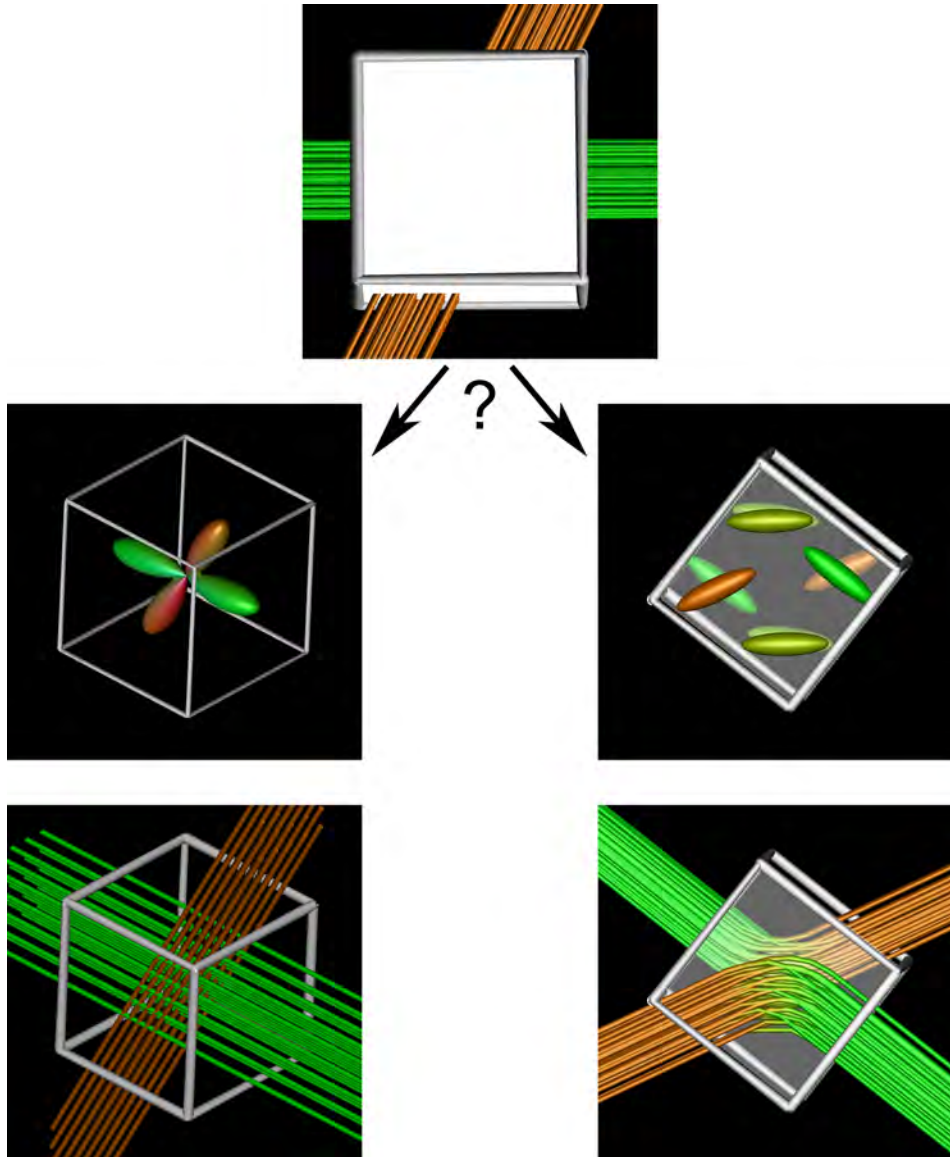
We evaluated the ALISA framework for four specific WM fiber bundles, and with DTI data sets acquired from healthy young subjects. By including association (SSCing and UF), projection (CST), and commissural (FM) fibers, we cover a wide variety of fiber structures with different size and location. In general, ALISA can also be applied to other WM structures and age ranges as long as the geometric differences across the time points are not too large (i.e., smaller than roughly five mm).

Nevertheless, in severe pathological conditions (Nimsky et al., 2005, 2006), correspondence between anatomically identical locations may not be warranted, which could

be problematic for the ALISA approach. Similar complications may arise in neonatology related research (van der Aa et al., 2011), where there can be tremendous changes in brain size and WM organization between follow-up scans may not be captured by the ALISA framework. Possible improvements might include a nonlinear registration from the template to the individual time points of each subject, but the stability and reproducibility of the nonlinear registration should be carefully monitored to determine whether this yields a benefit because of accurate anatomical correspondence or merely causes additional variability due to imperfect registration.

Finally, although ALISA has been evaluated with FT segmentations that were based on conventional DTI-based tractography—which nowadays may not be considered as the “optimal” model to perform tract reconstructions (e.g., Jones et al., 2013; Jeurissen et al., 2012)—our proposed framework will also be valid for tractography methods based on other approaches, such as, for instance, diffusion spectrum imaging, Q-ball imaging, and spherical deconvolution methods (Wedeen et al., 2008; Descoteaux et al., 2009; Jeurissen et al., 2011).

In summary, we have proposed and evaluated an automated longitudinal intra-subject analysis, coined ALISA, which is specifically designed to analyze tractography-based segmentations for longitudinally acquired DTI data sets. In contrast to across-subject automation, ALISA has comparable to even higher levels of accuracy and precision compared to manual segmentations. Being less time-consuming and more objective, ALISA will be beneficial for longitudinal studies, especially if data sets have been acquired at many time points.



To resolve multiple fiber populations within a voxel (top), a high angular resolution is beneficial if these populations are crossing (left), where a high spatial resolution is beneficial if they are kissing (right).

Chapter 5

HARDI and fiber tractography at 1 mm isotropic resolution

This chapter is based on:

S.B. Vos, M. Aksoy, Z. Han, S.J. Holdsworth, J.R. Maclaren, C.M.W. Tax, M.A. Viergever, A. Leemans, R. Bammer, “HARDI and fiber tractography at 1 mm isotropic resolution”. (in preparation)

Abstract

Multi-fiber diffusion MRI methods can estimate the orientations of multiple fiber populations within a voxel, improving the accuracy of fiber tractography over diffusion tensor-based tractography. These methods, however, cannot easily discern crossing fibers from kissing, branching, splaying, or bending fibers within a voxel. Higher spatial resolutions would aid in determining the exact locations and configuration of the populations. Ideally, we want a high angular resolution, required for the multi-fiber methods, as well as a high spatial resolution. The long scan times that this ideal scenario requires are often not feasible, and data acquisition becomes a trade-off between angular and spatial resolution. By investigating this trade-off, one could determine which of these two factors, if any, provides the largest gain. To do so, we combined advanced 3D DW EPI acquisitions with high-angular resolution diffusion imaging to create a unique DWI dataset with 1.0 mm true isotropic resolution and 100 diffusion-weighted directions. This dataset was reconstructed to create subsets of lower angular resolution and lower spatial resolution to compare the influence of both of these factors on fiber tractography. Tractography results from three fiber bundles are compared across these different spatial and angular resolutions, and evaluated both in a qualitative, visual, manner as well as quantitatively. Results show that the segmented fiber bundles are mostly invariant under changes in spatial resolution, but vary greatly with changes in angular resolution. This indicates that, when a trade-off should be made between angular and spatial resolution, it is most effective to invest in angular resolution.

5.1 Introduction

In recent years, diffusion MRI has attracted attention for its potential to quantify aspects of tissue microstructure that were previously unable to measure (e.g., Basser et al., 1994; Assaf et al., 2004; Alexander et al., 2010). Additionally, diffusion MRI data can be used for fiber tractography (FT): the virtual reconstruction of fiber tract pathways in the brain (e.g., Mori et al., 1999; Basser et al., 2000; Behrens et al., 2007; Jones, 2008a). Diffusion tensor imaging (DTI, Basser et al., 1994) describes the measured diffusion signal as a second-rank tensor, assuming a Gaussian diffusion profile. This assumption of Gaussianity, however, is violated by the complexity of the neuronal tissue in the brain (Frank, 2001). As a result, principal diffusion direction as used for tensor-based tractography may not reflect the underlying fiber populations (e.g., Pierpaoli et al., 2001), and DTI metrics are confounded by partial volume effects (e.g., Alexander et al., 2001, and Chapters 2 and 3).

High-angular resolution diffusion imaging (HARDI) methods have been proposed to better describe the measured diffusion profile (e.g., Frank, 2002; Tournier et al., 2004; Tuch, 2004; Descoteaux et al., 2007). Sampling the diffusion signals with a higher angular resolution on a single shell in q -space, orientation distribution functions (ODFs) can be estimated that allow for more accurate representations of diffusion in complex fiber architecture. Alternatively, q -space imaging methods, such as diffusion spectrum imaging (DSI, Wedeen et al., 2005, 2012b), sample a full three-dimensional (3D) Cartesian grid to estimate the diffusion propagator. These methods can be used to boost tractography performance, by more accurately tracking through regions of crossing fibers (Descoteaux et al., 2009; Fillard et al., 2011; Jeurissen et al., 2011; Wedeen et al., 2012b).

Another important aspect of diffusion MRI is the acquisition of each diffusion-weighted image (DWI). Traditionally, a single-short spin echo (SE) echo-planar imaging (EPI) readout is used for its high imaging speed (Mansfield and Pykett, 1978). However, single-shot EPI is prone to geometric image distortions, caused by local field inhomogeneities (Farzaneh et al., 1990). Higher in-plane resolution requires a longer readout that reduces the signal-to-noise ratio (SNR), and with increased spatial resolution the image distortions are increased as well (Skare et al., 2006). Isotropic resolution is critical in diffusion MRI (Vos et al., 2011; Jones et al., 2013), requiring a reduction in slice thickness to accompany higher in-plane resolution, but with decreasing slice thickness the slice profile deviates strongly from the prescribed rectilinear shape (Engstrom and Skare, 2013). For this reason, 3D acquisitions such as 3D DW-SSFP or 3D multi-slab EPI (McNab and Miller, 2008; McNab et al., 2009; O'Halloran et al., 2012; Engstrom and Skare, 2013) are more suitable for high isotropic image resolutions.

A high angular resolution is essential for accurate diffusion modeling per voxel, whereas a high spatial resolution is required for accurate localization of anatomy. Specifically, multi-fiber tractography can resolve multiple fibers within a voxel, but has a hard time distinguishing between crossing and kissing fibers (Tournier et al., 2011). A high spatial resolution, however, aids in making this distinction. So far, research has focused on improving either spatial or angular resolution, where we aim to bridge the two in this work. Specifically, we compare a unique dataset that offers both high spatial *and* high angular resolution versus subsamples of this dataset that have either a high spatial or high angular resolution. The overarching aim of this study was to determine which of these two factors, if any, provides the largest gain and when (if at all) there are diminishing returns.

5.2 Materials and methods

5.2.1 Data acquisition

A variant of the recently proposed 3D multi-slab EPI method by Engstrom and Skare (2013) was used to acquire high-resolution isotropic DWI data. Where in conventional 2D acquisitions each slice is Fourier-encoded only in-plane (k_x and k_y), 3D acquisitions also encode each slab along the z -direction, k_z . Here, a slab of 7 mm thickness was excited, and read out with a field-of-view (FOV_{SLAB}) of $232 \times 232 \times 8$ mm and an acquisition matrix ($\text{matrix}_{\text{SLAB}}$) of $232 \times 232 \times 8$ for true 1 mm isotropic resolution. The matrix was acquired by ‘stacking’ 2D EPI readouts along the z -dimension. Each of the 8 k_z phase-encodes was acquired in a separate excitation. Each in-plane EPI readout was performed with a GRAPPA acceleration factor of 4 and a partial Fourier factor of 0.7. A two-echo readout was used: the first echo was used for the imaging data, the second was used as navigator. Non-linear phase correction was applied before combining the k_z -encodes. The echo time of the imaging echo was 71.5 ms, for a TR of 7 s. As for most MR acquisitions, the slab profile—with a prescribed 7 mm thickness—was not perfectly rectangular. To account for slab boundary artifacts, only the center 5 k_z -encodes of 1 mm each were used. Thirty slabs were acquired and spaced in such a way that the combination of the center 5 mm of each slab formed a continuous coverage of 150 mm. Imaging was performed on a 3 T GE 750 unit with a Nova Medical 32-channel head coil.

For the HARDI acquisition scheme, 100 unique gradient orientations were acquired (Jones et al., 1999a) with a b -value of 1000 s/mm^2 and single-refocused diffusion preparation. To account for possible background gradients that could modify the diffusion-weighting orientation and magnitude (Neeman et al., 1991), each gradient orientation was acquired with both a ‘top-down’ and ‘bottom-up’ acquisition. As an example, a background-gradient along z might cause a prescribed diffusion-weighting along $[0 \ 0$

1] with $b=1000 \text{ s/mm}^2$ to have a higher actual b-value. Acquiring an image with a negative gradient orientation, [0 0 -1] in this case, would for instance have a b-value lower than 1000 s/mm^2 . Combining these two images would cancel out the background gradients (Neeman et al., 1991). In addition, these images have opposite eddy-current induced distortion which can be used to correct for these distortions (Bodammer et al., 2004).

To achieve DWI data with a high geometric fidelity, a high in-plane parallel imaging acceleration of 4 was used, as shown by Holdsworth et al. (2012) to greatly reduce EPI distortions. Additionally, each DWI was acquired with EPI phase-encoding (k_y) up and down ('blip up' and 'blip down') and corrected using the Jacobian-weighted reverse gradient polarity method (Chang and Fitzpatrick, 1992; Skare and Bammer, 2010).

Each gradient orientation was acquired with the 'top-down' and 'bottom-up' gradient direction, and both were acquired with EPI 'blip up' and 'blip down', for a total of $100 \times 2 \times 2 = 400$ DWIs. In addition, 40 images without diffusion-weighting were acquired ($b=0$ images, 20 with 'blip up' and 20 with 'blip down'). Because of the 3D nature of the sequence, the total acquisition time per image was $T_{ACQ} = TR \times Nk_z = 56 \text{ s}$, for a total acquisition time of $440 \times 56 \text{ s} = 24640 \text{ s} = 410\text{m}40\text{s} = 6\text{u}50\text{m}40\text{s}$. To acquire this amount of data, the total acquisition was fragmented to 20 sessions of 20.5 min. In each session, 20 DWIs and 2 $b=0$ -images were acquired: 5 unique gradient orientations acquired with top-down and bottom-up acquisitions and opposite EPI blips; and one $b=0$ image with opposite EPI blips. To ensure accurate repositioning over different scan sessions, and thus proper data fusion, a custom-made 'head holder' was created based on the geometry of the Nova Medical head coil—as determined via CT—and an anatomical MR scan of the subject's head. As a result, this head holder molded around the subject's head and fit tightly into the head coil for immobilization and near-perfect repositioning. The head coil used in this work (a Nova Medical 32-channel coil) had a noncircular cross-section so that the insertable head holder fit into the coil in only one unique way. This design was created using a 3D printer. A more detailed description of this positioning approach and its validation has been described in (Vos et al., 2013).

5.2.2 Image preprocessing

Prior to analysis, these data had to be fused from the different scan sessions into one dataset. First, each dataset was corrected for possible background gradients by an affine transformation of the corresponding top-down and bottom-up DWIs, using `elastix` (Klein et al., 2010). This was followed by the EPI distortion correction using the Jacobian-weighted reverse gradient polarity method (RGPM) using a multi-resolution b-spline registration (Chang and Fitzpatrick, 1992; Skare and Bammer, 2010). The order of these two image registrations was chosen such that the affine registration was done first, to

increase the image SNR for the nonlinear b-spline registration in the EPI distortion. Lastly, all datasets were combined, correcting each DWI for eddy current induced geometric distortions and subject motion by realigning all DWIs and b=0 images to the the b=0 image of the first session using `elastix` (Klein et al., 2010), with an affine coregistration technique and mutual information as the cost function (Pluim et al., 2003). In this whole procedure, the diffusion gradients were appropriately reoriented to account for subject motion (Leemans and Jones, 2009).

5.2.3 Reconstruction of datasets with different spatial and angular resolutions

The full 1 mm isotropic dataset with 100 directions (dubbed 100_1.0mm) was reconstructed into optimal subsets of 50 (50_1.0mm), 25 (25_1.0mm), and 15 (15_1.0mm) of the acquired directions. From the full set of 100 gradient directions, the subsets were selected based on their condition number (Skare et al., 2000; Dubois et al., 2006). The binomial coefficient of $\binom{100}{50}$ is roughly 10^{29} , making it impossible to calculate the condition number of each subset. Instead, 10^7 random subsets were created and from this the optimal subset was chosen. In addition, these datasets were also subsampled to 1.5 mm and 2.0 mm isotropic resolution (15_1.5mm and 15_2.0mm, 25_1.5mm and 25_2.0mm, etc).

5.2.4 Fiber tractography

For each reconstructed dataset, diffusion tensors were estimated using the iterative weighted least-squares approach (Veraart et al., 2013), and DTI-based fiber tractography was performed. Constrained-spherical deconvolution (CSD, Tournier et al., 2007) was used to calculate the fiber orientation distribution function (fODF) for all datasets with 25 or more gradient directions. The maximum order of spherical harmonics (L_{MAX}) depended on the number of directions ($L_{MAX}=8$ for 100 directions; 6 for 50; 4 for 30), and the single fiber response function was estimated using a recursive approach as proposed by Tax et al. (2013). Multi-fiber tractography was performed based on the fODF peaks (Jeurissen et al., 2011). All fODF estimation and tractography were performed in *ExploreDTI* (Leemans et al., 2009). From these whole-brain tractography results, several fiber bundles were segmented:

- the cortico-spinal tracts (CST) that terminate in the primary motor cortex (M1), were segmented as described in Wakana et al. (2007) and Chapter 4. The ROIs selecting M1 were 26 mm superior to the corpus callosum on the mid-sagittal slice;
- the trans-callosal bundle connecting the bilateral M1 areas, which will be abbreviated to M1–M1. The same M1 selecting ROIs were used as for the selection of the CST;
- the arcuate fasciculus (AF), as described in Catani et al. (2008).

5.2.5 Analysis

Volumetric overlap

To quantify the volumetric overlap between segmented fiber tract bundles from different datasets, a binary mask was created of all voxels intersected by the tract pathways included in that bundle. Because tracts are continuous space-curves, this tract-mask is not restricted to the voxel size of the dataset it was created from (as for instance demonstrated in tract density imaging, Calamante et al., 2010). For all datasets, the tract masks were created at a 1 mm isotropic resolution, and from these masks the volumetric overlap was quantified as the Dice similarity coefficient (Dice, 1945):

$$\text{overlap} = \frac{2(\text{mask}_A \cap \text{mask}_B)}{\text{mask}_A + \text{mask}_B} \quad (5.1)$$

where mask_A and mask_B are the tract masks of the reconstructed bundles to be compared, and \cap indicates the overlap of the masks. The Dice similarity is bounded between total overlap, 1, and no overlap, 0.

Anatomical correspondence

Volumetric overlap is one of the many possible criteria of fiber tract bundle correspondence. Termination points of fiber bundles are another important aspect. Because of the different configurations of the fiber bundles, this is evaluated differently each fiber bundle:

- Tracts from the CST should terminate in the M1 gyrus. The superior ROI used to select these tracts was drawn around M1, and the fraction of voxels in this ROI penetrated by fiber tracts was inspected for each reconstructed dataset;
- Transcallosal fibers that run from M1 to M1 were evaluated similar to the tracts from the CST;
- The segment of the AF investigated connects two language areas: Wernicke's and Broca's (Dejerine, 1895; Benson et al., 1973; Catani et al., 2005). Tract reconstructions were evaluated based on their ability to show cortical protrusions into these areas.

5.2.6 Methodological validation

From the full 100_1.0mm datasets, two 'test sets' were created where one random gradient direction was removed, making two very similar datasets. To demonstrate the validity of our analyses methods, we will first show the comparison between CSD-based tractography on these two test sets. Because they were nearly identical, only very minor changes in tractography results were expected. This provides a reference stan-

dard against which to compare the overlap values from the differently reconstructed datasets.

5.3 Results

5.3.1 EPI distortion correction

The importance of doing EPI distortion correction is shown in Fig. 5.1. Without this correction, tract bundles may be displaced or terminate incorrectly.



Figure 5.1: An example result from the Jacobian-weighted reverse gradient polarity method for a non-diffusion-weighted image. a,b) EPI distortions are most pronounced in the frontal lobe (as indicated by the arrows), but can also be observed in the occipital lobe (arrowheads). Correction by nonlinear image registration can reduce the extent of these distortions (c), in turn greatly improving the geometric correspondence between the brain and the brain MR image.

5.3.2 Dataset reconstruction

An example non-DWI and DWI at the acquired 1 mm isotropic resolution are shown in Fig. 5.2. The resulting DEC-maps of the full 100_1.0mm dataset and the datasets reconstructed at lower spatial resolutions are shown in an axial and coronal view in Figs. 5.3 and 5.4, respectively.

5.3.3 Methodological validation

The overlap between the fiber bundles in the test sets ranged from 0.83–0.89. The bundles with the highest (left CST) and lowest (right AF) overlap are shown in Fig. 5.5, to visualize where these differences occur. Although visually there are only minor differences in the reconstruction of these bundles, the volumetric overlap is significantly lower than 1 (which would have indicated perfect overlap).

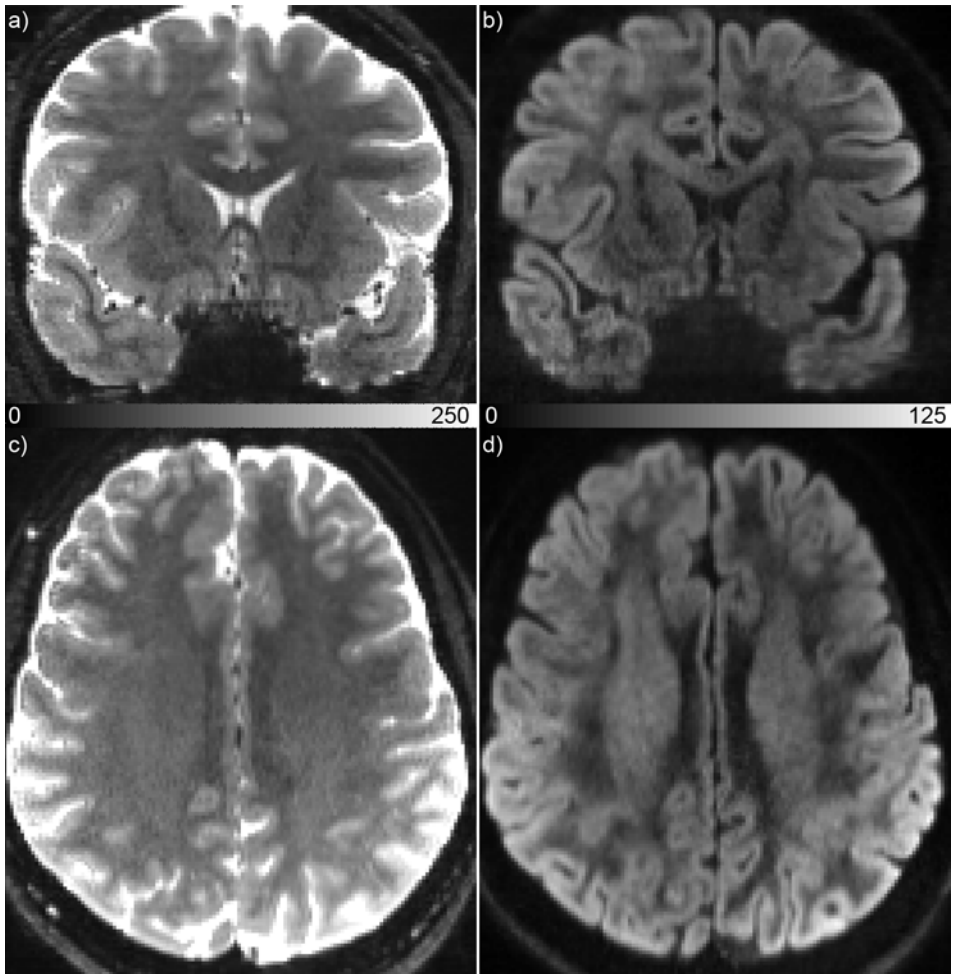


Figure 5.2: Coronal (a,b) and axial (c,d) images of a non-diffusion-weighted image (a,c) and diffusion-weighted image (b,d). The high 1 mm isotropic resolution gives a sharper transition between different tissue types, as can for instance be seen in the temporal lobes (a,b).

5.3.4 Comparison of spatial and angular resolution

Volumetric overlap

The overlap in reconstructed tract volumes is shown in Figs. 5.6-5.8, for the M1–M1 tracts, CST, and AF, respectively.

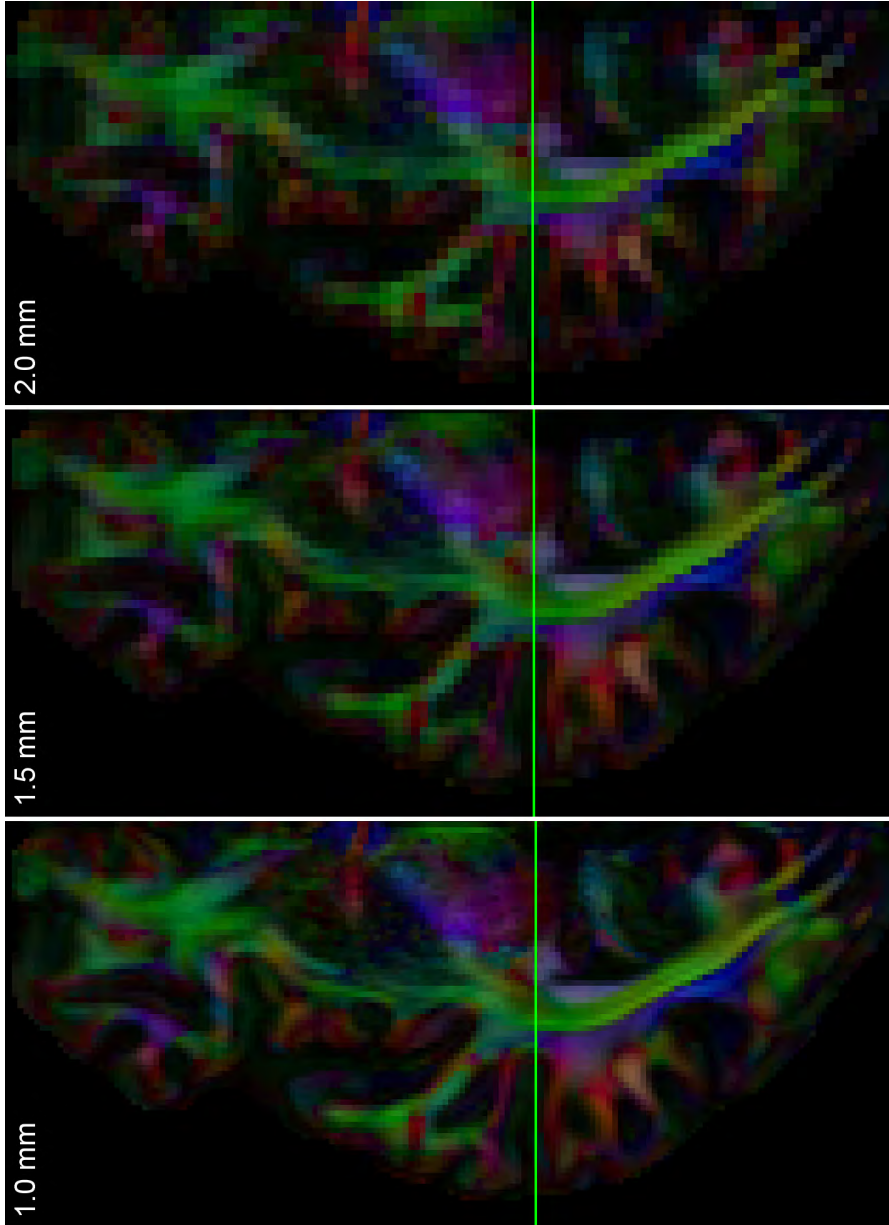


Figure 5.3: Axial views of the DEC-maps of datasets with 100 gradient directions reconstructed at different spatial resolutions: 1.0, 1.5, and 2.0 mm. The voxel volumes of these datasets are 1, 3.375, and 8 mm³, respectively. This is strongly reflected in the amount of partial volume effect, as most clearly seen in the optic radiation. The green lines indicate the location of the coronal view shown in Fig. 5.4.

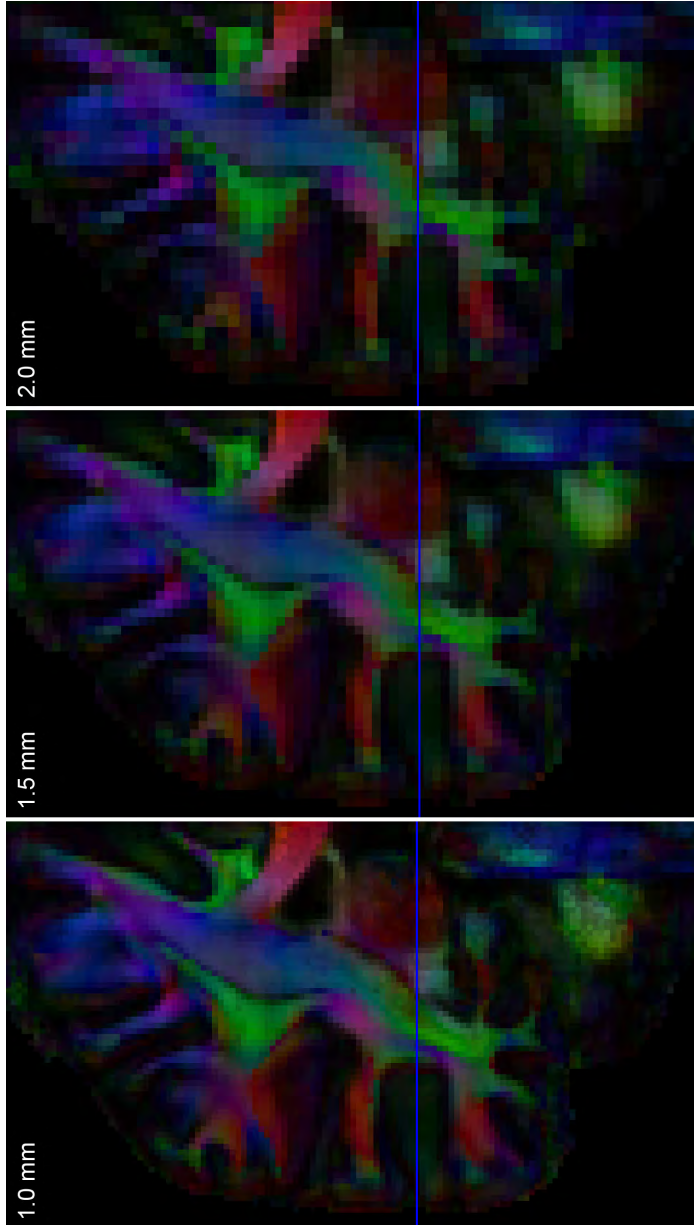


Figure 5.4: Coronal views of the DEC-maps of 100 gradient directions reconstructed at different spatial resolutions: 1.0, 1.5, and 2.0 mm. The voxel volumes of these datasets are 1, 3.375, and 8 mm³, respectively. This is strongly reflected in the amount of partial volume effect. The blue lines indicates the location of the axial view shown in Fig. 5.3.

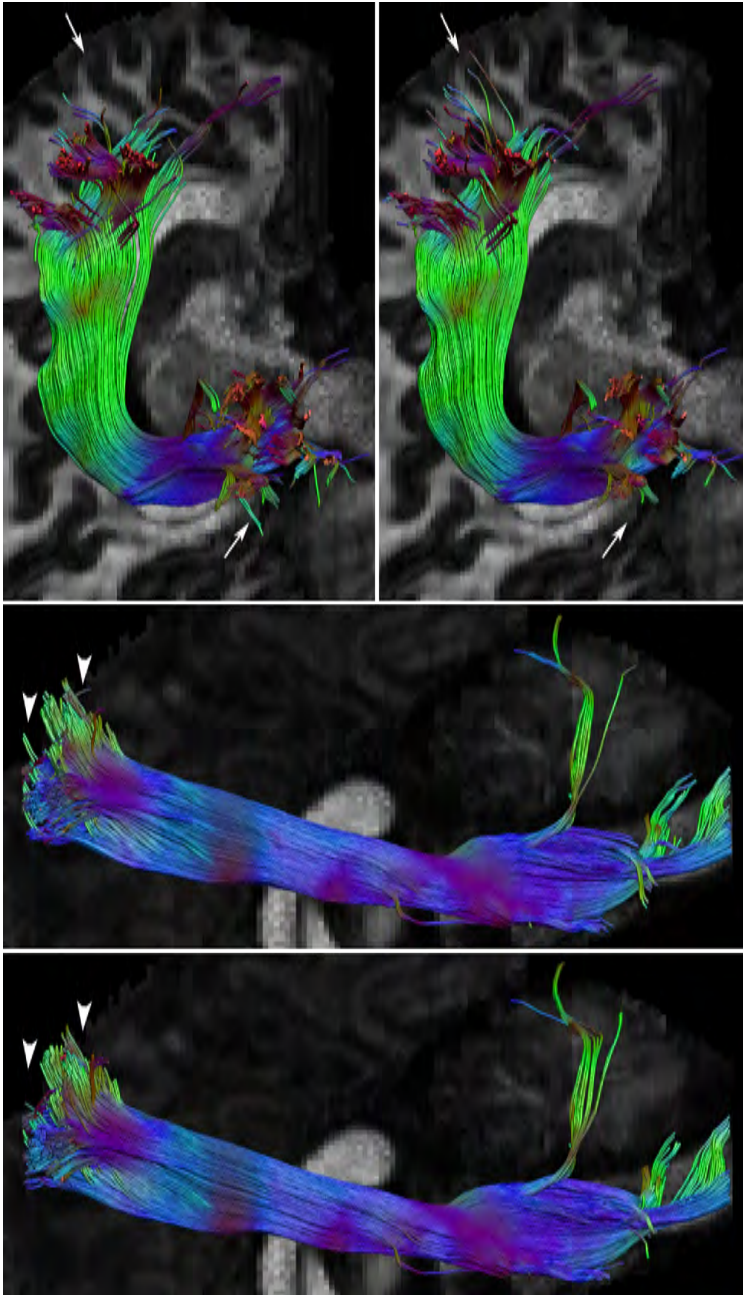


Figure 5.5: Test comparison of the fiber bundles between the two test sets with 99 directions for the left cortico-spinal tracts (CST) and right arcuate fasciculus (AF). For this test, CSD-based tractography was used. Of all five investigated bundles in this test example, the left CST has the highest overlap, 0.89, the right AF the lowest, 0.83. Very minor changes can be observed along the cores of the bundles, with the largest differences for the CST in the cerebellar projections (white arrowheads) and for the AF in its frontal and lateral temporal projections (white arrows).

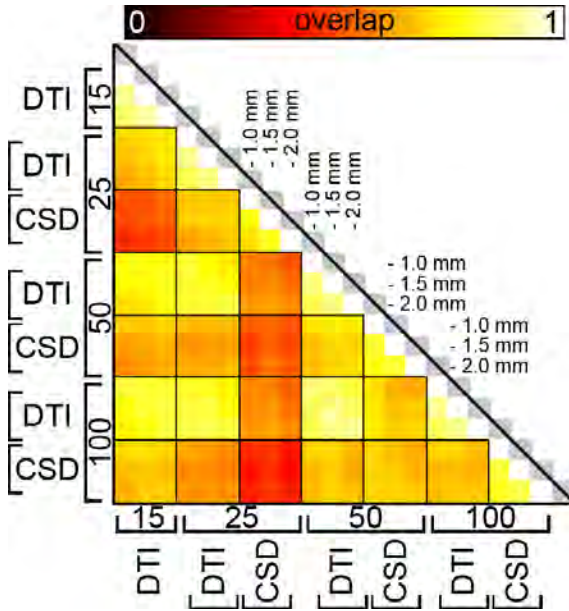


Figure 5.6: Volumetric overlap between the M1–M1 fiber tracts reconstructed from datasets with different spatial and angular resolutions. Datasets are grouped by number of directions and tractography approach (DTI vs. CSD), as indicated to the left and to the bottom. Each of those blocks consists of three datasets with different resolutions: 1.0 mm, 1.5 mm, and 2.0 mm. For each 3-by-3 block, these are ordered in increasing voxel volume top-to-bottom, and left-to-right (indicated in the top right half).

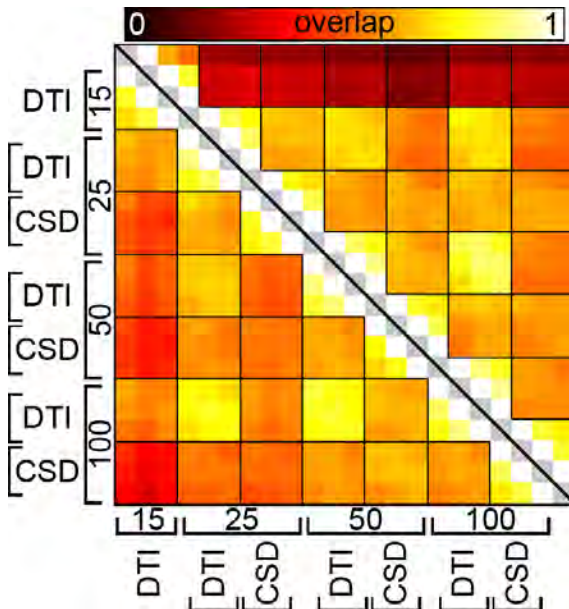


Figure 5.7: Volumetric overlap between the CST reconstructed from datasets with different spatial and angular resolutions. The bottom left half of the plot shows results for the left CST, the top right half the right CST. Datasets are grouped by number of directions and tractography approach (DTI vs. CSD). Each of those blocks consists of three datasets with different resolutions, as described in full detail in Fig. 5.6

For a selection of these tractography results, the volumetric overlap and mismatch is visualized. This allows for inspection of where differences are, facilitating the inter-

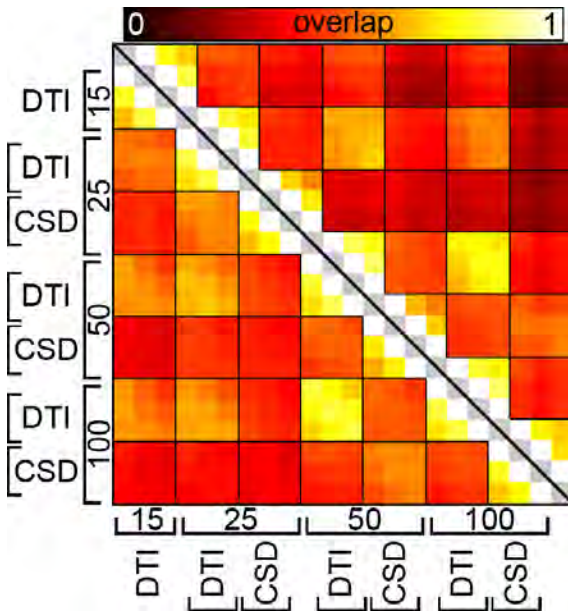


Figure 5.8: Volumetric overlap between the M1 fiber tracts reconstructed from datasets with different spatial and angular resolutions. The bottom left half of the plot shows results for the left AF, the top right half the right AF. Datasets are grouped by number of directions and tractography approach (DTI vs. CSD). Each of those blocks consists of three datasets with different resolutions, as described in full detail in Fig. 5.6

pretation of why these differences occur. Fig. 5.9 shows results for M1–M1 tracts for two comparisons: datasets 100_1.0mm and 25_1.0mm are compared, using DTI (a,b) and CSD (c,d). Comparisons for tract bundles from datasets with different spatial resolutions are shown in Fig. 5.10 for the left AF.

Anatomical correspondence

Fig. 5.11 shows clear trends in how well the right M1 region is penetrated by the CST, with DTI tractography on the 15 directions dataset giving a poor performance irrespective of the spatial resolution. All other datasets show very consistent results, with a high percentage of voxels in the medial parts of the M1 region visited. The CSD tractography with 100 directions showed the largest area of M1 intersected by fiber tracts, with especially a region more laterally being included in the segmented bundle that is absent in datasets with less directions. For the left CST, a significantly larger region of M1 was visited by tracts from CSD tractography than DTI tracking, irrespective of spatial and angular resolution. High spatial resolutions of 1.0 mm and 1.5 mm showed slightly larger visitation areas in the lateral parts of M1, which were absent in the 2.0 mm dataset.

For the fiber tracts connecting the bilateral M1 regions, there was more variation between datasets. Compared to the tracts from the CST, the M1–M1 tracts end up more laterally. This is consistent also in the left hemisphere. At lower angular resolutions (≤ 25 directions), DTI seems to outperform the CSD. At the highest angular resolution,

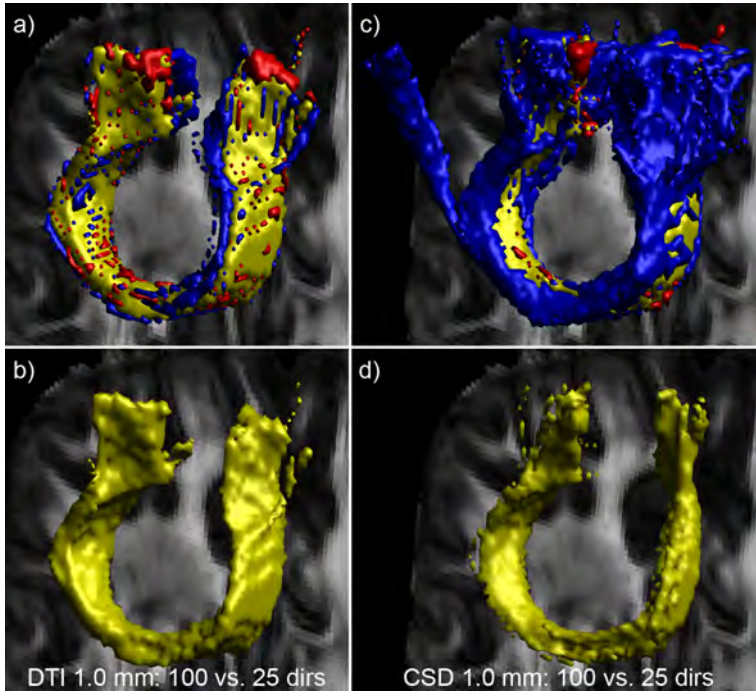


Figure 5.9: Renderings of overlap and mismatch between the M1–M1 tracts reconstructed with different angular resolutions. Panels a) and b) visualize results from comparing the 100_1.0mm and 25_1.0mm datasets using tensor-based tractography, which has a volumetric overlap of 0.80. Here, the yellow volume indicates overlap between the two reconstructed fiber bundles; red indicates voxels only included in the tracts from the 25_1.0mm dataset; blue indicates voxels only included in the tracts from the 100_1.0mm dataset. The right panels illustrate the comparison between the 100_1.0mm and 25_1.0mm datasets in a similar way, but then using CSD tractography. The volumetric overlap here is 0.42.

however, CSD shows a region on the lateral end of M1 that is visited by fiber tracts. This could also be seen in Fig. 5.9, where there was a clear mismatch between CSD tractography at 25 and 100 directions. The visitation in the left M1 area, similar findings were observed. Again, far lateral projections were present in the CSD tracts, but only in the 100_2.0mm and the 50_1.5mm datasets.

For the AF, qualitative scoring was performed on how well the different cortical projections were reconstructed in each dataset. An example comparison between AF bundles with different degrees of these projections is shown in Fig. 5.13. With increasing angular resolution, the cross-sectional volume of the AF increased. Regions at the interface between the AF and other fiber bundles, where the intra-voxel complexity is largest,

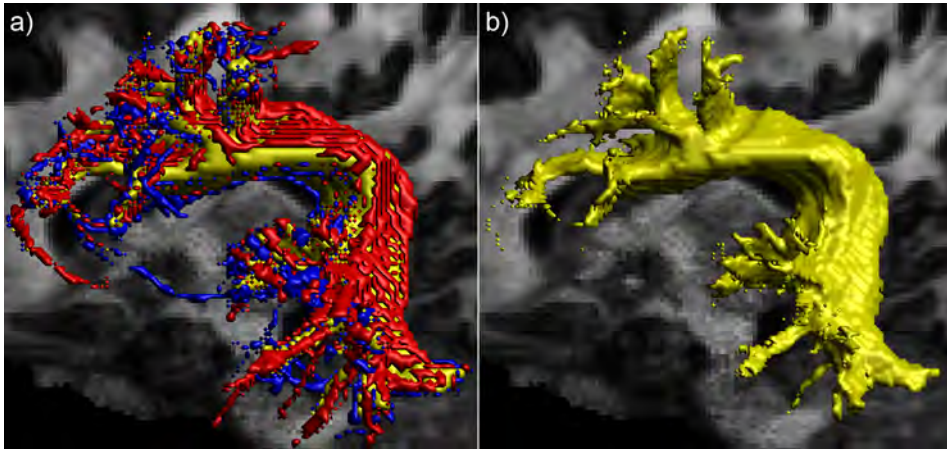


Figure 5.10: Renderings of overlap and mismatch between the AF reconstructed with different spatial resolutions. Results from comparing the 100_1.0mm and 100_2.0mm datasets using CSD-based tractography are shown. The yellow volume indicates overlap between the two reconstructed fiber bundles; red indicates voxels only included in the tracts from the 100_2.0mm dataset; blue indicates voxels only included in the tracts from the 100_1.0mm dataset. The overlap is 0.67.

are included at higher angular resolutions. This gives some explanation for the relatively low volumetric overlap between the AF in different reconstructed datasets. For the same reason, the datasets with a higher angular resolution show tracts that continue farther anteriorly and tracts that branch off laterally. The DTI tracts, as well as the CSD tracts based on only 25 directions, failed to include the wide range of projections into the temporal lobes. There are smaller differences in these temporal regions between the datasets with 50 and 100 gradient directions, most notably the inclusion of posteriorly-oriented tracts that projecting into a gyrus that was otherwise excluded (white arrows). Similarly small differences between the 50 and 100 gradients datasets were observed in the anterior portion of the AF. The largest difference is in the location of the most anterior segment (arrowheads), which terminates more superiorly for the 50 directions dataset than for the 100 directions dataset, but remain within the same gyrus. Similar trends were observed for the right AF.

5.4 Discussion

The purpose of this work was to give an overview of how different degrees of angular and spatial resolutions impact fiber tractography results. We used a state-of-the-art 3D DWI pulse sequence to acquire diffusion MRI data with a 1 mm isotropic resolution

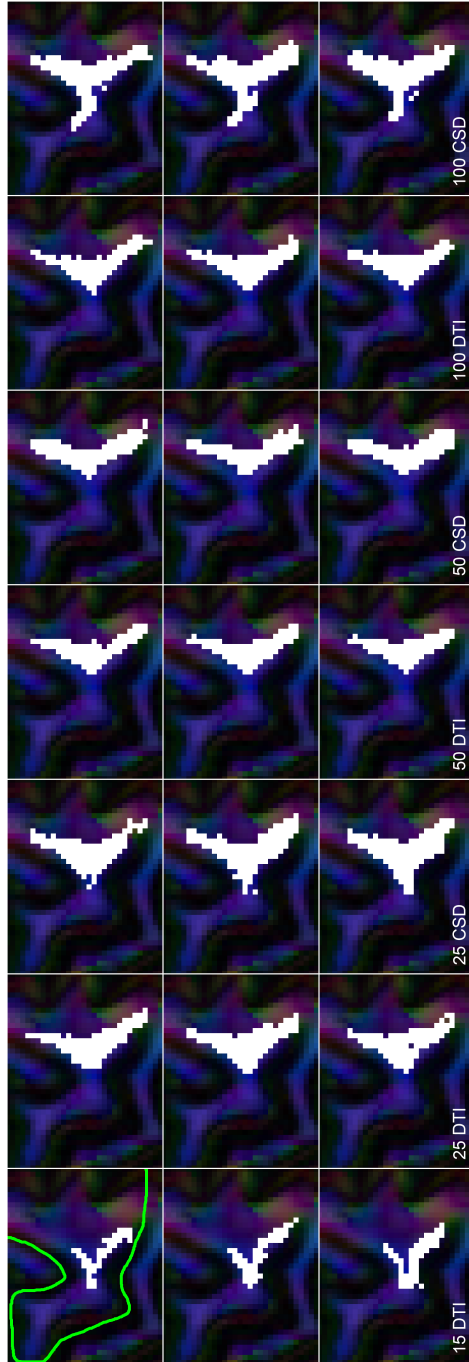


Figure 5.1.1: Visualization of where fiber tracts from the right cortico-spinal tract (CST) end up in the M1 gyrus. Each subpanel represents results from the different reconstructed datasets. The three rows are the different spatial resolutions, 1.0 (top), 1.5 (middle), and 2.0 mm (bottom). Each row is ordered from left to right: DTI 15, DTI 25, CSD 25, DTI 50, CSD 50, DTI 100, CSD 100 (similar to Figs. 5.6-5.8). White areas indicate voxels that were intersected by fiber tracts. The green line on the top left indicates the ROI that selects M1.

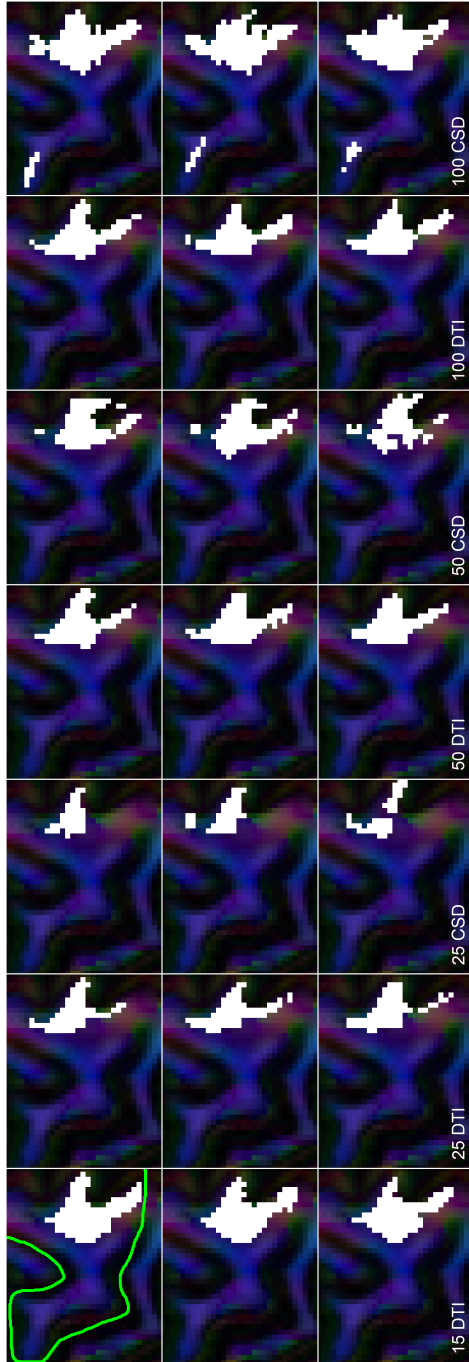


Figure 5.12: Visualization of where fiber tracts connecting the bilateral M1 regions end up in the right M1. Each subpanel represents results from the different reconstructed datasets. The three rows are the different spatial resolutions, 1.0 (top), 1.5 (middle), and 2.0 mm (bottom). Each row is ordered from left to right: DTI 15, DTI 25, CSD 25, DTI 50, CSD 50, DTI 100, CSD 100 (similar to Figs. 5.6-5.8). White areas indicate voxels that were intersected by fiber tracts. The green line on the top left panel indicates the ROI that selects M1.

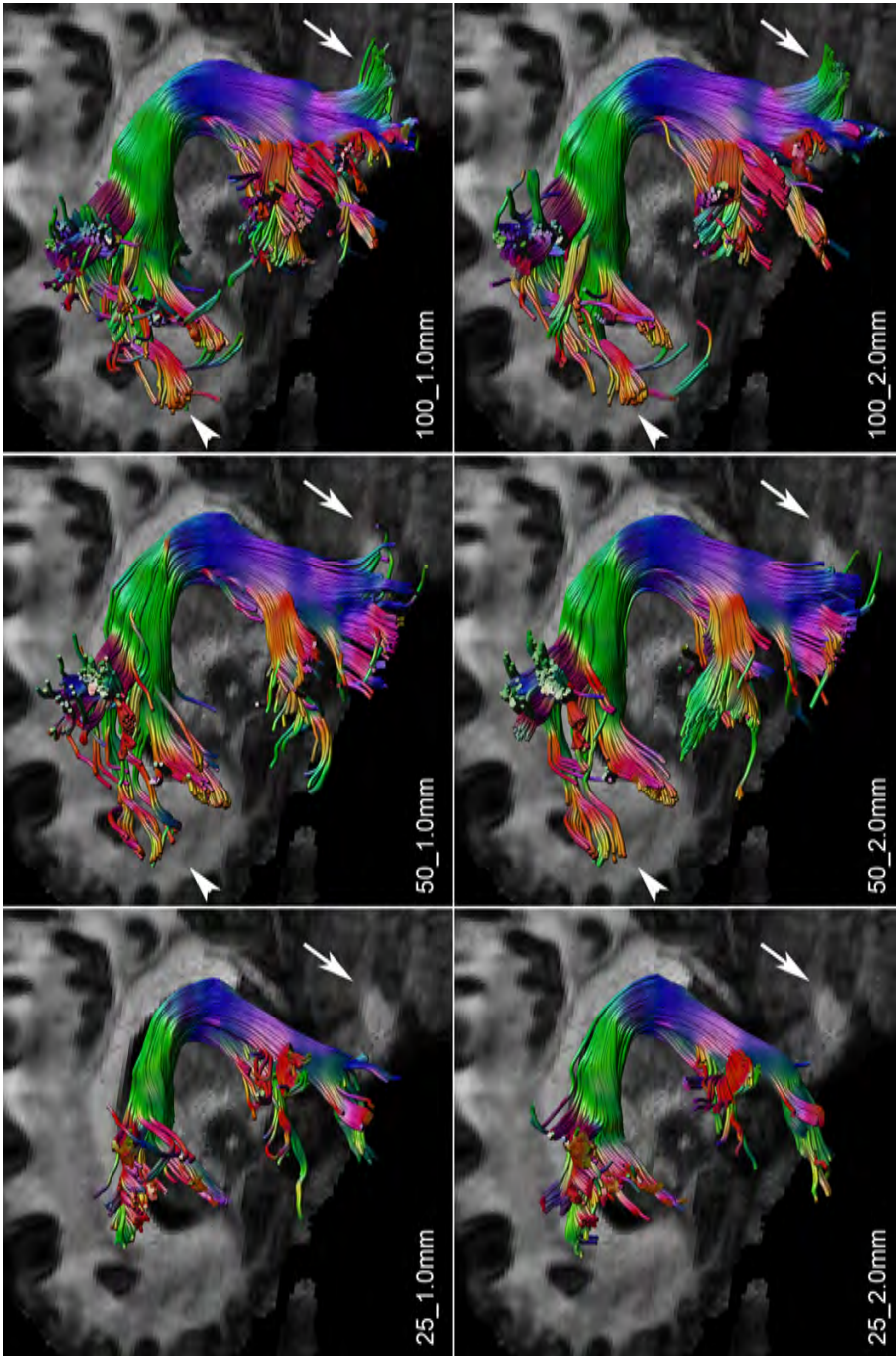


Figure 5.13: Examples of reconstructed arcuate fasciculus bundles for six different datasets at different angular and spatial resolutions. The arrows highlight differences in the temporal projections of the bundle, which increases strongly from 25 to 50 directions, and slightly further from 50 to 100 directions. For the anterior segment, indicated by the arrowheads, the 50 and 100 gradient directions datasets project into the same gyrus, though terminate at a different location. These projections are absent in the 25 directions dataset.

and a HARDI acquisition scheme with 100 gradient directions. Reconstructions of this dataset have been made with a lower angular, a lower spatial resolution, or both.

5.4.1 Methodological validation

Prior to comparing datasets with different angular and spatial resolution, a validation-like test was performed. The volumetric overlap between fiber bundles from two nearly identical datasets is in the range of 0.83-0.89, depending on the structure of interest (Fig. 5.5). The excellent structural correspondence between these different reconstructions can be appreciated along the length of the bundle. The differences in volumetric overlap are mostly caused by one or more fiber tract pathways that deviate from the core bundle. Additionally, very minor differences in bundle thickness may further decrease the overlap.

5.4.2 Analysis of reconstructed datasets

Volumetric overlap

The first quantification to compare the trade-off between angular and spatial resolution is volumetric overlap in reconstructed fiber tracts bundles. From Figs. 5.6-5.8 it is most obvious that the volumetric overlap between fiber bundle reconstructions is relatively invariant under changes in spatial resolution. The values near the diagonal indicate overlap between datasets with the same number of directions and tractography method, but different spatial resolutions. Most importantly, these values on the diagonal have high overlap values, ranging up to and exceeding those from the 'test sets'. Additionally, for each angular resolution and chosen tractography model, the '3-by-3 blocks' of different spatial resolutions shows very similar overlap values. This further indicates there is more variation as a result of changing angular resolution than because of spatial resolution.

Anatomical correspondence

In general, these comparisons showed very similar results to the quantitative analysis in terms of volumetric overlap: tractography results were relatively stable under changes in spatial resolution, whereas pronounced differences in tract endpoints were observed when changing the angular resolution. The M1-M1 fiber tracts showed the most striking difference, with tracts ending up in the lateral tip of the right M1 on the datasets with 100 gradient directions. In the left M1, these tracts were only observed at lower spatial resolutions, and very inconsistently. Given that the transcallosal fibers are involved in motor function, it may be expected that the tracts connecting these regions span the whole cortical area, explaining the origin of these lateral projections. For the left CST, the higher spatial resolutions had tracts in a slightly higher fraction of M1, indicating a benefit of higher spatial resolution. These regions, however, were only

included for high spatial *and* high angular resolution. This would mean that, should a trade-off be made between either type of resolution, these regions would be excluded.

The anatomical accuracy of fiber tracts is difficult to quantify, given that no ground truth of the wiring of the human brain exists. Additionally, none of these datasets can be regarded as the ‘gold standard’ for this work in particular. The full 100_1.0mm dataset has the highest angular and spatial resolution, which should provide the “best” results in terms of fiber tractography results. However, one could also argue that the higher SNR in the reconstructed 100_1.5mm or 100_2.0mm datasets provides a more stable and reliable result of the voxel-wise fODFs, and that this would result in the “best” results. Because of this lack of a reference standard, datasets can only be compared against each other, and to previously published work on neural anatomy (e.g., Catani et al., 2008).

5.4.3 Angular resolution

To discuss the influence of angular resolution in more detail, a division must be made between the tensor-based tractography and the CSD-based tractography. Fiber bundles reconstructed with DTI generally have a higher overlap at varying angular resolutions than tracts reconstructed with CSD. The tensor is a model with a low angular resolution, with tensor-based tracking following only the first eigenvector of the tensor. This is because sampling the diffusion profile at a higher resolution will mostly just improve the robustness of the fitted model, and not significantly alter the eigenvectors.

For CSD, each dataset was modeled with an L_{MAX} as high as possible to best utilize the angular resolution in that dataset. That means that CSD fits in the datasets with 25, 50, and 100 gradient directions had L_{MAX} values of 4, 6, and 8, respectively. Where higher harmonical orders allow for modeling of more acute fiber crossings, tractographic differences between these dataset with varying angular resolutions are expected. These differences in angular resolution result in different fODFs per voxel, which in turn affects the tractography that uses the fODF peaks. An excellent example of this is given in Fig. 5.9. CSD tractography on the 25_1.0mm and 100_1.0mm datasets (c,d) both show tracts in the typical transcallosal U-shape (overlap indicated by the yellow volume), similar to the DTI-based tractography (a,b). Only CSD tractography on the 100_1.0mm dataset shows a tract cluster branching of to a different part of the M1 gyrus that was not included in the other reconstructions in Fig. 5.9. This tract cluster is consistently present in the 100_1.0mm, 100_1.5mm, and 100_2.0mm datasets, and absent in all datasets with less directions. Visual inspection of the underlying fODFs showed subtle differences at the interface of the corpus callosum and the superior fronto-occipital fiber (data not shown), and allows for correct tracking through this region in the datasets with 100 directions.

5.4.4 Spatial resolution

As can be observed in Figs. 5.3 and 5.4, the difference in voxel sizes between the 1.0, 1.5, and 2.0 mm resolution datasets lead to pronounced differences in partial volume effects. As a result, a fiber bundle with a given cross-sectional shape would be significantly better represented with voxels of 1 mm isotropic than with voxels of 2 mm isotropic. Except in ideal cases where the shape fits exactly in the 2 mm voxel grid, it will appear larger on the lower resolution image. This effect is also present when performing fiber tractography based on images with different resolutions. Fig. 5.10 illustrates this concept nicely. The overlap between the tracts from the 100_1.0mm and 100_2.0mm (yellow) shows the main outline of the AF. However, along most of the length of the bundle there is a layer of voxels around this volume where only fiber tracts from the 100_2.0mm dataset intersect (red). Overlap is further reduced by the difference in tracts projecting into lateral and temporal cortical areas (visualized by the tangle of blue and red volumes).

5.4.5 Previous tractography reproducibility studies

Previous studies have been performed to investigate the reproducibility of tractography analyses (Ciccarelli et al., 2003; Heiervang et al., 2006; Malykhin et al., 2008; Kristo et al., 2013a,b, e.g.,). In these studies, either test-retest analyses were performed to investigate spatial correspondence of fiber bundles in multiple scans from one subject, or intra-rater agreement was examined to determine how reliable tract bundles can be segmented. Intra-rater agreement in DTI tractography was found to be in order of 0.82-0.98 (varying strongly depending on the fiber bundle; Malykhin et al., 2008), and overlap between fiber bundles in test-retest analyses showed similar correspondence (Kristo et al., 2013b). These values are in the same range as the ‘test set’ analyses performed in this work. Interestingly, tractography results from CSD have been shown to have a lower test-retest volumetric overlap, around 0.60-0.65, than DTI-based tracts, where the overlap range is 0.70-0.80 (Kristo et al., 2013b). The different reconstructions analyzed in this work could be considered some variant of test-retest or intra-subject repeatability, and our overlap values are in the same range as the previously reported reproducibility of CSD tractography.

5.4.6 Limitations

It must be noted that 50 gradient directions is enough to fit $L_{MAX}=8$, and that we have chosen for $L_{MAX}=6$ in our datasets with 50 directions. Visual inspection of the estimated response function and the resulting fODF glyphs revealed unstable results at 1.0 mm and 1.5 mm resolution, but acceptable results for the 2.0 mm resolution because of a higher SNR. This lowered spatial resolution could thus be traded for a higher angular resolution of the model. We concede that it is an arbitrary choice not to include

this option, and to choose for maintaining a fixed L_{MAX} per number of gradient directions. Similarly, it would have been possible for the CSD model with lower L_{MAX} for each dataset, to trade angular resolution for stability of the fit. Such analyses would be interesting to further determine an optimal combination of acquisition specifics and model parameters. We have chosen to refrain from including these analyses to maintain the focus of this work on the trade-off between angular and spatial resolution.

An important factor in the angular resolution is the b-value. The contrast between regions of high and low diffusion increases with b-value, which results in a higher effective angular resolution. For HARDI purposes, a b-value of 1000 s/mm² is considered to be lower than optimal, but is commonly used for CSD tractography in more clinically-oriented studies (e.g., Metzler-Baddeley et al., 2011) as well as technical studies (e.g., Reisert et al., 2012). The high spatial resolution used in this work prevented the use of b-values in the range of 2000-3000 s/mm², which would have increased TE and thus decreased SNR. The use of two signal averages to accommodate this was not regarded as an option because this would double the already extensive scan time. Performance of multi-fiber methods will generally increase with the number of acquired DWIs (Wedeen and Dai, 2011), with possibly limited gains at numbers of DWI over 100 (depending on the chosen method). Therefore, tractography is expected to be more accurate with increasing numbers of gradient directions, irrespective of the b-value used, for the datasets with different angular resolutions used here. As such, one would expect the trends in trade-off between angular and spatial resolution to be unchanged with higher b-values. Instead, an overall improvement in tractography performance would be expected as a result of higher b-values.

Would higher b-values have been used in this work, the effective angular resolution would have increased for all datasets, allowing for better characterization of crossing fibers. Alternatively, similar results could be obtained using less diffusion directions at a higher b-value (Tournier et al., 2007). Tractography results were comparative across different spatial resolutions, suggesting that spatial resolution could be sacrificed for angular resolution for improved tractography results—up to certain limits. With the increased SNR of larger voxels, this angular resolution could be obtained by increasing the b-value and/or more gradient directions.

A generally used method to calculate the response function of CSD is to set an FA threshold at some fixed value, such as 0.7 or 0.8 (Tournier et al., 2004). The calibration of the response function in CSD is critical for accurate fODF estimation (Parker et al., 2013), and the chosen FA threshold in this procedure greatly influences the estimated fODFs. Setting this FA threshold too high introduces spurious fODF peaks, which corrupts tractography. In this work, we had smaller voxels than typically used for CSD, and because of this a relatively low SNR. Smaller voxels would mean less partial voluming

and thus more orientational coherence within voxels, which would increase the FA. Similarly, low SNR increases the estimated FA (Jones and Basser, 2004). To address this, we have used a new recursive method to estimate the response function that provides better response function characterization and thus more reliable fODFs for tractography (Tax et al., 2013). In a comparative studies on the performance of different multi-fiber methods at b-values in the order of $b=1000 \text{ s/mm}^2$, CSD showed above average performance (Ramirez-Manzanares et al., 2011). This indicates that given the b-value used in this work, CSD is an appropriate model to use, which confirms a similar claim by Tournier et al. (2007).

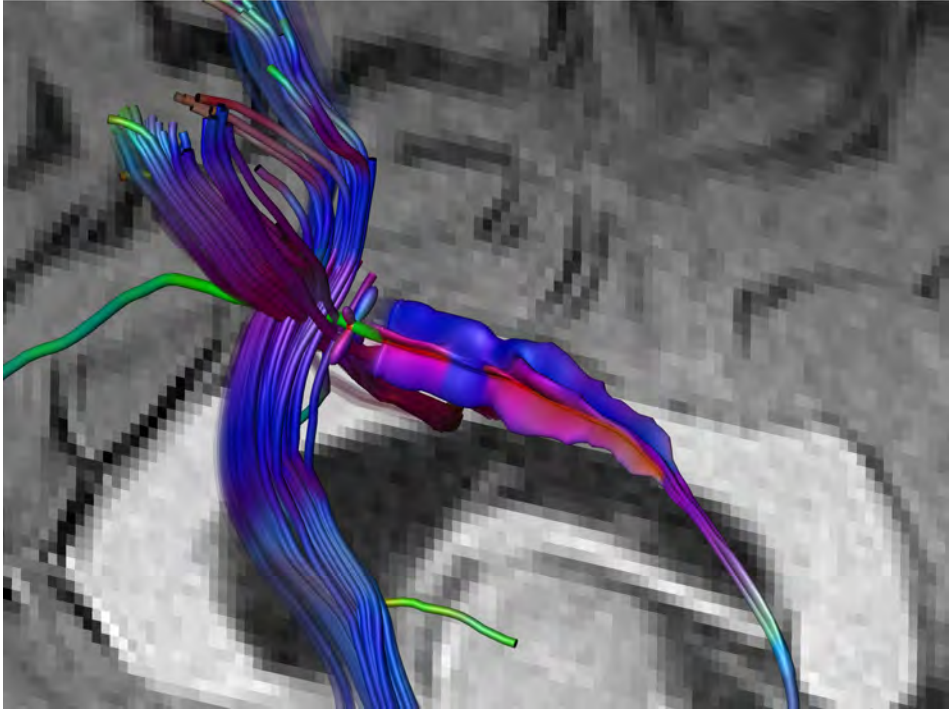
To create the lower resolution datasets, the acquired images were downsampled from the 1 mm isotropic dataset, which does not yield exactly the same images as when they would have been acquired at these resolutions. For instance, higher resolutions introduce larger geometric distortions, and the longer readout time prolongs the echo time and thus lowers SNR. The first aspect is largely addressed by using the RGPM for EPI distortions, and should have limited influence. The prolongation of TE is inherent in higher in-plane resolutions, since a larger part of k-space is sampled. With a partial Fourier factor of 0.7 and high parallel imaging factor used in this work, the effective TE is only slightly increased compared to standard acquisition with 2 mm isotropic resolution.

Another important factor in this trade-off, is that thicker slices can be acquired using 2D acquisitions. The 3D acquisition used here has a downside in that it has an acquisition time per volume of $TR \times Nk_z$ seconds, which is many times slower than 2D imaging. Important to note here is that 3D multi-slab has a higher SNR per unit time, or SNR efficiency (Engstrom and Skare, 2013), but the minimum scan time per volume is higher.

In this work, we have used a 3D multi-slab acquisition to acquire DWIs with a 1 mm isotropic resolution. To achieve true isotropic resolution, 3D acquisitions are critical. Slice profiles for 2D imaging are never truly rectangular, which introduces some smoothing along that direction. The slice profile becomes worse for thinner slices, rendering an actual 1 mm thin slice difficult to acquire. The 3D multi-slab method does not suffer from these slice profile imperfections in the same way, yielding true isotropic resolution. Another benefit of the 3D acquisition is that it is more SNR efficient than conventional 2D imaging (Engstrom and Skare, 2013). A downside is that the scan time is strongly increased compared to 2D imaging, by the need to acquire different k_z -encodes. To address this, Van et al. (2013a) have proposed a SENSE-like reconstruction to reconstruct all 3D slabs simultaneously, providing an increase in speed of roughly 25-50%.

5.4.7 Conclusion

Current studies that use tractography to investigate whole-brain connections or to segment pre-defined fiber bundles typically use a resolution in the order of 2 mm isotropic (e.g., Kleinnijenhuis et al., 2012; Kristo et al., 2013b). Developments on more demanding diffusion MRI models are being paralleled by more advanced image acquisition techniques. As a result, the decision for which of these two factors scan time should be used becomes ever more important, and difficult. In this work, we have given an overview of tractography results from datasets with varying spatial resolution and different numbers of diffusion-weighting directions. Correspondence between different spatial resolutions seems to be higher than correspondence between different angular resolutions. Where a high angular resolution allows for better characterization per voxel, high spatial resolution allows for better localization of fiber structures. Conceptually, therefore, the results in this work indicated that the gain in knowing the fiber orientations in more detail is more beneficial than knowing fiber locations more accurately. However visually pleasing the higher spatial resolution images appear, the detailed information required for accurate fiber tractography appears to be in the angular domain. High spatial *and* high angular resolution will be the ultimate combination. If a trade-off must be made between: i) increasing spatial resolution past current standards, ii) or investing scan time in higher angular resolutions, our results suggest that fiber tractography benefits the most from high angular resolutions.



The architecture of the the fiber tracts crossing the 'tract-of-interest' from the arcuate fasciculus visualized as a multi-fiber hyperstreamline

Chapter 6

Multi-fiber tractography visualizations for diffusion MRI data

This chapter has been submitted as:

S.B. Vos, M.A. Viergever, A. Leemans, “Multi-fiber tractography visualizations for diffusion MRI data”

Abstract

In recent years, several new diffusion MRI approaches have been proposed to explore microstructural properties of the white matter, such as Q-ball imaging and spherical deconvolution-based techniques to estimate the orientation distribution function. These methods can describe the estimated diffusion profile with a higher accuracy than the more conventional second-rank diffusion tensor imaging technique. Despite many important advancements, there are still inconsistent findings between different models that investigate the “crossing fibers” issue. Due to the high information content and the complex nature of the data, it becomes virtually impossible to interpret and compare results in a consistent manner. In this work, we present novel fiber tractography visualization approaches that provide a more complete picture of the microstructural architecture of fiber pathways: multi-fiber hyperstreamlines and streamribbons. By visualizing, for instance, the estimated fiber orientation distribution along the reconstructed tract in a continuous way, information of the local fiber architecture is combined with the global anatomical information derived from tractography. Facilitating the interpretation of diffusion MRI data, this approach can be useful for comparing different diffusion reconstruction techniques and may improve our understanding of the intricate white matter network.

6.1 Introduction

Diffusion MRI can be used to estimate the self-diffusion of water molecules *in vivo* (e.g., Le Bihan and Breton, 1985). Diffusion tensor imaging (DTI) describes the orientational preference of diffusion in the human brain, modeling it as a second-rank tensor (Basser et al., 1994). Based on the diffusion tensor framework, virtual reconstructions of white matter (WM) fiber pathways can be created with fiber tractography (e.g., Basser et al., 2000). To convey more information than merely the fiber trajectories, alternative approaches to the conventional streamlines and -tubes have been proposed: hyperstreamlines, showing the second and third eigenvectors and eigenvalues of the diffusion tensor as the cross-sectional shape of the streamtube (Zhang et al., 2003); and streamribbons, where the local width of the ribbon indicates the coefficient of planar diffusion (Westin et al., 2002; Atkinson et al., 2007). However, the additional information visualized in this way suffers from the same limitations inherent to DTI, i.e., the inability of the diffusion tensor to describe the diffusion correctly in regions of crossing or branching fiber tracts (e.g., Alexander et al., 2001, 2002; Jones, 2003; Tournier et al., 2011).

To overcome the limitations of DTI, several different methods have been proposed, e.g., Q-ball imaging (QBI; Tuch, 2004), constrained spherical deconvolution (CSD; Tournier et al., 2007), diffusion spectrum imaging (DSI; Wedeen et al., 2008)—each having different requirements in terms of the acquisition protocol. QBI and DSI, on the one hand, have a direct mathematical relation between the measured diffusion signals and the estimated diffusion orientation distribution function (ODF) and diffusion propagator, respectively. The propagator obtained from DSI represents the 3D probability of spin displacement, where the diffusion ODF (dODF) calculated by QBI yields only the orientational aspect of the spin displacement (Assemlal et al., 2011). On the other hand, CSD uses an estimated single fiber response function to deconvolve the DW intensities with this response function to obtain the fiber ODF (fODF), specifying the orientations of the underlying fiber populations. Tractography that makes use of these ODFs, which then is referred to as “multi-fiber” tractography, can take crossing fibers configurations into account, such as, for instance, in the centrum semiovale, where the cortico-spinal tracts (CST), arcuate fasciculus (AF), and lateral projections of the corpus callosum (defined in the remainder of this work as “latCC”) intersect one another (Behrens et al., 2007; Descoteaux et al., 2009; Fillard et al., 2011; Jeurissen et al., 2011; Wedeen et al., 2012b).

With a growing number of diffusion MRI researchers opting for these more advanced diffusion MRI methods over conventional DTI, especially for tractography purposes, it is becoming increasingly important to fully utilize the potential offered by these ap-

proaches (Jones et al., 2013). Despite the huge efforts invested in creating these new techniques, there are still several discrepancies and inconsistent findings between different algorithms (e.g., Jeurissen et al., 2012). To optimize the yield from diffusion data, it is important to understand the origins of these differences. In this context, data visualization plays an important role in facilitating the interpretation of high-dimensional diffusion MRI data. Visualization of the ODF is already possible on a local scale as voxel-wise glyph representations, which can be of great use to visualize the regional architectural complexity in known areas of crossing fibers (Leemans, 2011). However, as these local representations are only available for display at discrete positions (Kezele et al., 2008; Peeters et al., 2009; Prckovska et al., 2011), they are suboptimal to convey the anatomical continuity of fiber bundles. To date, and to the best of our knowledge, there are no fiber tractography visualization strategies that are specifically designed to address the interwoven and complex geometry of the WM fiber network (Wedeen et al., 2012b,a; Catani et al., 2012).

In this work, we introduce an approach to visualize the local tissue architecture along reconstructed fiber tracts in a continuous way, creating hyperstreamlines for multi-fiber tractography data. This means that microstructural information from advanced diffusion methods is combined with large-scale anatomical information obtained from fiber tractography. With this new visualization method, the ODF is visualized along the fiber tracts to clearly illustrate the regions of crossing fibers. Additionally, by reducing the ODFs to their principal fiber orientations, streamribbons can be constructed to emphasize the orientations of the crossing fiber populations. The proposed visualization approaches create more complete representations of the microstructural architecture in fibers that pass through regions of complex WM configurations. As a result, these multi-fiber tractography visualizations may aid in our understanding of white matter organization.

6.2 Materials and methods

Before describing the multi-fiber visualization methods in detail, we will first discuss why current DTI based tract visualization approaches (Zhang et al., 2003; Atkinson et al., 2007) are inappropriate for visualizing multi-fiber tractography data. Consider two fiber populations crossing at a 60° angle (Fig. 6.1a,b). When these two populations coexist within one voxel—assuming slow exchange between these populations (Alexander et al., 2001)—the resulting diffusion tensor can be estimated from the averaged diffusion weighted signals of the individual populations (as shown in Fig. 6.1c). The first eigenvector of this tensor (ϵ_1 , brown line in Fig. 6.1c) will be an average of the two fiber populations (white lines in Fig. 6.1c). In DTI based tractography, the tract orientation will be determined by ϵ_1 , with ϵ_2 and ϵ_3 always perpendicular to ϵ_1 (Fig. 6.1d).

In the case of crossing fibers, ϵ_1 is not necessarily parallel to one of the fiber populations as determined by the multi-fiber diffusion method (Fig. 6.1c). Consequently, ϵ_2 and ϵ_3 will not necessarily be perpendicular to the tract orientation for any of the two fiber populations, which means that the information visualized in this way will be misleading. The following will first detail the simulated fiber phantoms and in vivo data that will be used to demonstrate the concepts and benefits of our multi-fiber tractography visualizations.

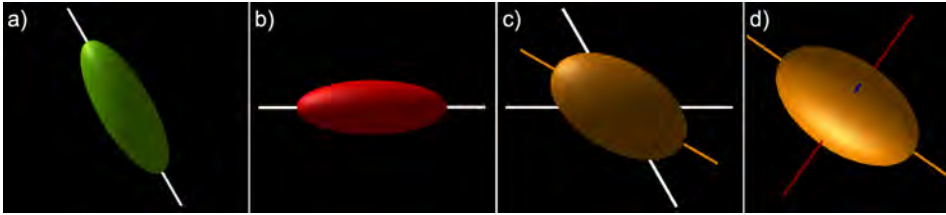


Figure 6.1: The conceptual difficulties of tensor-based visualizations of multi-fiber tractography data. In a) and b), two single fiber populations with their respective diffusion ellipsoids are shown. When these two coexist within one voxel (c), the first eigenvector (ϵ_1 , brown line) no longer corresponds to any of the underlying fiber orientations (white lines). d) The second (ϵ_2 , green) and third (ϵ_3 , blue) eigenvectors do not have a physical meaning with respect to the underlying fiber populations.

6.2.1 Simulations

To illustrate the concepts of the multi-fiber visualizations and to demonstrate the benefits over conventional tensor-based visualizations, we have created a toy example, where a configuration of three crossing neural fiber bundles has been simulated. It is designed in such a way that one bundle has a smaller cross-section, so that there are regions with both two and three fiber bundles intersecting each other, all crossing orthogonally (Fig. 6.2a,b). To demonstrate the difference between the multi-fiber hyperstreamlines and streamribbons, another simulated phantom was designed in which not all populations cross at 90° angles (Fig. 6.3a). Three fiber bundles were simulated, with two fiber populations crossing orthogonally (oriented inferior-superior and left-right) and one population oriented largely along the anterior-posterior axis. Defined in a spherical coordinate system, the orientations are: 1) inferior-superior, with azimuth angle $\theta=0^\circ$ and polar angle $\phi=90^\circ$; 2) left-right, at $\theta=90^\circ$ and $\phi=0^\circ$; and 3) mainly anterior-posterior, at $\theta=27^\circ$ and $\phi=0^\circ$. Both phantoms were generated with the following parameters: 60 gradient directions, a b-value of 2500 s/mm^2 , and each single fiber population having a fractional anisotropy and mean diffusivity of 0.7 and $0.7 \times 10^{-3} \text{ mm}^2/\text{s}$, respectively (Leemans et al., 2005). For regions with multiple fiber popula-

tions, we assume that there is only slow exchange between these populations (Alexander et al., 2001).

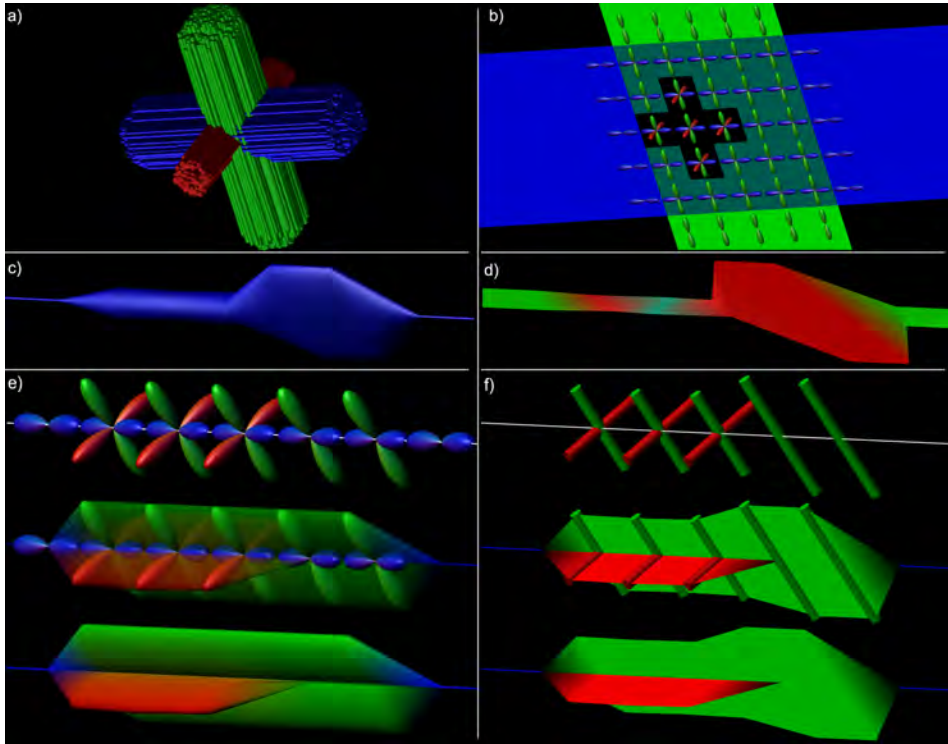


Figure 6.2: The global topology of a simulated fiber phantom is illustrated in a), with streamtubes color-encoded by the tract direction. The configuration was designed to contain distinct regions where two and three fiber populations intersect. fODF glyphs in this region clearly show these crossing populations (b). A single tract from the blue fiber bundle is shown in c) as tensor-based hyperstreamline and in d) as tensor-based streamribbon. In e), local fODF glyphs are shown along its trajectory, and a step-by-step creation of the hyperstreamline that envelops these glyphs. In f), the cylindrical glyph objects represent the distinct fODF peaks and the streamribbon is a continuous visualization of these peaks.

6.2.2 In vivo diffusion MRI data

Diffusion MRI datasets were acquired from two healthy subjects (a 25 year old female and a 25 year old male) on a Philips 3 T Achieva MR system (Philips Healthcare, Best, the Netherlands) using a single-shot spin echo EPI sequence, with one $b=0$ image and 60 diffusion-sensitizing directions acquired at a b -value of 2500 s/mm^2 (Jones et al., 1999a), using a SENSE acceleration factor of 2. The acquisition matrix of 112×112 was

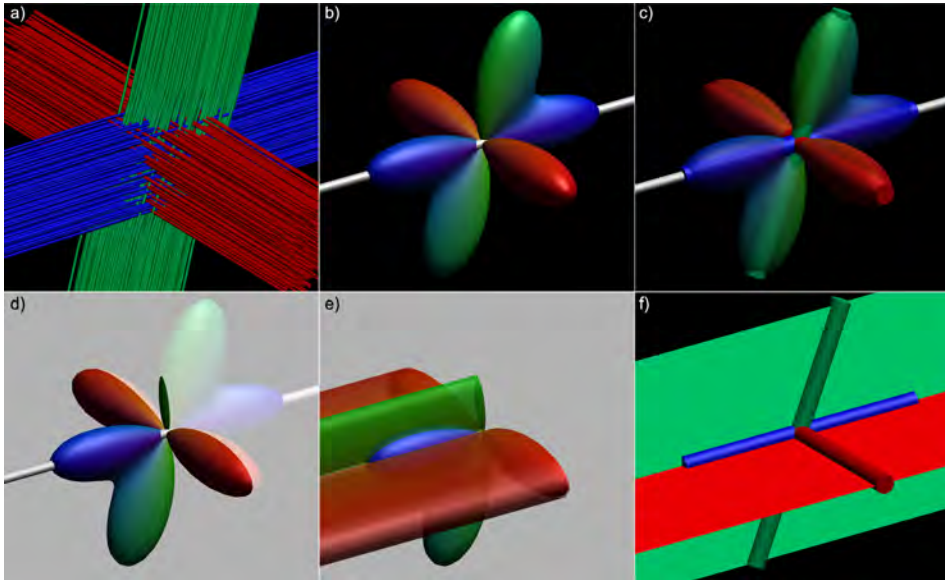


Figure 6.3: A single tract-of-interest from a simulated fiber configuration (a) is created as hyperstreamline (b-e) and streamribbon (c,f). In b), the fODF at a location along this tract (white tube); c) fODF shown semi-transparently with its peak orientations; d) fODF shown with the plane perpendicular to the tract orientation, delineating the amplitude of the hyperstreamline; e) the hyperstreamline; f) streamribbons are created of the fODF peaks that do not correspond to the tract orientation.

zero-filled to 128×128 with a field-of-view of $224 \times 224 \text{ mm}^2$, and 70 contiguous axial slices with thickness 2.0 mm were acquired. Sequence timings were $TE = 107 \text{ ms}$, $TR = 10.3 \text{ s}$ and the average SNR for both datasets was 20 (estimated from regions in the centrum semiovale; Sijbers and den Dekker, 2004). The subjects gave informed consent to participate in this study.

Prior to data analysis, the datasets were corrected for eddy current induced geometric distortions and subject motion by realigning all diffusion-weighted images to the $b=0$ image using `elastix` (Klein et al., 2010), with an affine transformation model and mutual information as the cost function (Pluim et al., 2003). In this procedure, the diffusion gradients were adjusted with the proper b -matrix rotation (Leemans and Jones, 2009).

6.2.3 Diffusion modeling and tractography

Examples of the proposed visualizations will be shown for two diffusion reconstruction methods: CSD (Tournier et al., 2007) and QBI (Tuch, 2004). CSD estimates a response

function of a single fiber population, assumes that all individual fiber populations are characterized by this function, and then deconvolves the acquired signal intensities to resolve the fODF (further details can be found in Tournier et al., 2007). In the QBI method employed, the acquired diffusion weighted signal is modeled using spherical harmonics, followed by the approximation of the dODF using the Funk-Radon transform (Tuch, 2004). Note that with these examples, we do not intend to provide a quantitative comparison between QBI and CSD, but rather demonstrate that our multi-fiber visualizations can be applied to different diffusion approaches. As such, standard QBI and CSD parameters were used as reported previously: Tuch (2004) and Descoteaux et al. (2007) for QBI; and Tournier et al. (2007) and Jeurissen et al. (2011) for CSD. Noteworthy is that, in contrast to the fODF (e.g., see Raffelt et al., 2012; Dell’Acqua et al., 2012), the dODF calculated with QBI is a spherical probability distribution, and thus normalized to unit probability over the sphere. To account for this difference, we have used two scaling approaches that yield comparable ODFs, both in their glyph representation and in their basis to form the hyperstreamline. For the dODF, standard “min-max” scaling was used, as proposed by Tuch (2004). For the fODF scaling, we have used a similar scaling, here called “normalization scaling”, where the amplitudes of the fODF in each voxel are scaled such that the maximum amplitude is equal to one. Deterministic fiber tractography was performed using the peak fiber orientations of the ODFs, where the number of unique fiber populations at each location, and their orientations, were computed as described in Jeurissen et al. (2011). ODF peak thresholds were defined as 10% of their maximum value. The maximum number of unique fiber populations was limited to three for all analyses. Fiber tractography using both methods was performed with the *ExploreDTI* diffusion MRI toolbox (Leemans et al., 2009).

6.2.4 Multi-fiber tractography visualization

The conventional representations of fiber pathways are either streamlines (e.g., Basser et al., 2000) or streamtubes (Catani et al., 2002; Zhang et al., 2003). Hyperstreamline and streamribbon approaches were originally designed with the purpose of visualizing the second and third eigenvectors and eigenvalues of the diffusion tensor (Zhang et al., 2003; Atkinson et al., 2007). With the tensor unable to characterize crossing fibers, the tensor-based hyperstreamlines cannot correctly visualize the local architecture. In the following sections, we will present the new multi-fiber tractography visualizations.

Multi-fiber hyperstreamlines

For DTI-based hyperstreamlines, the cross-sectional shape of the hyperstreamline at each tract position is determined by the orientation of the second and third eigenvectors (scaled as a function of the eigenvalues) of the diffusion tensor (Zhang et al., 2003). In the following, we extend this concept for diffusion MRI data with a higher angular

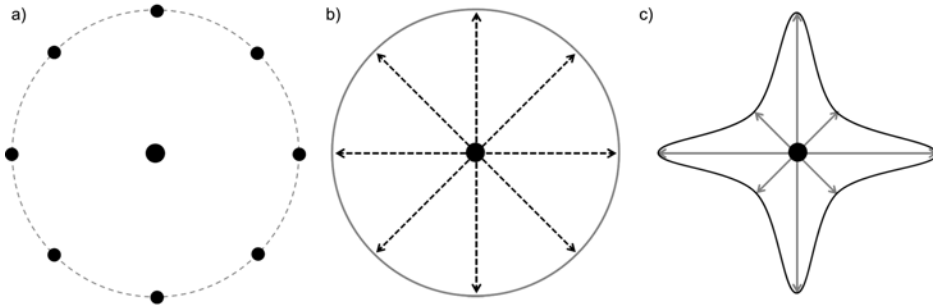


Figure 6.4: Conceptual illustration and example of the creation of a hyperstreamline. For a point \mathbf{r} along the tract, a number of points is defined in a circle around \mathbf{r} perpendicular to the tract orientation \mathbf{t} (a), and vectors from \mathbf{r} to these points are calculated (b). These vectors are then scaled according to the ODF amplitude along these vectors (c), delineating the cross-sectional shape of the hyperstreamline at point \mathbf{r} .

resolution, where the cross-sectional shape is defined by the ODF, instead of the tensor. For the “multi-fiber hyperstreamline”, the local shape of the hyperstreamlines is then determined by the three-dimensional ODF profile. At each tract position, \mathbf{r} , we define a circle with its center in \mathbf{r} and lying in the plane perpendicular to the tract orientation, \mathbf{t} (see Fig. 6.4a). The vectors from \mathbf{r} to the points on this circle (Fig. 6.4b) are then scaled by the ODF amplitude along these orientations to delineate the cross-section of the hyperstreamline (Fig. 6.4c). For a more detailed description, please refer to the pseudocode in Appendix 6.A. An example hyperstreamline of the simulated fiber phantom of Fig. 6.3a is shown in Fig. 6.3b-e. Notice that, by visualizing the ODF amplitude perpendicular to the tract orientation, the maximum ODF amplitude crossing the tract is not displayed if populations cross at other angles than 90° .

Multi-fiber streamribbons

Tract ribbons have initially been proposed to visualize the axial asymmetry of the diffusion tensor (Atkinson et al., 2007). In this work, we introduce “multi-fiber streamribbons” by reducing the ODFs along the tract to their principal peak orientations. In this way, streamribbons can be used for efficient visualization with a lower rendering complexity than streamtubes or hyperstreamlines (Atkinson et al., 2007; Leemans, 2011). For each ODF peak orientation that does not correspond with the tract orientation, a streamribbon is created—as shown in Figs. 6.2f and 6.3c,f—which means that in the case of three unique peaks, two streamribbons are created. For each existing ribbon, the angular deviation is calculated from the current ribbon orientation to the ODF peak or peaks at the next vertex along the tract. The ribbon is then connected to the peak that deviates the least. In those voxels where the ODF indicates a single fiber pop-

ulation, the streamribbons converge naturally to a streamline (Fig. 6.2f). Appendix 6.B presents pseudo-code on how the streamribbons are created.

Color-encoding

The conventional coloring of streamlines and -tubes shows the tract orientation at each vertex, providing additional visual cues about the tract orientation such as the “direction encoded color” (DEC) map proposed by (Pajevic and Pierpaoli, 1999). This coloring according to the diffusion orientation can still be used for our proposed visualizations, further enhancing the interpretation of the local microstructural organization. To this end, we propose such color-encoding scheme, termed ‘ODF color-encoding’, where:

- All tract vertices with a single fiber population are colored according to the tract direction;
- Vertices with two unique fiber populations, where one population corresponds to the tract direction, are colored according to the orientation of the population crossing the tract;
- Vertices with three or more populations have the individual points on the hyper-streamline circumference colored by the orientation of that point with respect to the tract vertex.

As an alternative to the proposed ODF color-encoding, where the orientations of the fiber populations are highlighted, it is also possible to highlight the number of fiber populations. This can be used to distinguish between regions with one, two, or more than two fiber populations more clearly (as also shown in Jeurissen et al., 2012)).

6.2.5 In vivo tract visualizations

In vivo examples of multi-fiber tractography visualization are shown for fiber tracts from the lateral projections of the corpus callosum (abbreviated as latCC), the corticospinal tract (CST), and the arcuate fasciculus (AF), all of which are known to intersect other WM structures (Tuch et al., 2003). In addition, tracts from the bilateral cingulum bundles are shown, as an example of fiber bundles with a relatively small cross-sectional area. To maintain the focus on the additional information conveyed by our new visualization approaches, these examples are only shown for the CSD results. For a specific configuration of AF pathways, however, we provide an example illustrating that both QBI and CSD based tractography results can benefit from multi fiber visualizations.

6.3 Results

6.3.1 Simulations

Fig. 6.2a shows an example fiber configuration, where there are regions with single fiber populations as well as regions with two and three fiber populations crossing, as can also be seen from the fODF glyphs (calculated from CSD) shown per voxel in Fig. 2b. The tensor-based hyperstreamline and streamribbon are shown in Figs. 6.2c and 6.2d, respectively. Creation of the hyperstreamline is shown in Fig. 6.2e. When displayed at each vertex of the fiber tract, the fODF glyphs in Fig. 6.2e illustrate the local microstructure, with one or two populations crossing the fiber tract, depending on the location along the tract—as can be verified from Figs. 6.2a and 6.2b. The step-by-step creation of the corresponding hyperstreamline is also shown in Fig. 6.2e, where the ODF color-encoding further highlights the architectural organization. The multi-fiber streamribbon is created by continuously connecting the peak orientations and magnitudes of the populations crossing the fiber tract. In Fig. 6.2f, the peak orientations are shown along the tract as cylinders with the streamribbons connecting these peaks and for two different color-encodings proposed in this work. Notice that the tensor-based visualizations (Figs. 6.2c and 6.2d) show some contrast along the tract between regions with one, two, and three fiber populations, but they do not visualize the orientations of the underlying fiber populations in an unambiguous way. The multi-fiber based visualizations, on the other hand, do show the fiber orientations very clearly, both as hyperstreamline and as streamribbons.

The simulated fiber phantom in Fig. 6.2 has three fiber populations that are oriented perpendicularly. Thus, the peak orientations were perpendicular to the tract direction, where the hyperstreamline envelops the full ODF profile (Fig. 6.2e). However, if populations are no longer orthogonal, the ODF profile perpendicular to the tract no longer describes the peak amplitude of the ODF. As a result, the hyperstreamline and streamribbons show different complementary characteristics of the fiber populations (as can be seen when comparing Figs. 6.3e and 6.3f).

6.3.2 In vivo tract visualizations

In the following subsections, in vivo examples of fiber bundles that pass through regions of complex fiber architecture are shown, demonstrating the additional information visualized with these new multi-fiber tractography representations.

Corpus callosum

Fiber tracts from the lateral projections of the corpus callosum (latCC) are displayed in Fig. 6.5. Hyperstreamlines are shown for subject one in an axial orientation (a) and

for subject two in a coronal orientation (b); with the tract segment in the boxed regions enlarged in c) and d), respectively. Fig. 6.5c,d also show that the ODF amplitudes perpendicular to the fiber tract pathway provide the cross-sectional shape of the multi-fiber hyperstreamline. When starting at the mid-sagittal region, the tract pathway first crosses the CST and then the AF, both clearly depicted in the ODF glyphs and the hyperstreamlines as the (blue/purple) inferior-superior and (green) anterior-posterior fiber populations, respectively. As can most clearly be observed in the hyperstreamline that is colored by the number of ODF peaks—indicated by the red arrow in d)—there are regions along this tract with three fiber populations. In c) and d), these tract segments can also be observed as the multi-fiber streamribbons.

Cortico-spinal tracts

Fiber tracts from the CST are shown in Fig. 6.6. Global overviews of the mid-sagittal slice of the brain with the hyperstreamline are shown in a) for subject one and e) for subject two. Fig. 6.6b,c shows how a small segment of the tract in the region of the pons—see yellow rectangle in a)—is visualized as a multi-fiber hyperstreamline. In d), the corresponding streamribbon is illustrated. For subject two, the hyperstreamline and streamribbon are shown in e-h). According to the known anatomy in this region, there are clear indications for left-right oriented transverse pontine fiber populations (also seen in Tournier et al., 2011; Aggarwal et al., 2013) and front-back oriented fiber populations of the middle cerebellar peduncle (Catani et al., 2008). More superiorly along the CST one can also clearly observe anterior-posterior oriented fiber populations crossing the tract, indicated by the red arrows in a) and e).

Arcuate fasciculus

Fig. 6.7 shows a multi-fiber visualization of the left arcuate fasciculus (AF). The hyperstreamline and streamribbon representations both illustrate the orientations of the fiber populations crossing the AF in accordance with the known local architecture. Enlargements of the indicated region—yellow rectangle in a)—are shown sagittally (b,c) and axially (d,e), clearly indicating that there are two other fiber populations (latCC in reddish and CST in bluish) crossing the AF in this region. A coronal view of the same tract segment is presented in d), showing the amplitudes of the fiber populations of the latCC and CST and their continuity along the tract pathway in more detail. As can be observed in Fig. 6.8, there are also anterior-posterior oriented fiber populations intersecting the AF at its more posterior part, corresponding with the inferior fronto-occipital fasciculus (Catani et al., 2008).

To demonstrate that multi-fiber tractography visualizations can depict the microstructural architecture not only for a single tract pathway but also for whole fiber bundles, Fig. 6.9 shows a comparison of the left AF between standard streamtubes (a), multi-

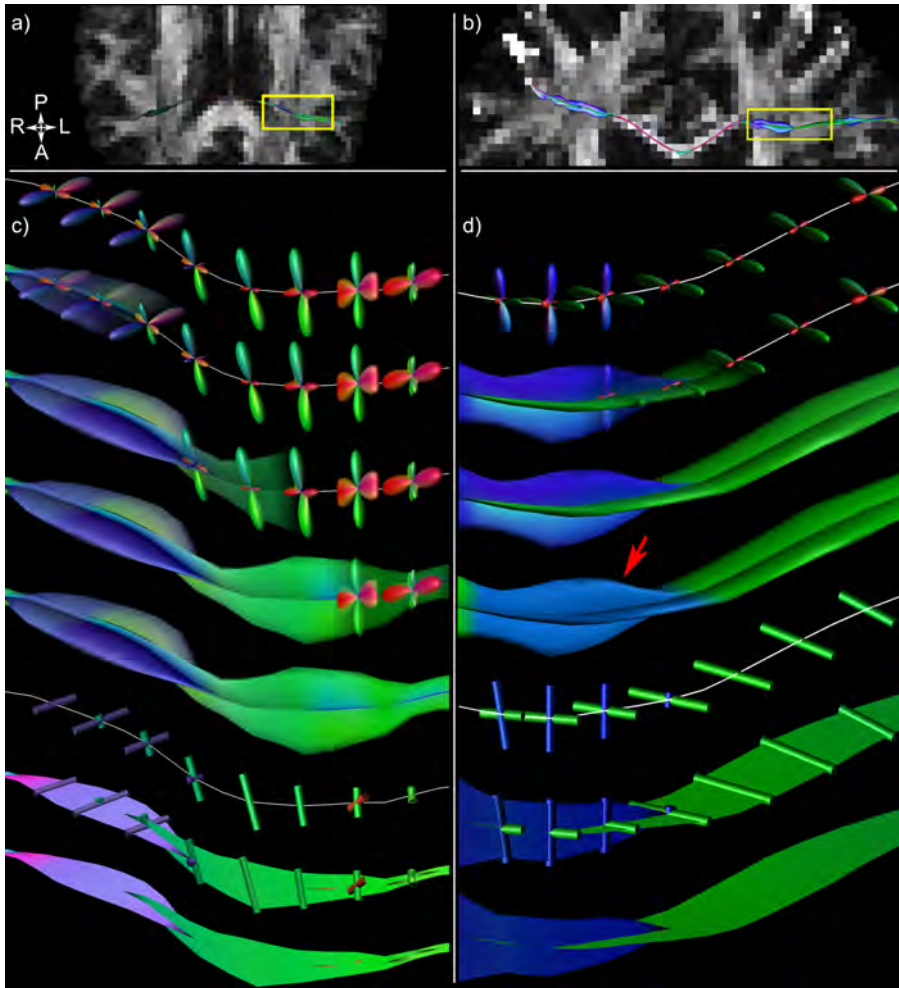


Figure 6.5: Axial (a) and coronal (b) slices of the brain of the two subjects (subject one: a) and c); subject two: b) and d)) are shown, with a tract from the lateral projections of the corpus callosum (latCC) visualized as multi-fiber hyperstreamline. The boxed regions in a) and b) are enlarged in c) and d), respectively, showing the construction procedures of the hyperstreamline and streamribbon. Starting from the middle of the brain, the fiber tracts first cross the cortico-spinal tracts (CST) before intersecting the arcuate fasciculus (AF) more laterally. From the visualizations in c) and d), regions with three distinct fiber populations can be seen along the tracts, i.e., where the AF and CST both cross the latCC pathway. This is highlighted when color-encoding the hyperstreamline by the number of ODF peaks (red arrow).

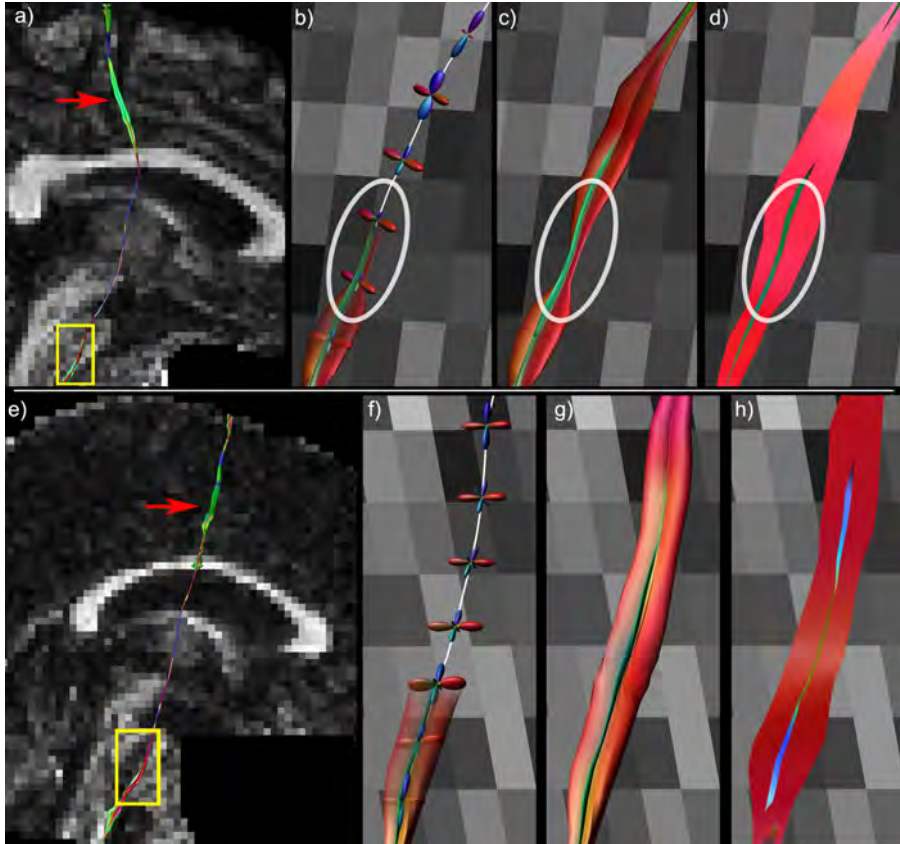


Figure 6.6: A global overview of the mid-sagittal slice of the brain with hyperstreamline is shown in a) for one subject. A segment of the cortico-spinal tract (CST) in the region of the pons—indicated on a) by the yellow rectangle—is enlarged in b-d). The multi-fiber hyperstreamline is shown in b) and c), indicating left-right (LR, red) and anterior-posterior (AP, green) oriented fiber populations. This can also be seen from the streamribbon representation in d). The white ellipses (b-d) highlight a region where the LR-oriented fibers are not perpendicular to the tract pathway, resulting in a hyperstreamline that does not reflect the full ODF amplitude, whereas the streamribbons do. For the second subject, f-h) show the multi-fiber hyperstreamline and streamribbon representations of a small segment of the tract pathway indicated by the yellow rectangle on e). Note that more superior along the CST one can detect prominent AP-oriented fiber populations that correspond to the arcuate fasciculus (red arrows in a and e).

fiber hyperstreamlines (b), and streamribbons (c) with orientation color-encoding. In d), the conventional streamtube representation is used, but with the orientation color-encoding from the ODF as shown in b).

When generating tractography data with different methods, subtle differences between them can be observed using the proposed visualization approaches (as illustrated in Fig. 6.10). A part of the right AF is shown with QBI-based tractography (a) and CSD-

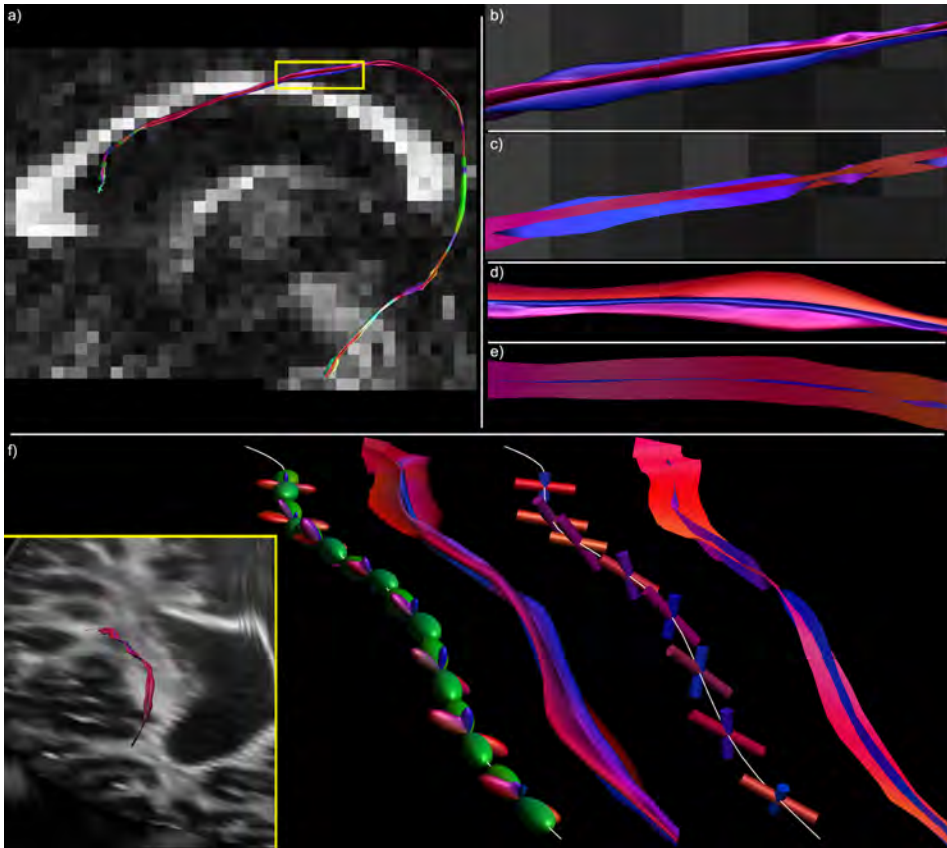


Figure 6.7: a) An example of the multi-fiber hyperstreamline and streamribbon is shown for a single tract of the arcuate fasciculus (AF). Tract segment indicated by the yellow rectangle in a) is shown in a sagittal (b,c) and axial (d,e) view, for both the hyperstreamline (b,d) and streamribbon (c,e). The same segment is shown in f) from a near coronal view angle, indicating (from left to right): the ODF glyphs along the tract; the corresponding multi-fiber hyperstreamline; the glyph objects representing the ODF peaks; and the corresponding multi-fiber streamribbon. The inset depicts the oblique viewing angle.

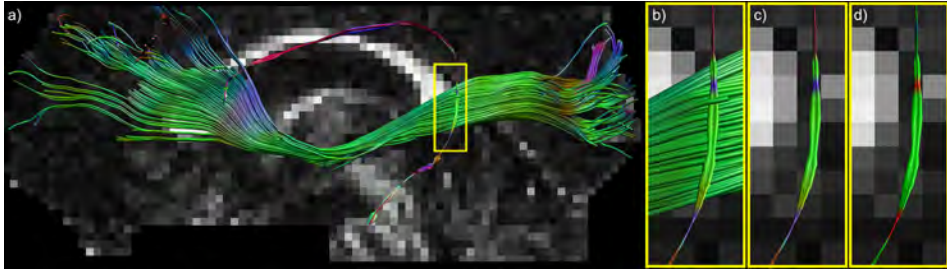


Figure 6.8: In a), the inferior fronto-occipital fasciculus is shown crossing a posterior part of the arcuate fasciculus (AF). Enlarging the region where these pathways cross (b) clearly illustrates that the hyperstreamline visualizes this anterior-posterior fiber population. For detailed interpretation, the hyperstreamline is shown in c) without the bundle. In d), the hyperstreamline is colored by the number of unique fiber populations—where red indicates 1, green is 2, and blue more than 2 fiber populations.

based tractography (b) with the conventional tract representation. For each approach, a single pathway is shown as a QBI hyperstreamline (c) and a CSD hyperstreamline (d), highlighting the subtle differences in ODF reconstruction between QBI and CSD in the superior portion of the AF as indicated with the red arrow. In e) and f), the AF pathways (green) are shown in combination with the post-hoc reconstructed latCC trajectories (red) in the region of the red arrow, confirming the intersection of (part of) the latCC pathways.

Cingulum

For the bilateral cingulum bundles (Fig. 6.11a), one tract pathway has been selected towards the bottom of the cingulum, i.e., an “edge” tract located more towards the interface with the corpus callosum (red in Fig. 11b), and one tract pathway that is located more at the “center” of the bundles (green in Fig. 6.11b). These “center” and “edge” tracts are shown in Figs. 6.11c,d and 6.11e,f respectively, from a frontal-superior angle with the same hyperstreamline settings. A strong difference in the width of the hyperstreamlines can be observed between the center (d) and edge (f) tracts, reflecting a marked difference in fiber architecture in these different regions of the cingulum. Notice that even the “center” tract shows left-right oriented populations along most of its trajectory.

6.4 Discussion

In this work, we have developed multi-fiber tractography visualization strategies that combine information of local white matter fiber architecture—e.g., the information captured by the dODF or fODF—with global anatomical information from fiber trac-

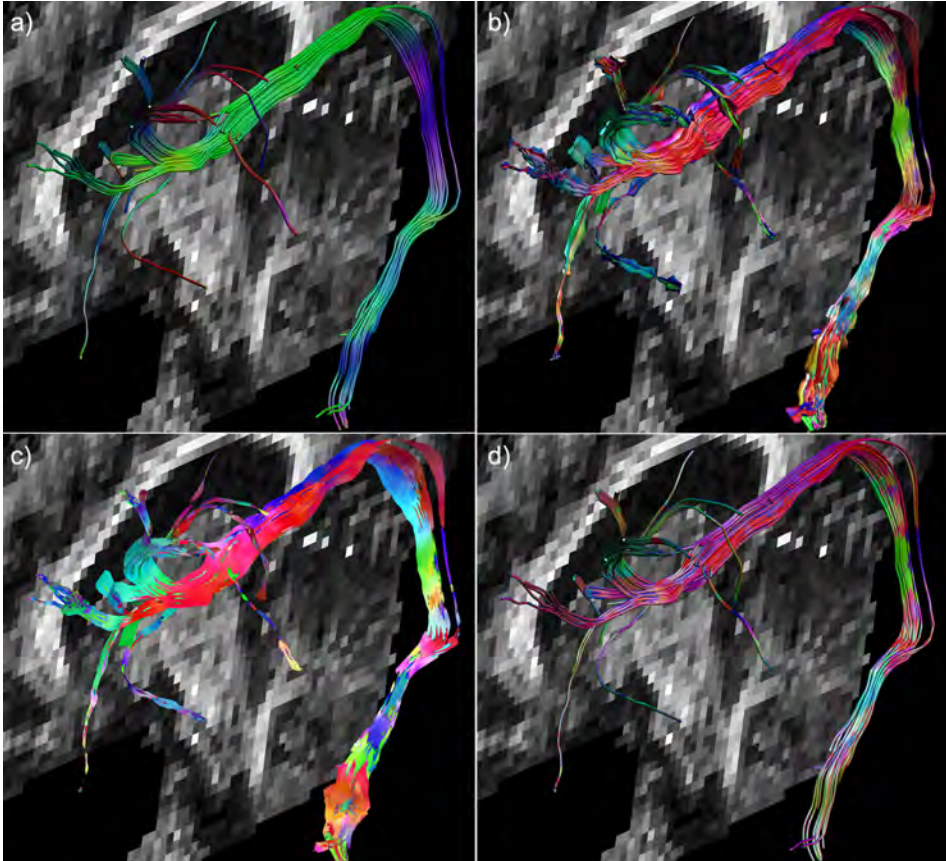


Figure 6.9: In a), the arcuate fasciculus (AF) is shown with its conventional streamtube representation and with color-encoding according to the tract direction. The multi-fiber hyperstreamline and streamribbon with the orientation color-encoding according to the ODF are shown in b) and c), respectively. Standard streamtubes have been visualized in d), but then using the ODF-based color-encoding used in b).

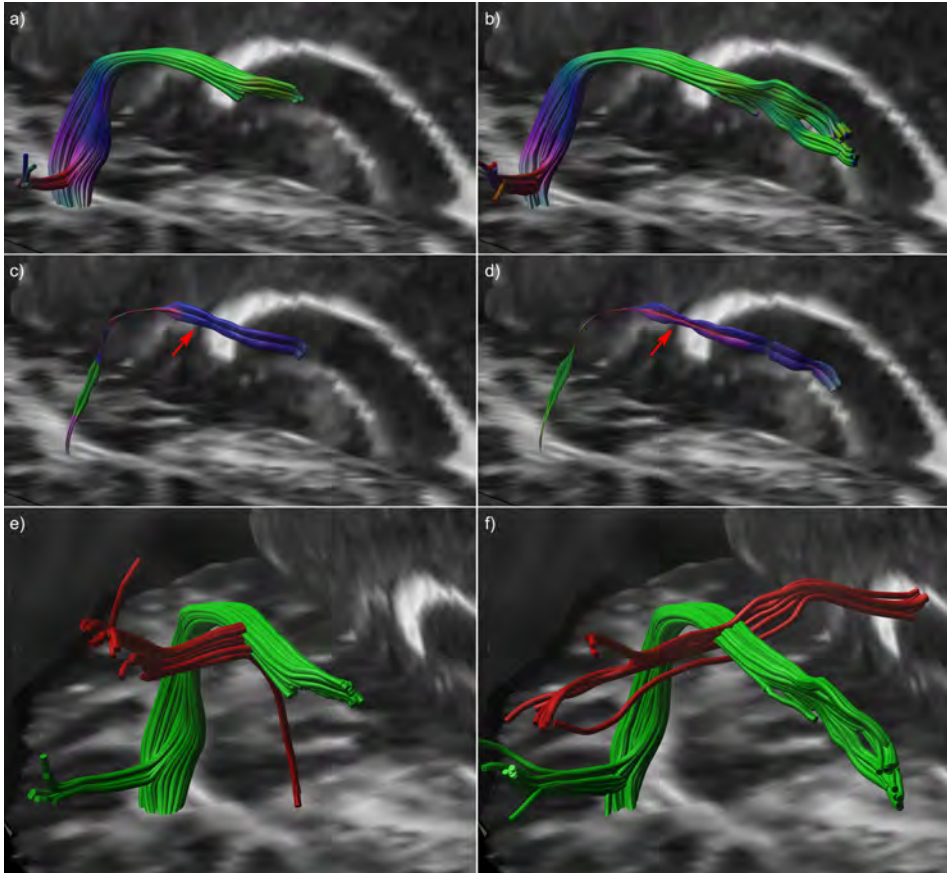


Figure 6.10: Hyperstreamline examples to compare different methods. The reconstructed arcuate fasciculus (AF) is shown for QBI (a) and for CSD (b). Single tracts from the QBI bundle and CSD bundle are shown as a multi-fiber hyperstreamline in c) and d), respectively. This visualization, both in cross-sectional shape as well as color-encoding, highlights an important difference between the two used methods. For CSD (d), clear left-right fiber populations (red) can be seen crossing the AF (indicated by the arrow), whereas QBI (c) does not display these populations: these lateral projections of the corpus callosum (latCC) could not be detected with QBI. Verification can be seen in e) and f), where the AF is shown in green and the latCC in red (seeded lateral to the AF it should target the corpus callosum, as seen in f).

tography, so as to create more complete representations of the microstructural organization of the WM. These visualizations will be made freely available to the community, as part of the *ExploreDTI* diffusion MRI toolbox (Leemans et al., 2009).

The two proposed approaches, multi-fiber hyperstreamlines and multi-fiber stream-ribbons, visualize different properties of the ODFs, with the most pronounced difference in situations where fiber populations are not orthogonal (as illustrated in Fig. 6.3). In vivo, when fiber population orientations will generally not be orthogonal, the two methods can be used to visualize complementary information from the ODF. An example of this can be observed in the pons, highlighted by the white ellipse in Fig. 6.6b-d. From the streamribbon (d), it is clear that the magnitudes of the fiber populations in the shown segment do not differ much. This can be verified from the ODF glyphs visualized along the tract (b), but this is not apparent in the hyperstreamline (c). In the

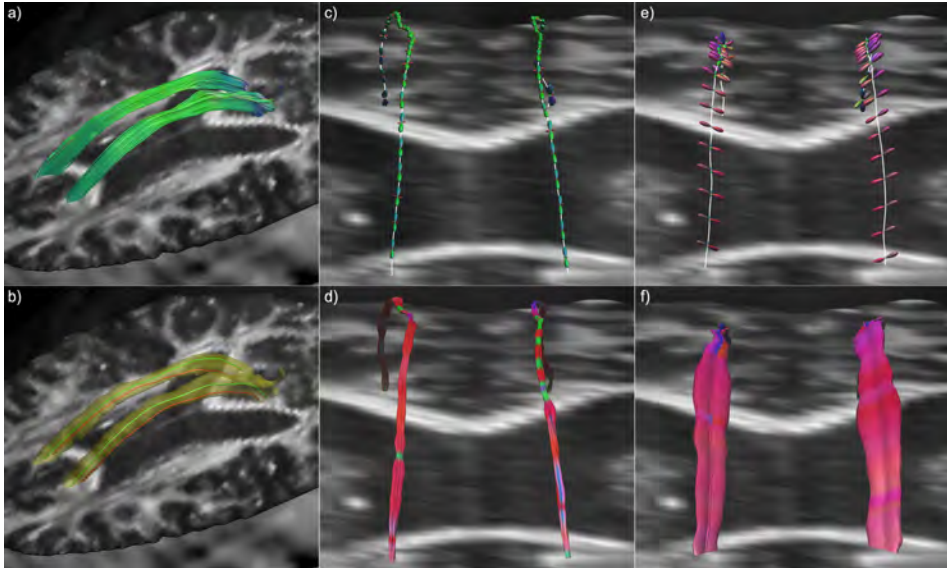


Figure 6.11: Superior segment of the bilateral cingulum bundles (a). From these full bundles—shown in b) as a yellow haze for anatomical reference—one tract has been selected at the center of each bundle (shown in green in b) and one tract at the interface of the corpus callosum (red in b). These “center” (c and d) and “edge” (e and f) tracts have been with the fODF glyphs along their trajectories (c and e) and as hyperstreamlines (d and f). Strong difference between the magnitudes of the left-right populations can be observed between c)-d) and e)-f). From the ODFs in c) it is difficult to interpret the continuity of orientation and magnitude of the left-right populations; whereas this is very easy from the hyperstreamlines in (d).

superior part of the AF (Fig. 6.7d,e), a similar difference in visualization of ODF properties can be seen between the hyperstreamline and the streamribbon. In general, for interpretation of the ODF peak magnitudes, the streamribbons are preferable. However, due to the two-dimensional nature of a ribbon, investigating the specific configuration of the streamribbons can be non-trivial. By reducing of the full ODF to their peak orientations, the information about the shape of the peaks is discarded, making it impossible to distinguish between sharp or very broad ODF peaks. The three-dimensional nature of the hyperstreamlines lends itself to more intuitive interpretations of the local architecture. In some situations, for instance in the absence of free water diffusion, the fODF is modeled as a very spiky function (e.g., Jansons and Alexander, 2003; Ye et al., 2012). In such cases, where fODF lobes resemble delta-peaks, the hyperstreamlines essentially “collapse” to streamribbons.

By comparing multi-fiber hyperstreamlines of fiber tracts reconstructed with two different approaches to estimate the ODF, we have demonstrated that this method can be used to show subtle differences between the results of the two methods that with conventional fiber tractography visualizations would have gone unnoticed. In Fig. 6.10, for instance, the latCC pathways were interdigitating the AF in only one of the diffusion methods as suggested by the hyperstreamlines. The validity of this observation was backed up by finding a difference in configuration of the latCC pathways between both approaches. However, it should be clear that in this work, it was not our aim to contrast different diffusion reconstruction methods in terms of “accuracy” or “validity”, but purely to illustrate that the proposed multi-fiber hyperstreamlines can be an exploratory means to investigate these methods more intuitively.

The proposed multi-fiber hyperstreamlines and streamribbons can be extended to any multi-fiber diffusion model. For instance, one could opt to display the ball-and-multiple-stick model (Behrens et al., 2007) using a streamribbon for each of the “stick” compartments when more than one “sticks” are present. Alternatively, the multiple-tensor approach (Peled et al., 2006) can be visualized by combining those diffusion ellipsoids that do not belong to the tract itself as hyperstreamlines or by using the principal diffusion directions to construct streamribbons.

When one is presented with a global view of an entire fiber bundle as in Fig. 6.9, distinguishing the shape of the individual hyperstreamlines becomes complicated. The amount of information in these hyperstreamlines and streamribbons could result in an image that is too cluttered for easy interpretation. As a more subtle alternative to visualize local architectural information, without making the images too complex to interpret, the hyperstreamlines can be reduced to simple streamtubes, while maintaining the ODF color-encoding. In addition, streamtubes have a lower computational

complexity compared with the multi-fiber hyperstreamlines, which could be another motivation to use the conventional streamtube shape.

The initial hyperstreamline and streamribbon approaches were designed with the purpose of visualizing the diffusion tensor in more detail (Zhang et al., 2003; Atkinson et al., 2007). Hyperstreamlines have also been used to convey information on the uncertainty in fiber orientation, where the width of the hyperstreamline represents the local “cone of uncertainty” of the first eigenvector (Jones, 2003; Jones et al., 2005b). Alternatively, streamsurfaces have been proposed to visualize regions of planar diffusion as surface structures (Zhang et al., 2003). For instance, at interfaces between fiber bundles where partial volume effects cause the diffusion profile to be more planar in shape, these streamsurfaces create a virtual delineation of the edges of these fiber bundles, aiding in the distinction between different fiber structures. However, measures of planar diffusion, as used in these streamsurfaces and in conventional streamribbons, are not specific for the underlying tissue microstructure and are heavily affected by the presence of crossing fiber architecture (e.g., see Ch. 2). By contrast, the proposed multi-fiber hyperstreamlines and streamribbons give more specific representations of the microstructural information obtained from diffusion MRI data.

Previous work on visualization of multi-fiber diffusion data has mainly focused on efficiently displaying the ODF glyphs not only locally but in larger regions of the brain. Interpretation of ODF profiles of each voxel in an entire imaging slice can become difficult by the immense amount of data visualized. Reducing the ODF to its peak orientations yields more easily interpretable data in such situations, with the additional benefit of being less memory-consuming and more rendering-efficient (Leemans, 2011). With the development of advanced interactive and exploratory tools for visualizing ODF glyphs, however, it has become possible to visualize the full ODFs efficiently in large quantities, e.g., for an entire slice (Shattuck et al., 2008; Peeters et al., 2009). Recent work has focused on representing the ODF glyphs at discrete points along a tract (Kezele et al., 2008; Prckovska et al., 2011), whereas the multi-fiber hyperstreamlines proposed in this work provide a continuous and, hence, a more intuitive representation of the data. To further emphasize this difference, an example of the discrete and continuous way to visualize a fiber trajectory is given in Fig. 6.12 using both DTI-based and multi-fiber reconstructions. Plotting the first eigenvectors yields the discrete version of a reconstructed tract, but the tract itself gives a continuous and, therefore, more intuitive representation of the data. This is also the case for the multi-fiber hyperstreamline, which—being also continuous—gives a more complete view compared to showing ODF glyphs only at discrete locations along the tract pathway. This observation is supported by the *in vivo* examples shown in Figs. 6.5c,d, 6.7f, and 6.11, where data interpretation for one continuous 3D object, the hyperstreamline, is more

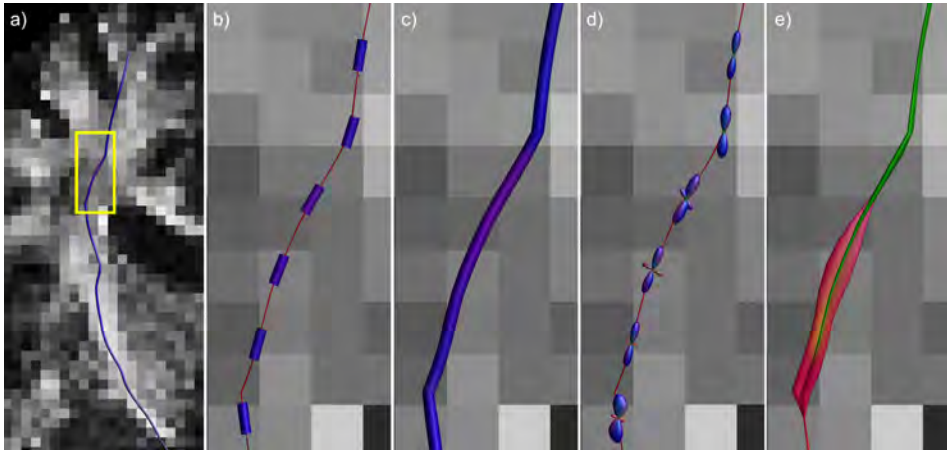


Figure 6.12: The difference between discrete and continuous visualization. A coronal overview of the tract to be visualized is seen in a), with the main eigenvector at discrete locations along the tract (b) and the tract itself (c). Analogous to b) and c), d) and e) show the fODF glyphs at discrete locations along the tract and the multi-fiber hyperstreamline, respectively. The continuity is difficult to grasp from the glyphs alone (b and d), whereas the continuous representations (c and e) give a more intuitive feel, are easier to interpret, and represent a more complete picture of the underlying WM pathway.

straightforward than for the individual 3D objects, which can obscure each other. Furthermore, as can be seen in Figs. 6.5a,b, 6.6a,e, hyperstreamlines can directly pinpoint the main areas of crossing fibers, where individual glyphs are less powerful. This observation can also be made in Fig. 2b of Kezele et al. (2008).

When trying to visualize the fiber architecture along a specific fiber tract, alternatives to the multi-fiber visualization method proposed here are possible. Conceptually, it might be very helpful to show which fiber pathways cross a specific tract-of-interest, as this shows information on the fiber organization at this tract-of-interest. However, showing these perpendicularly crossing pathways can clutter the image, obscuring the view of the tract-of-interest, as shown in Fig. 6.13a. The proposed methods provide a more succinct representation of the local tissue architecture, as shown in Fig. 6.13b for the multi-fiber hyperstreamline.

An important and promising clinical application of fiber tractography is surgical planning. Since the initial case reports in the literature (e.g., Coenen et al., 2001), its use in surgical planning is steadily growing. A recent overview on the use of tractography has foretold a promising future, stating that it “*will become established as a routine clinical investigation in many centers in the coming years*” (Ciccarelli et al., 2008). In

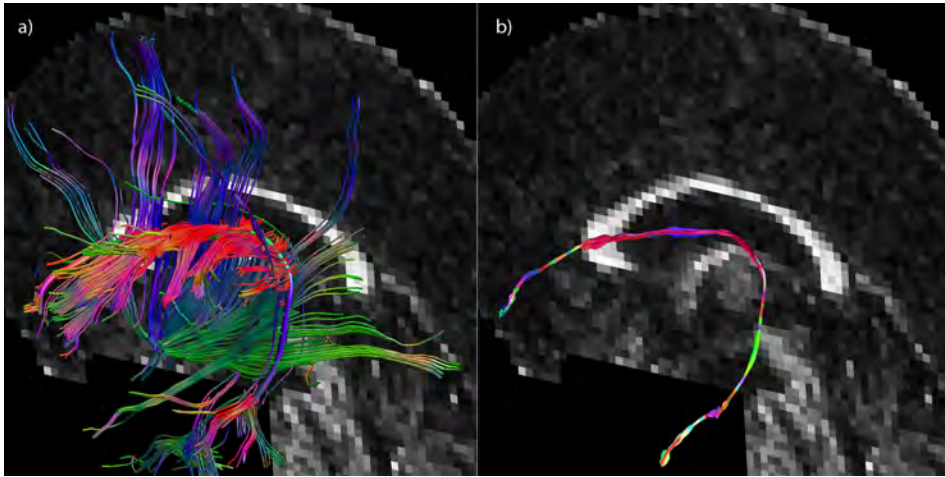


Figure 6.13: A single tract from the arcuate fasciculus (AF), the same as in Figures 6.7 and 6.8. a) Tract shown as a thick streamtube with fibers crossing this tract of interest shown as thinner streamtubes. b) Tract shown as multi-fiber hyperstreamline.

this prospect, Ciccarelli et al. (2008) believe that improvements in tractography visualizations are of paramount importance to fully benefit from tractography information. With several studies already demonstrating that post-surgical outcome is improved if fiber tracking is used in pre-operative planning (Witwer et al., 2002; Thudium et al., 2010), and predicting, to some degree, the clinical improvements after treatment (Bagadia et al., 2011; Castellano et al., 2012), any improvements in visualization of fiber tracts and local tissue microstructure can only be considered beneficial for surgical outcome.

Recent research shows that the vast majority of WM voxels contains more than one fiber population with approximately 25 to 50% containing more than two fiber populations, depending on the specific diffusion model (Jeurissen et al., 2012). This makes the use of ODF-based methods less of a luxury and more a necessity, both in biomedical research and clinical applications (e.g., Brunenberg et al., 2012; Metzler-Baddeley et al., 2012; Reijmer et al., 2012, 2013a; Kuhnt et al., 2013). More specifically, ODF-based multi-fiber tractography is beginning to show improved clinical results over tensor-based tracking, in the presence of tumors (Kuhnt et al., 2013) and in surgical target localization for deep brain stimulation (Brunenberg et al., 2012), which further stresses the need for multi-fiber visualization approaches.

In conclusion, we have shown that multi-fiber tractography visualizations can display the local fiber architecture along fiber trajectories, combining the detailed tissue char-

acterization captured in the ODF with the global anatomical information from multi-fiber tractography. These new visualization approaches create a more complete picture of the WM microstructure for tracts that traverse through areas of complex fiber configurations. By facilitating the interpretation of tractography data, these multi-fiber hyperstreamlines and streamribbons may improve our understanding of white matter characteristics.

Appendix 6.A

This appendix presents pseudo-code to generate the multi-fiber hyperstreamlines.

```

Calculate tract orientations,  $\mathbf{t}$ , at each tract position,  $\mathbf{r}$ 
Define  $N_{crf}$  as the number of points on the circumference of the
  hyperstreamline, which will define its cross-sectional area at
  each  $\mathbf{r}$ 
for  $n=1$ :number of tracts
  for  $i=1$ :number of positions along tract  $n$ 
    define  $N_{crf}$  points creating a unit circle around  $\mathbf{r}(n,i)$ , in
      the plane perpendicular to  $\mathbf{t}(n,i)$ . % the first and last
      point is the same, Fig. 6.4a
    calculate the vector from  $\mathbf{r}(n,i)$  to these points % Fig. 6.4b
    scale the amplitude of these vectors according to the ODF
      amplitude at  $\mathbf{r}(n,i)$  along these vectors % Fig. 6.4c
  end
end

```

Appendix 6.B

This appendix presents pseudo-code to generate the multi-fiber streamribbons.

```

Calculate tract orientations,  $\mathbf{t}$ , at each tract position,  $\mathbf{r}$ .
for  $n=1$ :number of tracts
  for  $i=1$ :number of positions along tract  $n$ 
    calculate orientations and magnitudes,  $\mathbf{P}$ , of the unique ODF
      peaks % in this work limited to 3
    remove the ODF peaks corresponding with the tract
      orientations % Fig. 6.2f, top
    for  $a=1$ :number of remaining ODF peaks

```

Multi-fiber tractography visualizations

```
    create a vector,  $\mathbf{K}(i,a)$ , from  $\mathbf{r}(n,i) - \mathbf{P}(a)$  to  $\mathbf{r}(n,i) + \mathbf{P}(a)$ 
end
    connect vectors from  $\mathbf{K}(i-1)$  to the vectors from  $\mathbf{r}(i)$  that have
    the smallest angular deviations % (Fig. 6.2f), In case of
    no peaks, the ribbon collapses to a streamline
end
end
```


Chapter 7

General discussion

Parts of this chapter are based on :

S.B. Vos, C.M.W. Tax, and A. Leemans, "Diffusion MRI and fiber tractography: The State-Of-The-Art and its Potential Impact on Patient Management", PET Clinics 8:3 PET/MRI and Evolving Techniques, eds. T.C. Kwee, H. Zaidi, published by Elsevier B.V.;

C.M.W. Tax, S.B. Vos, and A. Leemans, "Checking and correcting DTI data", Practical Handbook of DTI, eds. W. van Hecke, L. Emsell, S. Sunaert, to be published by Springer B.V.

7.1 Discussion of findings

Ever since the first *in vivo* MR measurements of anisotropic water diffusion in neuronal tissue, diffusion MRI is seen as having a great potential to investigate brain development, aging, and pathologies. To fulfill this potential, the entire diffusion MRI pipeline must be considered critically—from defining the research question, through data acquisition, analysis methods, and statistics to interpretation of results. The aim of this thesis was to improve this process, to make diffusion MRI a more sensitive and specific research tool.

Chapters 2 and 3 describe the influence of complex fiber architecture, e.g., crossing or bending fibers, on quantitative measures derived from DTI, including the FA and the MD. Results from these two chapters demonstrate that the interpretation of DTI data is confounded by macrostructural organization, such as the size and shape of fiber bundles. Inclusion of such factors in the final analysis is required to make accurate inferences on changes in tissue microstructure. **Chapter 4** presents a methodological improvement that increases the efficiency of longitudinal DTI studies using tractography-based analyses, possibly increasing the sensitivity of the analyses to detect diffusion changes over time. For optimal fiber tractography results, one would ideally have a higher spatial and a high angular resolution, which both come at the cost of extra scan time. **Chapter 5** gives an overview of the trade-off between having either a high angular resolution (up to 100 diffusion-weighting directions) or a high spatial resolution (up to 1 mm isotropic resolution). For tractography purposes, our results show that the largest gain is achieved by having a higher angular resolution that allows for a better fit of intra-voxel fiber crossings. Over the last decade, more diffusion MRI researchers opt for tractography based on methods beyond the diffusion tensor, i.e., multi-fiber methods. New visualization methods for these tractography results are described in **Chapter 6**, combining the local microstructural information from these diffusion methods with the more global tissue architecture as resolved by tractography.

7.1.1 Quantitative analysis of DTI data

The ‘birth’ of DTI has allowed for a very rapid growth of the use of diffusion MRI in research studies. DTI is still the most widely used approach because of its conceptual simplicity, the possibility to extract intuitive and quantitative scalar diffusion measures, such as the FA and MD, and the relatively short acquisition times (in the order of a few minutes). However, given the conceptual limitations of the diffusion tensor model, i.e., its inability to accurately model the diffusion profile in regions of complex fiber architecture, changes in these quantitative diffusion measures are not merely a reflection of underlying tissue microstructure. As a result, the interpretation of changes in these measures is nontrivial, and it is highly relevant to know what can and cannot

be concluded from observed changes in diffusion. This is highlighted by a recent publication by pioneering scientists in the diffusion MRI field to educate ‘end users’ of DTI on how to interpret their results (Jones et al., 2013).

In the first part of this thesis, several of these important considerations have been described that will help to disentangle true microstructural changes from confounding macrostructural factors. Contrary to general consensus, as illustrated by a recent review stating that “... *the mean ADC is largely unaffected* ...” (Tournier et al., 2011), the axonal configuration has a large effect on the MD as well. Table 2.1 shows a decrease in MD in crossing fiber (CF) voxels compared to single fiber (SF) voxels of roughly 8% in the CST and 3% in the AF. This large effect of tissue geometry on MD values has an effect on statistical testing: regions consisting of SF and CF voxels will have a larger spread in MD values than regions with purely SF voxels, increasing intra-region variance and therefore decreasing statistical power to detect inter-region or inter-subject differences. The planar diffusion coefficient C_p —used in Chapter 2 to distinguish SF voxels from CF voxels—can also be used to correct for the effect of fiber geometry on MD. As shown by Reijmer et al. (2012), including C_p in the statistical model increased the sensitivity to detect correlations between cognitive performance and DTI metrics.

Chapter 3 shows how tractography-based analyses of DTI metrics are influenced by the relative amount of partial volume voxels in fiber bundles. With larger bundles generally having a relatively smaller PVE, fiber bundles of different sizes have different contribution of partial volume voxels—at least for bundles with a convex cross-sectional area. The effects on group comparisons with or without co-varying for bundle volume is apparent from Table 3.1, where different left-right and male-female differences were observed when including volume as a covariate. Similar findings were shown in Metzler-Baddeley et al. (2012), where the fornix was investigated: a thin periventricular fiber bundles prone to CSF-contamination. MD changes were observed in an aging population, which were primarily driven by changes in volume due to atrophy.

Recent work by Szczepankiewicz et al. (2013) addresses the partial voluming issue in more detail. By quantifying the cross-sectional area at constant intervals along each tract they were able to describe the influence of partial voluming more accurately. Their analysis further included diffusion kurtosis parameters, where the radial kurtosis was also found to covary with the size of structures. More importantly, their results show that correction for bundle size, or volume, can increase the statistical power of analyses, which could result in the detection of smaller differences, or lets us use smaller study cohorts to detect the same diffusion differences.

7.1.2 Longitudinal diffusion MRI studies

Longitudinal DTI studies, where diffusion properties are investigated over time in the same study population, have the potential to capture subject-specific changes in microstructure (Johansen-Berg, 2010; Lebel and Beaulieu, 2011). Because longitudinal changes generally yield more specific information than cross-sectional observations, the interest to perform longitudinal DTI studies is increasing rapidly (e.g., Concha et al., 2007; Kumar et al., 2009; Sullivan et al., 2010; Yogarajah et al., 2010; Ljungqvist et al., 2010; Deprez et al., 2012). When following normal brain development in a group of subjects over a timespan of a few years, subtle intra-subject differences are visible that would have been lost in a cross-sectional set-up due to the larger inter-subject differences (Lebel and Beaulieu, 2011). In Lebel and Beaulieu (2011) for instance, a group of subjects was followed over several years of normal development, showing pronounced inter-subject differences in maturation processes. Alternatively, in breast cancer patients, Deprez et al. (2012) observed changes in white matter microstructure after patients finished chemotherapeutic treatment compared to pretreatment. The large inter-subject variation in treatment and physiological response to treatment complicates inter-subject comparison of how the brain is altered during the course of chemotherapeutic treatment. Consequently, investigating changes within individual subjects allows for a better-defined progression of microstructural properties (Deprez et al., 2012).

The benefit of longitudinally designed studies is that it allows to investigate the same area over time within individual subjects, which would yield a high sensitivity to change in that area. The assumption here is that exactly the region is selected at each time point. Given that the inter-subject morphological differences are generally larger than intra-subject differences, conventional methods specifically designed for cross-sectional data analysis, such as traditional voxel-based analysis or TBSS (e.g., Smith et al., 2006; Van Hecke et al., 2008b), may be suboptimal to benefit from the higher sensitivity. Tractography-based analyses that use manual ROI delineation to extract fiber bundles could provide good spatial correspondence in a subject-specific manner. Further, tractography-based analyses are conceptually robust towards growth or atrophy of fiber bundles, with the tract-selecting ROIs being drawn using anatomical landmarks, except in situations of significant non-linear growth or atrophy, or gross pathological changes (such as tumors). The downside to these analysis is the requirement for manual ROI delineation for all bundles on each time point for all subjects, which is a very tedious and time-consuming task. To address this, Chapter 4 presents an Automated Longitudinal Intra-Subject Analysis method (ALISA) that requires manual delineation of each fiber bundle of interest once for each subject, and then extracts these structure from all scans, or time points, of that subject. While this still requires the manual

delineation of fiber structures for each subject, it provides a speed-up factor equal to the number of times each subject is scanned. ALISA provides similar tract segmentations as manual delineations, and preserves the high level of precision that is typical for manual FT segmentations.

Another important, yet preliminary observation from Chapter 4 is that the ALISA method may provide fiber tract segmentations with a higher intra-subject consistency than manual delineations (Figs. 4.7-4.10). This could be a result of the higher SNR on the subject-specific template image, the average of all time points, which could allow for a better delineation of the anatomical landmarks. Additionally, any intra-rater variability present in the manual delineations is absent in FT segmentations from ALISA. These preliminary findings should be validated with a thorough comparison using intra-rater and inter-rater agreement in FT segmentations, to see if this is a genuine effect. Preferably, this should also include datasets with a longer time period between first and last scan, and with larger brain deformations, to see how generalizable these findings are for future studies. If intra-subject consistency is indeed increased by using ALISA, this will in turn increase the sensitivity to detect changes in diffusion measures.

7.1.3 Fiber tractography

An important aspect in the use of tractography, especially in a clinical setting, is the accuracy of the reconstructed tracts. Diffusion hardware phantoms allow for an objective evaluation of tractography based on different diffusion MRI methods. Comparing tractography results to a ground truth of these hardware phantoms, Fillard et al. (2011) have shown strong improvement in accuracy using multi-fiber vs. tensor-based tracking. However, none of the investigated methods performed perfectly. Even though the multi-fiber tractography can track through fiber crossings, it is virtually impossible for tractography algorithms to distinguish between fibers that cross or ‘kiss’ within a voxel (i.e., populations that enter a voxel, but bend instead of crossing; Tournier et al., 2011). Furthermore, there is no ground truth dataset of the wiring of a human brain, which means it is challenging to quantify the accuracy of in vivo tractography. Despite these issues, technical as well as clinical research has already shown benefits of using multi-fiber tractography (Witwer et al., 2002; Fillard et al., 2011; Brunenberg et al., 2012; Reijmer et al., 2012; Kristo et al., 2013b; Kuhnt et al., 2013).

Two important factors in the accuracy of fiber tractography are: i) how well can the intra-voxel fiber complexity be modeled, and ii) how well can different fiber populations be discriminated based on spatial location. The first requires a higher angular resolution, the second a higher spatial resolution. In Chapter 5 we have investigated the trade-off between these two factors, with the goals to determine which provides the largest gain in terms of fiber tractography. For the three fiber bundles investigated,

the AF, CST, and the tracts connecting the two primary motor areas, the largest gain comes from a higher angular resolution.

Independent of the chosen multi-fiber method, interpretation of the reconstructed fiber tracts is key for informed decision-making in a clinical setting. Where DT-based tractography has several visualization methods to display for instance the tensor shape or the cone of uncertainty along the tracts (Zhang et al., 2003; Jones et al., 2005b), visualizations of multi-fiber diffusion modeling are limited. Recent efforts in this direction have focused on representing orientation distribution function (ODF) glyphs at discrete points along a tract (Kezele et al., 2008; Prckovska et al., 2011). Chapter 6 has described a new visualization method to display properties of the ODF in a continuous fashion along the reconstructed fiber tracts. The ODF estimated from for instance CSD is a reflection of the local microstructure, and visualizing these tissue properties yields a more complete representation of the total tissue organization. The benefit of the continuous hyperstreamline over visualization of the ODF at discrete locations is largest when the fiber populations crossing a tract are smaller (e.g., Fig. 6.11).

For presurgical planning purposes, where fiber tractography is used to determine the location of intact fiber bundles, use of multi-fiber tractography methods is highly recommended (Fillard et al., 2011; Brunenberg et al., 2012; Jeurissen et al., 2012; Kristo et al., 2013b; Kuhnt et al., 2013). When the normal brain topology is disrupted by displacing lesions—such as tumors—fiber tractography may be an important tool in deciding on the surgical approach. Rendering of individual fiber tract bundles in their traditional streamline or streamtube representation only yields information on the trajectories of that selected fiber bundle. Rendering these tracts as multi-fiber hyperstreamlines instantly gives information on fiber structures intersecting that bundle, highlighting the presence and orientation of crossing fiber bundles. Knowledge of these crossing fiber bundles may lead the neurosurgical team to reconsider their surgical approach.

7.2 Future perspectives on diffusion MRI

The structure of this thesis, progressing from improving DTI analyses to the use of multi-fiber methods, is similar to the evolution of diffusion MRI as a research field. Although DTI has conceptual limitations that lower its specificity, DTI still has a great value. The widespread use of DTI throughout the world results in new insight into previously unknown aspects of brain physiology and pathophysiology. For all these DTI-based studies, improvements in the analysis of quantitative measures will lead to a better interpretation of results obtained in those studies. However, more advanced diffusion MRI methods have been shown to provide more specific information about the underlying microstructure that DTI is unable to capture. For neuroscientific purposes,

where scan time is general less limited, these methods will likely provide the largest advances in our understanding of the brain.

7.2.1 Clinical use of diffusion MRI

Where the use of DWI for lesion detection is well established (e.g., Vitali et al., 2011), the benefits of DTI or more advanced methods have yet to reach widespread clinical applications. In the coming years, however, the clinical use will gradually expand from its current applications. Diffusion kurtosis imaging has shown good results in tumor grade characterization on its own (Van Cauter et al., 2012). Within a multi-contrast analysis, including perfusion and spectroscopy, the use of DKI further boosts the diagnostic confidence in grading of brain tumours (Van Cauter et al., 2013). The higher specificity of DKI, and the results obtained in the studies by Van Cauter et al., suggest that similar increases in diagnostic confidence as well as treatment response monitoring are possible for cancer in other organs as well.

Alternatively, fiber tractography has shown its benefit in being included in the surgical planning procedure (e.g., Witwer et al., 2002). Multi-fiber tractography is conceptually more appropriate than DTI (e.g., Fillard et al., 2011; Jeurissen et al., 2011, 2012), has similar reproducibility as tensor-based tracking (e.g., Kristo et al., 2013b,a), and multi-fiber methods show anatomically more plausible tracts in case of a displacing lesion (Kuhnt et al., 2013). With more clinicians opting for multi-fiber tractography in their planning instead of DTI-based tractography, the benefits for surgery can only be expected to increase. This is further enhanced by finding optimal acquisition and visualization methods, as discussed in Chapters 5 and 6.

7.2.2 State-of-the-art diffusion MRI methods

As alternatives to DTI, many models have been proposed to quantify diffusion properties per voxel, including: CSD, dRL, QBI, DSI, DKI, DPI, NODDI, CHARMED, AxCaliber, ActiveAx, EAP, HOT, DOT, PAS-MRI, HYDI, SPF. Most of these techniques will not be discussed in this thesis, but this non-exhaustive list is merely given to indicate the wealth of new diffusion methods that have arisen over the last decade. With more methods being presented each year, the options for diffusion imaging grow at the possible expense of being able to easily compare results from all these methods and studies. The following paragraphs will give an overview of selected methods that can provide new quantitative diffusion measures.

The fiber orientation distribution functions (fODFs) calculated from spherical deconvolution method such as CSD can be used to quantify the diffusion properties of each of the detected fiber populations. The apparent fiber density (AFD; Raffelt et al., 2012) and the hindrance modulated orientational anisotropy (HMOA; Dell'Acqua et al., 2012)

both use fODF properties to do so. This means that diffusion properties of fiber populations crossing within one voxel can be disentangled, allowing the quantitative comparison of fiber bundle specific diffusion measures across a subject population (Raffelt et al., 2013).

Where CSD relies on modeling a single fiber model to estimate the fODF, other model-free approaches are also available. Diffusion spectrum imaging (DSI; Wedeen et al., 2005) uses a direction mathematical relation, the Fourier transform, between the signal measured in q -space and the diffusion profile. Full sampling of q -space requires hundreds of DWIs at high maximum b -values, or q -values, resulting in scan times unfeasible for clinical applications. The benefit, however, is that the full 3D q -space sampling gives a mathematically better quantification of diffusion. Over the years, faster image acquisition and compressed sensing in q -space have resulted in more clinically acceptable scan times (e.g., Bilgic et al., 2012; McNab et al., 2013), and DSI is now the method of choice for the large-scale Human Connectome Project (Setsompop et al., 2013; Sotiropoulos et al., 2013).

Another way to investigate tissue microstructure is to model it as multiple tissue compartments, for instance by combining models for intra-axonal and extra-axonal space. The Composite Hindered And Restricted Model of Diffusion (CHARMED; Assaf et al., 2004; Assaf and Basser, 2005) does this by modeling the intra-axonal space as cylinders that restrict diffusion and extra-axonal space that hinders diffusion. Changes in diffusion properties can then be ascribed more specifically to either or both of these compartments. Conceptually, this resembles DKI (Jensen et al., 2005), where the diffusion tensor and the kurtosis tensor described the hindered and restricted compartments, respectively. An important difference is that CHARMED models multiple fiber populations, which can give a more complete representation of diffusion.

In that same category of modeling true microstructural properties, Assaf et al. (2008) proposed a method to estimate the distribution of axonal diameters in a voxel: Ax-Caliber. Initial in vivo applications showed strong differences between the genu, midbody, and splenium of the corpus callosum (Barazany et al., 2009). The original method required a single fiber population and a priori knowledge of its orientation. Later modifications by Alexander et al. (2010); Zhang et al. (2011) resolved this by estimating not only the mean axon diameter and density instead of the full axon diameter distribution, which has the huge benefit of being able to image the entire brain on a clinical scanner. This method has great potential for neuroimaging, because axon diameters directly correlates with axonal conduction speed, which is one of the key aspects in neuronal function (Hursh, 1939).

The methods described so far are based on the traditional single pulsed diffusion-weighting (as shown in Fig. 1.3). Another method of diffusion-weighting is to replace the large gradient blocks before and after the 180° by oscillating gradients. Changing the frequency of the gradient oscillations sensitizes the signal to diffusion on different length scales (Gross and Kosfeld, 1969; Schachter et al., 2000). This allows the estimation of axonal diameters in vivo (Van et al., 2013b). A third method is using double pulsed gradients, where two blocks of diffusion-weighting are separated by a certain ‘mixing time’. This gives rise to a different diffusion MRI contrast that is especially informative in regions of low anisotropy such as the cortex (Mitra, 1995; Callaghan and Komlosh, 2002; Shemesh et al., 2010). The quantitative measures derived from these oscillating or double pulsed gradients give more direct information about the tissue structure, which puts them in a similar group of microstructural imaging methods as the CHARMED and AxCaliber.

All these microstructural imaging approaches require immense amounts of imaging data, scanner hardware performance, and scan time. This has so far limited the use of these methods in clinically-oriented studies. Significant improvements in diffusion acquisitions will see these techniques be applied in the coming years. With a further increase in use when these methods will become more widely available, they will have a tremendous impact on investigations of brain organization.

7.2.3 Advances in diffusion-weighted MR imaging

The key challenges in advancing diffusion MRI acquisition are threefold: higher, faster, and better. We want higher spatial resolutions, faster acquisition, and geometrically more accurate images. These three factors are heavily co-dependent, with a typical trade-off between one or the other, e.g. higher resolutions will take longer to acquire. The following sections will describe recent advances in acquisition, and expectations on which will prove the most beneficial to diffusion MRI in the coming years.

Higher spatial resolution

A higher resolution is achieved by acquiring a larger portion of k-space, further away from the center. This directly means you will have a longer readout, being slower in your acquisition. For EPI readouts, which are typically used, a longer readout will mean more $T2^*$ decay during the readout, causing blurring of the image. In the never-ending quest for higher spatial resolutions it is therefore imminent to address these restrictions. One way to reduce readout length is to use partial Fourier (or half-scan) acquisitions, or to increase the parallel imaging factor. Both of these options, however, reduce the SNR and may lead to additional image artefacts—and are therefore not the optimal solution. High-performance gradient systems (with higher maximum gradient amplitude and/or higher slew rates) will mean you traverse k-space faster, and have shown

to benefit image quality and acquisition speed (McNab et al., 2013). More complicated solutions are to let go of the standard single-shot EPI readout.

2D imaging

There are readout types other than the conventional single-shot EPI divide k-space into multiple sections. Several pulse sequences have been designed that do this, including short-axis PROPELLER EPI (SAP-EPI; Skare et al., 2006) and read-out segmented EPI (RS-EPI; Holdsworth et al., 2008). SAP-EPI acquires multiple rotating and overlapping “blades” in k-space that together create a full k-space (Fig. 7.1b). Instead, RS-EPI acquires several parallel adjacent and parallel “blinds” in k-space that combine to a full k-space (Fig. 7.1c). Combining blinds or blades per slice from subsequent acquisition means you can cover a larger portion of k-space without T_2^* blurring. However, since the individual blades or blinds are acquired after separate excitations this results in longer scan times. On the plus side, these techniques can provide a higher image resolution and quality, and have been shown to provide improved diagnostic confidence (Holdsworth et al., 2011). To address the downside in scan-time, all RS-EPI blinds can be acquired after a single excitation, which has been termed diffusion-weighted vertical gradient and spin echo EPI (DW-vGRASE; Engstrom et al., 2012). With scan time of DW-vGRASE being similar to the traditional single-short EPI, this is an important step towards fast and high-resolution DWIs.

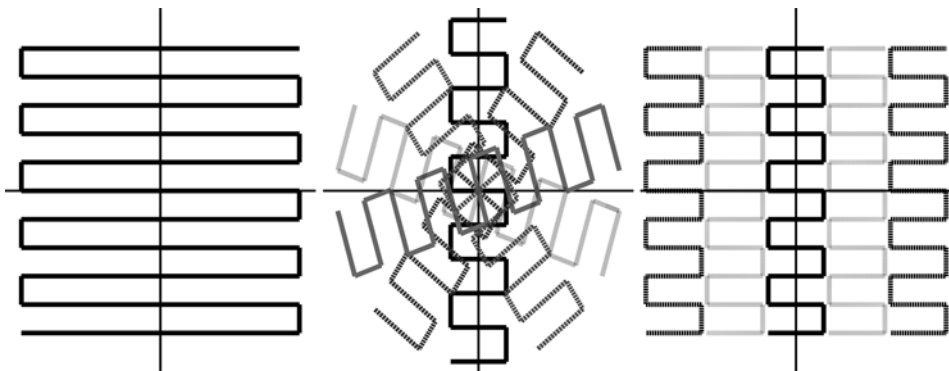


Figure 7.1: Single-shot EPI (left) uses a single long readout to fill the entire 2D k-space after a single excitation. Short-axis PROPELLER EPI (SAP-EPI, middle) uses multiple rotating “blades” to construct k-space. Readout-segmented EPI (RS-EPI, right) uses multiple parallel “blinds” to construct the whole k-space. Individual blades and blinds from SAP-EPI and RS-EPI are generally acquired after excitation.

3D imaging

These 2D imaging techniques are currently mostly used to acquire images with a high

in-plane resolution but a rather lower resolution in the slice-directions. Although this is optimal for clinical settings where DWI is used for lesion detection, (e.g., Holdsworth et al., 2011), quantitative diffusion MRI and fiber tractography require isotropic resolution (Vos et al., 2011; Jones et al., 2013). Standard 2D multi-slice methods will suffer from deteriorating slice profiles with thinner slices, which means that, for instance, instead of measuring a 1 mm thick slice that you prescribe you actually measure a broader slice of 1.5 or 2 mm. High-performance gradient systems can possibly improve this, but only up to certain limits. To go beyond this limit, 3D acquisitions will be required, where a larger FOV along the slice direction is encoded along that direction as well. Even at or before this limit, 3D acquisitions may be more time or SNR-efficient than 2D imaging. The main two options for 3D DWI are diffusion weighted steady-state free precession (DW-SSFP; McNab and Miller, 2008; O'Halloran et al., 2012) and multi-slab EPI (Engstrom and Skare, 2013).

The 3D multi-slab EPI is used in Chapter 5 to achieve a 1 mm true isotropic resolution. Each slab is k-space encoded in all three directions, and 30 slabs were used to cover the entire brain. As described in Engstrom and Skare (2013), the increased slab thickness and the more k-space data acquired provide a theoretical SNR benefit over 2D imaging. Even though more time is required to acquire each slab's 3D k-space, the SNR per unit time is still higher in than in 2D imaging. There is, however, an important trade-off between SNR, resolution, and scan time: thicker slabs mean higher SNR but also require more k_z -encodes for encoding, and thus more excitations. This rapidly increases the scan time for higher resolution images. Another important downside to 3D multi-slab is that multiple k_z -encodes are required to prevent aliasing in the z-direction (see Section 5.2.1). In Chapter 5, 5 of the 8 k_z -encodes were used for the final image, which means that 37.5% of the scanned data was unused. An important improvement to the 3D multi-slab was made by Van et al. (2013a), who proposed a SENSE-like reconstruction of all slabs combined, which foregoes the need to scan these 'anti-aliasing' scans and makes the acquisition significantly faster. As recently shown by Frost et al. (2013), 3D multi-slab can also be combined with RS-EPI, to ensure high-quality high-resolution images. A logical next step would be to attempt the combination of multi-slab with DW-vGRASE, although this may prove difficult in terms of correcting for shot-to-shot phase differences.

The 3D diffusion-weighted steady-state free precession sequence (3D DW-SSFP) was originally designed for post-mortem diffusion MRI by McNab and Miller (2008), and has recently been adapted for in vivo imaging (McNab et al., 2010; O'Halloran et al., 2012). 3D DW-SSFP is a fully 3D sequence, in that it excites the complete volume of interest (i.e. the entire head), and constructs a 3D k-space over multiple excitations. The sequence relies on maintaining a steady-state of all spins over these multiple excita-

tions, with only partial M_z recovery with TR significantly smaller than T1. As a result, the readouts are more closely spaced than in traditional spin echo DWI sequences, making it more time-efficient and SNR-efficient. Because TR is so much smaller than T1, the signal is not just T2-weighted but also T1-weighted, and dependent on the flip angle. Further, a traditional Stejskal-Tanner diffusion preparation is impossible to use, so the diffusion-weighting is built up over several TRs (Merboldt et al., 1989; Freed et al., 2001), making it even more time-efficient. The sequence is heavily dependent on maintaining the steady-state, which is notoriously difficult in the presence of motion like cardiac pulsation. Loss of the steady state leads to unrecoverable signal loss. Although efforts are being made to compensate the loss of steady-state, the sequence is still sensitive to cardiac pulsation (Bammer and O'Halloran, 2013; O'Halloran et al., 2013). Once these corrections can robustly maintain the steady-state, 3D DW-SSFP can start to fulfill its promise as an SNR-efficient acquisition method. The way DW-SSFP samples the 3D k-space means it has better characteristics in terms of scaling the sequence to higher spatial resolutions, than for instance 3D multislab EPI. This means that, when future studies look to break beyond the 1 mm isotropic resolution achieved so far, DW-SSFP would be the method of choice.

Even though Chapter 5 has shown that the angular information seems more important for tractography than higher spatial resolution, those results should not be generalized to indicate that higher spatial resolutions will not benefit diffusion MRI. Investigation of substructures in the brain, such as the hippocampus (Zeineh et al., 2012), will greatly benefit from the increase in spatial resolution these 3D acquisition techniques can provide. Additionally, quantification of diffusion measures, especially for DTI, will greatly benefit from higher spatial resolutions.

Geometrically accurate images

As shortly discussed in Chapter 5, susceptibility differences between air and tissue cause geometric distortions in EPI images. Single-shot EPI acquisitions are particularly prone to these susceptibility differences, and the susceptibility differences will cause local distortions of the object in the phase-encoding (PE) direction (Farzaneh et al., 1990; Skare et al., 2006). These geometric distortions are exacerbated when increasing the spatial resolution because this requires a larger part of k-space to be sampled. This limits the spatial resolution achievable in single-shot EPI acquisitions. Given that these air-tissue boundaries are inherently present in the head, the best one can do is mitigate their effects on the images. One way to do this is by parallel imaging methods, e.g., SMASH, SENSE, or GRAPPA (Sodickson and Manning, 1997; Pruessmann et al., 1999; Griswold et al., 2002). For EPI it is most efficient to undersample in the PE direction, effectively reducing the FOV in this direction, which provides the largest speed-up and the strongest reduction in distortions (Skare et al., 2006; Holdsworth et al., 2012).

Another way to reduce image distortions is to reduce the EPI readout length by using SAP-EPI, RS-EPI, or DW-vGRASE. The higher diagnostic confidence achieved with RS-EPI is partly because of the higher resolution, as mentioned earlier, and partly because of the reduced distortions in the image (Holdsworth et al., 2011). Alternatively, from a combined imaging and image processing perspective, it is also possible to reconstruct an undistorted image from two acquisitions with opposite PE directions (Chang and Fitzpatrick, 1992; Skare and Bammer, 2010), as used in Chapter 5 (Fig. 5.1). A downside to this method is that, for the best results, two images should be acquired per diffusion-weighting direction, doubling the scan time. Further, when distortions in the original images are too large the registration-based correction may yield suboptimal results.

Faster acquisition

Many DWIs must be acquired to most accurately measure the diffusion-weighted signal and estimate the diffusion, especially for the advanced methods. Single-shot EPI (SS-EPI) is the fastest method for MR image acquisition, and is therefore still the method of choice for DWI. As discussed above, this acquisition speed comes at the cost of several drawbacks. For standard clinical 3T scanners, spatial resolutions of 2 - 2.5 mm isotropic are generally used for HARDI protocols in clinical research studies (e.g., Lebel and Beaulieu, 2011; Reijmer et al., 2012; Szczepankiewicz et al., 2013). The high-performance Connectom gradients by Siemens can achieve higher resolutions in acceptable scan times, but this hardware is only available in a limited number of research groups. DW-vGRASE is a very promising technique, using a segmented EPI readout with only a small scan time increase (Engstrom et al., 2012). Another very important technique in faster DWI acquisition is multiband imaging, or simultaneous multi-slice imaging (Moeller et al., 2010; Setsompop et al., 2012b). Conceptually, two slices that are half a FOVz apart are excited and their combined signal is read out. Using parallel imaging methods, these two slices can then be separated. The great benefit of this concept is that this decreases the SNR less than in-plane parallel imaging (Setsompop et al., 2012b). Higher numbers of simultaneously acquired slices can be achieved, with a time gain equal to the number of simultaneous slices, with minimal SNR loss (Setsompop et al., 2012a). Currently, acceleration factors of 3 are most commonly used, leading to a strong increase in scan time efficiency (e.g., Setsompop et al., 2012a, 2013).

Future imaging perspectives

A strong benefit of the RGPM image distortion correction is that this is available to the community as part of the FSL package (Andersson et al., 2003; Smith et al., 2004). Currently, the state-of-the-art pulse sequences such as 3D DW-SSFP, 3D multi-slab, and DW-vGRASE are not publicly available and thus not widely used in diffusion MRI. As a result, these methods are generally only available in MR research groups dedicated to

diffusion MRI, and any clinical groups with close collaborations with these groups. Distribution of these sequences to the diffusion MRI community, similar to the widely and freely available software packages, would strongly increase the use of high-quality images for neuroimaging purposes. Although the strong differences in MRI vendor software systems makes this more difficult than sharing of image processing software, the benefits for the research community as a whole make this an effort worth investigating.

7.3 Conclusion

This goal of this thesis was to improve the analysis of diffusion MRI data, at all aspects of the research pipeline. Improvements to quantification and interpretation of DTI data have been presented that increase the specificity and sensitivity. DTI is still the mostly-used diffusion MRI model, which means that the findings presented here can provide useful insights to a large numbers of researchers. More advanced multi-fiber methods are primarily used for their ability to provide more accurate fiber tractography results. To best exploit the benefits of these methods, the effect of spatial and angular resolution on the accuracy of multi-fiber tractography results was investigated. These multi-fiber methods improve tractography by being able to better model the diffusion within each voxel. Visualization of these voxel-wise properties along the reconstructed fiber tracts, give a more complete representations of the acquired data.

The recent advances in the acquisition and modeling of diffusion MRI data enable the measurement of more direct microstructural parameters, which will play a large role in the future of neuroimaging and neuroscience. Until these new techniques are readily available for all researchers in the field, methods such as DTI and multi-fiber methods will remain invaluable techniques to investigate the brain. I hope, and expect, that the results presented in this thesis will contribute to more informed and well-considered interpretation of diffusion MRI studies.

REFERENCES

- Abraham J, Haut MW, Moran MT, et al., 2008. Adjuvant Chemotherapy for Breast Cancer: Effects on Cerebral White Matter Seen in Diffusion Tensor Imaging. *Clinical Breast Cancer* 8 (1), 88–91.
- Aggarwal M, Zhang J, Pletnikova O, et al., 2013. Feasibility of creating a high-resolution 3D diffusion tensor imaging based atlas of the human brainstem: A case study at 11.7T. *NeuroImage* 74 (0), 117–127.
- Alexander AL, Hasan KM, Lazar M, et al., 2001. Analysis of partial volume effects in Diffusion-Tensor MRI. *Magnetic Resonance in Medicine* 45 (5), 770–780.
- Alexander DC, Barker GJ, Arridge SR, 2002. Detection and modeling of non-Gaussian apparent diffusion coefficient profiles in human brain data. *Magnetic Resonance in Medicine* 48 (2), 331–340.
- Alexander DC, Hubbard PL, Hall MG, et al., 2010. Orientationally invariant indices of axon diameter and density from diffusion MRI. *NeuroImage* 52 (4), 1374–1389.
- Andersson JL, Skare S, Ashburner J, 2003. How to correct susceptibility distortions in spin-echo echo-planar images: application to diffusion tensor imaging. *NeuroImage* 20 (2), 870–888.
- Arfanakis K, Houghton VM, Carew JD, et al., 2002. Diffusion Tensor MR Imaging in Diffuse Axonal Injury. *American Journal of Neuroradiology* 23 (5), 794–802.
- Ashburner J, Friston KJ, 2000. Voxel-Based Morphometry - The Methods. *NeuroImage* 11 (6), 805–821.
- Ashburner J, Friston KJ, 2005. Unified segmentation. *NeuroImage* 26 (3), 839–851.
- Assaf Y, Basser PJ, 2005. Composite hindered and restricted model of diffusion (CHARMED) MR imaging of the human brain. *NeuroImage* 27 (1), 48–58.
- Assaf Y, Ben-Bashat D, Chapman J, et al., 2002. High b-value q-space analyzed diffusion-weighted MRI: Application to multiple sclerosis. *Magn. Reson. Med.* 47 (1), 115–126.
- Assaf Y, Blumenfeld-Katzir T, Yovel Y, et al., 2008. Ax-caliber: A method for measuring axon diameter distribution from diffusion MRI. *Magnetic Resonance in Medicine* 59 (6), 1347–1354.
- Assaf Y, Freidlin RZ, Rohde GK, et al., 2004. New modeling and experimental framework to characterize hindered and restricted water diffusion in brain white matter. *Magn. Reson. Med.* 52 (5), 965–978.
- Assemlal HE, Tschumperle D, Brun L, et al., 2011. Recent Advances in Diffusion MRI Modeling: Angular and Radial Reconstruction. *Medical Image Analysis* 15 (4), 369–396.
- Atkinson D, Batchelor PG, Clark CA, 2007. Track ribbons - visualising structural information in diffusion tensor axial asymmetry. In: *Proceedings of the 15th Annual Meeting of International Society for Magnetic Resonance in Medicine*, Berlin, Germany. p. 79.
- Bagadia A, Purandare H, Misra BK, et al., 2011. Application of magnetic resonance tractography in the perioperative planning of patients with eloquent region intra-axial brain lesions. *Journal of Clinical Neuroscience* 18 (5), 633–639.
- Bammer R, O'Halloran RL, 2013. On the Phase-Error Propagation in Diffusion-Weighted Steady State Free Precession (DW-SSFP) Imaging. In: *Proceedings of the 21th Annual Meeting of International Society for Magnetic Resonance in Medicine*, Salt Lake City, United States. p. 2083.

References

- Barazany D, Bassar PJ, Assaf Y, 2009. In vivo measurement of axon diameter distribution in the corpus callosum of rat brain. *Brain* 132 (5), 1210–1220.
- Bassar P, 1995. Inferring microstructural features and the physiological state of tissues from diffusion-weighted images. *NMR in Biomedicine* 8, 333–344.
- Bassar PJ, 2002. Relationships between diffusion tensor and q-space MRI. *Magnetic Resonance in Medicine* 47 (2), 392–397.
- Bassar PJ, Mattiello J, LeBihan D, 1994. MR Diffusion Tensor Spectroscopy and Imaging. *Biophysical Journal* 66 (1), 259–267.
- Bassar PJ, Pajevic S, Pierpaoli C, et al., 2000. In vivo fiber tractography using DT-MRI data. *Magnetic Resonance in Medicine* 44 (4), 625–632.
- Bastin ME, Muñoz Maniega S, Ferguson KJ, et al., 2010. Quantifying the effects of normal ageing on white matter structure using unsupervised tract shape modelling. *NeuroImage* 51 (1), 1–10.
- Beaulieu C, 2002. The basis of anisotropic water diffusion in the nervous system - a technical review. *NMR in Biomedicine* 15 (7-8), 435–455.
- Behrens T, Johansen-Berg H, Jbabdi S, et al., 2007. Probabilistic diffusion tractography with multiple fibre orientations: What can we gain? *NeuroImage* 34 (1), 144–155.
- Bendlin B, Fitzgerald M, Ries M, et al., 2010. White Matter in Aging and Cognition: A Cross-Sectional Study of Microstructure in Adults Aged Eighteen to Eighty-Three. *Developmental Neuropsychology* 35, 257–277.
- Bennett IJ, Madden DJ, Vaidya CJ, et al., 2010. Age-related differences in multiple measures of white matter integrity: A Diffusion Tensor Imaging study of healthy aging. *Human Brain Mapping* 31 (3), 378–390.
- Benson D, Sheremata W, Bouchard R, et al., 1973. Conduction Aphasia: A Clinicopathological Study. *Archives of Neurology* 28, 339–346.
- Bilgic B, Setsompop K, Cohen-Adad J, et al., 2012. Accelerated diffusion spectrum imaging with compressed sensing using adaptive dictionaries. *Magnetic Resonance in Medicine* 68 (6), 1747–1754.
- Bodammer N, Kaufmann J, Kanowski M, et al., 2004. Eddy current correction in diffusion-weighted imaging using pairs of images acquired with opposite diffusion gradient polarity. *Magn. Reson. Med.* 51 (1), 188–193.
- Bonekamp D, Nagae LM, Degaonkar M, et al., 2007. Diffusion Tensor Imaging in children and adolescents: Reproducibility, hemispheric, and age-related differences. *NeuroImage* 34 (2), 733–742.
- Bozzali M, Falini A, Franceschi M, et al., 2002. White matter damage in Alzheimer's disease assessed in vivo using Diffusion Tensor Magnetic Resonance Imaging. *Journal of Neurology, Neurosurgery & Psychiatry* 72., 742–746.
- Brown R, 1828. A brief account of microscopical observations made on the particles contained in the pollen of plants. *Philosophical Magazine* 4, 161–173.
- Brunenberg EJJ, Moeskops P, Backes WH, et al., 2012. Structural and Resting State Functional Connectivity of the Subthalamic Nucleus: Identification of Motor STN Parts and the Hyperdirect Pathway. *PLoS ONE* 7, e39061.
- Buchsbaum MS, Tang CY, Peled S, et al., 1998. MRI white matter diffusion anisotropy and PET metabolic rate in schizophrenia. *Neuroreport* 9 (0959-4965), 425–430.
- Caeyenberghs K, Leemans A, Geurts M, et al., 2010. Brain-behavior relationships in young traumatic brain injury patients: Fractional anisotropy measures are highly correlated with dynamic visuomotor tracking performance. *Neuropsychologia* 48 (5), 1472–1482.
- Calamante F, Tournier JD, Jackson GD, et al., 2010. Track-density imaging (TDI): Super-resolution white matter imaging using whole-brain track-density mapping. *NeuroImage* 53 (4), 1233–1243.
- Callaghan PT, Komlosch ME, 2002. Locally anisotropic motion in a macroscopically isotropic system: displacement correlations measured using double pulsed gradient spin-echo NMR. *Magn. Reson. Chem.* 40 (13), S15–S19.
- Castellano A, Bello L, Michelozzi C, et al., 2012. Role of diffusion tensor magnetic resonance tractography in predicting the extent of resection in glioma surgery. *Neuro-Oncology* 14 (2), 192–202.
- Catani M, Bodi I, Dell'Acqua F, 2012. Comment on "The Geometric Structure of the Brain Fiber Pathways". *Science* 337 (6102), 1605.
- Catani M, Howard RJ, Pajevic S, et al., 2002. Virtual In Vivo Interactive Dissection of White Matter Fasciculi in the Human Brain. *NeuroImage* 17 (1), 77–94.

- Catani M, Jones DK, Daly E, et al., 2008. Altered cerebellar feedback projections in Asperger syndrome. *NeuroImage* 41 (4), 1184–1191.
- Catani M, Jones DK, Ffytche DH, 2005. Perisylvian language networks of the human brain. *Annals of Neurology* 57 (1), 8–16.
- Cercignani M, 2011. Chapter 29: Strategies for Patient-Control Comparison of Diffusion MR Data. Oxford University Press.
- Cercignani M, Inglese M, Pagani E, et al., 2001. Mean Diffusivity and Fractional Anisotropy Histograms of Patients with Multiple Sclerosis. *American Journal of Neuroradiology* 22 (5), 952–958.
- Chang H, Fitzpatrick J, 1992. A technique for accurate magnetic resonance imaging in the presence of field inhomogeneities. *Medical Imaging, IEEE Transactions on* 11 (3), 319–329.
- Chang LC, Jones DK, Pierpaoli C, 2005. RESTORE: Robust estimation of tensors by outlier rejection. *Magnetic Resonance in Medicine* 53 (5), 1088–1095.
- Cheng YW, Chung HW, Chen CY, et al., 2011. Diffusion Tensor Imaging with cerebrospinal fluid suppression and signal-to-noise preservation using acquisition combining fluid-attenuated inversion recovery and conventional imaging: Comparison of fiber tracking. *European Journal of Radiology* 79 (1), 113–117.
- Chou MC, Lin YR, Huang TY, et al., 2005. FLAIR Diffusion-Tensor MR Tractography: Comparison of Fiber Tracking with Conventional Imaging. *AJNR Am J Neuroradiol* 26 (3), 591–597.
- Ciccarelli O, Behrens TE, Altmann DR, et al., 2006. Probabilistic diffusion tractography: a potential tool to assess the rate of disease progression in amyotrophic lateral sclerosis. *Brain* 129 (7), 1859–1871.
- Ciccarelli O, Catani M, Johansen-Berg H, et al., 2008. Diffusion-based tractography in neurological disorders: concepts, applications, and future developments. *The Lancet Neurology* 7 (8), 715–727.
- Ciccarelli O, Parker GJM, Toosy AT, et al., 2003. From diffusion tractography to quantitative white matter tract measures: a reproducibility study. *NeuroImage* 18 (2), 348–359.
- Clark CA, Barrick TR, Murphy MM, et al., 2003. White matter fiber tracking in patients with space-occupying lesions of the brain: a new technique for neurosurgical planning? *NeuroImage* 20 (3), 1601–1608.
- Clark KA, Nuechterlein KH, Asarnow RF, et al., 2011. Mean diffusivity and fractional anisotropy as indicators of disease and genetic liability to schizophrenia. *Journal of Psychiatric Research* 45 (7), 980–988.
- Clayden J, Storkey A, Bastin M, 2007. A Probabilistic Model-Based Approach to Consistent White Matter Tract Segmentation. *Medical Imaging, IEEE Transactions on* 26 (11), 1555–1561.
- Cleveland G, Chang D, Hazlewood C, 1976. Nuclear magnetic resonance measurement of skeletal muscle: anisotropy of the diffusion coefficient of the intracellular water. *Biophysical Journal* 16, 1043–1053.
- Coenen VA, Krings T, Mayfrank L, et al., 2001. Three-dimensional Visualization of the Pyramidal Tract in a Neuronavigation System during Brain Tumor Surgery: First Experiences and Technical Note. *Neurosurgery* 49 (1), 86–93.
- Colby JB, Soderberg L, Lebel C, et al., 2012. Along-tract statistics allow for enhanced tractography analysis. *NeuroImage* 59 (4), 3227–3242.
- Concha L, Beaulieu C, Collins DL, et al., 2009. White-matter diffusion abnormalities in temporal-lobe epilepsy with and without mesial temporal sclerosis. *Journal of Neurology, Neurosurgery & Psychiatry* 80 (3), 312–319.
- Concha L, Beaulieu C, Gross DW, 2005a. Bilateral limbic diffusion abnormalities in unilateral temporal lobe epilepsy. *Annals of Neurology* 57 (2), 188–196.
- Concha L, Beaulieu C, Wheatley BM, et al., 2007. Bilateral White Matter Diffusion Changes Persist after Epilepsy Surgery. *Epilepsia* 48 (5), 931–940.
- Concha L, Gross DW, Beaulieu C, 2005b. Diffusion Tensor tractography of the Limbic System. *AJNR Am J Neuroradiol* 26 (9), 2267–2274.
- Conturo TE, Lori NE, Cull TS, et al., 1999. Tracking neuronal fiber pathways in the living human brain. *Proceedings of the National Academy of Sciences* 96 (18), 10422–10427.
- Cook PA, Bai Y, Nedjati-Gilani S, et al., 2006. Camino: open-source diffusion-MRI reconstruction and processing. In: *Proceedings of the 14th Annual Meeting of International Society for Magnetic Resonance in Medicine, Seattle, United States*. p. 1876.

References

- Courchesne E, Chisum HJ, Townsend J, et al., 2000. Normal Brain Development and Aging: Quantitative Analysis at in Vivo MR Imaging in Healthy Volunteers. *Radiology* 216 (3), 672–682.
- Danielian LE, Iwata NK, Thomasson DM, et al., 2010. Reliability of fiber tracking measurements in diffusion tensor imaging for longitudinal study. *NeuroImage* 49 (2), 1572–1580.
- Davis SW, Dennis NA, Buchler NG, et al., 2009. Assessing the effects of age on long white matter tracts using Diffusion Tensor tractography. *NeuroImage* 46 (2), 530–541.
- de Luis-García R, Westin CF, Alberola-López C, 2013. Geometrical constraints for robust tractography selection. *NeuroImage*, In press.
- de Ruyter MB, Reneman L, Boogerd W, et al., 2012. Late effects of high-dose adjuvant chemotherapy on white and gray matter in breast cancer survivors: Converging results from multimodal magnetic resonance imaging. *Human Brain Mapping* 33 (12), 2971–2983.
- Dejerine J, 1895. *Anatomie de centres nerveux*. Rueff et Cie.
- DeKaban A, 1978. Changes in brain weights during the span of human life: relation of brain weights to body heights and body weights. *Annals of Neurology* 4, 345–356.
- Dell'Acqua F, Simmons A, Williams SC, et al., 2012. Can spherical deconvolution provide more information than fiber orientations? Hindrance modulated orientational anisotropy, a true-tract specific index to characterize white matter diffusion. *Hum. Brain Mapp.*, In press.
- Deprez S, Amant F, Smeets A, et al., 2012. Longitudinal Assessment of Chemotherapy-Induced Structural Changes in Cerebral White Matter and Its Correlation With Impaired Cognitive Functioning. *Journal of Clinical Oncology* 30 (3), 274–281.
- Deprez S, Amant F, Yigit R, et al., 2011. Chemotherapy-induced structural changes in cerebral white matter and its correlation with impaired cognitive functioning in breast cancer patients. *Human Brain Mapping* 32 (3), 480–493.
- Deprez S, Billiet T, Sunaert S, et al., 2013. Diffusion tensor MRI of chemotherapy-induced cognitive impairment in non-CNS cancer patients: a review. *Brain Imaging and Behavior*, 1–27.
- Descoteaux M, Angelino E, Fitzgibbons S, et al., 2007. Regularized, fast, and robust analytical Q-ball imaging. *Magn. Reson. Med.* 58 (3), 497–510.
- Descoteaux M, Deriche R, Knosche TR, et al., 2009. Deterministic and Probabilistic Tractography based on Complex Fibre Orientation Distributions. *IEEE Transactions on Medical Imaging* 28 (2), 269–286.
- Dice L, 1945. Measures of the amount of ecologic association between species. *Ecology* 26, 297–302.
- Douaud G, Jbabdi S, Behrens TE, et al., 2011. DTI measures in crossing-fibre areas: Increased diffusion anisotropy reveals early white matter alteration in MCI and mild Alzheimer's disease. *NeuroImage* 55 (2), 880–890.
- Dubois J, Dehaene-Lambertz G, Perrin M, et al., 2008. Asynchrony of the early maturation of white matter bundles in healthy infants: Quantitative landmarks revealed noninvasively by Diffusion Tensor Imaging. *Human Brain Mapping* 29 (1), 14–27.
- Dubois J, Poupon C, Lethimonnier F, et al., 2006. Optimized diffusion gradient orientation schemes for corrupted clinical DTI data sets. *MAGMA* 19 (3), 134–143.
- Einstein A, 1905. Über die von der molekularkinetischen Theorie der Wärme geforderte Bewegung von in ruhenden Flüssigkeiten suspendierten Teilchen. *Ann. Phys.* 322 (8), 549–560.
- Eluvathingal TJ, Hasan KM, Kramer L, et al., 2007. Quantitative Diffusion Tensor tractography of association and projection fibers in normally developing children and adolescents. *Cereb. Cortex* 17 (12), 2760–2768.
- Emsell L, Leemans A, Langan C, et al., 2009. A DTI tractography study of the cingulum in euthymic bipolar I disorder. In: *Proceedings of the 17th Annual Meeting of International Society for Magnetic Resonance in Medicine*, Hawaii, USA. p. 1224.
- Engstrom M, Bammer R, Skare S, 2012. Diffusion weighted vertical gradient and spin echo. *Magn Reson Med* 68 (6), 1755–1763.
- Engstrom M, Skare S, 2013. Diffusion-weighted 3d multislabs echo planar imaging for high signal-to-noise ratio efficiency and isotropic image resolution. *Magnetic Resonance in Medicine*, In press.
- Ennis DB, Kindlmann G, 2006. Orthogonal tensor invariants and the analysis of diffusion tensor

- magnetic resonance images. *Magn. Reson. Med.* 55 (1), 136–146.
- Faria AV, Hoon A, Stashinko E, et al., 2011. Quantitative analysis of brain pathology based on {MRI} and brain atlases – Applications for cerebral palsy. *NeuroImage* 54 (3), 1854–1861.
- Farzaneh F, Riederer SJ, Pelc NJ, 1990. Analysis of T2 limitations and off-resonance effects on spatial resolution and artifacts in echo-planar imaging. *Magnetic Resonance in Medicine* 14 (1), 123–139.
- Fieremans E, Jensen JH, Helpert JA, 2011. White matter characterization with diffusional kurtosis imaging. *NeuroImage* 58 (1), 177–188.
- Fillard P, Descoteaux M, Goh A, et al., 2011. Quantitative Evaluation of 10 Tractography Algorithms on a Realistic Diffusion MR Phantom. *NeuroImage* 56 (1), 220–234.
- Fjell AM, Westlye LT, Greve DN, et al., 2008. The relationship between Diffusion Tensor Imaging and volumetry as measures of white matter properties. *NeuroImage* 42 (4), 1654–1668.
- Fox NC, Scahill RI, Crum WR, et al., 1999. Correlation between rates of brain atrophy and cognitive decline in AD. *Neurology* 52 (8), 1687–1689.
- Frank LR, 2001. Anisotropy in High Angular Resolution Diffusion-Weighted MRI. *Magnetic Resonance in Medicine* 45 (6), 935–939.
- Frank LR, 2002. Characterization of anisotropy in high angular resolution diffusion-weighted MRI. *Magnetic Resonance in Medicine* 47 (6), 1083–1099.
- Freed D, Scheven U, Zielinski L, et al., 2001. Steady-state free precession experiments and exact treatment of diffusion in a uniform gradient. *Journal of Chemical Physics* 115, 4249–4258.
- Frost R, Miller K, Porter D, et al., 2013. 3D multi-slab diffusion-weighted readout-segmented echo-planar imaging with real-time cardiac-reordered k-space acquisition. In: *Proceedings of the 21th Annual Meeting of International Society for Magnetic Resonance in Medicine*, Salt Lake City, United States. p. 54.
- Geschwind N, 1965. Disconnexion syndromes in animals and man. *Brain* 88, 237–294.
- Giorgio A, Watkins K, Chadwick M, et al., 2010. Longitudinal changes in grey and white matter during adolescence. *NeuroImage* 49 (1), 94–103.
- Gong G, Shi F, Concha L, et al., 2008. Insights into the sequence of structural consequences of convulsive status epilepticus: A longitudinal MRI study. *Epilepsia* 49 (11), 1941–1945.
- Griswold MA, Jakob PM, Heidemann RM, et al., 2002. Generalized autocalibrating partially parallel acquisitions (GRAPPA). *Magn. Reson. Med.* 47 (6), 1202–1210.
- Gross B, Kosfeld R, 1969. Anwendung der spin-echo-methode der messung der selbstdiffusion. *Messtechnik* 77, 171–177.
- Guevara P, Duclap D, Poupon C, et al., 2012. Automatic fiber bundle segmentation in massive tractography datasets using a multi-subject bundle atlas. *NeuroImage* 61 (4), 1083–1099.
- Hagler DJ, Ahmadi ME, Kuperman J, et al., 2009. Automated white-matter tractography using a probabilistic diffusion tensor atlas: Application to temporal lobe epilepsy. *Human Brain Mapping* 30 (5), 1535–1547.
- Hagmann P, Cammoun L, Gigandet X, et al., 2008. Mapping the Structural Core of Human Cerebral Cortex. *PLoS Biology* 6 (7), e159.
- Hanyu H, Shindo H, Kakizaki D, et al., 1997. Increased water diffusion in cerebral white matter in Alzheimer's disease. *Gerontology* 43, 343–351.
- Hasan KM, Iftikhar A, Kamali A, et al., 2009. Development and aging of the healthy human brain uncinate fasciculus across the lifespan using Diffusion Tensor tractography. *Brain Research* 1276, 67–76.
- Hasan KM, Walimuni IS, Abid H, et al., 2011. A review of diffusion tensor magnetic resonance imaging computational methods and software tools. *Computers in Biology and Medicine* 41 (12), 1062–1072.
- Heiervang E, Behrens T, Mackay C, et al., 2006. Between session reproducibility and between subject variability of diffusion MR and tractography measures. *NeuroImage* 33 (3), 867–877.
- Holdsworth S.J. Van A, Skare S, Bammer R, 2012. Comparison Between EPI and RS-EPI at High Acceleration Factors. In: *Proceedings of the 20th Annual Meeting of International Society for Magnetic Resonance in Medicine*, Melbourne, Australia. p. 4212.
- Holdsworth S, Yeom K, Skare S, et al., 2011. Clinical Application of Readout-Segmented Echo-Planar Imaging for Diffusion-Weighted Imaging in Pediatric Brain. *American Journal of Neuroradiology* 32 (7), 1274–1279.

References

- Holdsworth SJ, Skare S, Newbould RD, et al., 2008. Readout-segmented EPI for rapid high resolution diffusion imaging at 3T. *European Journal of Radiology* 65 (1), 36–46, 3 Tesla MR.
- Hsu JL, Leemans A, Bai CH, et al., 2008. Gender differences and age-related white matter changes of the human brain: A Diffusion Tensor Imaging study. *NeuroImage* 39 (2), 566–577.
- Hsu JL, Van Hecke W, Bai CH, et al., 2010. Microstructural white matter changes in normal aging: A Diffusion Tensor Imaging study with higher-order polynomial regression models. *NeuroImage* 49 (1), 32–43.
- Huang H, Zhang J, Wakana S, et al., 2006. White and gray matter development in human fetal, newborn and pediatric brains. *NeuroImage* 33 (1), 27–38.
- Huisman TA, Schwamm LH, Schaefer PW, et al., 2004. Diffusion Tensor Imaging as Potential Biomarker of White Matter Injury in Diffuse Axonal Injury. *American Journal of Neuroradiology* 25 (3), 370–376.
- Hursh J, 1939. Conduction velocity and diameter of nerve fibers. *American Journal of Physiology* 127, 131–139.
- Huster RJ, Westerhausen R, Kreuder F, et al., 2009. Hemispheric and gender related differences in the midcingulum bundle: A DTI study. *Human Brain Mapping* 30 (2), 383–391.
- Jansons KM, Alexander DC, 2003. Persistent angular structure: new insights from diffusion magnetic resonance imaging data. *Inverse Problems* 19 (5), 672–83.
- Jensen JH, Helpert JA, Ramani A, et al., 2005. Diffusional kurtosis imaging: The quantification of non-gaussian water diffusion by means of magnetic resonance imaging. *Magn. Reson. Med.* 53 (6), 1432–1440.
- Jernigan TL, Baare WF, Stiles J, et al., 2011. Postnatal brain development: Structural imaging of dynamic neurodevelopmental processes. *Progress in Brain Research* 189, 77–92.
- Jeurissen B, Leemans A, Jones DK, et al., 2011. Probabilistic fiber tracking using the residual bootstrap with constrained spherical deconvolution. *Human Brain Mapping* 32, 461–479.
- Jeurissen B, Leemans A, Tournier JD, et al., 2010. Estimating the number of fiber orientations in diffusion MRI voxels: a constrained spherical deconvolution study. In: *Proceedings of the 18th Annual Meeting of International Society for Magnetic Resonance in Medicine*, Stockholm, Sweden. p. 573.
- Jeurissen B, Leemans A, Tournier JD, et al., 2012. Investigating the prevalence of complex fiber configurations in white matter tissue with diffusion MRI. *Human Brain Mapping* In Press.
- Johansen-Berg H, 2010. Behavioural relevance of variation in white matter microstructure. *Current Opinion in Neurology* 23 (4), 351–358.
- Jones D, 2008a. Tractography Gone Wild: Probabilistic Fibre Tracking Using the Wild Bootstrap With Diffusion Tensor MRI. *Medical Imaging, IEEE Transactions on* 27 (9), 1268–1274.
- Jones D, Leemans A, 2011. Diffusion tensor imaging. *Methods Mol Biol* 711, 127–144.
- Jones DK, 2003. Determining and visualizing uncertainty in estimates of fiber orientation from Diffusion Tensor MRI. *Magnetic Resonance in Medicine* 49 (1), 7–12.
- Jones DK, 2004. The effect of gradient sampling schemes on measures derived from Diffusion Tensor MRI: A Monte Carlo study. *Magnetic Resonance in Medicine* 51 (4), 807–815.
- Jones DK, 2008b. Studying connections in the living human brain with Diffusion MRI. *Cortex* 44 (8), 936–952.
- Jones DK, 2010. Precision and Accuracy in Diffusion Tensor Magnetic Resonance Imaging. *Topics in Magnetic Resonance Imaging* 21 (2), 87–99.
- Jones DK, Bassler PJ, 2004. Squashing peanuts and smashing pumpkins": How noise distorts diffusion-weighted MR data. *Magnetic Resonance in Medicine* 52 (5), 979–993.
- Jones DK, Catani M, Pierpaoli C, et al., 2006. Age effects on Diffusion Tensor Magnetic Resonance Imaging tractography measures of frontal cortex connections in schizophrenia. *Human Brain Mapping* 27 (3), 230–238.
- Jones DK, Cercignani M, 2010. Twenty-five pitfalls in the analysis of diffusion MRI data. *NMR Biomed.* 23 (7), 803–820.
- Jones DK, Horsfield M, Simmons A, 1999a. Optimal strategies for measuring diffusion in anisotropic systems by Magnetic Resonance Imaging. *Magnetic Resonance in Medicine* 42 (3), 515–525.
- Jones DK, Knosche TR, Turner R, 2013. White matter integrity, fiber count, and other fallacies: The

- do's and don'ts of diffusion MRI. *NeuroImage* 73, 239–254.
- Jones DK, Lythgoe D, Horsfield MA, et al., 1999b. Characterization of White Matter Damage in Ischemic Leukoaraiosis with Diffusion Tensor MRI. *Stroke* 30 (2), 393–397.
- Jones DK, Symms MR, Cercignani M, et al., 2005a. The effect of filter size on VBM analyses of DT-MRI data. *NeuroImage* 26 (2), 546–554.
- Jones DK, Travis AR, Eden G, et al., 2005b. PASTA: Pointwise assessment of streamline tractography attributes. *Magnetic Resonance in Medicine* 53 (6), 1462–1467.
- Jones DK, Williams SCR, Gasston D, et al., 2002. Isotropic resolution Diffusion Tensor Imaging with whole brain acquisition in a clinically acceptable time. *Human Brain Mapping* 15 (4), 216–230.
- Karus A, Hofer S, Frahm J, 2009. Separation of Fiber Tracts within the Human Cingulum Bundle using Single-Shot STEAM DTI. *The Open Medical Imaging Journal* 3, 21–27.
- Keller TA, Just MA, 2009. Altering Cortical Connectivity: Remediation-Induced Changes in the White Matter of Poor Readers. *Neuron* 64 (5), 624–631.
- Kezele I, Poupon C, Perrin M, et al., 2008. Mean q-Ball Strings Obtained by Constrained Procrustes Analysis with Point Sliding. In: Metaxas D, Axel L, Fichtinger G, et al. (Eds.), *Lecture Notes in Computer Science*. Vol. 5241. Springer Berlin Heidelberg, pp. 1034–1041–.
- Kitchen CM, 2009. Nonparametric vs Parametric Tests of Location in Biomedical Research. *American Journal of Ophthalmology* 147 (4), 571–572.
- Klein S, Staring M, Murphy K, et al., 2010. elastix: A Toolbox for Intensity-Based Medical Image Registration. *IEEE Transactions on Medical Imaging* 29, 196–205.
- Kleinnijenhuis M, Barth M, Alexander DC, et al., 2012. Structure Tensor Informed Fiber Tractography (STIFT) by combining gradient echo MRI and diffusion weighted imaging. *NeuroImage* 59 (4), 3941–3954.
- Koay CG, 2011. Chapter 16: Least Squares Approaches to Diffusion Tensor Estimation. Oxford University Press.
- Kraus MF, Susmaras T, Caughlin BP, et al., 2007. White matter integrity and cognition in chronic traumatic brain injury: a diffusion tensor imaging study. *Brain* 130 (10), 2508–2519.
- Kristo G, Leemans A, Gelder B, et al., 2013a. Reliability of the corticospinal tract and arcuate fasciculus reconstructed with DTI-based tractography: implications for clinical practice. *European Radiology* 23 (1), 28–36.
- Kristo G, Leemans A, Raemaekers M, et al., 2013b. Reliability of two clinically relevant fiber pathways reconstructed with constrained spherical deconvolution. *Magn. Reson. Med.*, In Press.
- Kuhnt D, Bauer MH, Egger J, et al., 2013. Fiber tractography based on diffusion tensor imaging compared with high-angular resolution diffusion imaging with compressed sensing: Initial experience. *Neurosurgery* 72, A165–175.
- Kumar R, Husain M, Gupta RK, et al., 2009. Serial Changes in the White Matter Diffusion Tensor Imaging Metrics in Moderate Traumatic Brain Injury and Correlation with Neuro-Cognitive Function. *Journal of Neurotrauma* 26 (4), 481–495.
- Lange W, 1975. Cell number and cell density in the cerebellar cortex of man and other mammals. *Cell Tiss Res* 157, 115–124.
- Le Bihan D, Breton E, 1985. Imagerie de diffusion in-vivo par resonance magnetique nucleaire. *Comptes-Rendus de l'Académie des Sciences* 93, 27–34.
- Le Bihan D, Mangin JF, Poupon C, et al., 2001. Diffusion Tensor Imaging: Concepts and applications. *Journal of Magnetic Resonance Imaging* 13 (4), 534–546.
- Lebel C, Beaulieu C, 2011. Longitudinal Development of Human Brain Wiring Continues from Childhood into Adulthood. *The Journal of Neuroscience* 31 (30), 10937–10947.
- Lebel C, Caverhill-Godkewitsch S, Beaulieu C, 2010. Age-related regional variations of the corpus callosum identified by Diffusion Tensor tractography. *NeuroImage* 52 (1), 20–31.
- Lebel C, Walker L, Leemans A, et al., 2008. Microstructural maturation of the human brain from childhood to adulthood. *NeuroImage* 40 (3), 1044–1055.
- Leemans A, 2011. Chapter 19: Visualization of Diffusion MRI Data. Oxford University Press.
- Leemans A, Jeurissen B, Sijbers J, et al., 2009. ExploreDTI: a graphical toolbox for processing, analyzing, and visualizing diffusion MR data. In:

References

- Proceedings of the 17th Annual Meeting of International Society for Magnetic Resonance in Medicine, Hawaii, USA. p. 3536.
- Leemans A, Jones DK, 2009. The B-matrix must be rotated when correcting for subject motion in DTI data. *Magnetic Resonance in Medicine* 61 (6), 1336–1349.
- Leemans A, Sijbers J, Backer SD, et al., 2006. Multiscale white matter fiber tract coregistration: A new feature-based approach to align Diffusion Tensor data. *Magnetic Resonance in Medicine* 55 (6), 1414–1423.
- Leemans A, Sijbers J, Verhoye M, et al., 2005. Mathematical framework for simulating Diffusion Tensor MR neural fiber bundles. *Magnetic Resonance in Medicine* 53 (4), 944–953.
- Liu RSN, Lemieux L, Bell GS, et al., 2003. A longitudinal study of brain morphometrics using quantitative Magnetic Resonance Imaging and difference image analysis. *NeuroImage* 20 (1), 22–33.
- Ljungqvist J, Nilsson D, Ljungberg M, Sorbo A, et al., 2010. Longitudinal study of the diffusion tensor imaging properties of the corpus callosum in acute and chronic diffuse axonal injury. *Brain Injury* 32, 370–378.
- Madden D, Bennett I, Song A, 2009. Cerebral White Matter Integrity and Cognitive Aging: Contributions from Diffusion Tensor Imaging. *Neuropsychology Review* 19 (4), 415–435.
- Madsen KS, Baare WF, Skimming A, et al., 2011. Brain microstructural correlates of visuospatial choice reaction time in children. *NeuroImage* 58 (4), 1090–1100.
- Madsen KS, Baare WF, Vestergaard M, et al., 2010. Response inhibition is associated with white matter microstructure in children. *Neuropsychologia* 48 (4), 854–862.
- Malykhin N, Concha L, Seres P, et al., 2008. Diffusion Tensor Imaging tractography and reliability analysis for limbic and paralimbic white matter tracts. *Psychiatry Research: Neuroimaging* 164 (2), 132–142.
- Mansfield P, Pykett I, 1978. Biological and medical imaging by NMR. *Journal of Magnetic Resonance* (1969) 29 (2), 355–373.
- Marquardt D, 1963. An Algorithm for Least-Squares Estimation of Nonlinear Parameters. *Journal of the Society for Industrial and Applied Mathematics* 11, 431–441.
- McNab JA, Edlow BL, Witzel T, et al., 2013. The Human Connectome Project and beyond: Initial applications of 300 mT/m gradients. *NeuroImage In Press* (0).
- McNab JA, Gallichan D, Miller KL, 2010. 3D steady-state diffusion-weighted imaging with trajectory using radially batched internal navigator echoes (TURBINE). *Magn. Reson. Med.* 63 (1), 235–242.
- McNab JA, Jbabdi S, Deoni SC, et al., 2009. High resolution diffusion-weighted imaging in fixed human brain using diffusion-weighted steady state free precession. *NeuroImage* 46 (3), 775–785.
- McNab JA, Miller KL, 2008. Sensitivity of diffusion weighted steady state free precession to anisotropic diffusion. *Magnetic Resonance in Medicine* 60 (2), 405–413.
- Merboldt K, Bruhn H, Frahm J, et al., 1989. MRI of "diffusion" in the human brain: new results using a modified CE-FAST sequence. *Magnetic Resonance in Medicine* 9, 423–429.
- Metzler-Baddeley C, Jones DK, Belaroussi B, et al., 2011. Frontotemporal Connections in Episodic Memory and Aging: A Diffusion MRI Tractography Study. *The Journal of Neuroscience* 31 (37), 13236–13245.
- Metzler-Baddeley C, O'Sullivan MJ, Bells S, et al., 2012. How and how not to correct for CSF-contamination in diffusion MRI. *NeuroImage* 52 (2), 1394–1403.
- Mitra PP, 1995. Multiple wave-vector extensions of the NMR pulsed-field-gradient spin-echo diffusion measurement. *Phys. Rev. B* 51 (21), 15074–15078.
- Moeller S, Yacoub E, Olman CA, et al., 2010. Multiband multislice GE-EPI at 7 tesla, with 16-fold acceleration using partial parallel imaging with application to high spatial and temporal whole-brain fMRI. *Magn. Reson. Med.* 63 (5), 1144–1153.
- Mori S, Crain BJ, Chacko VP, et al., 1999. Three-dimensional tracking of axonal projections in the brain by Magnetic Resonance Imaging. *Annals of Neurology* 45 (2), 265–269.
- Mori S, Oishi K, Jiang H, et al., 2008. Stereotaxic white matter atlas based on diffusion tensor imaging in an {ICBM} template. *NeuroImage* 40 (2), 570–582.
- Moseley M, Cohen Y, Kucharczyk J, et al., 1990. Diffusion-weighted MR imaging of anisotropic water diffusion in cat central nervous system. *Radiology* 176 (2), 439–445.

- Mukherjee P, Miller JH, Shimony JS, et al., 2001. Normal Brain Maturation during Childhood: Developmental Trends Characterized with Diffusion-Tensor MR Imaging. *Radiology* 221 (2), 349–358.
- Neeman M, Freyer J, Sillerud L, 1991. A simple method for obtaining cross-term-free images for diffusion anisotropy studies in NMR microimaging. *Magnetic Resonance in Medicine* 21, 138–143.
- Nimsky C, Ganslandt O, Hastreiter P, et al., 2005. Intraoperative Diffusion-Tensor MR Imaging: Shifting of White Matter Tracts during Neurosurgical Procedures - Initial Experience. *Radiology* 234 (1), 218–225.
- Nimsky C, Ganslandt O, Merhof D, et al., 2006. Intraoperative visualization of the pyramidal tract by diffusion-tensor-imaging-based fiber tracking. *NeuroImage* 30 (4), 1219–1229.
- Niogi SN, Mukherjee P, 2010. Diffusion Tensor Imaging of Mild Traumatic Brain Injury. *Journal of Head Trauma Rehabilitation* 25, 241–255.
- O'Donnell LJ, Westin CF, Golby AJ, 2009. Tract-based morphometry for white matter group analysis. *NeuroImage* 45 (3), 832–844.
- O'Halloran RL, Aksoy M, Van AT, et al., 2012. 3D isotropic high-resolution diffusion-weighted MRI of the whole brain with a motion-corrected steady-state free precession sequence. *Magnetic Resonance in Medicine*, In Press.
- O'Halloran RL, Van AT, Aboussouan E, et al., 2013. Prospective Correction Rigid-Body Motion-Induced Phase for Diffusion-Weighted SSFP Imaging. In: *Proceedings of the 21th Annual Meeting of International Society for Magnetic Resonance in Medicine*, Salt Lake City, United States. p. 3210.
- Oouchi H, Yamada K, Sakai K, et al., 2007. Diffusion Anisotropy Measurement of Brain White Matter Is Affected by Voxel Size: Underestimation Occurs in Areas with Crossing Fibers. *AJNR Am J Neuroradiol* 28 (6), 1102–1106.
- Otsu N, 1979. A Threshold Selection Method from Gray-Level Histograms. *IEEE Transactions on Systems, Man and Cybernetics* 9 (1), 62–66.
- Pajevic S, Pierpaoli C, 1999. Color schemes to represent the orientation of anisotropic tissues from diffusion tensor data: Application to white matter fiber tract mapping in the human brain. *Magn. Reson. Med.* 42 (3), 526–540.
- Papadakis NG, Martin KM, Mustafa MH, et al., 2002. Study of the effect of CSF suppression on white matter diffusion anisotropy mapping of healthy human brain. *Magnetic Resonance in Medicine* 48 (2), 394–398.
- Parker G, Marshall D, Rosin P, et al., 2013. A pitfall in the reconstruction of fibre ODFs using spherical deconvolution of diffusion MRI data. *NeuroImage* 65 (0), 433–448.
- Pasternak O, Sochen N, Gur Y, et al., 2009. Free water elimination and mapping from Diffusion MRI. *Magnetic Resonance in Medicine* 62 (3), 717–730.
- Peeters THJM, Prckovska V, van Almsick R, et al., 2009. Fast and sleek glyph rendering for interactive HARDI data exploration. In: *IEEE Pacific Visualization Symposium*. pp. 153–160.
- Peled S, Friman O, Jolesz F, et al., 2006. Geometrically constrained two-tensor model for crossing tracts in DWI. *Magnetic Resonance Imaging* 24 (9), 1263 – 1270.
- Pfefferbaum A, Sullivan EV, 2003. Increased brain white matter diffusivity in normal adult aging: Relationship to anisotropy and partial voluming. *Magnetic Resonance in Medicine* 49 (5), 953–961.
- Pierpaoli C, Barnett A, Pajevic S, et al., 2001. Water Diffusion Changes in Wallerian Degeneration and Their Dependence on White Matter Architecture. *NeuroImage* 13 (6), 1174 – 1185.
- Pierpaoli C, Jezzard P, Basser PJ, et al., 1996. Diffusion Tensor MR Imaging of the human brain. *Radiology* 201 (3), 637–648.
- Pierpaoli C, Jones DK, 2004. Removing CSF Contamination in Brain DT-MRIs by Using a Two-Compartment Tensor Model. In: *Proceedings of the 12th Annual Meeting of International Society for Magnetic Resonance in Medicine*, Kyoto, Japan. p. 1215.
- Pluim JPW, Maintz JBA, Viergever MA, 2003. Mutual-information-based registration of medical images: a survey. *IEEE Transactions on Medical Imaging* 22 (8), 986–1004.
- Prckovska V, Peeters THJM, Van Almsick M, et al., 2011. Fused DTI/HARDI Visualization. *IEEE Transactions on Visualization and Computer Graphics* 17 (10), 1407–1419.
- Price G, Cercignani M, Parker GJ, et al., 2008. White matter tracts in first-episode psychosis: A {DTI} tractography study of the uncinate fasciculus. *NeuroImage* 39 (3), 949 – 955.

References

- Pruessmann KP, Weiger M, Scheidegger MB, et al., 1999. SENSE: Sensitivity encoding for fast MRI. *Magnetic Resonance in Medicine* 42 (5), 952–962.
- Raffelt D, Smith R, Tournier JD, et al., 2013. Tractographic Threshold-Free Cluster Enhancement: Whole-Brain Statistical Analysis of Diffusion MRI Measures in the Presence of Crossing Fibres. In: *Proceedings of the 21th Annual Meeting of International Society for Magnetic Resonance in Medicine*, Salt Lake City, United States. p. 841.
- Raffelt D, Tournier JD, Rose S, et al., 2012. Apparent Fibre Density: A novel measure for the analysis of diffusion-weighted magnetic resonance images. *NeuroImage* 59 (4), 3976–3994.
- Ramirez-Manzanares A, Cook PA, Hall M, et al., 2011. Resolving axon fiber crossings at clinical b-values: An evaluation study. *Medical Physics* 38 (9), 5239–5253.
- Rathi Y, Malcolm J, Michailovich O, et al., 2010. Biomarkers for Identifying First-Episode Schizophrenia Patients using Diffusion Weighted Imaging. In: *Proceedings of the MICCAI, 2010*, Beijing, China. pp. 657–665.
- Reese T, Heid O, Weisskoff R, et al., 2003. Reduction of eddy-current-induced distortion in diffusion MRI using a twice-refocused spin echo. *Magnetic Resonance in Medicine* 49 (1), 177–182.
- Reich DS, Ozturk A, Calabresi PA, et al., 2010. Automated vs. conventional tractography in multiple sclerosis: Variability and correlation with disability. *NeuroImage* 49 (4), 3047–3056.
- Reijmer YD, Brundel M, de Bresser J, et al., 2013a. Microstructural White Matter Abnormalities and Cognitive Functioning in Type 2 Diabetes: A diffusion tensor imaging study. *Diabetes Care* 36 (1), 137–144.
- Reijmer YD, Leemans A, Caeyenberghs K, et al., 2013b. Disruption of cerebral networks and cognitive impairment in Alzheimer disease. *Neurology* 80, 1370–1377.
- Reijmer YD, Leemans A, Heringa SM, et al., 2012. Improved sensitivity to cerebral white matter abnormalities in Alzheimer's disease with spherical deconvolution based tractography. *PLoS ONE* 7, e44074.
- Reisert M, Kellner E, Kiselev V, 2012. About the Geometry of Asymmetric Fiber Orientation Distributions. *Medical Imaging, IEEE Transactions on* 31 (6), 1240–1249.
- Resnick SM, Pham DL, Kraut MA, et al., 2003. Longitudinal Magnetic Resonance Imaging Studies of Older Adults: A Shrinking Brain. *The Journal of Neuroscience* 23 (8), 3295–3301.
- Rohde GK, Barnett AS, Basser PJ, et al., 2004. Comprehensive approach for correction of motion and distortion in Diffusion-Weighted MRI. *Magnetic Resonance in Medicine* 51 (1), 103–114.
- Sage CA, van Hecke W, Peeters R, et al., 2009. Quantitative Diffusion Tensor Imaging in amyotrophic lateral sclerosis: Revisited. *Human Brain Mapping* 30 (11), 3657–3675.
- Sala S, Agosta E, Pagani E, et al., 2010. Microstructural changes and atrophy in brain white matter tracts with aging. *Neurobiology of Aging In Press*.
- Salat DH, Tuch D, Greve DN, et al., 2005. Age-related alterations in white matter microstructure measured by Diffusion Tensor Imaging. *Neurobiology of Aging* 26 (8), 1215–1227.
- Schachter M, Does M, Anderson A, et al., 2000. Measurements of Restricted Diffusion Using an Oscillating Gradient Spin-Echo Sequence. *Journal of Magnetic Resonance* 147 (2), 232–237.
- Schlaug G, Marchina S, Norton A, 2009. Evidence for Plasticity in White-Matter Tracts of Patients with Chronic Broca's Aphasia Undergoing Intense Intonation-based Speech Therapy. *Annals of the New York Academy of Sciences* 1169 (1), 385–394.
- Scholz J, Klein MC, Behrens TE, et al., 2009. Training induces changes in white-matter architecture. *Nature Neuroscience* 12, 1370–1371.
- Selnes P, Aarsland D, Bjornerud A, et al., 2013. Diffusion Tensor Imaging Surpasses Cerebrospinal Fluid as Predictor of Cognitive Decline and Medial Temporal Lobe Atrophy in Subjective Cognitive Impairment and Mild Cognitive Impairment. *Journal of Alzheimer's Disease* 33 (3), 723–736.
- Setsompop K, Cohen-Adad J, Gagoski B, et al., 2012a. Improving diffusion MRI using simultaneous multi-slice echo planar imaging. *NeuroImage* 63 (1), 569–580.
- Setsompop K, Gagoski BA, Polimeni JR, et al., 2012b. Blipped-controlled aliasing in parallel imaging for simultaneous multislice echo planar imaging with reduced g-factor penalty. *Magn. Reson. Med.* 67 (5), 1210–1224.
- Setsompop K, Kimmlingen R, Eberlein E, et al., 2013. Pushing the limits of in vivo diffusion MRI for

- the Human Connectome Project. *NeuroImage In Press* (0).
- Shattuck DW, Chiang MC, Barysheva M, et al., 2008. Visualization Tools for High Angular Resolution Diffusion Imaging. In: *Proceedings of the MIC-CAI, 2008, New York City, USA*. pp. 298–305.
- Shemesh N, Ozarslan E, Komlosh ME, et al., 2010. From single-pulsed field gradient to double-pulsed field gradient MR: glean new microstructural information and developing new forms of contrast in MRI. *NMR Biomed.* 23 (7), 757–780.
- Sijbers J, den Dekker A, 2004. Maximum likelihood estimation of signal amplitude and noise variance from MR data. *Magn. Reson. Med.* 51 (3), 586–594.
- Skare S, Bammer R, 2010. Jacobian weighting of distortion corrected EPI data. In: *Proceedings of the 18th Annual Meeting of International Society for Magnetic Resonance in Medicine, Stockholm, Sweden*. p. 5063.
- Skare S, Hedehus M, Moseley ME, et al., 2000. Condition Number as a Measure of Noise Performance of Diffusion Tensor Data Acquisition Schemes with MRI. *Journal of Magnetic Resonance* 147 (2), 340–352.
- Skare S, Newbould RD, Clayton DB, et al., 2006. Propeller EPI in the other direction. *Magnetic Resonance in Medicine* 55 (6), 1298–1307.
- Smith SM, Jenkinson M, Johansen-Berg H, et al., 2006. Tract-based spatial statistics: Voxelwise analysis of multi-subject diffusion data. *NeuroImage* 31 (4), 1487 – 1505.
- Smith SM, Jenkinson M, Woolrich MW, et al., 2004. Advances in functional and structural {MR} image analysis and implementation as FSL. *NeuroImage* 23, Supplement 1 (0), S208–S219, <ce:title>Mathematics in Brain Imaging</ce:title>.
- Snook L, Paulson LA, Roy D, et al., 2005. Diffusion tensor imaging of neurodevelopment in children and young adults. *NeuroImage* 26 (4), 1164–1173.
- Sodickson DK, Manning WJ, 1997. Simultaneous acquisition of spatial harmonics (SMASH): Fast imaging with radiofrequency coil arrays. *Magn. Reson. Med.* 38 (4), 591–603.
- Song SK, Sun SW, Ju WK, et al., 2003. Diffusion Tensor Imaging detects and differentiates axon and myelin degeneration in mouse optic nerve after retinal ischemia. *NeuroImage* 20 (3), 1714 – 1722.
- Song SK, Sun SW, Ramsbottom MJ, et al., 2002. Demyelination Revealed through MRI as Increased Radial (but Unchanged Axial) Diffusion of Water. *NeuroImage* 17 (3), 1429 – 1436.
- Sotiropoulos SN, Jbabdi S, Xu J, et al., 2013. Advances in diffusion MRI acquisition and processing in the Human Connectome Project. *NeuroImage In Press* (0).
- Stejskal E, Tanner J, 1965. Spin diffusion measurements: spin echoes in the presence of a time-dependent field gradient. *The Journal of Chemical Physics* 42 (1), 288–292.
- Suarez RO, Commowick O, Prabhu SP, et al., 2012. Automated delineation of white matter fiber tracts with a multiple region-of-interest approach. *NeuroImage* 59 (4), 3690 – 3700.
- Sullivan EV, Pfefferbaum A, 2007. Neuroradiological characterization of normal adult ageing. *British Journal of Radiology* 80 (Special Issue 2), S99–S108.
- Sullivan EV, Rohlfing T, Pfefferbaum A, 2010. Quantitative fiber tracking of lateral and interhemispheric white matter systems in normal aging: Relations to timed performance. *Neurobiology of Aging* 31 (3), 464 – 481.
- Szczepankiewicz F, Latt J, Wirestam R, et al., 2013. Variability in diffusion kurtosis imaging: Impact on study design, statistical power and interpretation. *NeuroImage* 76 (0), 145–154.
- Taoka T, Morikawa M, Akashi T, et al., 2009. Fractional Anisotropy-Threshold Dependence in Tract-Based Diffusion Tensor Analysis: Evaluation of the uncinata fasciculus in Alzheimer disease. *AJNR Am J Neuroradiol* 30 (9), 1700–1703.
- Tax CM, Jeurissen B, Vos SB, et al., 2013. Recursive calibration of the fiber response function for spherical deconvolution of diffusion MRI data. *NeuroImage, In Press*.
- Thudium MO, Campos AR, Urbach H, et al., 2010. The Basal Temporal Approach for Mesial Temporal Surgery: Sparing the Meyer Loop With Navigated Diffusion Tensor Tractography. *Neurosurgery* 67, 385–390.
- Tournier JD, Calamante F, Connelly A, 2007. Robust determination of the fibre orientation distribution in diffusion MRI: Non-negativity constrained super-resolved spherical deconvolution. *NeuroImage* 35 (4), 1459 – 1472.

References

- Tournier JD, Calamante F, Gadian DG, et al., 2004. Direct estimation of the fiber orientation density function from diffusion-weighted MRI data using spherical deconvolution. *NeuroImage* 23 (3), 1176–1185.
- Tournier JD, Mori S, Leemans A, 2011. Diffusion Tensor Imaging and Beyond. *Magnetic Resonance in Medicine* 65 (6), 1532–1556.
- Tuch DS, 2004. Q-ball imaging. *Magn. Reson. Med.* 52 (6), 1358–1372.
- Tuch DS, Reese TG, Wiegell MR, et al., 2002. High angular resolution diffusion imaging reveals intravoxel white matter fiber heterogeneity. *Magnetic Resonance in Medicine* 48 (4), 577–582.
- Tuch DS, Reese TG, Wiegell MR, et al., 2003. Diffusion MRI of Complex Neural Architecture. *Neuron* 40 (5), 885–895.
- Van AT, Aksoy M, Holdsworth S, et al., 2013a. Slab Profile Encoding Reconstruction for Minimizing 'Venetian Blind Artifact' in 3D Diffusion-weighted Multislab Acquisition. In: *Proceedings of the 21th Annual Meeting of International Society for Magnetic Resonance in Medicine*, Salt Lake City, United States. p. 121.
- Van AT, Holdsworth SJ, Bammer R, 2013b. In vivo investigation of restricted diffusion in the human brain with optimized oscillating diffusion gradient encoding. *Magn. Reson. Med.* In press.
- Van Cauter S, Sima D, Croitor Sava A, et al., 2013. Comparison of diffusion kurtosis imaging, dynamic susceptibility weighted imaging and short echo time chemical shift imaging for grading gliomas. In: *Proceedings of the 21th Annual Meeting of International Society for Magnetic Resonance in Medicine*, Salt Lake City, United States. p. 518.
- Van Cauter S, Veraart J, Sijbers J, et al., 2012. Gliomas: Diffusion Kurtosis MR Imaging in Grading. *Radiology* 263 (2), 492–501.
- van der Aa NE, Leemans A, Northington FJ, et al., 2011. Does Diffusion Tensor Imaging-Based Tractography at 3 Months of Age Contribute to the Prediction of Motor Outcome After Perinatal Arterial Ischemic Stroke? *Stroke* 42 (12), 3410–3414.
- Van Hecke W, Leemans A, Backer SD, et al., 2010a. Comparing isotropic and anisotropic smoothing for voxel-based DTI analyses: A simulation study. *Human Brain Mapping* 31 (1), 98–114.
- Van Hecke W, Leemans A, D'Agostino E, et al., 2007. Nonrigid Coregistration of Diffusion Tensor Images Using a Viscous Fluid Model and Mutual Information. *Medical Imaging, IEEE Transactions on* 26 (11), 1598–1612.
- Van Hecke W, Leemans A, Sage CA, et al., 2011. The effect of template selection on diffusion tensor voxel-based analysis results. *NeuroImage* 55 (2), 566–573.
- Van Hecke W, Leemans A, Sijbers J, et al., 2008a. A tracking-based Diffusion Tensor Imaging segmentation method for the detection of diffusion-related changes of the cervical spinal cord with aging. *Journal of Magnetic Resonance Imaging* 27 (5), 978–991.
- Van Hecke W, Nagels G, Leemans A, et al., 2010b. Correlation of cognitive dysfunction and diffusion tensor MRI measures in patients with mild and moderate multiple sclerosis. *J. Magn. Reson. Imaging* 31 (6), 1492–1498.
- Van Hecke W, Sijbers J, D'Agostino E, et al., 2008b. On the construction of an inter-subject Diffusion Tensor Magnetic Resonance atlas of the healthy human brain. *NeuroImage* 43 (1), 69–80.
- Van Hecke W, Sijbers J, De Backer S, et al., 2009. On the construction of a ground truth framework for evaluating voxel-based Diffusion Tensor MRI analysis methods. *NeuroImage* 46 (3), 692–707.
- Veraart J, Sijbers J, Sunaert S, et al., 2013. Weighted linear least squares estimation of diffusion {MRI} parameters: Strengths, limitations, and pitfalls. *NeuroImage* 81 (0), 335–346.
- Verhoeven JS, Sage CA, Leemans A, et al., 2010. Construction of a stereotaxic DTI atlas with full diffusion tensor information for studying white matter maturation from childhood to adolescence using tractography-based segmentations. *Human Brain Mapping* 31 (3), 470–486.
- Vitali P, Maccagnano E, Caverzasi E, et al., 2011. Diffusion-weighted MRI hyperintensity patterns differentiate CJD from other rapid dementias. *Neurology* 76 (20), 1711–1719.
- Voineskos AN, Lobaugh NJ, Bouix S, et al., 2010. Diffusion Tensor tractography findings in schizophrenia across the adult lifespan. *Brain* 133, 1494–1504.
- Voineskos AN, Rajji TK, Lobaugh NJ, et al., 2012. Age-related decline in white matter tract integrity and cognitive performance: A DTI tractography and

- structural equation modeling study. *Neurobiology of Aging* 33 (1), 21–34.
- Vos SB, Aksoy M, J. M, et al., 2013. High-spatial and high-angular resolution diffusion imaging with a fragmented acquisition scheme. In: *Proceedings of the 21th Annual Meeting of International Society for Magnetic Resonance in Medicine*, Salt Lake City, United States. p. 3195.
- Vos SB, Viergever MA, Leemans A, 2011. The anisotropic bias of fractional anisotropy in anisotropically acquired DTI data. In: *Proceedings of the 19th Annual Meeting of International Society for Magnetic Resonance in Medicine*, Montreal, Canada. p. 1945.
- Wakana S, Caprihan A, Panzenboeck MM, et al., 2007. Reproducibility of quantitative tractography methods applied to cerebral white matter. *NeuroImage* 36 (3), 630–644.
- Wakana S, Jiang H, Nagae-Poetscher LM, et al., 2004. Fiber Tract-based Atlas of Human White Matter Anatomy. *Radiology* 230 (1), 77–87.
- Wedeen V, Dai G, 2011. Diffusion-limited diffusion MRI and a universal optimum b-value. In: *Proceedings of the 19th Annual Meeting of International Society for Magnetic Resonance in Medicine*, Montreal, Canada. p. 1965.
- Wedeen V, Wang R, Schmahmann J, et al., 2008. Diffusion spectrum magnetic resonance imaging (DSI) tractography of crossing fibers. *NeuroImage* 41 (4), 1267–1277.
- Wedeen VJ, Hagmann P, Tseng WYI, et al., 2005. Mapping complex tissue architecture with diffusion spectrum magnetic resonance imaging. *Magnetic Resonance in Medicine* 54 (6), 1377–1386.
- Wedeen VJ, Rosene DL, Wang R, et al., 2012a. Response to comment on "The Geometric Structure of the Brain Fiber Pathways". *Science* 337 (6102), 1605.
- Wedeen VJ, Rosene DL, Wang R, et al., 2012b. The Geometric Structure of the Brain Fiber Pathways. *Science* 335 (6076), 1628–1634.
- Westin CF, Maier SE, Mamata H, et al., 2002. Processing and visualization for diffusion tensor MRI. *Medical Image Analysis* 6 (2), 93–108.
- Westlye LT, Walhovd KB, Dale AM, et al., 2009. Life-Span Changes of the Human Brain White Matter: Diffusion Tensor Imaging (DTI) and Volumetry. *Cereb. Cortex* 20 (9), 2055–2068.
- Wheeler-Kingshott CAM, Cercignani M, 2009. About "axial" and "radial" diffusivities. *Magnetic Resonance in Medicine* 61 (5), 1255–1260.
- Wilson M, Tench CR, Morgan PS, et al., 2003. Pyramidal tract mapping by Diffusion Tensor Magnetic Resonance Imaging in multiple sclerosis: improving correlations with disability. *Journal of Neurology, Neurosurgery & Psychiatry* 74 (2), 203–207.
- Witwer BP, Moftakhar R, Hasan KM, et al., 2002. Diffusion-tensor imaging of white matter tracts in patients with cerebral neoplasm. *Journal of Neurosurgery* 97 (3), 568–575.
- Ye W, Portnoy S, Entezari A, et al., 2012. An Efficient Interlaced Multi-Shell Sampling Scheme for Reconstruction of Diffusion Propagators. *Medical Imaging, IEEE Transactions on* 31 (5), 1043–1050.
- Yendiki A, Panneck P, Srinivasan P, et al., 2011. Automated Probabilistic Reconstruction of White-Matter Pathways in Health and Disease Using an Atlas of the Underlying Anatomy. *Frontiers in Neuroinformatics* 5, 1–12.
- Yogarajah M, Focke NK, Bonelli SB, et al., 2010. The structural plasticity of white matter networks following anterior temporal lobe resection. *Brain* 133 (8), 2348–2364.
- Yogarajah M, Powell H, Parker G, et al., 2008. Tractography of the parahippocampal gyrus and material specific memory impairment in unilateral temporal lobe epilepsy. *NeuroImage* 40 (4), 1755–1764.
- Yoshiura T, Wu O, Zaheer A, et al., 2001. Highly diffusion-sensitized MRI of brain: Dissociation of gray and white matter. *Magnetic Resonance in Medicine* 45 (5), 734–740.
- Zarei M, Damoiseaux JS, Morgese C, et al., 2009. Regional White Matter Integrity Differentiates Between Vascular Dementia and Alzheimer Disease. *Stroke* 40 (3), 773–779.
- Zeineh MM, Holdsworth S, Skare S, et al., 2012. Ultra-high resolution diffusion tensor imaging of the microscopic pathways of the medial temporal lobe. *NeuroImage* 62 (3), 2065–2082.
- Zhang H, Hubbard PL, Parker GJ, et al., 2011. Axon diameter mapping in the presence of orientation dispersion with diffusion MRI. *NeuroImage* 56 (3), 1301–1315.
- Zhang J, Evans A, Hermoye L, et al., 2007. Evidence of slow maturation of the superior longitudinal

References

- fasciculus in early childhood by diffusion tensor imaging. *NeuroImage* 38 (2), 239–247.
- Zhang S, Demiralp C, Laidlaw DH, 2003. Visualizing Diffusion Tensor MR Images Using Streamtubes and Streamsurfaces. *IEEE Transactions on Visualization and Computer Graphics* 9, 454–462.
- Zhang Y, Zhang J, Oishi K, et al., 2010. Atlas-guided tract reconstruction for automated and comprehensive examination of the white matter anatomy. *NeuroImage* 52 (4), 1289–1301.

ABBREVIATIONS

AD	axial diffusivity [10^{-3} mm ² /s]
ADC	apparent diffusion coefficient [10^{-3} mm ² /s]
AF	arcuate fasciculus
ALISA	automated longitudinal intra-subject analysis
CC	corpus callosum
CF	crossing fiber(s)
CSD	constrained spherical deconvolution
CSF	cerebrospinal fluid
CST	cortico-spinal tracts
DEC	diffusion-encoded color
DTI	diffusion tensor imaging
DWI	diffusion-weighted imaging / diffusion-weighted image
EPI	echo-planar imaging
FA	fractional anisotropy
FM	forceps major
FT	fiber tractography
HARDI	high-angular resolution diffusion imaging
latCC	lateral projections of the CC
MD	mean diffusivity [10^{-3} mm ² /s]
MRI	magnetic resonance imaging
ODF	orientation distribution function (fiber ODF, fODF; diffusion ODF, dODF)
PVE	partial volume effect
QBI	Q-ball imaging
RD	radial diffusivity [10^{-3} mm ² /s]
ROI	region-of-interest
SF	single fiber(s)
SSCing	superior segment of the cingulum
Tr	Trace [10^{-3} mm ² /s]
UF	uncinate fasciculus
WM	white matter

SAMENVATTING

Analyse- en visualisatiemethoden voor de interpretatie van diffusie MRI data

Achtergrond

Om te begrijpen hoe het brein zich ontwikkelt gedurende ons leven, en wat er in het zieke brein misgaat, is medische beeldvorming van grote waarde. Met behulp van MRI kunnen we, zonder schade aan te richten, scans maken van de hersenen waarop de globale structuur daarin te zien is. Om een zo gedetailleerd mogelijk idee te krijgen van de veranderingen die daar plaatsvinden gedurende ons leven, is het van belang een zo gevoelig mogelijke scantechniek te hebben. Diffusiegewogen MRI, kortweg diffusie MRI, is zo'n zeer gevoelige techniek. Diffusie MRI is gevoelig voor de diffusie van watermoleculen in de hersenen. De witte stof in de hersenen bevat de zenuwuitlopers (axonen) die verschillende gebieden in de grijze stof (ook wel hersenschors of cortex genoemd) verbinden. De structuur van de axonen, zoals het celmembraan en de omringende myelineschede, beïnvloeden de diffusie, wat ervoor zorgt dat watermoleculen makkelijker in de lengterichting van axonen kunnen bewegen dan dwars op de axonen. Dit diffusiepatroon kan gemeten worden met diffusie MRI. Schade aan deze structuren is meestal één van de eerste stappen in het ziekteproces, en de veranderde diffusie die dit ten gevolge heeft is in een heel vroeg stadium van de ziekte waar te nemen op diffusie MRI scans.

Waar diffusie in een glas water isotroop is (gelijk in alle richtingen), zorgt de voorkeursrichting voor diffusie langs de axonen ervoor dat de diffusie in de witte stof anisotroop is, en is dus afhankelijk van de richting waarin je de diffusie meet. Door meerdere scans te maken die elk de diffusie in een andere richting meten kunnen we het diffusiepatroon in de hersenen in kaart brengen. De meest gebruikte methode om dit te beschrijven is diffusietensor MRI (DTI), waar de hoeveelheid en richting van diffusie wordt beschreven met een model. Verschillende kwantitatieve maten kunnen uit dit model gehaald worden, waarvan de twee meest gebruikte de gemiddelde diffusie (mean diffusion, MD) en de fractionele anisotropie (FA) zijn. De MD geeft aan hoeveel

Samenvatting

diffusie er is. De FA is een maat voor hoe sterk de voorkeursrichting van diffusie is langs de axonen: hoe sterker die voorkeursrichting, hoe hoger de FA. Bij schade aan de axonen, vaak microstructurele schade genoemd, ondervinden de watermoleculen minder hinder van de axonale structuur, wat meestal gepaard gaat met een verlaging van de FA en verhoging van de MD. De correlatie tussen de MD/FA en de integriteit van axonen kan van waarde zijn om afwijkingen te detecteren.

Diffusie MRI scans kunnen ook gebruikt worden om de verbindingen tussen hersengebieden te reconstrueren, een concept dat tractografie genoemd wordt. De voorkeursrichting van diffusie is gelijk aan de richting van de axonen, en door deze voorkeursrichting te volgen van voxel naar voxel kunnen er virtuele reconstructies van de vezelbundels in het brein gemaakt worden. Met behulp van anatomische kennis kan dan bijvoorbeeld een specifieke vezelbundel in de witte stof worden geselecteerd. Deze bundels zijn verzamelingen axonen die twee gebieden in de cortex met elkaar verbinden. Dit kan gebruikt op zijn beurt gebruikt worden om de interne structuur van de witte stof te visualiseren.

In de afgelopen jaren is DTI voor wetenschappelijke doeleinden gebruikt om bijvoorbeeld te kijken of er een verschil is tussen groepen patiënten en gezonde controles, hoe het brein ontwikkelt gedurende het groeien, en hoe het brein verouderd. DTI is hiervoor uitermate geschikt, omdat het een heel gevoelige techniek is.

Verbetering van analyse van DTI data

Helaas is de specificiteit van DTI niet optimaal. Dit betekent dat als er een verschil wordt gemeten in de diffusiewaarden tussen twee groepen (bijvoorbeeld tussen patiënten en controles), de oorzaak hiervan niet altijd gerelateerd is aan de onderliggende microstructuur van het weefsel. Een belangrijke reden hiervoor is dat het model van DTI niet 100% nauwkeurig is. Zoals in elk model worden ook in DTI bepaalde aannames gedaan om het model bruikbaar te maken. Eén aanname in DTI is niet correct als vezelpopulaties elkaar kruisen in een voxel. Met de hoge complexiteit van de hersenen, waar heel veel regio's met elkaar verbonden zijn, is dit zeker niet altijd het geval. In voxels waar deze aanname niet correct is, hangen de MD en de FA niet alleen af van de ware microstructuur, maar ook van andere factoren.

Hoofdstukken 2 en 3 hebben tot doel deze specificiteit te verbeteren, door te achterhalen welke andere factoren de MD en FA beïnvloeden. Van de FA is bijvoorbeeld bekend dat in voxels met meerdere vezelpopulaties de FA verlaagd is. De sterke voorkeursrichting van de diffusie langs de axonen is dan aanwezig voor beide populaties, en de uiteindelijke voorkeursrichting is dus minder sterk. De FA in zo'n voxel is dan niet meer een directe weergave van de integriteit van het weefsel. Dit heet het partieel volume effect. In hoofdstuk 2 wordt aangetoond dat als er meerdere vezelpopulaties in één

voxel zijn, dat dan de geschatte MD van die voxel afhankelijk is van de oriëntatie van de vezelpopulaties onderling, en de relatieve volume-fracties in de voxel. Uit simulaties blijkt dat zelfs als de MD van beide kruisende populaties gelijk is, de uiteindelijk geschatte MD niet gelijk is aan de MD van de individuele populaties. Gezien de MD een waarde is die enkel de gemiddelde diffusie in de voxel aangeeft, is deze bevinding dan ook zeer contra-intuïtief.

Een veelgebruikte manier om de gemiddelde FA of MD van specifieke anatomische locaties te berekenen is met behulp van tractografie. De FA-waarden van alle voxels binnen een specifieke witte-stofbundel worden dan gemiddeld tot één waarde per persoon, om vervolgens deze waarde te vergelijken tussen groepen personen. Op de grens van twee vezelbundels zit meestal een rand van voxels met meer dan één bundel, wat de FA en MD dus beïnvloedt. Voor grote vezelbundels is het aantal voxels aan de grens relatief klein en voor kleine vezelbundels is dit aantal relatief groot. Als gevolg hiervan is de invloed van het partieel volume effect groter voor kleinere bundels. In hoofdstuk 3 is te zien dat bundelgrootte een belangrijke factor is die de FA en MD waarden beïnvloedt. Het negeren van deze invloed kan de uitkomst van analyses veranderen, en moet dus worden geïncorporeerd in de analyse en interpretatie van de resultaten. Zo was er alleen een significant verschil tussen mannen en vrouwen in het corpus callosum (de hersenbalk: de structuur die de twee hersenhelften verbindt) als er gecorrigeerd werd voor het verschil in volume van deze bundel tussen mannen dan vrouwen.

Het selecteren van vezelbundels in de hersenen voor zo'n analyse vergt veel handmatig werk, zeker in studies met grote patiëntenpopulaties. Om deze bundelselectie te automatiseren zijn de afgelopen jaren meerdere technieken ontwikkeld. Het gebruik van deze automatische methoden vergt minder of geen handmatig werk, met het nadeel dat de kwaliteit van de bundelselectie niet even hoog is als die van de handmatige methoden. Het gevolg kan zijn dat de diffusiewaarden die berekend worden binnen deze automatisch geselecteerde bundels meer zullen variëren dan in handmatig geselecteerde bundels, en dat er dus minder goed een verschil tussen groepen kan worden waargenomen. Dit probleem is nog relevanter in longitudinale studies, waar gekeken wordt naar het verloop van diffusiewaarden in dezelfde proefpersonen over DTI scans gemaakt op verschillende tijdstippen. Dit soort studies is potentieel zeer gevoelig voor het detecteren van microstructurele veranderingen, omdat er gekeken wordt naar de ontwikkeling binnen personen over een verloop van enkele uren, dagen, maanden, of zelfs jaren in plaats van over groepen op één moment in tijd. Het zou zonde zijn als deze gevoeligheid wordt tenietgedaan door het introduceren van variatie door mogelijk inaccuraat automatische bundelselectie. Om de hoeveelheid handmatig werk in dit soort longitudinale studies te verkleinen wordt in hoofdstuk 4 een methode gepresenteerd die de selectie van vezelbundels automatiseert voor alle scans van één proefper-

Samenvatting

soon. Dit reduceert de hoeveelheid handwerk met een factor die gelijk is aan het aantal scans van iedere persoon, zonder dat de resultaten verslechteren. Het lijkt er zelfs op dat de automatische longitudinale methode een hogere betrouwbaarheid heeft in het selecteren van bundels dan handmatige selectie.

Optimalisatie van scanprotocollen voor tractografie

Het reconstrueren van de verbindingen tussen hersengebieden op basis van diffusie MRI data wordt veel gebruikt om beter te begrijpen hoe ons brein verbonden is, en of er een verschil is in deze verbindingen tussen groepen mensen. Tractografie op basis van DTI maakt gebruik van de geschatte voorkeursrichting van diffusie. Zoals gezegd kan het model inaccuraat zijn als er meerdere vezelpopulaties in een voxel aanwezig zijn. Nieuwere analysetechnieken binnen diffusie MRI maken het mogelijk om per voxel meerdere populaties te modelleren, en dus een betere benadering te krijgen van de onderliggende structuur in het weefsel. Dit verhoogt de kwaliteit van de gereconstrueerde vezelbanen. Om deze microstructurele complexiteit binnen een voxel goed te kunnen modelleren is het nodig het diffusiesignaal te meten onder zoveel mogelijk hoeken, dus met een hoge 'angulaire resolutie' (zogenaamde HARDI-technieken). Om de fijnere structurele details in de hersenen goed te kunnen weergeven is een hoge spatiale resolutie echter ook van belang. Omdat scantijd beperkt is in klinische situaties is het niet haalbaar om een hoge spatiale én een hoge angulaire resolutie te hebben. In hoofdstuk 5 wordt een afweging tussen deze twee factoren beschreven, om te bepalen welke van het grootste belang is voor goede tractografie resultaten. Vanuit de huidige klinische standaard van diffusie MRI scans lijkt het beter om een 'normale' spatiale resolutie (voxels van $2 \times 2 \times 2$ mm) te gebruiken en de scantijd te investeren in een hogere angulaire resolutie.

Verbeterde visualisatie van tractografie-resultaten

De verbeterde karakterisering van het gemeten diffusiesignaal bij HARDI-methoden geeft een meer accurate weergave van de microstructuur per voxel. Kennis van de microstructuur kan helpen bij het begrijpen van mogelijke afwijkingen. Het is daarom van belang de microstructuur zo compleet mogelijk weer te geven. Tractografie is hiervoor een uitermate geschikte methode, omdat het over een langere afstand de locatie en oriëntatie van de lokale vezelpopulaties op een continue wijze laat zien. In hoofdstuk 6 wordt een nieuwe visualisatietechniek gepresenteerd die niet alleen de oriëntatie van de vezelbanen laat zien, maar ook de lokale structuur van het weefsel op elke plek langsheen de vezelbaan. Ten opzichte van huidige voxel-gebaseerde methoden geeft deze visualisatie een meer continue representatie van de lokale structuur, die het interpreteren van de complexe structuur vergemakkelijkt.

Toekomstperspectief

Ondanks de conceptuele beperkingen is diffusietensor MRI nog steeds het meestgebruikte model in diffusie MRI, door het grote gebruiksgemak en korte scantijd. Om de opbrengst van alle toekomstige DTI studies te vergroten is het van essentieel belang te weten hoe we de resultaten moeten interpreteren, en de bevindingen beschreven in dit proefschrift dragen daaraan bij. De komende jaren zal DTI nog gebruikt gaan worden in ontelbare studies naar ziektes van het zenuwstelsel, om te achterhalen wat voor processen zich in het brein afspelen.

Om een nog beter beeld te krijgen van de hersenen zijn er in de laatste jaren methoden gepresenteerd die direct de microstructuur meten op basis van diffusie MRI scans, zoals de diameter van axonen. Als hierin veranderingen gemeten worden is dit direct te relateren aan de axonen zelf, zonder dat andere, versturende, factoren hier invloed op hebben (zoals bij DTI gebeurt in het geval van kruisende vezelbundels). Deze nieuwe technieken vergen echter langere scantijden, wat niet in alle studies haalbaar is. Recente verbeteringen in scantechnieken zorgen ervoor dat het scannen van de MRI data sneller gaat, wat de toepasbaarheid van de nieuwe diffusie MRI technieken vergroot. Het integreren van deze technieken in (klinische) onderzoeksstudies zal dan ook een grote stap vooruit zijn in het begrijpen van de structuur van de hersenen. Op het moment is het echter belangrijk dat we de technieken die we nu gebruiken zo goed mogelijk gebruiken en begrijpen.

PUBLICATIONS

Papers in international journals

C.M.W. Tax, B. Jeurissen, **S.B. Vos**, M.A. Viergever, and A. Leemans, "Recursive calibration of the fiber response function for spherical deconvolution of diffusion MRI data". *NeuroImage*, 2013, In Press.

S.B. Vos, D.K. Jones, B. Jeurissen, M.A. Viergever, and A. Leemans, "The influence of complex white matter architecture on the mean diffusivity in diffusion tensor MRI". *NeuroImage*, 2012, 59 (3), pages 2208-2216.

S.B. Vos, D.K. Jones, M.A. Viergever, and A. Leemans, "Partial volume effect as a hidden covariate in DTI analyses". *NeuroImage*, 2011, 55 (4), pages 1566-1576.

S.B. Vos, M.A. Viergever, A. Leemans, "Multi-fiber tractography visualizations for diffusion MRI data". Submitted.

S.H. Aarnink, **S.B. Vos**, A. Leemans, T.L. Jernigan, K.S. Madsen, and W.F.C. Baaré, "Automated Longitudinal Intra-Subject Analysis (ALISA) for diffusion MRI tractography". Submitted.

A.T. Van, M. Aksoy, S.J. Holdsworth, D. Kopeinigg, **S.B. Vos**, R. Bammer. "Slab profile encoding (PEN) for minimizing slab boundary artifact in 3D diffusion-weighted multislab acquisition". Submitted.

J.R. Maclaren, Z. Han, **S.B. Vos**, N. Fischbein, R. Bammer. "Test-retest reliability of brain volume measurements". Submitted.

Book chapters

S.B. Vos, C.M.W. Tax, and A. Leemans, “Diffusion MRI and fiber tractography: The State-Of-The-Art and its Potential Impact on Patient Management”, PET Clinics 8:3 PET/MRI and Evolving Techniques, eds. T.C. Kwee, H. Zaidi, published by Elsevier B.V.

C.M.W. Tax, **S.B. Vos**, and A. Leemans, “Checking and correcting DTI data”, Practical Handbook of DTI, eds. W. van Hecke, L. Emsell, S. Sunaert, to be published by Springer B.V.

Conference abstract (first-author only)

S.B. Vos, C.M.W. Tax, and A. Leemans, “Importance of tractography seeding resolution for super-resolution in tract density imaging”. ISMRM workshop on ‘Diffusion as a Probe of Neural Tissue Microstructure’, Podstrana, Croatia, 2013.

S.B. Vos, M. Aksoy, Z. Han, S.J. Holdsworth, C. Seeger, J. Maclaren, A. Brost, A. Leemans, R. Bammer, “HARDI and fiber tractography at 1 mm isotropic resolution”. ISMRM, Salt Lake City, United States, 2013, p. 842.

S.B. Vos, M. Aksoy, J. Maclaren, Z. Han, S.J. Holdsworth, A. Brost, C. Seeger, A. Leemans, R. Bammer, “High-spatial and high-angular resolution diffusion imaging with a fragmented acquisition scheme”. ISMRM, Salt Lake City, United States, 2013, p. 3195.

S.B. Vos, M.A. Viergever, A. Leemans, “Visualizing fiber pathways in regions with complex white matter architecture”. ISMRM, Melbourne, Australia, 2012, p. 1914.

S.B. Vos, M.A. Viergever, A. Leemans, “Tract Coherence Imaging (TCI): Quantifying the intra-voxel fiber tract heterogeneity”. ISMRM, Melbourne, Australia, 2012, p. 3586.

S.B. Vos, D.K. Jones, M.A. Viergever, A. Leemans, “The anisotropic bias of fractional anisotropy in anisotropically acquired DTI data”. ISMRM, Montreal, Canada, 2011, p. 1945.

S.B. Vos, M.A. Viergever, A. Leemans, “The appearance of the apparent diffusion coefficient in complex fiber architecture”. ISMRM, Montreal, Canada, 2011, p. 1999.

S.B. Vos, D.K. Jones, M.A. Viergever, A. Leemans, “Mean diffusivity changes in crossing fibers voxels in DTI”. CONNECT meeting Tel Aviv, Israel, 2011.

S.B. Vos, D.K. Jones, M.A. Viergever, A. Leemans, “Partial volume effect as a hidden covariate in tractography based analyses of fractional anisotropy: Does size matter?”. ISMRM, Stockholm, Sweden, 2010, p. 113.

PRIZES AND AWARDS

Summa Cum Laude Award at the 2013 ISMRM meeting for the work titled: “HARDI and Fiber Tractography at 1 mm isotropic resolution”.

“Best Movie Award” in the Art of Neuroscience competition, part of the Brain Awareness Week 2013. Submission titled “The intergalactic brain”.

White Matter Study Group “Best Poster Award” at the 2012 ISMRM meeting for the work titled: “Tract Coherence Imaging (TCI): Quantifying the intra-voxel fiber tract heterogeneity”.

“Best first article award 2011” at the ImagO graduate school conference (“Partial volume effect as a hidden covariate in DTI analyses”).

Nominated for the White Matter Study Group “Best Poster Award” at the 2011 ISMRM meeting for the work titled: “The appearance of the apparent diffusion coefficient in complex fiber architecture”.

Educational ISMRM stipend:

- ISMRM diffusion workshop on “Diffusion as a Probe of Neural Tissue Microstructure”, Podstrana, Croatia, 2013;
- 20th annual ISMRM meeting in Melbourne, Australia, 2012;
- 19th annual ISMRM meeting in Montreal, Canada, 2011;
- 18th annual ISMRM meeting in Stockholm, Sweden, 2010.

DANKWOORD

De lijst van mensen die op welke manier dan ook aan de totstandkoming van dit proefschrift hebben bijgedragen is gigantisch. Graag zou ik iedereen hier uitgebreid bedanken, maar ik beperk me tot de meest belangrijke mensen om niet meer pagina's dankwoord te hebben dan hoofdstukken.

Alexander, voor mij is het onmogelijk te bedenken hoe de afgelopen vier jaar er uit hadden gezien zonder jouw invloed: ik had me geen betere begeleider kunnen voorstellen. Al bij de eerste twee keren dat we elkaar spraken, mijn sollicitatiegesprekken, was het duidelijk dat jij een overschot aan ideeën had waar geen tien promovendi tegenop konden werken. Die gezonde bron van ideeën werkte erg motiverend, en was een constante herinnering wat mij ten doel stond als ik in het wetenschapswereldje verder wilde. Met alle project-gerelateerde details vaak al over Skype besproken hadden we in onze, vaak ongeplande, gesprekken de tijd de belangrijkste zaken van het leven, en de wetenschap te bespreken. Mede daardoor heb ik het idee dat ik qua output, kennis, en ervaring op geen enkele manier meer uit mijn PhD had kunnen halen.

Beste Max, ik waardeer en bewonder hoe je naast alle officiële taken nog zo veel tijd en energie kunt hebben voor het begeleiden van iedereen bij het ISI. Hoewel de puur inhoudelijke aspecten vaak al met Alexander tot in de puntjes besproken waren, zijn er nog genoeg aspecten van mijn proefschrift, en zeker mijn vorming als wetenschapper, waar jouw inbreng van onschatbare waarde is geweest. De kunst van de politiek in de wetenschap, en alles dat daarbij komt kijken, bezit je tot in de puntjes, en ik ben je zeer dankbaar voor alle gesprekken die we daar gepland en ongepland over gehad hebben. Ik verwacht in mijn verdere carrière hier nog veel gebruik van te gaan maken.

Roland, as a group leader at Stanford University, my request for a research visit to your lab must have been one out of many, and I am incredibly grateful for the opportunity you have given me to join you and the wonderful group of scientists and people you have gathered around you. I must admit I still can't believe that it only took four emails over a single weekend from my initial request to your invitation. Similarly, I can't believe how fast the six-month visit was over. I have greatly enjoyed my time working with

Dankwoord

you, and would have loved to continue working on the topic if situations would have allowed it. Your technical knowledge on diffusion acquisition techniques, as well as your vision on the future of diffusion MRI is something I value greatly. I really appreciate your support, continuing long after I left your lab.

Geachte leden van de promotie-commissie: prof. dr. Biessels, prof. dr. Braun, prof. dr. Lagendijk, prof. dr. Niessen, and prof. dr. Norris. Dank voor het beoordelen van mijn proefschrift. Ik kijk er naar uit met u in discussie te gaan over de inhoud van mijn proefschrift.

Mijn beide paranimfen, Hans en Hugo. Hans, ik durf er bijna op te wedden dat ik de afgelopen vier jaar vaker jou gemaïld heb dan alle andere mensen bij elkaar, en zo hoort het :) Alle frustraties die ik gemaïld heb hadden bijna een therapeutische werking, en het tot in detail uitleggen waarom iets niet werkte, ware het nu in Matlab of qua schrijven, was vaak genoeg om de oplossing al te zien. Gelukkig deed de overvloed aan digitale interactie niet af aan de daardwerkelijke interactie, of dat nu poolen, spelletjes, eten, bieren, voetbal, jammien, of whatever was. Hugo, hoewel het imago van ons als roddeltantes natuurlijk ver overdreven is, heb ik me erg goed vermaakt met al het niet-roddelen tussen ons onderling, en met de rest van de gang. Het feit dat we samen begonnen zijn en netjes gelijk zijn blijven lopen qua planning was een mooie competitie, en het heeft me in de laatste maanden erg geholpen met jou te hebben over alle thesis-gerelateerde dingen. Een betere partner-in-crime voor Ardennenweekenden, Sinterklaasgedichten, de tien-over-vier moppen, en promotiestukjes had ik me niet kunnen wensen. Ik heb geen enkele twijfel dat jullie de twee beste personen zijn mij bij te staan in mijn verdediging.

Derek, it has been a true pleasure collaborating with you in these past years. Your input in Chapters 2 and 3 has strongly improved their message and clarity. I appreciate it that even at the busiest of conferences you have taken the time for a quick chat and discussion, not just about current projects but about my future as well.

To all my colleagues at Stanford, I'd like to thank you all for welcoming me at the Lucas Center. Julian and Daniel most of all: for all the times up Windy Hill and any other rides we did, but mostly for the openness with which you regard other people. With such characters, it is no surprise you have such wonderful wives/girlfriends as Jana and Erica, to which my gratitude also extends for all the times you opened your houses to me for dinner, beers, and freshly-baked pancakes. Alex, ever since our banishment to the 'no-light' zone, we've had some great fun during coffee breaks, meetings, drinks, and dinners. I hope you find as much joy in your next job(s) as I've had in mine. Murat and Sam, I cannot believe how much I have learned from you guys on diffusion acquisition and recon! Your knowledge and experience is amazing, and it has been my

privilege to have had you as go-to people to hassle anytime I was stuck on something. Murat: generic. Is. Awesome. Period. It might never be all that you wish it to be, but it is an amazing feat to have created such a sequence environment. Natalie, thanks for your cakes, and your dedication in our scanning sessions. Donna, thanks again for all your effort in helping me with those tons of official documents. Many thanks as well to the other members of the 'Bammergroup' family, Anh, Chris, Eric, Eric, Heiko, Melvyn, Raf—and of course Andreas, Emily, and Prachi (it doesn't matter how often you say you're not part of the group, you are): you have all made my stay a wonderful time that I wouldn't have missed for the world!

Michiel, ik was erg blij om de eerste dagen in Californië iemand te hebben om me met de basisdingen te helpen. Hoewel we elkaar daarvoor slechts enkele keren kort gesproken hebben was je openheid en behulpzaamheid een grote steun in de eerste weken daar. De avonden in 'the Attic', San Mateo, waren fantastisch, met onze Hollandse blik op de Amerikaanse barcultuur, en de gesprekken over werk, sport, en privé waren voor mij zeer mooie uitstapjes uit mijn voornamelijk Palo Alto-centered wereldje.

Maaïke, in de korte tijd dat je in 2011 bij het ISI hebt gezeten hebben we elkaar aardig snel gevonden, eerst als 'naar-huis-fiets' buddy en snel daarna als 'ach, laten we nog maar ergens een drankje gaan doen na de borrel' persoon. Superleuk dat we de avonden gezelligheid zonder moeite weer opgepakt hebben toen je terug in 't land was. Ik hoop dat we dat nog vaak zullen doen.

Maartje, mijn standaard vrijdagmiddagborrel-maatje van de eerste jaren. Gezellig dat we als collega's en oud-collega's zo vaak zijn wezen borrelen. Onze gesprekken over naar het buitenland gaan hebben erg geholpen, zowel in die keuze zelf als met alles wat daar bij komt kijken. Al een goed sushi-restaurant gevonden daar?

Nynke, het was geweldig al die tijd bij jou op de kamer te zitten, we hebben super veel plezier gehad op de kamer.

Chantal, op de ISMRM in Melbourne bleek al dat je supergemotiveerd en -getalenteerd was, en mede daardoor heb ik ontzettend veel gehad aan de discussies die we gevoerd hebben over de projecten waar we samen aan gewerkt hebben. Voor het geval je 't vergeet als ik weg ben: don't worry :)

Mede-musISI Robin, Mieke, Floris, Nynke, Pim, en Chantal: onze oefensessies heb ik erg veel lol aan beleefd, zowel het spelen zelf als de gezellige pizza-eet-pauzes en de drankjes achteraf. Hoe klein en amateuristisch ook, het concertje op het Ardennen-weekend vond ik erg gaaf.

Dankwoord

Yael, ik heb het al die jaren heel leuk gevonden om de klinische kant van het diffusie MRI onderzoek te bespreken met je, en hoop dat ons project de komende maanden dan eindelijk echt af komt.

Jacqueline, Marjan, en Renée, heel erg bedankt dat vragen over randzaken rondom promoveren altijd met één bezoekje of belletje snel door jullie geregeld werd.

I like to thank my coauthors, all of whom have had a great influence on the papers.

A very big thanks to all other colleagues from within and outside of the ISI, for all the great times during work, after-work drinks, pre/post-conference trips, conferences, conference after-parties, courses, and other meetings: dankjewel/thanks/tak/tack/ grazie/danke for making those occasions extremely enjoyable.

Fi, Pjotr, Mike, en Samme, bedankt voor de maandelijkse uitvluchten naar het Shavnar-continent. Zowel de serieuze speelsessies als de middagen vol met onzin waren heerlijk! Om gelijke redenen, Sebas, wil ik jou bedanken voor alle Werewolf- en Mage-sessies, en vooral de gezelligheid de afgelopen jaren buiten RPG.

Anette, allereerst natuurlijk bedankt voor de introductie van Tripel Karmeliet, en alle andere keren dat we gezellig in de stad een biertje zijn gaan drinken. Je tips als promotie-ervaringsdeskundige hebben voor wat extra rust gezorgd tijdens mijn promotie. Kimmy, onze gezellige squash-dates direct na werk waren goed om de gedachten gelijk even te verzetten. Walter en Dominique bedankt voor de lol tijdens en na de jamsessies, wat kan muziek toch heerlijk zijn. Hanneke, Hylkje, Jeroen voor alle gezellige etentjes of borrels in Utrecht, Amsterdam, of nog verder weg.

Elmer en Elma, wat fijn om te weten dat ik altijd jullie volledige steun heb, ook al leidt het me soms tijdelijk weg van jullie. De weekendjes weg waren heerlijk! Femke, ik vind het supergezellig dat wij nu goed als vrienden met elkaar omgaan.

Arna, mijn gevoel van thuis-zijn bij jou was een gevoel van rust dat ik naast alle drukte zo hard nodig had, en blijf hebben. Onze vele verre vakanties waren echt super, en de ontspannende weken in de Atlas, Californië en op Sardinië hebben er voor gezorgd dat mijn hoofd niet geëxplodeerd is van drukte, en dat we in al die mooie reizen nog beter elkaar zijn gaan aanvoelen. Behalve in de laatste maanden van thesis-stress was het altijd mogelijk in jouw armen even mijn gedachten te resetten. Dat dat in 2012 lange tijd niet mogelijk was heeft daar niets aan veranderd, en mijn respect en liefde voor jou alleen maar vergroot.

ABOUT THE AUTHOR

Sjoerd Vos werd op 3 april 1986 geboren in Utrecht, waarna hij opgroeide in Maarssen. In 2004 behaalde hij het VWO diploma aan RSG Brokledede, in Breukelen. Die september begon hij zijn bachelor-studie Medische Natuurwetenschappen aan de Vrije Universiteit Amsterdam, een studie die alle aspecten van de exacte wetenschappen beslaat. September 2007 begon hij zijn master Medical Natural Sciences, waarin hij zich specialiseerde in Medical Physics. Het onderzoek van zijn master thesis deed hij bij de afdelingen Radiologie en Fysica en Medische Technologie op het VU Medisch Centrum, waar hij werkte aan automatische brein volume metingen op basis van MRI scans van multiple sclerose patienten. Na zijn afstuderen in september 2009 begon hij zijn promotieonderzoek bij het Image Sciences Instituut binnen het UMC Utrecht. Een deel van zijn onderzoek heeft hij uitgevoerd tijdens een bezoek van zes maanden aan het Radiological Sciences Lab en het Center for Quantitative Neuroimaging bij Stanford University, in Californië, de Verenigde Staten. Hier heeft hij samengewerkt met Roland Bammer op hoge-resolutie acquisities van diffusiegewogen MRI. Het werk van zijn promotie is gebundeld in dit proefschrift.

Sjoerd Vos was born on April 3 1986 in Utrecht, the Netherlands. He finished high school in the summer of 2004, graduating from RSG Brokledede, Breukelen. September 2004 he started his science-wide bachelor's program 'Medical Natural Sciences' at the VU University in Amsterdam. For his Master's he specialized in 'Medical Physics'. The research for his master's thesis was performed at the departments in Radiology and Physics and Medical Technology at the VU University Medical Center, where he worked on improving automated brain volume measurements from MRI scans for MS patients. Following graduation in September 2009, he started a PhD at the Image Sciences Institute, within the University Medical Center Utrecht, the Netherlands. During his PhD he spent six months at the Radiological Sciences Lab and the Center for Quantitative Neuroimaging at Stanford University, working with Roland Bammer on high-resolution diffusion MRI acquisitions. The results of this work are described in this thesis.